

Development of Biomimetic Microfluidic Platforms for Cellular Interaction Studies

A DISSERTATION  
SUBMITTED TO THE FACULTY OF  
UNIVERSITY OF MINNESOTA  
BY

Xiaojie Wu

IN PARTIAL FULFILLMENT OF THE REQUIREMENTS  
FOR THE DEGREE OF  
DOCTOR OF PHILOSOPHY

Christy L. Haynes, Advisor

August, 2016



## Acknowledgements

I feel very grateful to have the opportunity to study Chemistry at University of Minnesota and the experience of studying abroad is very memorable and valuable to me.

First of all, I would like to sincerely and deeply thank my advisor, Christy Haynes, for her continuous support during my doctoral studies. She is dedicated to create a free and comfortable working environment for every student working in the lab. Her patience, motivation, immense knowledge, leadership, and passion, all these characteristics impact me and I learned enormous things from her. As a non-native speaker, I also got a lot of guidance on English writing and presentation skills from my advisor. I could not have imaged having a better advisor and mentor for my PhD study and I am very proud to be one of the graduates from this group.

I am very lucky to work with all the talented people in the Haynes group. I would like to appreciate the help from Dr. Donghyuk Kim, who transferred me all the experimental techniques and led me enter the field of microfluidics. I would like to thank Dr. Sarah Gruba, Dr. Zhe Gao, Ashlyn Young, Molly Newbold, and Emily Cliff, and I really enjoy working together with these people in my research. Dr. Yu-Shen Lin, Dr. Melissa Maurer-Jones, Dr. Secil Koseoglu, Dr. Ben Manning, Dr. Audrey Meyer, Dr. Antonio Campos, Dr. Solaire Finkenstaedt-quinn, Dr. Katie Hurley, Dr. Ian Gunsolus, Dr. Hattie Ring, Victoria Szlag, Tian Qiu, Joseph Buchman, Sunipa Parmanik, Bo Zhi, Hyunho Kang, I am very grateful to all of them for their help in my research and life. I truly believe all the lab mates graduated from our group will be very successful in the future.

Last but not least, I want to express my gratitude to my parents and especially my wife. I would not have been able to finish my PhD degree without their continuous support and encouragement in the last five years. My wife, Mengjiao Sun, the most important person in my life, has sacrificed so much to support my career.

## **Dedication**

This dissertation is dedicated to my family: my father, Xili Wu, my mom, Shuwei Wang, and my wife, Mengjiao Sun.

## Abstract

Achieving a better understanding of cellular interactions with other critical components in physiological microenvironments is an urgent challenge due to the fact that critical cellular behaviors are delicately regulated by the complexity of the biological system. Factors influencing cellular behaviors include interactions with the surrounding cell types and biological molecules, as well as a range of biophysical factors, such as pressure, flow, and chemical gradients. With a better understanding of environmental impacts on cellular behaviors, mechanistic insights on the pathogenesis of diseases and advances in medical treatment will be provided.

Because the technical difficulties of traditional cell assays have limited the systematic study of cellular interactions, novel platforms with the ability to represent cellular interactions in a quick, spatiotemporal-resolved, and biomimetic manner would be welcomed by the research community. Microfluidics, one of the novel techniques used frequently for cell biology studies, is able to introduce the cellular interactions into an *in vivo*-like microenvironment with high spatiotemporal resolution, also allowing the quantification of cellular behaviors at the single cell level. The aim of this thesis is to develop biomimetic microfluidic platforms to mechanistically study cellular interactions in the context of different biological processes. First, Chapter 1 of this thesis reviews the application of microfluidics in the field of cellular interactions with focus on advances of microfluidics in single cell analysis and *in vivo*-like microenvironment generation. The following chapters separately discuss the topics including cell-drug interactions (Chapter 2), cell migration within complex gradient patterns (Chapter 3), the interactions between

cell migration and angiogenesis growth (Chapter 4), heterotypic cellular interactions in a biomimetic environment (Chapter 5), and the effects of shear rates on cellular adhesion behaviors (Chapter 6).

In Chapter 2, we developed a microfluidic platform containing stable chemical gradients to assess the drug effects on neutrophil migration, which is the key characteristic of inflammatory diseases. By tracking the migration of single neutrophils, we achieved quantification of various parameters, including average velocity, orientation, and overall effectiveness of migration. In addition to examining neutrophil migratory behaviors, the cytotoxicity of drug candidates was also evaluated to reveal a comprehensive understanding about the drug effects on neutrophil function. In Chapter 3 and 4, we continued to study neutrophil migration in more complicated *in vivo*-like microenvironments. To be specific, a three-dimensional endothelial cell layer was cultured in the microfluidic channel, and neutrophil transendothelial migration was monitored under various chemical gradient patterns such that the competitive and synergistic effects among different cytokine molecules were determined. Furthermore, the interactions between neutrophil migration and endothelial angiogenesis were studied by inducing angiogenic growth of the endothelial cell layer in the microfluidic channel. We found that larger endothelial cell angiogenic growth area induced significantly more neutrophil migration while the process of neutrophil migration was able to stabilize the endothelial cell structure even in the presence of an angiogenesis inhibitor that decreases the angiogenic growth of endothelial cells. After detailed evaluation of neutrophil migration in different conditions, a biomimetic microfluidic model was used in Chapter 5

to study heterotypic cellular interactions between endothelial cells and HeLa cancer cells. Three critical environmental factors, including chemical gradients, flow rate, and hypoxia, were separately introduced into the microfluidic model to determine the effect of each factor on cellular interactions. Also, all these three factors were combined together into a single microfluidic device to investigate the overall effects on cellular interactions, which provides an *in vitro* approach to predict the cellular behaviors in the context of cancer. In the last chapter (Chapter 6), a simple microfluidic system was established to explore the relationship between shear rates and cell adhesion behaviors. Two major blood cell types, platelets and neutrophils, were injected through the endothelial cell covered-microfluidic channels with different dimensions, and the results suggest that the expression of receptor molecules participating in the cell adhesion is selective to the dimension of microfluidic channel. This conclusion reveals the novel insights on the mechanisms of cell adhesion in various shear rate conditions and provides deeper understandings about the pathogenesis of blood-based diseases.

Overall, the research presented in this thesis focuses on using microfluidic platforms to characterize cellular interactions with biological complexity, in hopes of advancing our understanding about cellular behaviors in the pathogenesis of relevant diseases. All the findings reported in this thesis indicate that the application of microfluidic platform enables the recapitulation of *in vivo* physiological microenvironments and predicts the cellular behaviors occurring in human body, successfully bridging the gap between current *in vitro* and *in vivo* approaches.

## Table of Contents

Acknowledgements	i
Dedication	ii
Abstract	iii
List of Tables	xii
List of Figures	xiii
List of Abbreviations and Symbols	xx

### Chapter 1

<b>Development of Biomimetic Microfluidic Platform for Cellular Interaction Studies</b>	<b>1</b>
1-1. Introduction	2
1-2. Microfluidics in the study of cellular interactions	3
1-3. Single cell analysis in cellular interactions	4
1-3-1. Microfluidics for single cell manipulation	6
1-3-1-1. Magnetic manipulation	6
1-3-1-2. Optical manipulation	8
1-3-1-3. Mechanical manipulation	9
1-3-1-4. Dielectrophoretic manipulation	10
1-3-1-5. Other manipulation	11
1-3-2. Microfluidics for single cell detection	12
1-3-2-1. Single cell activation and secretion	12
1-3-2-2. Quantitative analysis of cell migration	14

1-3-2-3. Pharmaceutical research	16
1-4. Reconstitution of <i>in vivo</i> microenvironments	17
1-4-1. Reconstitution of biophysical and biochemical complexity	17
1-4-1-1. The interactions between cells and flow	19
1-4-1-2. Hypoxic effects on cellular responses	20
1-4-1-3. Biomimetic cell-cell interaction models	21
1-4-2. Organ-on-a-chip	22
1-4-2-1. Lung-on-a-chip	22
1-4-2-2. Liver-on-a-chip	24
1-4-2-3. Heart-on-a-chip	25
1-4-2-4. Body-on-a-chip	25
1-5. Conclusions	26

## **Chapter 2**

<b>Exploring Inflammatory Disease Drug Effects on Neutrophil Function</b>	29
2-1. Introduction	30
2-2. Experimental details	34
2-2-1. Device fabrication	34
2-2-2. Neutrophil isolation	35
2-2-3. Cell viability assay	36
2-2-4. Microfluidic chemotaxis experiments	37
2-2-5. Analysis of chemotaxis data	38

2-2-6. Calcium imaging	39
2-3. Results and discussion	40
2-3-1. Confirmation of chemical gradients in microfluidic device	40
2-3-2. Neutrophil viability after drug treatment	42
2-3-3. Neutrophil chemotaxis with drug incubation	45
2-3-4. Intracellular calcium imaging	49
2-4. Conclusions	51

### **Chapter 3**

#### **Recapitulation of *in vivo*-like Neutrophil Transendothelial Migration using a Microfluidic Platform**

	54
3-1. Introduction	54
3-2. Experimental details	57
3-2-1. Device fabrication	57
3-2-2. Endothelial cell culture	58
3-2-3. Device preparation	58
3-2-4. Neutrophil isolation	60
3-2-5. Neutrophil transendothelial migration experiments	60
3-2-6. Receptor expression	62
3-2-7. Numerical simulation and fluorescence imaging	62
3-2-8. Confocal imaging	63
3-3. Results and discussion	64

3-3-1. Characterization of neutrophil TEM system	64
3-3-2. Neutrophil TEM under single chemoattractant gradients	69
3-3-3. The role of endothelial cell layer in neutrophil transmigration	76
3-3-4. Neutrophil TEM under competing chemoattractant gradients	81
3-3-5. Synergistic chemoattractant effects on neutrophil TEM	84
3-4. Conclusions	89

## **Chapter 4**

### **A Versatile Microfluidic Platform for the Study of Angiogenesis and**

<b>Inflammation</b>	91
4-1. Introduction	92
4-2. Experimental details	95
4-2-1. Device fabrication	95
4-2-2. Endothelial cell culture and neutrophil isolation	96
4-2-3. Device preparation	97
4-2-4. Neutrophil migration experiments	98
4-2-5. Angiogenesis inhibitor experiments	101
4-2-6. Receptor expression	105
4-2-7. Numerical simulation and fluorescence gradient imaging	107
4-2-8. Confocal imaging	107
4-3. Results and discussion	108
4-3-1. Characterization of the microfluidic device	108

4-3-2. Neutrophil migration with endothelial angiogenesis	115
4-3-3. The effects of an angiogenesis inhibitor on neutrophil migration	123
4-3-4. The effects of neutrophils on the stability of the angiogenesis structure	129
4-4. Conclusion	134

## **Chapter 5**

### **Microfluidic Study of Endothelial Cell-HeLa Cell Interactions under Biomimetic**

<b>Conditions</b>	136
5-1. Introduction	137
5-2. Experimental details	140
5-2-1. Device fabrication	140
5-2-2. Cell culture	141
5-2-3. Device preparation	141
5-2-4. Cell co-culture experiments	143
5-2-5. Numerical simulation	147
5-2-6. Fluorescence imaging and permeability measurement	148
5-2-7. Confocal imaging	149
5-3. Results and discussion	149
5-3-1. Characterization of the cell co-culture model	149
5-3-2. The effects of chemical gradients	154
5-3-3. The effects of flow rate	164
5-3-4. The hypoxic and the combined effects	172

5-4. Conclusion	180
-----------------	-----

## **Chapter 6**

<b>Platelet and Neutrophil Adhesion Study Using Microfluidic System</b>	182
6-1. Introduction	183
6-2. Experimental details	185
6-2-1. Device fabrication	185
6-2-2. Cell culture and isolation	185
6-2-3. Endothelial cell coating of a microfluidic channel	187
6-2-4. Cell injection experiments	188
6-2-5. Surface adhesion molecule expression of endothelial cells	189
6-2-6. The effects of flow rate on platelet and neutrophil aggregation	189
6-3. Results and discussion	190
6-3-1. Characterization of the microfluidic system	190
6-3-2. Platelet adhesion	192
6-3-3. Neutrophil adhesion	199
6-3-4. The interactions between neutrophils and platelets	203
6-4. Conclusions	208
Perspective	212
References	214
Curriculum Vitae	226

## List of Tables

### Chapter 4

Table 4-1. The results of neutrophil numbers and projected angiogenic endothelial cell area of three different conditions analyzed by two researchers.	103
Table 4-2. The intraclass correlation coefficient results calculated by SPSS Statistics software.	104

## List of Figures

### **Chapter 1**

Figure 1-1. Microfluidic devices for single cell manipulation.	7
Figure 1-2. Microfluidic devices for single cell detection.	13
Figure 1-3. Reconstitution of biophysical and biochemical microenvironments using microfluidic devices.	18
Figure 1-4. Organ-on-a-chip systems.	23

### **Chapter 2**

Figure 2-1. Simplified schematic diagram of the IL-8 signaling pathway in neutrophil chemotaxis.	32
Figure 2-2. Trajectories of neutrophils in the control sample and schematic of the microfluidic gradient device used in the experiment.	41
Figure 2-3. Cytotoxic effects of each drug on neutrophil viability, as determined by the MTT assay.	44
Figure 2-4. The inhibitory effects of each drug on neutrophil chemotaxis.	46
Figure 2-5. The effects of theophylline on mobilization of intracellular $Ca^{2+}$ activated by 10 ng/mL IL-8.	50

### **Chapter 3**

Figure 3-1. Characterization of neutrophil TEM microfluidic device.	65
Figure 3-2. Fluorescence gradients along different directions in the gel chamber.	67

Figure 3-3. Confocal images of endothelial cell layer in three different microfluidic devices.	68
Figure 3-4. Bright-field images of neutrophil TEM after 5 h neutrophil injection under single chemoattractant gradients.	71
Figure 3-5. Quantitative analysis of neutrophil TEM after 1 h and 5 h neutrophil injection under various single chemoattractant gradients.	72
Figure 3-6. Comparison of gradient profiles in single chemoattractant gradients and no gradient conditions.	73
Figure 3-7. Neutrophil migration results under no gradient conditions.	74
Figure 3-8. SEM images of collagen gel porous fiber structure and the morphological changes of neutrophils.	77
Figure 3-9. Bright-field images of neutrophil transmigration without endothelial cells at 5 h after neutrophil injection.	78
Figure 3-10. Neutrophil TEM at 5 h in chemoattractant-free condition and receptor expression in the presence of 50 ng/mL IL-8.	79
Figure 3-11. Characterization of neutrophil TEM under competing gradients.	82
Figure 3-12. Examination of synergistic effects by mixing two different chemoattractants in the right side channel.	85
Figure 3-13. Synergistic effects of any two chemoattractants in separate channels.	86
Figure 3-14. The comparison of 25 ng/mL and 50 ng/mL competing gradients conditions.	87

## **Chapter 4**

Figure 4-1. Illustration of determining the locations of neutrophils in the gel scaffold at 1 h and 5 h after neutrophil injection.	99
Figure 4-2. Comparison of 1 h and 5 h images to determine the location of debris or other non-cell objects.	100
Figure 4-3. Illustration of selecting angiogenic endothelial cells in the gel scaffold for projected angiogenic cell area calculation.	102
Figure 4-4. Characterization of the microfluidic device.	110
Figure 4-5. The comparison of endothelial angiogenesis with 20 and 50 ng/mL of VEGF stimulation.	111
Figure 4-6. Epifluorescence imaging of endothelial angiogenesis after 2 day incubation.	112
Figure 4-7. Fluorescence imaging of chemical gradients in the microfluidic device.	113
Figure 4-8. The results of neutrophil migration in the presence of endothelial angiogenesis.	117
Figure 4-9. Data analysis of neutrophil migration at different VEGF concentrations.	118
Figure 4-10. Fluorescence imaging of p-selectin and ICAM-1 molecule expression on endothelial cells under different VEGF treatment conditions.	119
Figure 4-11. SEM images of micro-scale structure in pure gel solution without cells at different time points.	122
Figure 4-12. The inhibitory effects of endostatin on projected angiogenic endothelial cell area in the angiogenesis channel.	125

Figure 4-13. Time-dependent studies of projected angiogenic cell area change in the presence of different concentrations of endostatin.	126
Figure 4-14. The comparison of neutrophil numbers migrating into the angiogenesis channel with and without endostatin.	127
Figure 4-15. Comparison of adhesion molecule expression with and without 20 $\mu\text{g}/\text{mL}$ endostatin for p-selectin expression and ICAM-1 expression.	128
Figure 4-16. The effects of neutrophil migration on the stability of angiogenesis structures in the presence of endostatin.	131
Figure 4-17. Analysis of projected angiogenic endothelial cell area in the angiogenesis channel after 1 h and 5 h endostatin addition.	132
Figure 4-18. Fluorescence intensities indicating integrin receptor expression on VEGF treated-endothelial cells under various IL-8 concentrations.	133

## **Chapter 5**

Figure 5-1. Schematic of microfluidic device used in chemical gradient experiments.	151
Figure 5-2. The permeability measurements of HeLa cell layer and endothelial cell layer using the fluorescence intensity profiles of FITC-dextran solution across the cell-gel interface after 5 h diffusion.	152
Figure 5-3. 3D confocal imaging of cell layers on the side wall of the gel scaffold within the microfluidic device.	153
Figure 5-4. Single cell type culture in the device for incubation time optimization.	155
Figure 5-5. The results of VEGF antibody studies.	156

Figure 5-6. COMSOL simulation results of 50 ng/mL IL-8 gradient in the channels.	159
Figure 5-7. The effects of chemical gradients on cell migration after 48 h incubation.	160
Figure 5-8. The effects of different chemical gradients on cell migration after 24 h incubation.	161
Figure 5-9. The effects of different chemical gradients on cell migration after 48 h incubation.	162
Figure 5-10. The effects of different chemical gradients on cell migration after 24 h incubation.	163
Figure 5-11. COMSOL simulation result of shear rate in the side channel.	165
Figure 5-12. The bright-field image of cell migration with a pipette tip inserted into the inlets but no flow rate introduced at 48 h.	166
Figure 5-13. The effects of flow rate on cell migration after 48 h medium flowing.	168
Figure 5-14. Confocal imaging of endothelial cell layer after 48 h cell co-culture in different conditions.	169
Figure 5-15. The cell culture medium containing 10 $\mu$ M FITC-dextran is flowed into the right side channel.	171
Figure 5-16. Schematic of microfluidic device used for hypoxia effects study.	173
Figure 5-17. The condition optimization for nitrogen gas and chemical reaction flowing in oxygen concentration calibration.	174
Figure 5-18. The effects of hypoxia on cell migration during microfluidic cell co-culture.	175

Figure 5-19. The combined effects of three different physiological factors on cell migration.	178
Figure 5-20. Comparison of cell migration data in various conditions at the 48 h time point.	179

## **Chapter 6**

Figure 6-1. The schematic of 20% narrow channel.	191
Figure 6-2. The fluorescence intensities of vWF antibody binding on endothelial cell surface under control and flow rate activation conditions.	193
Figure 6-3. The effects of ADP pre-activation on platelet adhesion on endothelial cell layer.	195
Figure 6-4. The effects of shear rate levels on platelet aggregation.	196
Figure 6-5. The aggregation of platelets without ADP pre-activation after flowing through different microfluidic channels.	197
Figure 6-6. The aggregation of platelets with ADP pre-activation after flowing through different microfluidic channels.	198
Figure 6-7. The fluorescence intensities of ICAM-1 antibody binding on endothelial cell surface under control and flow rate activation conditions.	200
Figure 6-8. The effects of shear rate levels on neutrophil aggregation.	201
Figure 6-9. The aggregation of neutrophils after flowing through different microfluidic channels.	202
Figure 6-10. The results of neutrophil adhesion on endothelial cell layer.	204

Figure 6-11. The results of neutrophil adhesion on endothelial cell layer with or without activated platelets.	205
Figure 6-12. The effects of p-selectin antibody incubation on cell adhesion.	207
Figure 6-13. The effects of CD41/CD61 antibody incubation on cell adhesion.	209
Figure 6-14. The effects of CD11b antibody incubation on neutrophil adhesion.	210

## **List of Abbreviations and Symbols**

2D: two-dimensional

3D: three-dimensional

ADP: adenosine diphosphate

APC: allophycocyanin

ATCC: American Type Culture Collection

CAM: chick chorioallantoic membrane

CI: chemotactic index

CMFDA: 5-chloromethylfluorescein

COPD: chronic obstructive pulmonary disease

CTCs: circulating tumor cells

CXCR2: chemokine C-X-C motif receptor-2

DAPI: 4,6-diamidino-2-phenylindole dilactate

DEP: dielectrophoretic

DMEM: Dulbecco's Modified Eagle Medium

DMSO: dimethyl sulfoxide

ECI: effective chemotactic index

ECM: extracellular matrix

EDTA: ethylenediaminetetraacetic acid

EGTA: ethylene glycol tetraacetic acid

eNOS: endothelial nitric oxide synthase

EpCAM: epithelial cell adhesion molecule

ESI-MS: electrospray ionization mass spectrometry

FDA: Food and Drug Administration

FITC: fluorescein isothiocyanate

fMLP: N-formyl-methionyl-leucyl-phenylalanine

GEF: guanine exchange factor

GM-CSF: granulocyte/macrophage colony-stimulating factor

HBSS: Hank's buffered salt solution

HSA: human serum albumin

ICAM-1: intercellular adhesion molecule-1

ICC: intraclass correlation coefficients

IL-8: interleukin-8

L-NMMA: L-N<sup>G</sup>-monomethyl arginine citrate

LTB4: leukotriene B4

MAP: mitogen-activated protein

MEMS: microelectromechanical system

MI: motility index

MLCK: myosin light chain kinase

MMP: matrix metalloproteinase

MTF: muscular thin film

MTT: 3-(4,5-dimethylthiazol-2-yl)-2,5- diphenyltetrazolium bromide

NEMS: nanoelectromechanical system

PBS: phosphate-buffered saline

PDL: poly-D-lysine

PDMS: polydimethylsiloxane

PFA: paraformaldehyde

PI3K: phosphoinositide 3-kinase

PK-PD: pharmacokinetics-pharmacodynamics

PLC: phospholipase C

PPP: platelet poor plasma

PRP: platelet rich plasma

SEM: standard error of the mean

SEM: scanning electron microscope

TEM: transendothelial migration

TNF- $\alpha$ : tumor necrosis factor-alpha

$\mu$ CCA: micro cell culture analog

VEGF: vascular endothelial growth factor

vWF: von-Willebrand factor

## Chapter 1

### Development of Biomimetic Microfluidic Platforms for Cellular Interaction Studies

#### Adapted from:

Kim, D.; Wu, X.; Young, A.; Haynes, C. L., *Acc. Chem. Res.* **2014**, 47, 1165-1173.

Wu, X.\*; Gruba, S.\*; Haynes, C. L., *J. Am. Chem. Soc.*, **2016**, *In preparation*.

## **1-1. Introduction**

Investigation of cellular interactions in complicated biological systems is gaining popularity since there is an urgent demand for mechanistic understanding of cellular behavior and cell-initiated disease pathogenesis, which is essential for developing novel treatment approaches. For example, examination of interactions between cancer cells and human immune cells will be helpful for medical advances in cancer treatment.<sup>1</sup> In addition to significant research efforts studying heterotypic cellular interactions, the responses of cells to other surrounding factors, including various biophysical (flow rate, gradient, and oxygen level) and biochemical (biological and drug molecules) signals, are also of significant interest.<sup>2,3</sup> These biophysical and biochemical factors contribute to critical cellular behaviors in disease pathogenesis, such as the platelet thrombus formation under elevated flow rate.<sup>4</sup> With this context in mind, the concept of “cellular interaction” discussed herein refers to the interaction of cells with external factors that may induce changes in cellular function.

To characterize the how different environmental factors influence cellular behaviors and functions, researchers have made great efforts to apply traditional *in vivo* and *in vitro* analytical techniques. However, traditional *in vivo* methods using animal models suffer from time-consuming experimental procedures and poor reproducibility within complicated biological systems while traditional *in vitro* methods do not fully recapitulate the biological systems. In this chapter, a powerful analytical platform, microfluidics technology, is introduced in detail to demonstrate how these platforms can

overcome limitations of conventional assays and reveal novel insights about cellular interactions.

## **1-2. Microfluidics in the study of cellular interactions**

Microfluidics is a field of technology that explores the handling of minute amounts of liquids in tiny micrometer scale channels. The development of microfluidics was inspired by the micromachining technologies developed in the semiconductor industry, which are also known as micro and nanoelectromechanical system (MEMS and NEMS) processes.<sup>5</sup> As a bioanalytical tool, microfluidics has the following advantages: (1) the ability to use extremely low amount of reagents; (2) low cost of device fabrication; (3) supports high throughput and multiplex analysis in short time; (4) carry out sample preparation and detection with high resolution and sensitivity; and (5) fast heat and mass transfer for media and environmental exchange. Due to these promising advantages, microfluidics has been successfully employed in a variety of bioanalytical fields to replace traditional assays, including single cell analysis (cell sorting, cellular interaction studies, and cell-based assays),<sup>6</sup> nucleic acid research (gene microarrays and PCR amplification),<sup>7,8</sup> protein reaction and crystallization,<sup>9</sup> biochemical monitoring,<sup>10</sup> drug discovery,<sup>11</sup> and *in vitro* diagnostics (clinical and veterinary diagnostics).<sup>12</sup> In addition to fabricating microfluidic devices from standard MEMS and NEMS processes, the introduction of soft-lithography techniques, especially using the molding of biocompatible polymers, significantly advances the application of microfluidic devices in the study of cellular biology.<sup>13</sup> Polydimethylsiloxane (PDMS), a common material widely used for polymer

device fabrication, is optically transparent, biocompatible, and gas permeable, which explains the strong preference to use this material for cellular biology studies. Hydrogels, such as collagen and chitosan, are being explored as scaffold materials due to the special mechanical and biochemical properties.<sup>14</sup> With hydrogel scaffold formation inside microfluidic channels, three-dimensional (3D) cellular structures simulate *in vivo* microenvironments; thus, microfluidics can serve as a biomimetic platform to predict cellular behaviors in real biological systems.

Among all microfluidic device applications mentioned above, this chapter focuses on high-resolution single cell analysis and bio-mimicking studies since these two areas are critical to characterize cellular interactions. Single cell analysis reveals accurate and quantitative information about the responses of individual cells to environmental changes while bulk analysis yields insight into the average behaviors of cells during interaction processes. Using microfluidic devices to create biomimetic microenvironments will reduce the costs and numbers of animals sacrificed while bridging the gap between *in vitro* and *in vivo* assays.

### **1-3. Single cell analysis in cellular interactions**

With the rapid development of new analytical techniques, the focus of biophysical and bioanalytical chemistry has gradually shifted from investigating only ensemble cellular behavior and bulk cell contents to performing analysis at the single cell level. The motivation for this shift is attributable to two major factors. First, single cell analysis is one of the best ways to dig deeply into the features of a particular cell type, often

revealing real-time behavior or quantitative information during cellular interaction processes. Second, even within a largely homogeneous cell population, subtle microenvironmental changes or inherent stochastic factors in a small sub-population may result in cell cycle malfunction or disease state transition. Exploration of these heterogeneities using single cell analyses will not only reveal mechanistic insights into the cellular behavior, but also elucidate the relationship between cell-specific changes and biological phenomena pertaining to disease-related dysfunction.

In recent years, various state-of-the-art single cell analysis techniques have been developed to characterize cellular behaviors in the context of interacting with environmental complexity. The major technical areas include optical methods, electrochemical analysis, and imaging-based mass spectroscopy. One representative optical approach for single cell analysis is super-resolution fluorescence microscopy, which overcomes the diffraction limit of Abbe's law and achieves spatial resolution in the tens of nanometers. With the help of super-resolution fluorescence microscopy, researchers are able to track subcellular dynamics visually, such as protein localization in endocytic pathway,<sup>15,16</sup> neural circuitry screening,<sup>17</sup> nanoscale configuration of intracellular components,<sup>18,19</sup> and biological membrane dynamics.<sup>20,21</sup> Coherent Raman scattering spectroscopy is another category of optical approaches that produces molecular "fingerprints" for small biomolecules inside single cells. The application of coherent Raman scattering spectroscopy covers lipid profile generation,<sup>22,23</sup> protein degradation,<sup>24</sup> chromosome dynamics visualization,<sup>25</sup> and cell-drug interactions.<sup>26</sup> Single cell electrochemistry is a powerful method to monitor cellular communication either through

exocytosis or ion channel release. Electrodes fabricated at the micro- or nanoscale can be used to quantitatively monitor real-time electrical and chemical responses in single cells, revealing cell communication during various biological processes, such as exocytosis,<sup>27</sup> oxidative stress,<sup>27</sup> ion channel activity,<sup>28</sup> and during pharmaceutical treatment.<sup>29</sup> Mass spectroscopy is a popular label-free technique to measure the molecular contents in biological samples, and a large amount of single cell mass spectroscopy is based on imaging modes where one can visualize the spatial distribution of chemical compositions by their molecular masses. Since a wide range of biological targets can be detected using mass spectroscopy imaging without prior knowledge of their presence and in a label-free manner, mass spectroscopy imaging is especially favorable in clinical and pharmaceutical research.<sup>30,31</sup> In addition to these three major technical areas, recently, microfluidics has been adopted by the research community to study cell biology at the single cell level due to the increased resolution and sensitivity, high throughput, low cost, miniaturization and automation.

### **1-3-1. Microfluidics for single cell manipulation**

One promising advantage of microfluidics in single cell research is the ability to manipulate single cells by employing different types of forces within the microchannels; thus, the cells of interest can be selected for advanced single cell analysis. In this section, several common microfluidic techniques are introduced for single cell manipulation.

#### **1-3-1-1. Magnetic manipulation**

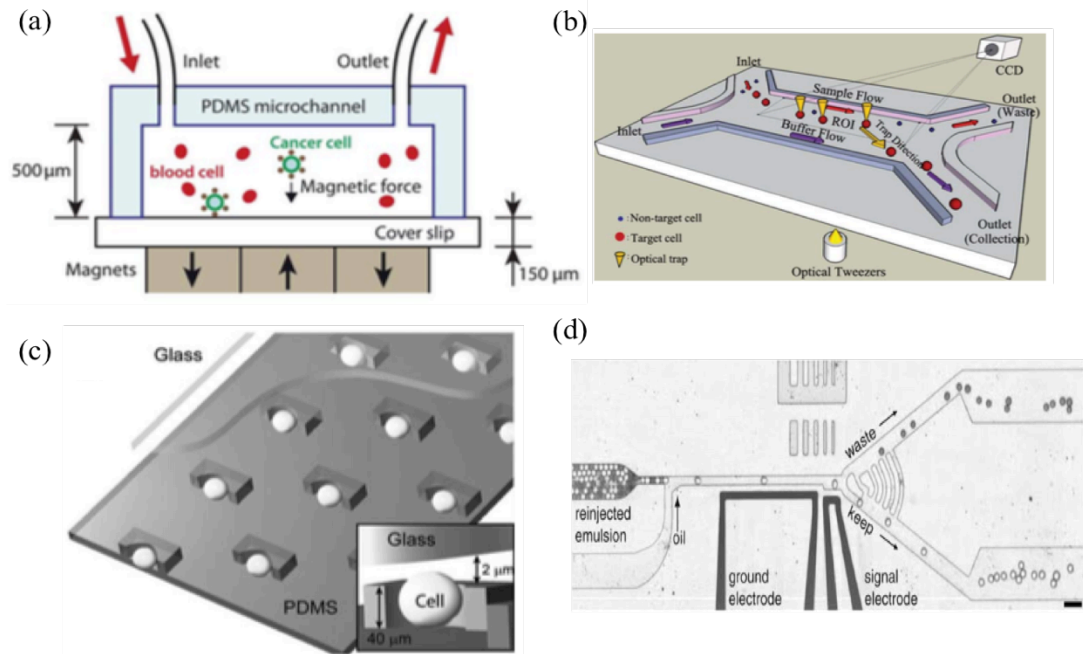


**Figure 1-1. Microfluidic devices for single cell manipulation. (a) Magnetic single cell manipulation to capture magnetic microbead-labeled cancer cells in blood samples. Reproduced from Ref. 32 with permission. (b) Optical tweezers to guide target cells move into the desired channel by generating optical scattering and gradient forces. Reproduced from Ref. 37 with permission. (c) U-shaped trap array developed in a microfluidic device to isolate cells through mechanical manipulation. Reproduced from Ref. 40 with permission. (d) Dielectrophoretic separation of single cells combined with the droplet encapsulation. Reproduced from Ref. 45 with permission.**

In the magnetic manipulation mode, target cells are labeled with antibodies coupled to nano/micro-magnetic beads and isolated through the interaction with magnetic fields inside microfluidic devices. The relatively small sizes of magnetic beads induce little detrimental effect on cellular function and viability. Because of the high specificity and efficiency of antibody affinity agents, magnetic manipulation is quite suitable for rare cell type separation, especially in obtaining circulating tumor cells (CTCs). Using epithelial cell adhesion molecule (EpCAM) antibody-coated magnetic microbeads to label the biological samples, researchers demonstrated the highly efficient isolation of CTCs in microfluidic channels with different magnetic structures (Fig. 1-1(a)).<sup>32-34</sup> Following capture, cancer cells can be further analyzed using other detection methods. In some instances, the native magnetic properties of cells are employed to act as the driving force for separation. Wu et al. designed a new microfluidic magnetophoretic separator to isolate the paramagnetic deoxygenated red blood cells from malaria-infected blood samples, greatly improving the separation efficiency compared to previous methods.<sup>35</sup> One interesting application of magnetic manipulation is that some cells can be chemically treated to change the magnetic properties without immuno-magnetic labeling; for example, live cardiomyocytes change from diamagnetic to paramagnetic via myoglobin oxidation with sodium nitrite and can be isolated using a magnetic microfluidic system.<sup>36</sup>

### **1-3-1-2. Optical manipulation**

Optical manipulation, also known as optical tweezers, is gaining more attention due to its non-contact and contamination-free manipulation process. To be specific, optical

manipulation uses a focused laser beam to generate an electric field gradient that contains optical scattering and gradient forces. Scattering forces tend to push cells away from the source of light, whereas gradient forces attract cells to the focal point. The balance between scattering forces and gradient forces is dependent on the refractive index of the cells compared to the surrounding fluid. Since the laminar flow nature of microfluidics facilitates the targeted cells being focused by a laser beam to a desired area easily, the recovery rate and purity of cell population are significantly improved (Fig. 1-1(b)).<sup>37</sup> Liberale et al. reported that the integration of micro-optical tweezers inside microfluidic devices not only allows stable single-cell trapping, but also enables complementary mechanical, chemical, and spectroscopic analyses.<sup>38</sup> However, the major drawback of microfluidic optical manipulation is low throughput compared to conventional optical assisted cell sorting. To address this issue, Chen et al. reported an innovative 3D microfluidic device capable of sorting cells at a throughput of 23,000 cells per second with 90% purity.<sup>39</sup> This performance is realized by exciting laser-induced cavitation bubbles within a microchannel to generate high-speed liquid jets that deflect cells focused by 3D sheath flows.

### **1-3-1-3. Mechanical manipulation**

The introduction of specific microstructures into microfluidic systems will cause changes in fluid dynamics that promote collection of single cells. These microstructures can be fabricated directly inside the microfluidic channels to separate cells, and include features such as microfilters, microwells, dam structures, and microgrippers. An early study

utilized a device consisting of arrays of physical U-shaped hydrodynamic trapping structures to trap only single cells (Fig. 1-1(c)).<sup>40</sup> Additionally, rates of cell death and division were studied after cell trapping. Lin et al. presented a microfluidic sieve-like trap array to exert precise control over the positioning of single cells on protein micropatterns.<sup>41</sup> Various paired micropattern configurations allowed the positioning of different cell populations side by side on multiple pattern clusters. In other work, a microfluidic device was designed with arrays of bypass structures for trapping individual cells without the need for surface modification.<sup>42</sup> With a high single cell trapping efficiency (~90%) achieved, cell apoptotic analysis and anticancer drug effects were examined.

#### **1-3-1-4. Dielectrophoretic (DEP) manipulation**

Similar to optical manipulation, cells can be moved by the forces generated in a non-uniform electric field via dielectrophoretic (DEP) cell positioning. Dependent on the properties of the surrounding medium and polarity of the target cells, the electric field force is able to draw cells to the field maximum or minimum. When the cells move in the direction of a strong electric field, it is called positive DEP; on the contrary, negative DEP means that the cells move toward the weak electric field. Wang et al. employed a set of electrodes in the sidewall of microchannels to generate negative DEP forces that repel cells from the sidewalls, and these lateral negative DEP forces could be adjusted to position cells at different equilibrium points for flowing into different outlet channels.<sup>43</sup> Moon et al. developed a continuous separation method combining hydrodynamic

fractionation and DEP separation to obtain CTCs from a spiked blood cell sample.<sup>44</sup> DEP separation plays a role in precise post-processing to enhance the efficiency of cell isolation after initial hydrodynamic fractionation, and the blood cells were removed with an efficiency of more than 94%. In addition to isolating cells in buffer solutions, emulsified droplets can be created inside the microchannels to encapsulate single cells for DEP separation, which provides a safe and rapid way to analyze individual cells, including gene mutation identification and enzyme reaction (Fig. 1-1(d)).<sup>45</sup>

#### **1-3-1-5. Other manipulation**

There are some other techniques to manipulate single cells within microfluidic devices, such as acoustophoresis, droplet microfluidics, and passive cell sorting. Acoustophoresis refers to the movement of cells in response to an acoustic pressure wave, which is a label-free cell handling technique with little detrimental effect and high spatial resolution. The application of acoustic waves in microfluidic cell sorting was performed by Ding et al., wherein tunable acoustic waves precisely directed cells into different outlet channels in continuous flow.<sup>46</sup> Droplets in one phase surrounded by another immiscible phase were generated in the microfluidic channels through co-flowing these two laminar fluids simultaneously. The main function of droplet microfluidics is for molecular analysis of single cell lysates since using droplets provides independent biochemical reactors with ultra-small volumes that reduce dilution effects. Zinchenko et al. established a protocol for the creation of monodisperse droplets in microfluidic devices, and single *E. coli* cells were continuously compartmentalized for a directed evolution experiment.<sup>47</sup> Passive cell

sorting is a category of cell manipulation methods that does not require labeling and only relies on the inherent differences in cellular physical properties (e.g., size, shape, and density). One typical manifestation of passive fluid phenomena is Dean flow, which is caused by the inertial forces that emanate from boundary effects of fluid flow adjacent to the channel walls. Warkiana et al. exploited the Dean vortex flows to isolate label-free CTCs from blood with high throughput and purity.<sup>48</sup> Other passive isolation methods, mainly focusing on deterministic lateral displacement and pinched flow, can be found in these specific reviews.<sup>49,50</sup>

### **1-3-2. Microfluidics for single cell detection**

As discussed above, microfluidics technology has the excellent ability to achieve single cell resolution by using different manipulation methods. However, microfluidics is not a detection technique during single cell analysis, and the characterization of cellular behaviors is still dependent on the use of traditional detection tools (e.g., microscopy) paired with microfluidics. Much recent work focuses on combining microfluidic systems with traditional detection approaches for single cell characterization, which may provide analysis in a rapid, sensitive, and high throughput fashion. A few exemplary microfluidic single cell detection examples are described below.

#### **1-3-2-1. Single cell activation and secretion**

Within biological systems, cells are activated by various environmental signals and respond by performing specific functions, such as releasing a series of signaling

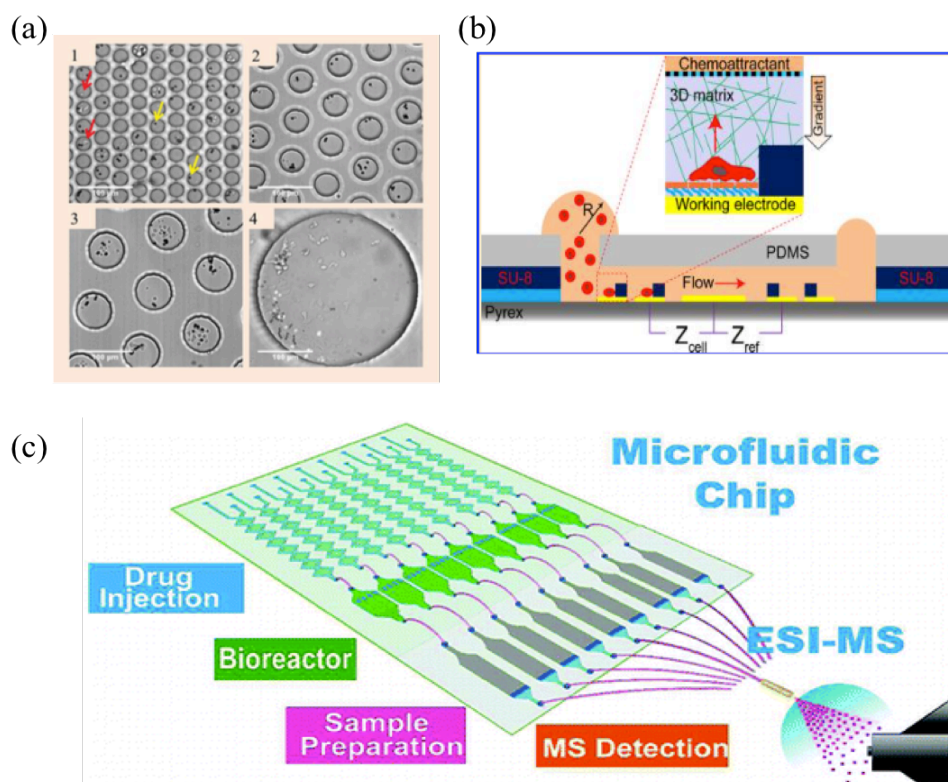


**Figure 1-2. Microfluidic devices for single cell detection. (a) Single cell activation and secretion assays within the microfluidic microarray (1-4 show different scale bars). Reproduced from Ref. 51 with permission. (b) Cell migration studies in 3D matrix based on the electric impedance signal change. Reproduced from Ref. 57 with permission. (c) Microfluidic device connected with mass spectrometry for examining the pharmaceutical effects on cellular functions. Reproduced from Ref. 59 with permission.**

molecules. The environmental factors initiating the cell activation range from cytokines, pathogens, and bacteria, to other cells and biophysical events. Investigating cellular responses to these external factors is crucial to understand cellular behaviors in the context of biological interactions as well as the mechanism behind relevant disease pathogenesis. The study of pooled cell populations using conventional assays may hide the heterogeneity of cellular response. Microfluidics is a suitable platform for exploring cell activation and secretion since the high spatiotemporal resolution at the single cell level will provide more quantitative information about natural cellular heterogeneity. Herein, two examples are introduced to reveal the significance of microfluidics technology in cell activation and secretion studies. Zaretsky et al. developed a deep microwell platform that allows capture and growth of primary T lymphocytes with minimal perturbation. Quantitative data about gene expression, cell activation, and proliferation can be obtained at the single cell level through 72 h live cell imaging (Fig. 1-2(a)).<sup>51</sup> In another example, Deng et al. reported an integrated microfluidic system designed for isolation, purification and single-cell secretomic profiling of CTCs from whole blood. An enhanced poly-L-lysine barcode pattern was created on the chip for efficient capture of CTC cells for subsequent secreted protein profiling, and the cells exhibited highly heterogeneous secretion profiles of interleukin-8 (IL-8) and vascular endothelial growth factor (VEGF).<sup>52</sup>

### **1-3-2-2. Quantitative analysis of cell migration**

Cell migration has been recognized as another hallmark of immune response and disease pathogenesis.<sup>53</sup> By following endogenous chemical gradients of signaling molecules, cells are able to migrate toward target sites and play their important defensive role against pathogen invasion or accelerating disease progression. For instance, neutrophils, the major type of white blood cells in the human immune system, migrate to the infection sites once receiving an inflammatory signal; on the other hand, cancer cells circulate in the blood to search for new tumor sites. Compared to traditional assays, microfluidic platforms facilitate the creation of stable chemical gradients with high spatiotemporal resolution, allowing quantitative tracking of single cell migration instead of characterizing the movement of cell populations. Neutrophil directional migration, critical in the immune response to inflammation, has been studied extensively using microfluidic platforms. In fact, our group has established chemical gradients within microfluidic devices by mixing flow streams in a series of serpentine channels, allowing the laminar flow property of flow streams carrying different cytokine concentrations to set up the gradient for neutrophil migration studies. We tracked the migration of individual neutrophils in the presence of competing gradients,<sup>54</sup> endothelial cell interaction,<sup>55</sup> and drug inhibitors,<sup>56</sup> which provide a detailed mechanistic understanding of neutrophil migratory behaviors. Nguyen et al. efficiently captured single metastatic cancer cells using an on-chip microstructure array while the migration of cancer cells into 3D matrixes were recorded with a change in impedance of the patterned electrodes (Fig. 1-2(b)).<sup>57</sup>

### **1-3-2-3. Pharmaceutical research**

Probing the effects of drugs on cellular behavior is of great importance in drug discovery, which is a time-consuming, complicated, and costly endeavor. Hence, people have made great efforts to develop robust, rapid, and high-throughput approaches to address current limitations in the field of pharmaceutical research. As a powerful bioanalytical platform, microfluidics offers numerous advantages in drug discovery-related work over other biological assays, such as sustaining highly parallel and multiplex detection, fast drug screening with small volume consumption, and automated dynamic data processing. Moreover, cell culture systems, even organ-like microenvironments have been created inside microfluidic devices to replace traditional animal models for drug discovery; a detailed description can be found in the organ-on-a-chip section below. One typical application of microfluidic systems in drug-cell interaction studies is the evaluation of drug cytotoxicity. Sarkar et al. presented a droplet microfluidics-based approach to examine the dynamics of drug uptake and cytotoxicity in drug-sensitive and drug-resistant breast cancer cells. An integrated droplet generation and microarray were used to encapsulate single cells for real-time imaging while heterogeneous drug effects were found for drug-sensitive cells, and uniformly low uptake was showed in drug-resistant cells.<sup>58</sup> Chen et al. performed drug-induced cell metabolism measurements using microfluidic chip electrospray ionization mass spectrometry (ESI-MS, Fig. 1-2(c)).<sup>59</sup> Drug molecules were injected through the micro-chamber to incubate with microfluidic-cultured cells, and the released metabolites were easily identified by ESI-MS without contamination even in the complex biological matrices.

#### **1-4. Reconstitution of *in vivo* microenvironments**

The human body is a complex and precisely operating system involving numerous molecules, cells, tissues and organs. There is a rich variety of cellular interactions in the human body to regulate biological functions; investigation of the mechanisms behind these cellular interactions is critical for medical innovation in disease treatment. Traditional *in vivo* assays using animal models are not always able to correlate with human results; also, expensive and time-consuming procedures are disadvantages of *in vivo* assays. The study of cellular interactions within an *in vivo*-like microenvironment is a good alternative approach for the biological research community to replace or compliment animal studies. Due to recent advances in microfabrication techniques and biomaterial research, microfluidics is one of the ideal platforms to provide a microengineered cell culture model with biomimetic environments, from a system that allows the researcher to vary independent biophysical or biochemical factors to complicated tissue- or organ-like configurations. In a physiologically relevant context, cellular behaviors observed within microfluidic *in vitro* models may be able to recapitulate or predict realistic situations inside human body.

##### **1-4-1. Recapitulation of biophysical and biochemical complexity**

To recapitulate *in vivo*-like microenvironments using microfluidics, the research community starts by introducing independent biophysical or biochemical factors into the microfluidic device design. The text below focuses on three different biophysical/biochemical factors: fluid shear stress, physiological hypoxia, and

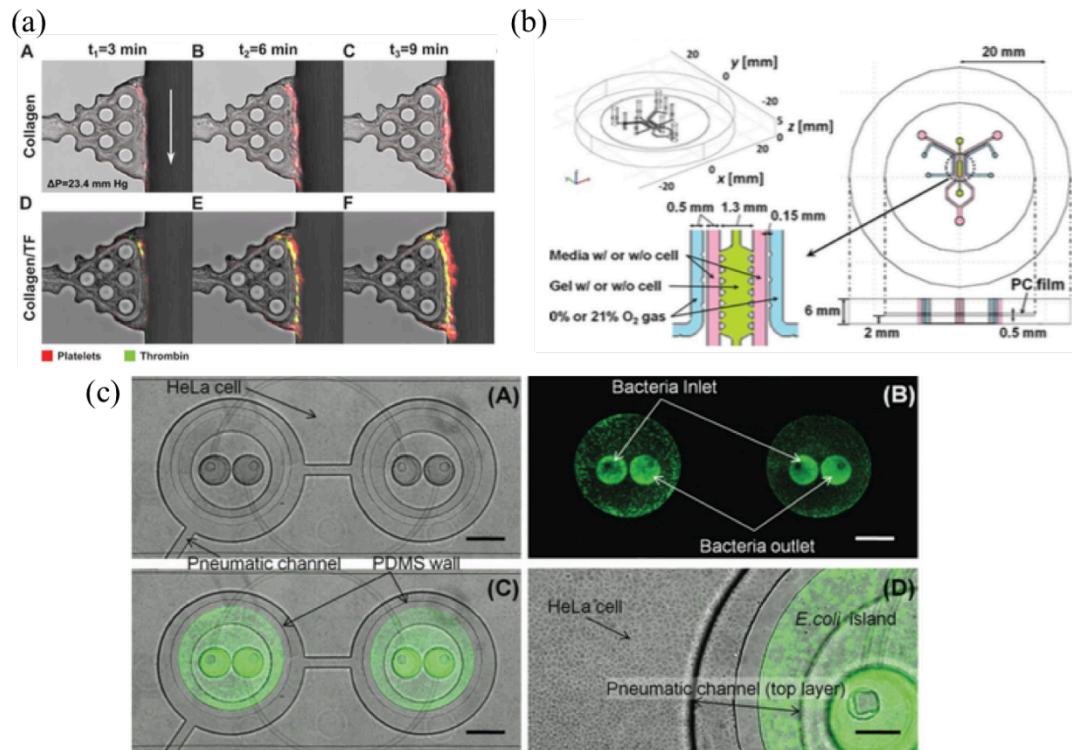


**Figure 1-3. Recapitulation of biophysical and biochemical microenvironments using microfluidic devices. (a) A complicated hemodynamic model to study the mechanisms of platelet clot formation in a biomimetic blood vessel. Dynamic studies of platelet (red) and thrombin (green) development on collagen (A-C) or collagen/TF scaffolds (D-F). Reproduced from Ref. 62 with permission. (b) Microfluidic device setup for the creation of oxygen gradients across a gel region containing cell culture. Reproduced from Ref. 66 with permission. (c) HeLa cell-bacteria co-culture system in a microfluidic device. The figures show the (A) HeLa cell monolayer, (B) GFP-expressing *E. coli* localized in the bacterial islands, (C) cell co-culture, and (D) magnified view of cell co-culture. Reproduced from Ref. 69 with permission.**

biomimetic cell-cell interactions, which are three fundamental *in vivo* characteristics that regulate cellular behaviors.

#### **1-4-1-1. The interactions between cells and flow**

One significant difference between true *in vivo* conditions and traditional *in vitro* cell culture is the existence of flow in blood vessels. Shear stress caused by fluid flow is recognized as an essential parameter that influences cellular behaviors, not only mechanically changing the cellular cytoskeleton and morphology, but also regulating biological function, such as adhesion and secretion.<sup>60</sup> Using microfluidic channels, the fluid is kept in a laminar flow regime, which is the same as that in blood vessels; in addition, accurate mimic of fluid behaviors can be achieved with high spatiotemporal resolution and easy adjustment. One simple example where this strength is demonstrated is a study where renal tubular epithelial cells were exposed to fluid shear stress in a microfluidic chip, and the data indicate that the reorganization of intracellular F-actin and translocation of channel proteins are regulated by the shear stress microenvironment.<sup>61</sup> In another example, Muthard et al. created a complicated hemodynamic model to study platelet clot formation in the presence of controlled transthrombus permeation and wall shear stress, which are able to significantly change clot structure, height, and composition (Fig. 1-3(a)).<sup>62</sup> There are two interesting examples that extend the cell-flow interactions to material and biosensor research. Varma et al. presented the first genetically coded cell sensors that fluoresce in a quantitative fashion upon fluid shear stress pathway activation.<sup>63</sup> Specifically, the up-regulation of mechanosensitive proteins induced by a

range of shear stress intensities and durations was detected, systematically assessing the physiological implications of shear stress in microfluidic devices. Tang et al. observed the detachment of cells on temperature-responsive surfaces in a shear stress-dependent mode, which may be useful for cell culture surface design in tissue engineering.<sup>64</sup>

#### **1-4-1-2. Hypoxic effects on cellular responses**

Hypoxia, known as the deprivation of adequate oxygen supply within the human body, plays a critical role in regulating cellular behaviors including migration, proliferation, and differentiation. Especially in the context of cancer, hypoxia is a characteristic feature inside solid tumors and promotes tumor progression as well as resistance to therapy.<sup>65</sup> Hypoxia also regulates the cellular fate of stem cells in most instances. Instead of using large oxygen variable incubators, microfluidic platforms are able to sustain desired oxygen gradients in a precisely controlled fashion with short equilibration time. To develop hypoxic conditions, a pre-programmed gas mixture containing low oxygen concentration or a chemical reaction that consumes oxygen is flowed into microfluidic channels to decrease the oxygen level in cell culture microenvironments. Funamoto et al. reported a microfluidic device with a 3D cell culture gel region and a pair of peripheral gas channels for suitable gas mixture injection (Fig. 1-3(b)).<sup>66</sup> Under uniform hypoxic conditions or oxygen concentration gradients, the migratory studies of human breast cancer cells were performed, indicating enhanced migration compared to normoxia. A sophisticated microfluidic device combining a hydrodynamic trapping array and hypoxic gas control system demonstrated that hypoxia impairs the function of microencapsulated

islets at the single islet level, showing a heterogeneous pattern reflected in intracellular calcium, mitochondrial energetics, and redox activity.<sup>67</sup> Chang et al. employed an oxygen scavenging chemical reaction method to create oxygen gradients that play the important role in guiding cell migration and mediating cell-drug interactions.<sup>68</sup> This method is advantageous because it is free of gas cylinders and flow control systems.

### **1-4-1-3. Biomimetic cell-cell interaction models**

The introduction of microfluidic devices into cell-cell interaction studies brings the great opportunity to investigate cellular behaviors in a temporally, spatially, and chemically resolved manner. In a realistic setting, cellular interactions are mediated by a variety of biophysical and biochemical factors, which are generally not well-represented within conventional cell-based assays, but can be achieved in microfluidic devices. Kim et al. studied the interaction between *E. coli* and HeLa cells in a device controlled by pressure-driven microfluidics (Fig. 1-3(c)).<sup>69</sup> Through culturing *E. coli* cells as a biofilm in an island region surrounded by HeLa cell monolayer, the co-culture results reveal that *E. coli* cells display a spatial bias when colonizing within HeLa cells, and insight on how *E. coli* outcompetes commensal bacteria was provided. Zervantonakis et al. developed a 3D tumor-vascular interface to characterize tumor cell intravasation with the signaling from tumor-endothelial interactions and biochemical factors secreted from co-existing macrophages.<sup>70</sup> Another 3D microfluidic cell co-culture platform was created by separating different cell types with a porous membrane and multiple physiological elements, including fluid flow shear and subendothelial matrix, were introduced into the

device simultaneously.<sup>71</sup> This model offers the advantages of greater control of the cellular microenvironments and the potential for high throughput experimentation.

### **1-4-2. Organ-on-a-chip**

Organ-on-a-chip is a novel concept referring to the simulation of physiological functions and structures of entire organs or organ systems based on cell culture microfluidic platforms. The limitations of current drug development strategies inspired the organ-on-a-chip concept. Traditional cell-based assays focus only on studying molecular mechanisms in cell-drug interactions rather than revealing cellular behaviors in complicated *in vivo* microenvironments. Meanwhile, animal models are too often poor predictors of human biological response. These shortcomings of traditional approaches in combination with recent advances in the fields of cell biology, biomaterials, microfabrication technologies and tissue engineering have facilitated the emergence of organ-on-a-chip platforms.<sup>72-74</sup> For the purpose of recapitulating organ-like environments, a wide range of aforementioned technologies, such as 3D cell culture, microelectrode integration, and chemical gradient generation, must be incorporated into the microfluidic device, which is a great challenge for the research community. Despite the technical challenge, several successful organ-on-a-chip examples have been established to study cellular biology questions.

#### **1-4-2-1 Lung-on-a-chip**

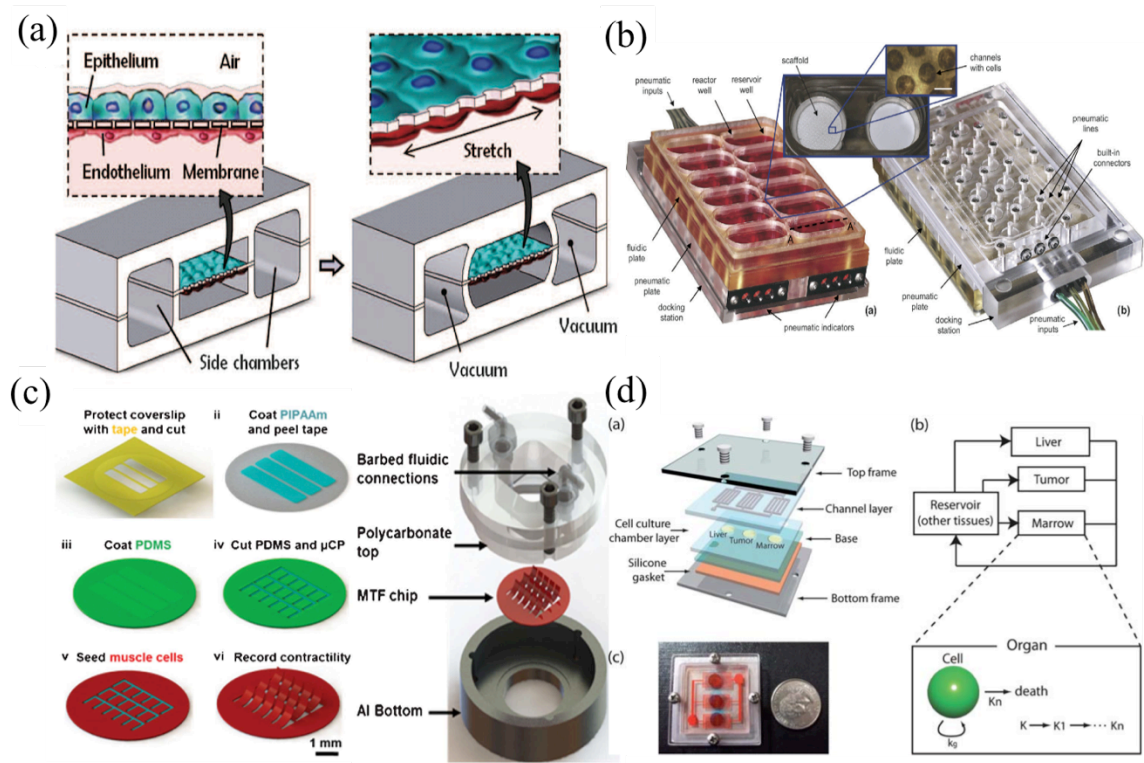


**Figure 1-4. Organ-on-a-chip systems. (a) Lung-on-a-chip: reconstitution and visualization of complex organ-level responses involved in pulmonary inflammation and infection. Reproduced from Ref. 75 with permission. (b) Liver-on-a-chip: 3D liver cell culture to assess the oxygen consumption and transport in perfused multiwells. Reproduced from Ref. 76 with permission. (c) Heart-on-a-chip: developed Muscular Thin Film (MTF) assay to explore the structure function relationship and drug dose effects of anisotropic cardiac myocytes. Reproduced from Ref. 77 with permission. (d) Body-on-a-chip: operating multiple compartments with different organ functions or various cell types in a single integrated device to predict drug effects. Reproduced from Ref. 78 with permission.**

A bio-inspired microdevice based on human alveolar-capillary interfaces was created to simulate the fundamental unit of the human lung through bonding two symmetric microchannels separated by one thin flexible porous PDMS membrane (Fig. 1-4(a)).<sup>75</sup> This sandwich design enables air flow into the upper compartment with epithelial cells coating the membrane and medium circulation in the lower compartment where endothelial cells are incubated on the other side of the membrane. Vacuum exerted in two side chambers provides the pressure to stretch opposite cell layers at the air-liquid interface, simulating pulmonary breathing movements. Direct visualized results demonstrate that the medium containing cytokine molecules up-regulated the expression of adhesion molecules produced by endothelial cells and induced transmigration of leukocytes through confluent cell layers, whereas cyclic mechanical strain had no impact on inflammatory response. In nanotoxicological studies, physiological strain was shown to enhance toxic and immunological effects of silica nanoparticles as well as increase epithelial or endothelial uptake of various nanomaterials.<sup>75</sup>

#### **1-4-2-2 Liver-on-a-chip**

Hepatotoxicity is recognized as one of the major issues that cause side effects during drug treatment. A reliable and efficient *in vitro* liver-on-a-chip platform equipped with electronic controlled pneumatic micropumps was reported to sustain 3D liver cell culture and high throughput observation (Fig. 1-4(b)).<sup>76</sup> The assembled multiwell plate contained 12 bioreactors in which hundreds of tissues were maintained under constant fluidic perfusion and kept functionally viable after one-week culture. Furthermore, the model of

oxygen distribution in each chamber was generated using a computational tool to predict gas transfer and consumption, which was consistent with the luminescence-based concentration measurements and proved to be dependent on a first-order reaction mechanism. This study provides an *in vitro* model that captures the complexity of an *in vivo* organ in a scalable and easy-to-use format for future drug discovery.

### **1-4-2-3 Heart-on-a-chip**

Replicating relevant *in vitro* cardiac tissue is an urgent need for drug testing due to the high risk of heart failure resulting from unforeseen drug toxicities, even for some currently marketed drugs. The novel Muscular Thin Film (MTF) assay has been proposed to explore the structure-function relationship and drug dose effects on anisotropic cardiac myocytes to overcome the shortcomings of traditional single cell studies and isotropic cardiac assays (Fig. 1-4(c)).<sup>77</sup> The MTF device is composed of a metallic temperature controller, embedded microelectrodes, an elastomeric thin film array for cardiac cell culture, and a transparent top suited for optical screening. Deflection of each cantilever in the array after electrophysiological stimulation is recorded to calculate diastolic and systolic stresses, which did not show significant differences by culturing cells on four patterns with different gap distances between neighboring cantilevers. The effects of drug doses on cardiac contractility were evaluated to reveal that architectural changes in tissue were dependent on the drug concentrations in a wide range.

### **1-4-2-4 Body-on-a-chip**

The rapid progress in the field of organ-on-a-chip has aroused researchers' interests in building pharmacokinetics-pharmacodynamics (PK-PD) models of drugs in multi-organ-involved microenvironments to replace the studies concentrating on single specific organs. The creation of micro cell culture analog ( $\mu$ CCA) techniques aim to operate multiple compartments with different organ functions or various cell types in one integrated device. One precursor study employed a compact three-chamber  $\mu$ CCA to assemble liver, tumor, and marrow cell lines by connecting them with fluidic channels that delivered common medium for disparate tissues (Fig. 1-4(d)).<sup>78</sup> The gravity-generated flow excluded the application of an external pump and prevented bubble formation, and this unique flow recirculation manner permitted cells to retain viability for three days. A brief comparison of drug cytotoxicity in theoretical PK-PD models and dynamic  $\mu$ CCA conditions proved that experimental results could satisfactorily fit the computational estimates, and the combination of the two approaches offered a novel reinforced method to predict drug effects in complex biological systems.

## **1-5 Conclusions**

As described above, microfluidics is a smart tool for cellular interaction studies due to two important features: the abilities to monitor single cells with high spatiotemporal resolution and mimic *in vivo* physiological microenvironments. According to the properties of target cells and detection methods, individual cells are isolated using different strategies, such as magnetic, optical, mechanical, and electrical manipulation; meanwhile, the responses of cells with external stimuli, chemical gradients, and drug

molecules can be studied in a quantitative and sensitive fashion. Creating a biomimetic microenvironment within microfluidic devices has been achieved to identify the effects of biophysical and biochemical complexity on cellular behaviors. Moreover, the network system with organ-like configurations and functions has been developed based on microfluidic platforms to examine cellular biology in the complicated milieu, bridging the gap between traditional *in vitro* cell-based assays and *in vivo* animal models. In short, these efforts allow microfluidics technology to shed light on important challenges in cell biology, especially understanding the mechanisms of cellular interactions with environmental complexity.

Despite the significant advances made in the field of microfluidics research, there are several issues that need to be addressed in future innovation. First, as mentioned above, microfluidic single cell analysis is still limited to conventional detection methods, such as optical microscopy methods, electrochemical detection, and mass spectrometry. Future research efforts that enable state-of-art detection on microfluidic platforms such as surface-enhanced Raman scattering, nuclear magnetic resonance, or acoustic/evanescent wave detection would provide much needed detailed chemical information. Second, in the context of biomimetic microfluidic techniques, the lack of available human cells is one of the major challenges. Most of the cells currently in use are not sufficiently stable for long-term *in vitro* culture, making realistic application of organ-on-a-chip difficult. The development of stem cells is still in an ethical conflict but may provide a solution to this shortcoming. Lastly, microfluidics technology in cell biology studies requires skilled

users to undertake the intricate processes from device fabrication to in-device cell culture; hence, there is an urgent need for simplification and automation of microfluidic devices. In the following thesis chapters, the presented work focuses on the combination of single cell analysis and biomimetic microenvironment to study the interactions of cells with essential environmental factors (e.g., chemical gradients, drug molecules, different cell types, fluid shear stress, and hypoxia) under physiologically relevant environments at the individual cell level. To be specific, the drug effects on neutrophil migration under chemical gradients are studied in Chapter 2 while neutrophil transendothelial migration in the presence of complicated gradient patterns and angiogenesis structures are reported in Chapters 3 and 4, respectively. In Chapter 5, a microfluidic cell co-culture model is presented that combines various physiological factors together, such as chemical gradients, flow rate, and hypoxia. The relationship between shear rate and cell adhesion behaviors is studied in detail in the last chapter.

## **Chapter 2**

### **Exploring Inflammatory Disease Drug Effects on Neutrophil Function**

**Adapted from:**

Wu, X.; Kim, D.; Young, A. T.; Haynes, C. L., *Analyst*, **2014**, *139*, 4056-4063.

## 2-1. Introduction

Neutrophils are the dominant white blood cells in the human body, and they play a significant role in the first line immunological response.<sup>1</sup> Neutrophil dysfunction is often found to be involved in neutrophilic inflammation, including acute severe subtypes of asthma<sup>2,3</sup> and chronic obstructive pulmonary disease (COPD),<sup>4,5</sup> ranking as the fourth leading cause of death worldwide.<sup>6</sup> Despite the fact that neutrophilic inflammation endangers human health, only a few pharmacological treatments are available and effective to treat neutrophilic inflammation. The pathophysiology of neutrophilic inflammation is characterized by neutrophil accumulation around infection sites due to aberrant neutrophil chemotaxis and impaired apoptotic pathways,<sup>5,7</sup> as such, there is a clear need to understand the underlying neutrophil biology in hopes of developing alternative approaches to slow down neutrophil chemotaxis and remove persistent neutrophils.<sup>8</sup>

Chemotaxis is a dynamic process whereby cells move in response to chemical gradients of signaling molecules called chemokines. Interleukin-8 (IL-8), one of the most well-defined primary chemokines that regulates neutrophil movement, is responsible for promoting neutrophil chemotaxis and activating the pathogenesis of neutrophil inflammatory diseases.<sup>9,10</sup> The neutrophil intracellular pathway triggered by IL-8 offers several pharmaceutical targets, such as the receptor chemokine C-X-C motif receptor-2 (CXCR2), the signal transducer enzyme phosphoinositide 3-kinase (PI3K), and intracellular free  $\text{Ca}^{2+}$ , all of which perform important functions in the neutrophil chemotactic cascade (Fig. 2-1). IL-8 initiates neutrophil chemotaxis through binding to

seven-transmembrane domain receptors (CXCR1 and CXCR2) located on the surface of neutrophils. Although activation of both CXCR1 and CXCR2 is able to initiate a series of neutrophil signaling processes, the rate of receptor internalization is more rapid with CXCR2 than CXCR1, and a lower dose of IL-8 is required for CXCR2 activation.<sup>11,12</sup> Following the translocation of CXCR receptors to the cytoplasmic granules mediated by G proteins, which are a family of proteins transmitting signals from extracellular stimuli to the interior of the cell - G $\beta\gamma$  subunits activate PI3K and phospholipase C (PLC) pathways to govern downstream signal transduction elements. PI3K and its main lipid products are involved in a variety of cellular processes, such as cell survival, cytoskeleton rearrangement, and cell transformation; more importantly, PI3K is responsible for the cell polarization that controls the direction of neutrophil migration.<sup>13</sup> PLC-molecules can be divided into three categories ( $\beta$ ,  $\gamma$  and  $\delta$ ), and the activation of the PLC- $\beta$  isoform not only mediates the function of protein kinases, but also leads to an increased level of intracellular free Ca<sup>2+</sup>.<sup>14</sup> The relationship between Ca<sup>2+</sup> and chemotaxis is still in dispute, although it has been suggested that Ca<sup>2+</sup> is involved in the contraction of the cell rear and uropod, which is an underlying step in the movements of cells.<sup>15</sup> Clarification of the role of Ca<sup>2+</sup> in neutrophil chemotaxis is necessary to understand and manipulate the signaling pathway.

In this work, we exploit single cell bioanalytical approaches to evaluate the physiological effects of three drugs aimed at the aforementioned targets. Inhibition of CXCR2 function with an antagonist downregulates the neutrophil migratory response in the biological cascade, potentially decreasing the number of cells infiltrating site of interest. A number

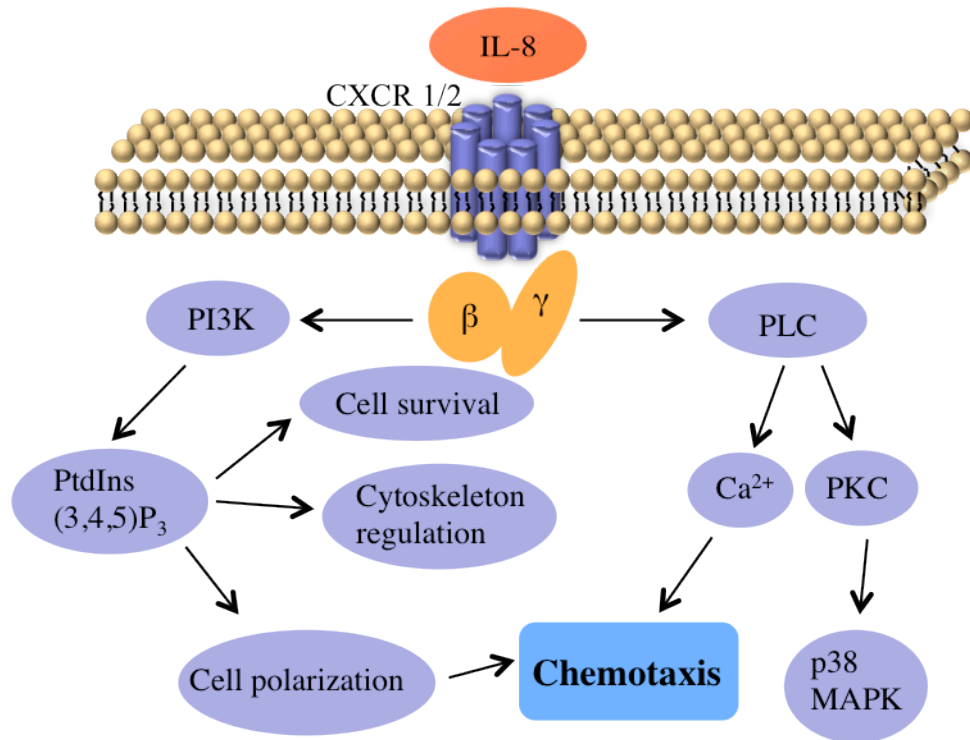


**Figure 2-1. Simplified schematic diagram of the IL-8 signaling pathway in neutrophil chemotaxis.**

of CXCR2 antagonists have been identified by pharmaceutical companies, and some of them are already in preclinical trials.<sup>16</sup> SB225002, a common CXCR2 antagonists, was employed herein to determine the impacts of receptor antagonism on neutrophil chemotaxis and viability. The PI3K inhibitor, LY294002, has been studied extensively during the past two decades,<sup>17,18</sup> however, the precise role of this inhibitor in neutrophil chemotaxis, including temporal regulation and concentration optimization, is still not clear. Also, LY294002 is expected to suppress neutrophil viability since PI3K has been identified as a survival factor for neutrophils.<sup>19</sup> The connection between neutrophil chemotaxis and cytosolic  $\text{Ca}^{2+}$  levels can be determined by introducing a drug considered to influence both chemotactic behaviors and the mobilization of intracellular  $\text{Ca}^{2+}$ . Theophylline is a common respiratory drug that alleviates the symptoms of COPD patients. Previous research has revealed that theophylline induces the inhibition of neutrophil chemotaxis in both healthy control and patient samples,<sup>20,21</sup> likely by decreasing cytosolic  $\text{Ca}^{2+}$  concentration.<sup>22</sup> A deep investigation about the impacts of theophylline on neutrophil chemotaxis and intracellular  $\text{Ca}^{2+}$  is required to test this hypothesized role of  $\text{Ca}^{2+}$  in neutrophil chemotaxis and accurately describe drug action mechanisms.

Conventional chamber-based assays, such as use of the Boyden chamber,<sup>23</sup> Dunn Chamber<sup>24</sup> and agarose gel assays,<sup>25</sup> introduce chemokine concentration gradients between two separate chambers containing buffer and concentrated signaling molecules. Although these assays are straightforward and convenient, the variable chemical gradients decay with time and only ensemble measurements are obtained, limiting the

systems and effects that can be probed with these methods. Microfluidics is a technology that enables the precise manipulation of fluid flows at the microscale.<sup>26</sup> Simple microfluidic platforms can be used to create dynamic and stable chemical gradients with high spatiotemporal resolution due to the accurate and precise control over laminar flow in microchannels. Additionally, optically transparent microfluidic platforms allow tracking of individual cells during chemotaxis in a real-time and quantitative fashion. Furthermore, compared to the simplistic environment in traditional methods, microfluidic techniques sustain a more complicated *in vivo*-like milieu with dynamic fluid flow and complex biological media so that cellular behaviors can be monitored in a physiologically relevant environment.

## **2-2. Experimental details**

### **2-2-1. Device fabrication**

Microfluidic devices were fabricated using standard photolithography protocols. First, a film (CAD/Art Service Inc., Bandon, OR) with lightproof background and transparent channel patterns was used to transfer the device design onto a chrome photomask plate via UV light exposure to an AZ1518 positive photoresist coating (Nanofilm, Westlake Village, CA). After exposure, the photomask was placed in 351 developer solution (Rohm and Hass Electronic Materials LLC, Marlborough, MA) to remove cross-linked photoresist in the channels, and the exposed chrome layer was etched down in the chrome etchant solution (Cyantek Corporation, Fremont, CA). The final step was carried out in

the piranha solution (1:1 volume ratio of 30% hydrogen peroxide and 99.9% sulfuric acid, Avantor Performance Materials, Phillipsburg, NJ) to remove the remaining photoresist. Following photomask fabrication, a 4-inch silicon wafer was spin-coated with 100  $\mu\text{m}$  thick negative photoresist SU-8 50 (Microchem, Newton, MA) and then underwent the first baking step. The channel patterns were then transferred to the SU-8 mold through the previously prepared photomask by UV exposure. After the second baking process, the silicon wafer was developed in SU-8 developer (Microchem, Newton, MA) to dissolve the unexposed photoresist, and the device patterns remained on the substrate. A mixture of Sylgard 184 silicone elastomer base and curing agent (Ellsworth Adhesives, Germantown, WI) in 10:1 mass ratio was slowly poured on the completed SU-8 mold after degassing, and then incubated on the hot plate at 95°C overnight. The polydimethylsiloxane (PDMS) layer was cut and punched for inlet and outlet holes. Finally, the PDMS layer was attached to the glass substrate permanently using oxygen plasma at 100 L/h oxygen flow rate and 100 W for 10 seconds. The fabricated devices were sterilized by injecting 70% v/v ethanol solution into channels and exposed to UV light overnight before use.

### **2-2-2. Neutrophil isolation**

Freshly drawn whole human blood samples with ethylenediaminetetraacetic acid (EDTA) as an anticoagulant were prepared by Memorial Blood Center (St. Paul, MN) according to IRB protocol E&I ID no. 07809. All the samples were collected from healthy donors as demonstrated by a screening questionnaire that meets the Food and Drug

Administration (FDA) guidelines, and neutrophil isolation was performed immediately following blood draws. 5 mL of blood sample was layered carefully over the same volume of mono-poly resolving medium (Fisher Scientific, Waltham, MA) and centrifuged to obtain distinct density gradients. The neutrophil band was collected and purified using red blood cell lysis buffer (Miltenyi Biotec Inc., Auburn, CA) according to the previously reported protocol.<sup>27</sup> The final neutrophil pellet was re-suspended in Hank's buffered salt solution (HBSS, Fisher Scientific, Waltham, MA) containing 2% human serum albumin (HSA, Sigma-Aldrich, St. Louis, MO).

### **2-2-3. Cell viability assay**

Pure neutrophils were diluted to the density of  $6 \times 10^5$  cells/mL in HBSS medium and seeded in 96-well plate with 100  $\mu$ L in each well. Neutrophils were incubated with different concentrations of drugs (CXCR2 antagonist SB225002, EMD Millipore, Billerica, MA; PI3K inhibitor LY294002 or theophylline, Sigma-Aldrich, St. Louis, MO) for specific time periods (30 min, 90 min, or 150 min) in the incubator at 37°C under 5% CO<sub>2</sub>. After incubation, the well plate was centrifuged to remove medium, and the cells were incubated with 100  $\mu$ L of 0.5 mg/mL 3-(4,5-dimethylthiazol-2-yl)-2,5-diphenyltetrazolium bromide (MTT, Sigma-Aldrich, St. Louis, MO) solution for 2 h. The water-insoluble purple formazan crystals only produced by the living cells were dissolved in 150  $\mu$ L of dimethyl sulfoxide (DMSO, Sigma-Aldrich, St. Louis, MO). The plate was placed on the orbital shaker for 20 min to facilitate complete crystal dissolution. Finally, 100  $\mu$ L of DMSO solution was transferred to another new 96-well plate for UV-Vis

absorption measurements. Optical density was monitored at 570 nm, with 655 nm as a reference, using a microplate reader (Bio Tek, Winnoski, VT), and the cell viability was calculated using equation (1). The data in each condition were recorded from five different blood samples (donors).

$$\text{viability (\%)} = \left( \frac{\text{sample abs}_{570 \text{ nm}} - \text{sample abs}_{655 \text{ nm}}}{\text{control abs}_{570 \text{ nm}} - \text{control abs}_{655 \text{ nm}}} \right) \times 100\% \quad (1)$$

#### **2-2-4. Microfluidic chemotaxis experiments**

Prior to using microfluidic devices, the channels were rinsed with sterilized Milli-Q water (Millipore, Billerica, MA), and 20  $\mu\text{L}$  of 250  $\mu\text{g}/\text{mL}$  human fibronectin (Sigma-Aldrich, St. Louis, MO) solution was injected through the cell inlet to cover the cell culture chamber. The devices were kept in the biosafety hood for 40 min before introducing neutrophils. Neutrophils at a density of  $3\text{-}5 \times 10^6$  cells/mL were incubated with specific concentrations of drugs at  $37^\circ\text{C}$  under 5%  $\text{CO}_2$  for 30 min, 90 min, or 150 min. After that, 5-10  $\mu\text{L}$  of neutrophils were injected through the cell inlet to achieve suitable population (30-60 cells in the viewable  $400 \mu\text{m} \times 1280 \mu\text{m}$  area) in the microfluidic cell culture chamber, and then the device was kept in the biohood for another one hour to enhance neutrophil adhesion to the fibronectin-coated glass. Two medium inlets were connected to syringes containing 10 ng/mL IL-8 (Sigma-Aldrich, St. Louis, MO) solution and HBSS buffer to achieve a 0-10 ng/mL IL-8 gradient within the observation channel. The flow rate was kept at 100  $\mu\text{L}/\text{h}$ , which will generate minimum shear-induced impact on neutrophil chemotaxis. The migratory patterns of neutrophils within the IL-8 gradient

were recorded using time-lapse imaging mode (every 10 s for 20 min) in Metamorph imaging software on an inverted microscope with a 10× objective (Nikon, Melville, NY) and a CCD camera (QuantEM, Photometrics, Tucson, AZ). Three biological replicates were performed for each condition.

### **2-2-5. Analysis of chemotaxis data**

In the cell culture chamber, the trajectories of 15 or more randomly-chosen neutrophils were analyzed (Fig. 2-2(a)). Neutrophil chemotaxis was quantified using three parameters, motility index (MI), chemotactic index (CI), and effective chemotactic index (ECI), which have been employed to describe neutrophil chemotaxis previously.<sup>28</sup> The MI value describes the total possible movement of neutrophils and is defined as the ratio of final straight migratory distance ( $d_{\text{final}}$ ) and the maximum displacement ( $d_{\text{max}}$ ).

$$\text{MI} = d_{\text{final}}/d_{\text{max}}$$

where  $d_{\text{max}}$  is the product of average velocity of the tracked cell and total observed time.

CI represents the orientation of neutrophils during migration and is defined as the ratio of the final distance in the gradient direction ( $d_x$ ) and the entire migration distance of a cell ( $d_{\text{total}}$ ).

$$\text{CI} = d_x/d_{\text{total}}$$

The third parameter, ECI, is defined as the product of MI and CI, and depicts the overall effectiveness of neutrophil chemotaxis. These three parameters from individual neutrophils were calculated and plotted as histograms reflecting average values and

standard error of the mean (SEM). Unpaired t-tests with  $\alpha=0.05$  were used for statistical comparison.

#### **2-2-6. Calcium imaging**

Neutrophils were prepared in HBSS buffer containing 2% HSA at the density of  $4-5 \times 10^6$  cells/mL. For loading cells with the intracellular  $\text{Ca}^{2+}$ -sensitive fluorophore fura-2 AM (Sigma-Aldrich, St. Louis, MO), 1 mL of neutrophil suspension was incubated with 1  $\mu\text{L}$  of 1 mM fura-2 AM at  $37^\circ\text{C}$  under 5%  $\text{CO}_2$  for 30 min. Neutrophils were centrifuged twice to remove extra fura-2 AM, and then divided into two tubes of 500  $\mu\text{L}$  solution. One population was re-suspended using  $\text{Ca}^{2+}$ -free HBSS medium (Sigma-Aldrich, St. Louis, MO) supplemented with 2% HSA and 2 mM ethylene glycol tetraacetic acid (EGTA, Sigma-Aldrich, St. Louis, MO), and the other one was kept in normal ( $\text{Ca}^{2+}$ -containing) HBSS medium supplemented with 2% HSA. These two tubes were further split into 100  $\mu\text{L}$  aliquots for incubation with different doses of theophylline. All the samples were put on ice in the dark until use. Before  $\text{Ca}^{2+}$  imaging, each sample was incubated at  $37^\circ\text{C}$  for 5 min and re-suspended in 100  $\mu\text{L}$  of the same fresh media. A 100  $\mu\text{L}$  neutrophil suspension in each tube was placed on the center of a petri dish without fixing agent and the fluorescence intensity was monitored at 495 nm using 340/380 nm dual wavelength excitation through a 40 $\times$  oil immersion objective on an inverted microscope (Nikon, Melville, NY). The change in fluorescence intensity induced by addition of 2  $\mu\text{L}$  500 mg/mL IL-8 solution was recorded.

Calibration of  $\text{Ca}^{2+}$  concentrations was performed by pipetting 2  $\mu\text{L}$  of 25 mM digitonin (Sigma-Aldrich, St. Louis, MO), a cell-permeabilizing agent, into the cell suspension for the maximum fluorescence ratio ( $R_{\text{max}}$ ) and then 5  $\mu\text{L}$  of 0.4 M EGTA for the minimum fluorescence ratio ( $R_{\text{min}}$ ). Intracellular  $\text{Ca}^{2+}$  levels activated by IL-8 were calculated according to the equation (2).<sup>29</sup>

$$[\text{Ca}^{2+}] = K_d \left( \frac{R - R_{\text{min}}}{R_{\text{max}} - R} \right) \left( \frac{S_{f2}}{S_{b2}} \right) \quad (2)$$

where  $K_d$  is the effective dissociation constant for the probe molecule (220 nM),  $S_{f2}$  is the minimum excitation intensity at 380 nm, and  $S_{b2}$  is the maximum excitation intensity at 380 nm. Neutrophil autofluorescence without added fura-2 AM was also measured following the same procedures and subtracted in the calculation.

## **2-3. Results and discussion**

### **2-3-1. Confirmation of chemical gradients in microfluidic device**

The microfluidic device is composed of three inlets, many serpentine channels, and one cell culture chamber (Fig. 2-2(b)). At each node in the microfluidic serpentine channels, the fluid splits into two streams and mixes via diffusion, with the neighboring stream carrying a different concentration of chemokines. When the fluid arrives in the cell culture chamber at the end of the pyramidal network, all the streams combine and form a concentration gradient perpendicular to the direction of streams. The concentration gradient profile is constant during experiments since the rate of molecular diffusion in each stream is much slower than the flow rate used in the experiment, which prevents the

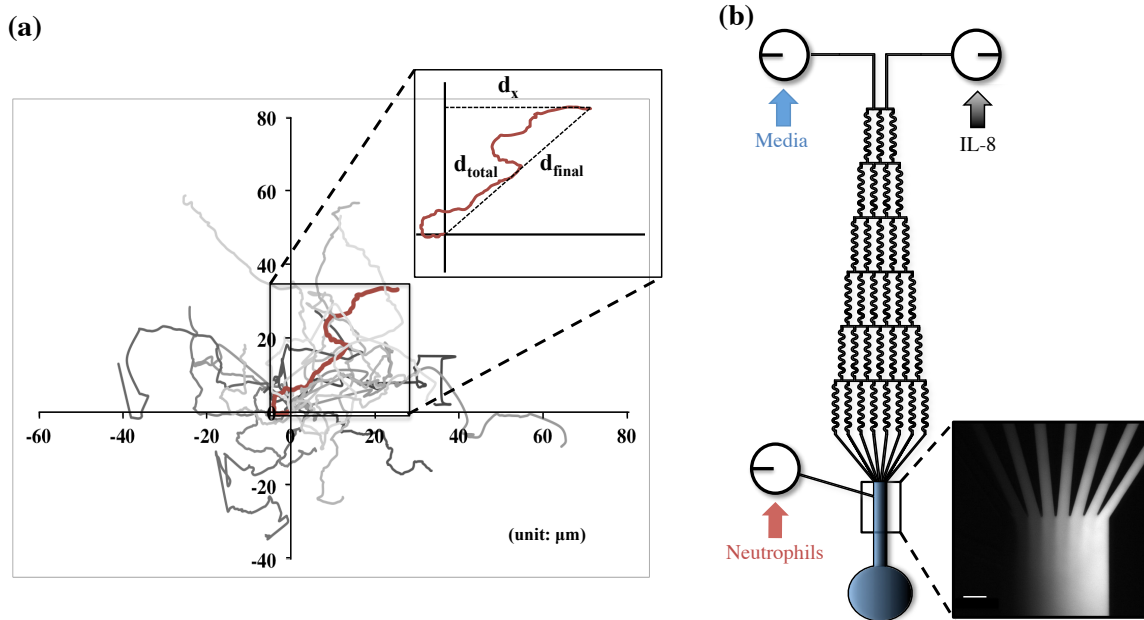


**Figure 2-2. (a) Trajectories of neutrophils in the control sample. The highlighted migratory routine of single neutrophils shows how data was processed for analysis. (b) Schematic of microfluidic gradient device used in the experiment and confirmation of chemical gradient with fluorescence imaging. (scale bar: 100  $\mu\text{m}$ ).**

nondirectional diffusion of chemokine molecules across the cell culture chamber. The fluorescence imaging shown in Fig. 2-2(b) confirms the formation of chemical gradients in the cell culture chamber with gradually increasing fluorescence intensity from left to right.

### **2-3-2. Neutrophil viability after drug treatment**

The effects of drugs, at varying doses and time periods, on neutrophil viability were evaluated using a traditional colorimetric MTT assay. The presence of 10  $\mu\text{M}$  CXCR2 antagonist SB225002 for 100  $\mu\text{L}$  of  $6 \times 10^5$  cells/mL neutrophils induced about 40% decrease in neutrophil viability versus the control condition after 150 min incubation, while 30 and 90 min incubation times caused smaller decreases in viability (Fig. 2-3(a)). These compromised viabilities are likely attributable completely to drug cytotoxicity as none of the incubation times are long enough to induce spontaneous neutrophil apoptosis.<sup>30</sup> In addition, the same trends of viability reduction were observed while exposed to 1  $\mu\text{M}$  and 100 nM SB225002. These results imply that SB225002 blocks the surface receptor sites accompanied with the internalization of antagonist, resulting in decreased neutrophil viability. The introduction of the PI3K inhibitor LY294002 only reveals moderate cytotoxic effects on neutrophils. Approximately a 20% reduction in neutrophil viability was observed after 90 and 150 min treatment at all the concentrations, and 30 min incubation had almost no effect on neutrophil viability (Fig. 2-3(b)). Previous studies suggested that PI3K played an important part in the anti-apoptotic system activated by granulocyte/macrophage colony-stimulating factor (GM-CSF),<sup>31,32</sup> and

LY294002 was revealed to suppress the survival effects of this cytokine. Since there was no GM-CSF in the neutrophil medium to activate the PI3K pathway, the cytotoxic effects of LY294002 on neutrophils were limited as precedent work suggests. The evaluation of neutrophil viability after theophylline incubation was also in agreement with the previous reports that indicated a significant drop in neutrophil viability.<sup>33</sup> Unlike the dose-dependent effects displayed in previous reports, neither the therapeutic plasma concentration (10  $\mu$ M) nor excessive amounts of theophylline (100  $\mu$ M and 1 mM) showed any reduction in neutrophil viability with 30 min incubation. For 90 min incubation, theophylline induced a 40% reduction in viability at all the three concentrations, and all the drug concentrations induced a 50% decrease in neutrophil viability with 150 min incubation (Fig. 2-3(c)). Theophylline is known to down-regulate the expression of *bcl-2*, a protein in eosinophils and B cells that protects cells against apoptotic stimuli,<sup>34</sup> however, this explanation cannot be employed herein due to the absence of *bcl-2* expression in neutrophils. Another study demonstrated that theophylline augments granulocyte apoptosis by inhibiting the adenosine  $A_{2A}$  receptor after 16 h culture,<sup>35</sup> but this long time incubation made it impossible to discriminate between the contribution of spontaneous neutrophil apoptosis and drug-induced cell death. A detailed investigation of the immunomodulatory effects of theophylline on neutrophil apoptosis is clearly needed.

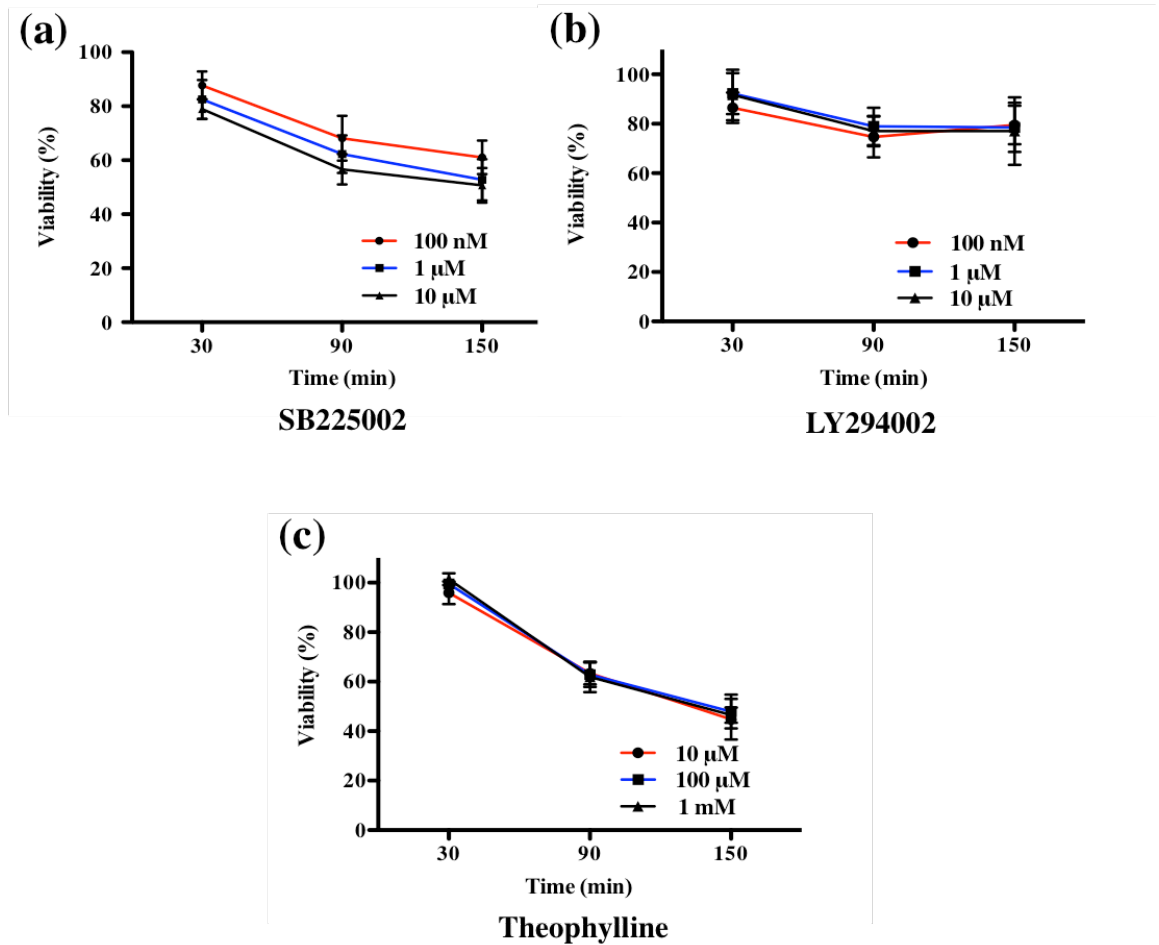


**Figure 2-3. Cytotoxic effects of each drug on neutrophil viability, as determined by the MTT assay. (a) Percent of neutrophil viability compared to the control condition after incubation with 100 nM, 1 μM, and 10 μM of SB225002 at different time points. (b) Percent of neutrophil viability compared to the control condition after incubation with 100 nM, 1 μM, and 10 μM of LY294002 at different time points. (c) Percent of neutrophil viability compared to the control condition after incubation with 10 μM, 100 μM, and 1 mM of theophylline at different time points. Error bar represents standard error of the mean.**

Based on the results herein, the CXCR2 antagonist SB225002 and theophylline both greatly shorten neutrophil life span quickly while the PI3K inhibitor LY294002 was less effective at inducing neutrophil apoptosis. SB225002 and theophylline are more potent drugs than LY294002 in accelerating neutrophil apoptosis, but the risk of SB225002 acting on other CXCR2-expressing cells and the common cytotoxicity of theophylline on immune cells should be considered for the future use.

### **2-3-3. Neutrophil chemotaxis with drug incubation**

Neutrophil chemotaxis under a 0-10 ng/mL IL-8 gradient was monitored in the gradient microfluidic device before and after drug treatment. Neutrophil migration patterns were quantified using the aforementioned three numerical parameters: MI, CI and ECI. Compared to the viability results reported above, neutrophil chemotaxis was not as sensitive to the low concentrations of CXCR2 antagonist, and no suppressive effect was observed under 100 nM and 1  $\mu$ M drug conditions (Fig. 2-4(a)). The addition of 10  $\mu$ M SB225002 resulted in a significant decrease in CI value after 90 and 150 min incubation while also causing an 80% decline in the ECI value after 150 min incubation. These results suggest that CXCR2 antagonism has remarkable impacts on the direction and effectiveness of neutrophil chemotaxis in a concentration- and time-dependent fashion without altering neutrophil motility. The  $IC_{50}$  of SB225002 for inhibiting neutrophil chemotaxis through CXCR2 antagonism is between 1  $\mu$ M and 10  $\mu$ M, which is much higher than the reported value ( $IC_{50} = 22$  nM).<sup>36</sup> This reported value was obtained using conventional chamber-based assays where all cells are assumed to be alive and

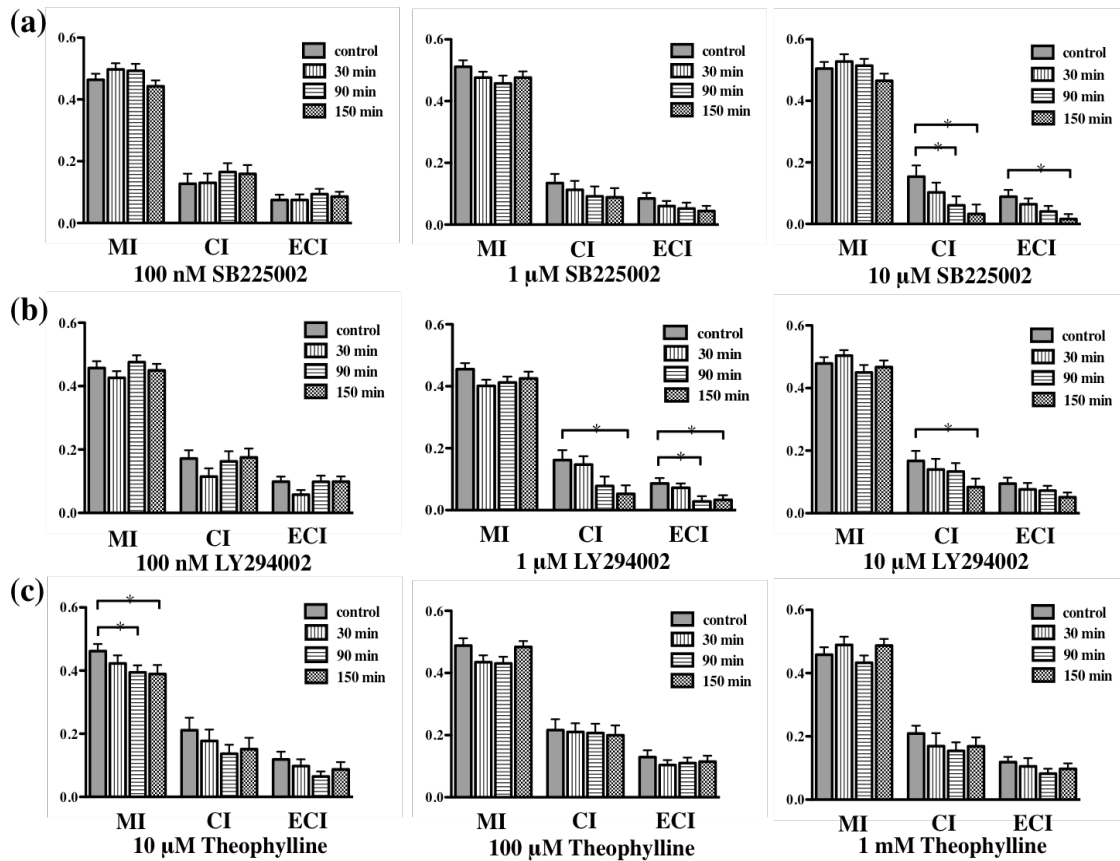


**Figure 2-4. The inhibitory effects of each drug on neutrophil chemotaxis (\*,  $p < 0.05$ , using a two-tailed unpaired t-test). (a) MI, CI, and ECI values after 100 nM, 1  $\mu$ M, and 10  $\mu$ M SB225002 treatment for control, 30 min, 90 min, and 150 min. (b) MI, CI, and ECI values after 100 nM, 1  $\mu$ M, and 10  $\mu$ M LY294002 treatment for control, 30 min, 90 min, and 150 min. (c) MI, CI, and ECI values after 10  $\mu$ M, 100  $\mu$ M, and 1 mM theophylline treatment for control, 30 min, 90 min, and 150 min.**

responding to the chemokine signal; however, dead cells induced by CXCR2 antagonist cannot migrate into the chemokine chamber and are retained in the medium chamber. In this fashion, chamber-based assays overestimate the inhibitory effects of SB225002 on neutrophil chemotaxis by ignoring the cytotoxicity of the drug. On the contrary, defunct neutrophils cultured in the microfluidic device are removed by the fluid flow or barely move on the bottom; these cells were eliminated from the data analysis, and only effective neutrophil chemotaxis was collected and analyzed.

Neutrophils exposed to varying concentrations of LY294002 showed distinct chemotactic behaviors. Similar to SB225002, 100 nM LY294002 had no major effect on neutrophil chemotaxis (Fig. 2-4(b)), and 10  $\mu$ M induced a significant decrease in the CI value after 150 min incubation, which confirms the conclusion that PI3K regulates the cellular polarization in the IL-8 signaling pathway and LY294002 interrupts the PI3K-involved neutrophil migration. Meanwhile, 1  $\mu$ M of LY294002 resulted in about a 70% reduction in CI signal after 150 min incubation as well as a statistically significant drop in ECI values after 90 and 150 min treatment. These results suggest that PI3K modulates neutrophil chemotaxis via a positive feedback loop wherein two cytokines function both upstream and downstream of one another. Although there is no literature precedent for the involvement of PI3K in a positive feedback loop, the phospholipid product PtdInsP<sub>3</sub> and downstream Rho GTPases have been reported to activate each other in a positive feedback relationship.<sup>37</sup> Herein, we speculate that neutrophils exposed to 10  $\mu$ M LY294002 are short of activated PI3K and PtdInsP<sub>3</sub>, which activates the positive feedback loop between PtdInsP<sub>3</sub> and Rho GTPases to stimulate the production of

PtdInsP<sub>3</sub>, thus preventing the inhibitory effects of LY294002. Unlike SB225002, the IC<sub>50</sub> of LY294002 for inhibiting neutrophil chemotaxis in this study was around 1 μM, close to the known value (IC<sub>50</sub> = 1.4 μM),<sup>38</sup> since LY294002 induces smaller cytotoxic impacts on neutrophils than SB225002, and the contribution of cytotoxic effects to IC<sub>50</sub> is limited for LY294002. This also supports our belief that the cytotoxic effects of drugs must be considered in the measured IC<sub>50</sub> values.

Theophylline, a current medication for COPD, indicates a completely opposite trend in neutrophil chemotaxis inhibition compared to the other drugs. At therapeutic concentration, 10 μM theophylline caused a significant decrease in MI value after 90 and 150 min incubation, with no significant change in CI and ECI values (Fig. 2-4(c)). Two larger concentrations, 100 μM and 1 mM, did not indicate any significant difference in the three numerical parameters, which suggests that theophylline only lowers the motility of neutrophils around the optimal concentration without any influence on the polarization and effectiveness of neutrophil chemotaxis. These results contradict the observation found in the previous studies that theophylline is a potent inhibitor for neutrophil chemotaxis.<sup>20-22</sup> As mentioned above, drug cytotoxicity can lead to overestimated chemotaxis in the traditional chamber-based assays by impeding neutrophil migration by increasing cell apoptosis rather than damaging chemotactic pathway. Theophylline induces a great drop in neutrophil viability instead of inhibiting

In sum, our results demonstrate that SB225002 and LY294002 decrease polarization and effectiveness of neutrophil chemotaxis at different optimal concentrations, but theophylline only decreases motility of neutrophils at therapeutic concentration.

#### **2-3-4. Intracellular calcium imaging**

To determine the role of  $\text{Ca}^{2+}$  in neutrophil chemotaxis, the effects of theophylline on the mobilization of intracellular  $\text{Ca}^{2+}$  during theophylline treatment were assessed using single cell ratiometric fluorescence imaging. In the medium containing  $\text{Ca}^{2+}$ , the concentrations of intracellular  $\text{Ca}^{2+}$  after 10 ng/mL IL-8 activation were determined at varying theophylline doses and incubation times. Compared to the control sample, the presence of 1 mM theophylline induced a significant decrease in intracellular  $\text{Ca}^{2+}$  after 30 and 150 min incubation (Fig. 2-5(a)), which indicates that theophylline suppresses the elevation of  $\text{Ca}^{2+}$  level in the IL-8 signaling pathway. The fluorescence images clearly show that the number of bright cells increases greatly after IL-8 stimulation without theophylline treatment (Fig. 2-5(c)); however, the elevation of intracellular  $\text{Ca}^{2+}$  was almost totally inhibited with 1 mM theophylline treatment after 150 min (Fig. 2-5(d)). In addition to the high dose, 10  $\mu\text{M}$  theophylline also significantly inhibited  $\text{Ca}^{2+}$  increase after 90 min incubation. Although there is no statistically significant inhibition for 100  $\mu\text{M}$  of theophylline, the average value of intracellular  $\text{Ca}^{2+}$  level at each time point was lower than that of the control sample. Combined with theophylline's apparent minimal effect on neutrophil chemotaxis, it appears that neutrophil chemotaxis is independent of the alteration in intracellular  $\text{Ca}^{2+}$ . In the  $\text{Ca}^{2+}$ -free medium, no significant change in intracellular  $\text{Ca}^{2+}$  levels was observed for any of the theophylline doses, accounting for the control cell behavior (where the influence of  $\text{Ca}^{2+}$  in the media was significant). These results suggest that the function of theophylline in IL-8 signaling pathway is to block the entry of  $\text{Ca}^{2+}$  into cells. First, the intracellular  $\text{Ca}^{2+}$  levels of the control

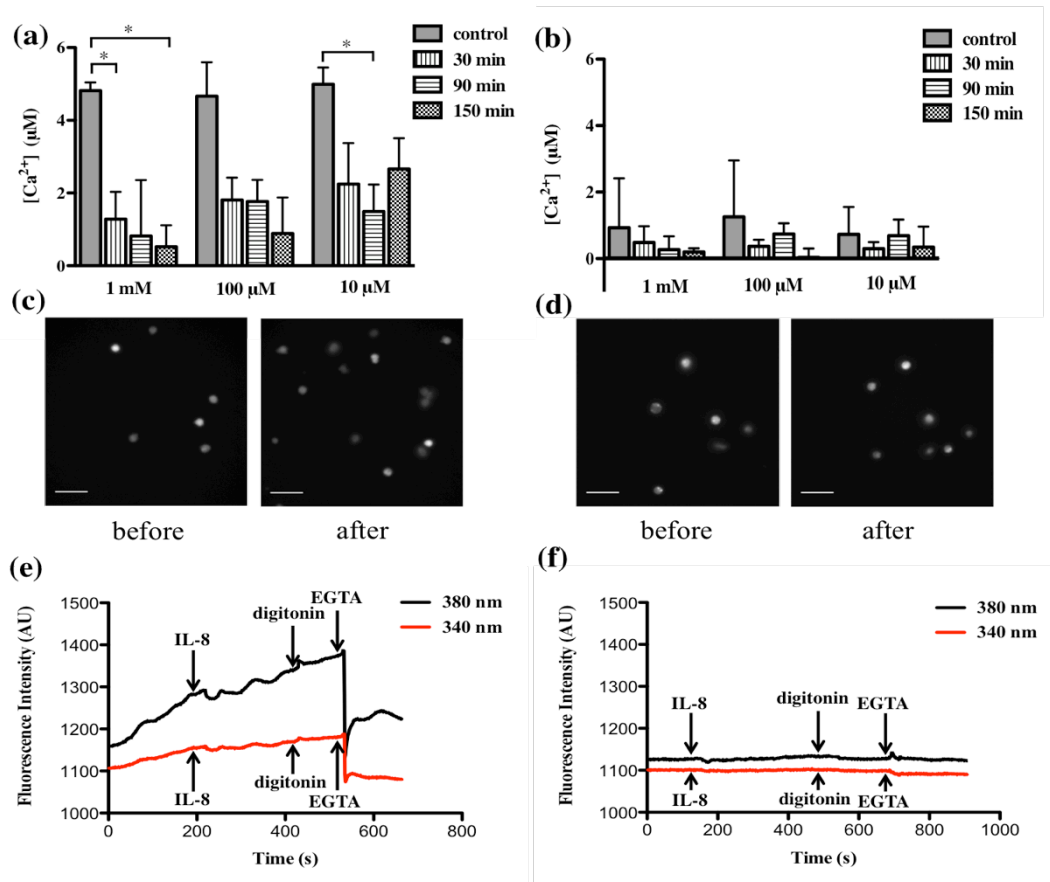


**Figure 2-5.** The effects of theophylline on mobilization of intracellular  $Ca^{2+}$  activated by 10 ng/mL IL-8 (\*,  $p < 0.05$ , using a two-tailed unpaired t- test). (a) Incubation with 10 mM, 100 mM, or 1 mM theophylline in the medium containing  $Ca^{2+}$ . (b) Incubation with 10 mM, 100 mM, and 1 mM theophylline in  $Ca^{2+}$ -free medium. (c) Fluorescence imaging of control sample before and after the addition of IL-8. (d) Fluorescence imaging of 150 min incubation sample with 1 mM theophylline before and after the addition of IL-8. The real-time calcium imaging curve in  $Ca^{2+}$ -containing medium: (e) Control condition; (f) Incubation with 1 mM theophylline for 150 min. (Scale bar in all the images: 50 µm).

conditions in  $\text{Ca}^{2+}$ -free medium are much lower than those in  $\text{Ca}^{2+}$ -containing medium, which indicates that IL-8 activation triggers the influx of extracellular  $\text{Ca}^{2+}$  and the absence of extracellular  $\text{Ca}^{2+}$  resulted in the small  $\text{Ca}^{2+}$  concentrations for the control conditions. Second, the conclusion that theophylline inhibits influx of extracellular  $\text{Ca}^{2+}$  is also confirmed by the real-time calcium imaging curve (Fig. 2-5(e) and (f)). After incubation with 1 mM theophylline for 150 min, the addition of digitonin, a cell-permeabilizing agent that allows entry of extracellular  $\text{Ca}^{2+}$ , induced a tiny increase in  $\text{Ca}^{2+}$  level; however, the addition of digitonin resulted in the maximum fluorescence measured for the control condition.

#### **2-4. Conclusions**

Three representative drugs were employed in this work to determine the drug effects on neutrophil function. Through the drug cytotoxicity assays, we found that the CXCR2 antagonist SB225002 and theophylline induced significant decreases in neutrophil viability at all tested concentrations while the PI3K inhibitor LY294002 produced mild decrease in neutrophil viability. This indicates that SB225002 and theophylline are more potent drugs to accelerate neutrophil apoptosis. A microfluidic device with a highly stable chemokine gradient was employed to quantify neutrophil chemotaxis with and without drug treatment. More importantly, the microfluidic platform was used to monitor neutrophil chemotaxis independent of drug cytotoxicity and demonstrated that the conventional chamber-based assays likely overestimate the inhibitory effects of drugs due to the unaccounted for drug cytotoxicity. SB225002 was shown to mediate neutrophil

chemotaxis in a time- and concentration-dependent manner while LY294002 triggered a positive feedback loop of PtdInsP<sub>3</sub> and Rho GTPases in the IL-8 signaling pathway at high doses. Theophylline indicated slight capability to slow neutrophil chemotaxis, and further investigation revealed that the alteration of intracellular Ca<sup>2+</sup> had no effect on neutrophil chemotaxis but was inhibited by theophylline treatment. The exploration of drug effects on neutrophil function can be used to determine the biological implications of various relevant drugs and provide significant insights on drug development for neutrophilic inflammation.

## Chapter 3

### Recapitulation of *in vivo*-like Neutrophil Transendothelial Migration using a Microfluidic Platform

Adapted from:

Wu, X.; Kim, D.; Young, A. T.; Haynes, C. L., *Analyst*, **2015**, *140*, 5055-5064.

### 3-1. Introduction

As the most abundant white blood cell type, neutrophils function as the primary immune cells in various relevant diseases and recruit to the sites of infection through the endothelial cell layer in response to the physiological signals generated from invading microorganisms or local macrophages.<sup>1,2</sup> Neutrophil transendothelial migration (TEM) is a key multi-step process involved in inflammation since the activation of endothelial cells enables the capture of bypassing neutrophils and triggers the subsequent neutrophil inflammatory responses.<sup>3,4</sup> The highly orchestrated interactions between endothelial cells and neutrophils include the initial neutrophil rolling on endothelium, firm adhesion mediated by receptor molecules on cell surfaces, transcellular or paracellular extravasation, and final migration towards the inflammation locus.<sup>1,5,6</sup> Investigation of the neutrophil TEM process will shed light on the detailed mechanisms of cellular interactions between neutrophils and endothelial cells, also accelerating fundamental understanding of pathogenesis in neutrophil-related diseases.

Various traditional methods, such as the Boyden chamber<sup>7,8</sup> and transwell assays,<sup>9</sup> have been employed to recapitulate the *in vivo* leukocyte TEM processes; however, these approaches are not able to accurately represent the characteristics based on two main limitations: (1) conventional methods cannot achieve stable long-lasting chemical gradients to support the quantitation of neutrophil TEM and (2) these methods build up endothelial cell layers on a two-dimensional (2D) substrate that only facilitates neutrophil TEM observation through the basement membrane while ignoring the recruitment in other directions. The chemical gradients generated by the chamber-based assays rely on

the free diffusion of molecules between two separated chambers such that the shapes of gradients decay quickly and the results of neutrophil TEM cannot be interpreted in a quantitative and controllable fashion. In addition, the upright filter membrane set up for endothelial cell layer culture cannot reflect the whole picture of neutrophil TEM in different directions and introduces the contribution of gravity into neutrophil TEM, inspiring consideration of an improved platform to study the mechanisms of neutrophil migratory behaviors.

Microfluidic technology, devices that allow the manipulation of small volume fluids in microchannels,<sup>10</sup> is promising for recapitulation of the *in vivo* neutrophil TEM process, especially with the inclusion of three-dimensional (3D) hydrogel matrices.<sup>11-14</sup> The compact fibrous hydrogel structure, combined with the small dimensions of microfluidic devices, facilitate the creation of predictable, reproducible, and long-term stable chemical gradients with high spatiotemporal resolution so that the neutrophil TEM process can be characterized in a real-time and quantitative manner. More importantly, the inclusion of hydrogel materials not only provides mechanical support for the growth of an endothelial cell layer in the perpendicular direction, but also successfully models extracellular matrix (ECM) with realistic biophysical properties. With these efforts, a highly robust and accurate microfluidic model can be developed to study the neutrophil TEM process. Several previous examples have studied neutrophil migration through the endothelial cell layer using microfluidic platforms,<sup>15-18</sup> but these efforts failed to account for the real configuration of blood vessels or the various cellular stimuli. One promising advantage of our device design compared to the existing microfluidic assays is the introduction of

multiple chemical gradients in different directions relative to the endothelial cell layer. In an *in vivo* setting, the neutrophil TEM process occurring at one specific site is guided by an array of chemoattractants gradients in different directions released from various biological sources; however, the existing microfluidic assays cannot recapitulate this microenvironment and only characterize neutrophil TEM without the complexity of multiple chemical gradients. The goal of this work was to build on previous efforts to create a versatile microfluidic platform, more similar to the complex physiological milieu, to study the critical process of neutrophil TEM.

Chemoattractants are the signaling molecules responsible for inducing neutrophil migration and activating endothelial cells in the neutrophil TEM process.<sup>19,20</sup> Herein, we considered neutrophil TEM under the influence of three inflammatory chemoattractants: interleukin-8 (IL-8), N-formyl-methionyl-leucyl-phenylalanine (fMLP), and leukotriene B4 (LTB4). IL-8, one of the primary chemoattractants initiating *in vivo* neutrophil TEM, is known to enhance cell adherence to matrix proteins, endothelium, and tissues to promote cell recruitment.<sup>21</sup> Similar to IL-8, LTB4 is another type of host-derived chemoattractant that is known to induce cell adhesion, activation, and formation of reactive oxygen species.<sup>22,23</sup> On the contrary, fMLP is a formylated short peptide of bacterial origin and functions as an intense chemoattractant for several cell types.<sup>24</sup> As mentioned above, the introduction of various chemical gradients within our microfluidic device is able to establish the hierarchy of these three chemoattractants through developing competing chemical gradients in two opposing symmetric channels, which

enables mechanistic investigation of neutrophil migratory signaling cascades during decision-making process.

## **3-2. Experimental details**

### **3-2-1. Device fabrication**

Standard photolithography protocols were applied to fabricate microfluidic devices. The design of the device was printed on a film (CAD/Art Service Inc., Bandon, OR) with transparent channel patterns and a lightproof background. Through the exposure to UV light, channel patterns were transferred onto a chrome photomask plate coated with AZ1518 positive photoresist layer (Nanofilm, Westlake Village, CA). Then, the exposed chrome layer was etched down in the chrome etchant solution (Cyantek Corporation, Fremont, CA). To remove the residual photoresist, the photomask was immersed in piranha solution (1:1 volume ratio of 30% hydrogen peroxide and 99.9% sulfuric acid, Avantor Performance Materials, Phillipsburg, NJ) and then washed using deionized (DI) water. After the preparation of the photomask, the microfluidic device mold was fabricated by spin-coating a 4-inch silicon wafer with 120- $\mu\text{m}$ -thick negative SU-8 50 photoresist (MicroChem, Newton, MA). The channel patterns were imprinted on the SU-8 mold through the previously made photomask *via* UV exposure following an initial baking step. The silicon wafer was placed in SU-8 developer (MicroChem, Newton, MA) to remove the photoresist without exposure, and the channel patterns were left on the mold. A 10:1 mass ratio mixture of Sylgard 184 silicone elastomer base and curing agent

(Ellsworth Adhesives, Germantown, WI) was poured on the SU-8 mold and kept on a hot plate at 95 °C overnight. Medium channel reservoirs and gel chamber inlets were punched at appropriate points in the polydimethylsiloxane (PDMS) layer using 3.5 mm and 1 mm disposable biopsy punches (Integra Miltex, Plainsboro, NJ), respectively. Finally, the PDMS layer was cut and then permanently attached to a glass slide by using oxygen plasma for 10 seconds at 100 L/h oxygen flow rate and 100 W.

### **3-2-2. Endothelial cell culture**

The human endothelial cell line hy926, a phenotype suitable for neutrophil-endothelial cell interaction studies,<sup>16,25,26</sup> was purchased from American Type Culture Collection (ATCC, Manassas, VA) and stored in liquid nitrogen storage container (MVE XC33/22, Select Genetics, Washington, PA). Upon thawing, endothelial cells were dispensed into a 75 cm<sup>2</sup> flask containing 20 mL of Dulbecco's Modified Eagle Medium (DMEM, formula: 4mM L-glutamine, 4.5 g/L L-glucose, and 1.5 g/L sodium pyruvate, Gibco, Carlsbad, CA) supplemented with 10% fetal bovine serum and 1% penicillin and streptomycin (Sigma-Aldrich, St. Louis, MO). Cells were fed every other day and, when necessary, cells were detached using 1× trypsin solution (Sigma-Aldrich, St. Louis, MO) for device injection. Endothelial cells were only used between the third and tenth passages.

### **3-2-3. Device preparation**

First, microfluidic devices were filled with 30 µL of 1 mg/mL poly-D-Lysine (PDL) solution (Sigma-Aldrich, St. Louis, MO) and incubated for 4 h under 5% CO<sub>2</sub> at 37 °C.

After the completion of surface coating, devices were rinsed with 30  $\mu$ L of sterilized Milli-Q water (Millipore, Billerica, MA) twice to remove excess PDL solution that may cause damage to cells. Prior to introducing gel, devices were placed in the oven at 65  $^{\circ}$ C for 24 to 48 h so that the hydrophobicity of devices was restored. Collagen type I gel solution (BD Biosciences, San Jose, CA), one common hydrogel material used for simulating extracellular matrix,<sup>12,15,27</sup> was diluted to a concentration of 2 mg/mL and injected into the gel chamber through the gel inlet. To avoid the evaporation of gel solution, all the devices were kept in humid pipette boxes after the gel injection and a thermally induced polymerization was carried out under 5% CO<sub>2</sub> at 37  $^{\circ}$ C for 30 min. The porous fiber structure of the resulting collagen gel was visualized using a scanning electron microscope (SEM). Two drops of polymerized collagen gel solution were added on a small piece of silicon wafer for water evaporation and the dried gel was coated with 5-nm-thick platinum. The sample was observed at 10 kV using a field emission scanning electron microscope (Jeol 6700F, JEOL USA, Peabody, MA).

After the gel polymerization, 20  $\mu$ L of cell culture medium was forcibly injected into each channel of the microfluidic device, and the medium in all six reservoirs was aspirated before loading endothelial cells. Endothelial cells were trypsinized and re-suspended in the cell culture medium for a proper density ( $1.5 - 2 \times 10^6$  cells/mL), and then 20  $\mu$ L of endothelial cells were seeded into a reservoir of the bottom channel to enable the cell layer to attach on the side wall of gel because of the pressure difference between the bottom channel and side channels. Following an initial incubation under 5% CO<sub>2</sub> at 37  $^{\circ}$ C for 30 min, the medium was aspirated from the bottom reservoirs, and 30

$\mu\text{L}$  of fresh medium was added in each reservoir. Finally, all the devices were placed in the  $\text{CO}_2$  incubator (New Brunswick Scientific, Edison, NJ) overnight for confluent growth of the endothelial cell layer. For the conditions without an endothelial cell layer, the same procedure was used except for the addition of endothelial cells in the devices.

#### **3-2-4. Neutrophil isolation**

Ethylenediaminetetraacetic acid (EDTA)-anticoagulated freshly drawn human blood samples were prepared by Memorial Blood Center (St. Paul, MN). Immediately after blood samples were collected, neutrophils were separated and purified using a previously reported isolation protocol.<sup>28</sup> Carefully, 5 mL of blood sample was layered on the same volume of mono-poly resolving medium (Fisher Scientific, Waltham, MA) and promptly centrifuged to obtain a distinct neutrophil band. Neutrophils were washed using red blood cell lysis buffer (Miltenyi Biotec Inc., Auburn, CA) several times (2.5 mL for each time) until only white cells were left at the bottom of centrifuge tube. The final neutrophil pellet was re-suspended in Hank's buffered salt solution (HBSS, Fisher Scientific, Waltham, MA) containing 2% human serum albumin (HSA, Sigma-Aldrich, St. Louis, MO) at a cell density between  $4 - 5 \times 10^6$  cells/mL.

#### **3-2-5. Neutrophil transendothelial migration experiments**

Before introducing neutrophils into the device, the medium in each of the reservoirs terminating the bottom and left channels was replaced with 30  $\mu\text{L}$  of HBSS buffer while medium in each reservoir of the right channel was changed to 30  $\mu\text{L}$  of chemoattractant

solution (IL-8 and fMLP, Sigma-Aldrich, St. Louis, MO; LTB<sub>4</sub>, Cayman Chemical, Ann Arbor, MI). Different chemoattractant solutions were placed in the two opposing side channels for competing gradient conditions, and HBSS buffer was placed in the both channels in the chemoattractant-free condition. It took approximately 2 h to achieve completely stable diffusion of chemoattractant molecules in the gel scaffold. Then, 5  $\mu$ L of neutrophils of the desired density were added into the bottom channel of the device. Neutrophil TEM was monitored using MetaMorph ver. 7.7.5 imaging software (images recorded every other hour for 5 h) on an inverted microscope equipped with a 10 $\times$  objective (Nikon, Melville, NY) and a CCD camera (QuantEM, Photometrics, Tucson, AZ). Data from neutrophils collected from three different donors were measured in each condition.

To obtain the endothelial cell conditioned medium, 100  $\mu$ L of endothelial cells at 3 - 4  $\times$  10<sup>6</sup> cells/mL were seeded on a 96 well plate and mixed with 100  $\mu$ L of chemoattractant solution (20 ng/mL, 40 ng/mL or 100 ng/mL) to make sure that the final concentration of endothelial cells and chemoattractants were equal to those used in single gradient conditions. The plate was placed in the 5% CO<sub>2</sub> incubator at 37 °C overnight. Then, the conditioned medium containing all the secreted molecules and chemoattractants was collected and added into the right side channel of the microfluidic device with 30  $\mu$ L in each reservoir. After achieving a stable chemical gradient, 5  $\mu$ L of 4 - 5  $\times$  10<sup>6</sup> cells/mL neutrophils were injected into the bottom channel, and neutrophil migration was tracked using the bright-field microscope.

### **3-2-6. Receptor expression**

The prepared device with an endothelial cell layer was incubated with the desired chemoattractant solution in the right side channel or both side channels for 7 h (the first 2 h for chemoattractant diffusion and the following 5 h for endothelial cell activation) without the addition of neutrophils. After that, all the channels were washed twice using 1× phosphate-buffered saline (PBS, Sigma-Aldrich, St. Louis, MO) solution by filling one reservoir with 40 μL PBS and letting it flow along the channels to fill the other one. Then, 30 μL of allophycocyanin (APC) conjugated p-selectin antibody (5 μg/mL) or ICAM-1 antibody solution (2.5 μg/mL) (eBioscience, San Diego, CA) was added into each reservoir of the bottom channel while 1× PBS was added into the other reservoirs for 2 h adhesion molecules labeling. Finally, fluorescence agents were washed using 1× PBS twice and the devices were imaged on the microscope. The fluorescence intensity of receptor molecule expression was measured with a 20x objective (Nikon, Melville, NY) using MetaMorph software (Molecular Devices, Sunnyvale, CA).

### **3-2-7. Numerical simulation and fluorescence imaging**

Chemical gradients of 50 ng/mL fMLP in the gel chamber were verified using the molecular diffusion module in simulation software COMSOL 4.3b. Diffusion coefficients for fMLP in the collagen gel, free solution and endothelial cell layer were assumed to be  $6.99 \times 10^{-11} \text{ m}^2/\text{s}$ ,  $4.2 \times 10^{-10} \text{ m}^2/\text{s}$ , and  $9.55 \times 10^{-11} \text{ m}^2/\text{s}$ , respectively.<sup>15</sup> In addition, 100 μM of rhodamine 6G in HBSS buffer was employed to replace chemoattractants solution in the right side channel for the visualization of chemical gradients. The fluorescence

intensities in the gel chamber were recorded using MetaMorph ver. 7.7.5 imaging software at different time points. For the endothelial cell layer permeability experiment, 10  $\mu\text{M}$  of FITC-dextran (Sigma-Aldrich, St. Louis, MO) was placed in the bottom channel while HBSS buffer was added into side channels. After 2 h diffusion of fluorescence solution, the flux balance at the endothelial cell- gel interface was developed to calculate the permeability:

$$J = -D \frac{\partial C}{\partial x}$$

where,  $J$  is flux,  $D$  is diffusion coefficient of FITC-dextran ( $6.75 \times 10^{-11} \text{ m}^2/\text{s}$ ) in the collagen gel and  $x$  is the position.

$$\text{Flux} = -P\Delta C$$

where,  $P$  is permeability and  $C$  is concentration.

### **3-2-8. Confocal imaging**

After the formation of endothelial cell layer on the side wall of collagen gel, DMEM medium in all reservoirs was removed, and the channels were rinsed with  $1\times$  PBS solution using the same method detailed in the receptor expression experimental procedure. PBS was aspirated from all the reservoirs, and the wash step was repeated twice. Following the PBS wash, 30  $\mu\text{L}$  of 4% (wt/vol) paraformaldehyde (PFA, Sigma-Aldrich, St. Louis, MO) was added to each reservoir to fix the cells for 15 min. PFA was washed with PBS using the same steps above and then 30  $\mu\text{L}$  of 0.1% (vol/vol) Triton X-100 (Sigma-Aldrich, St. Louis, MO) was placed in each reservoir for permeabilization of endothelial cell membranes, allowing fluorescence reagent to enter the cells more easily.

After incubation with Triton X-100 for 5 min, endothelial cells were washed with PBS twice and 30  $\mu\text{L}$  of the mixture containing 4,6-diamidino-2-phenylindole dilactate (DAPI dilactate) at the working concentration (5  $\mu\text{g}/\text{mL}$ ) and rhodamine phalloidin (6.6  $\mu\text{M}$ ) (Life Technologies, Carlsbad, CA) was added in each reservoir for staining the cells. The petri dish containing devices was wrapped with aluminum foil and placed in the dark for 1 h incubation. Before imaging, microfluidic devices were washed with PBS again to remove excess fluorescence reagents. The 3D configuration of the endothelial cell layer was imaged using a Nikon A1R MP confocal microscope. Finally, all the slices were deconvoluted using AutoQuant X 3.0.4 software (Media Cybernetics, Rockville, MD) and processed with Imaris software (Bitplane AG, Zurich, Switzerland).

### **3-3. Results and discussion**

#### **3-3-1. Characterization of neutrophil TEM system**

The microfluidic device consists of two side channels, one bottom channel and the central gel chamber that separates these three channels (Fig. 3-1(a) and (b)). In our design, endothelial cells attached to the side wall of collagen gel are activated by the chemoattractants originating from the side channels; meanwhile, neutrophils in the bottom channel received the biological signals from endothelial cells and complete the TEM process along the direction of the chemical gradients. The prerequisite for establishing chemical gradients in the collagen gel is the stable diffusion of chemoattractant molecules between two symmetrical side channels. Due to the solid 3D

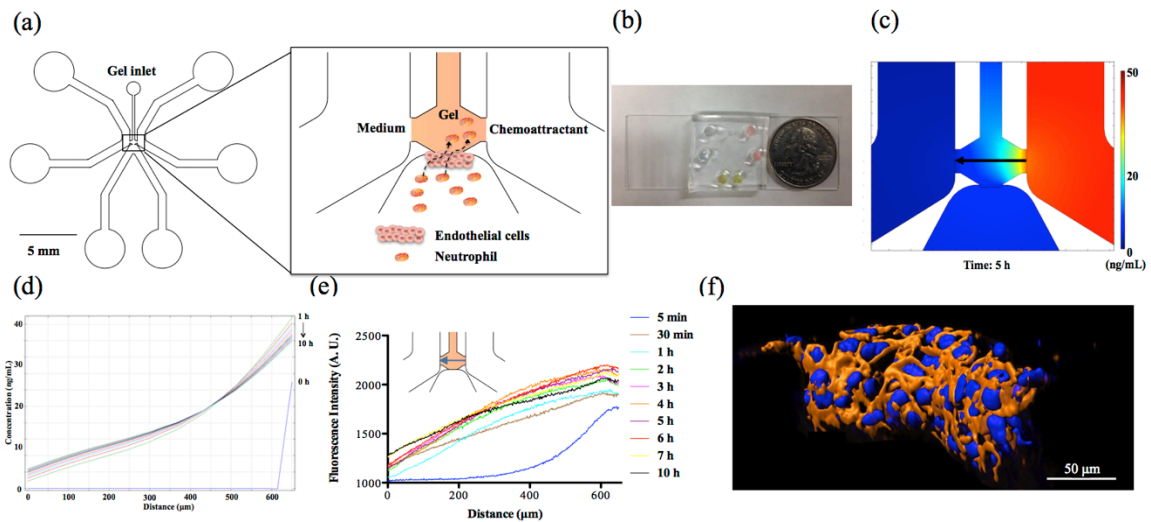


**Figure 3-1. Characterization of neutrophil TEM microfluidic device. (a) Schematic of microfluidic device design. Endothelial cells (not to scale) are cultured on the side wall of the collagen gel, and chemoattractant solution or medium is placed in the side channels for developing chemical gradients. The black arrow line indicates the migration route of neutrophils across the endothelial cell layer. (b) Photograph of a real device from the top view. (c) COMSOL simulation of a chemical gradient after 5 h diffusion using 50 ng/mL fMLP in the right side channel. The black arrow indicates the direction of gradient from high concentration to low concentration. (d) The COMSOL simulation results of the chemical gradient induced by 50 ng/mL fMLP. (e) The visualization of the fluorescence gradient at the center line of the gel chamber at different time points. (f) Deconvoluted confocal imaging of endothelial cell layer cultured on the side wall of the gel (blue indicates cell nucleus stained by DAPI and orange represents cytoskeletal F-actin labeled by rhodamine phalloidin).**

cross-linked network of collagen gel, molecular diffusion is confined at a slow and uniform rate that promotes the long-term stabilization of the chemical gradient. To verify the diffusion characteristics of chemoattractant molecules, theoretical simulation and experimental fluorescence imaging have been employed to observe the chemical gradient in the collagen gel. The simulation result (Fig. 3-1(d)) using finite element method software COMSOL 4.3b reveals that the chemical gradient across the center line in the gel chamber produced by 50 ng/mL fMLP solution is linear and stable from 1 h to 10 h diffusion (Fig. 3-1(c) shows the diffusion of fMLP molecules at 5 h), which is suitable for examining neutrophil TEM with reproducible spatiotemporal resolution. Also, the chemical gradient was visualized at different time points by placing rhodamine 6G solution in the right side channel and monitoring the fluorescence gradient across the center line in the gel chamber; this experiment demonstrated that a stable fluorescent gradient can be achieved after 2 h diffusion, and there is no apparent decay until 10 h (Fig. 3-1(e)). The profiles of chemical gradients are similar between those apparent in the COMSOL simulation and the empirical fluorescence imaging results, but it takes longer than expected (2 h vs. 1 h as predicted by COMSOL) to reach stable diffusion for fluorescence imaging; as a result, 2 h was used as the wait time for gradient formation before neutrophil injection. Since the diffusion coefficient is directly relevant to the molecular weight, the established rhodamine 6G (~479 Da) gradient will be very similar to fMLP (~437 Da) and LTB4 (~340 Da) conditions. Although IL-8 has a much higher molecular weight (~ 8.4 kDa) than the other two chemoattractants, this difference is likely compromised in the highly compact gel structure such that all of the

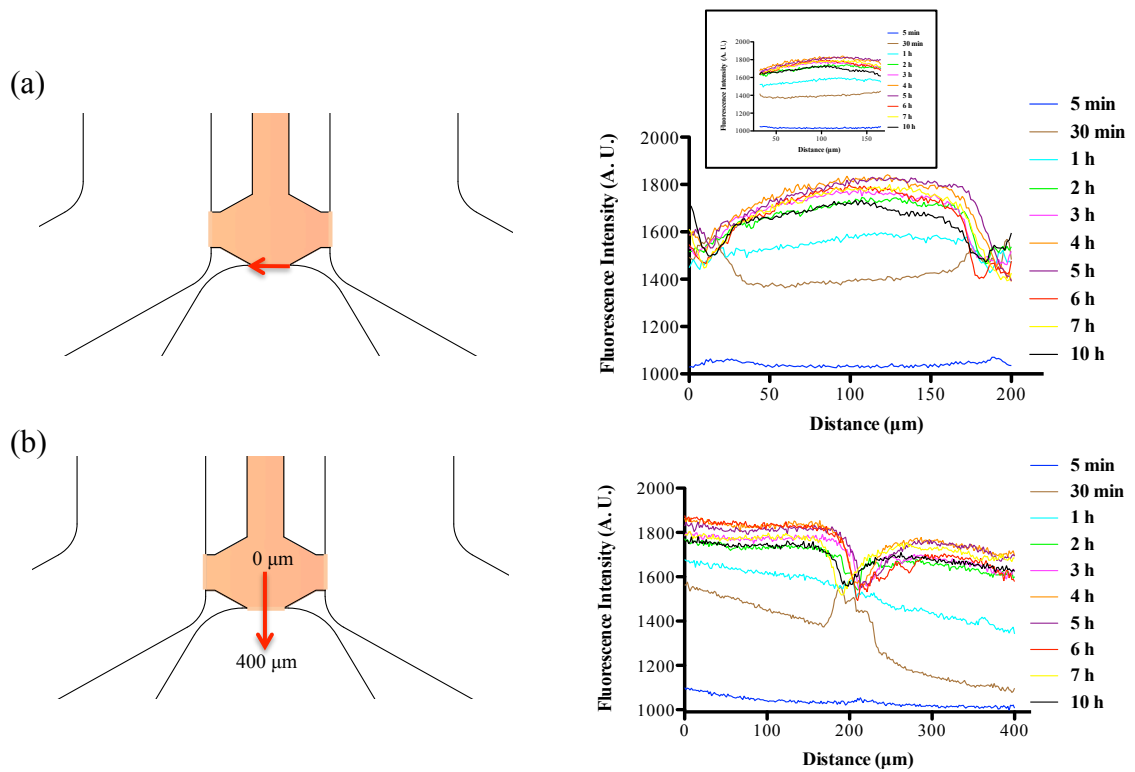


**Figure 3-2. Fluorescence gradients along different directions in the gel chamber. The fluorescence gradients (a) at the interface of the gel chamber and the endothelial cell layer and (b) in the vertical direction from the gel chamber to the endothelial cell channel (the burst change of fluorescence intensities are caused by the autofluorescence of endothelial cells and the autofluorescence was subtracted from the gradient in the inset picture).**

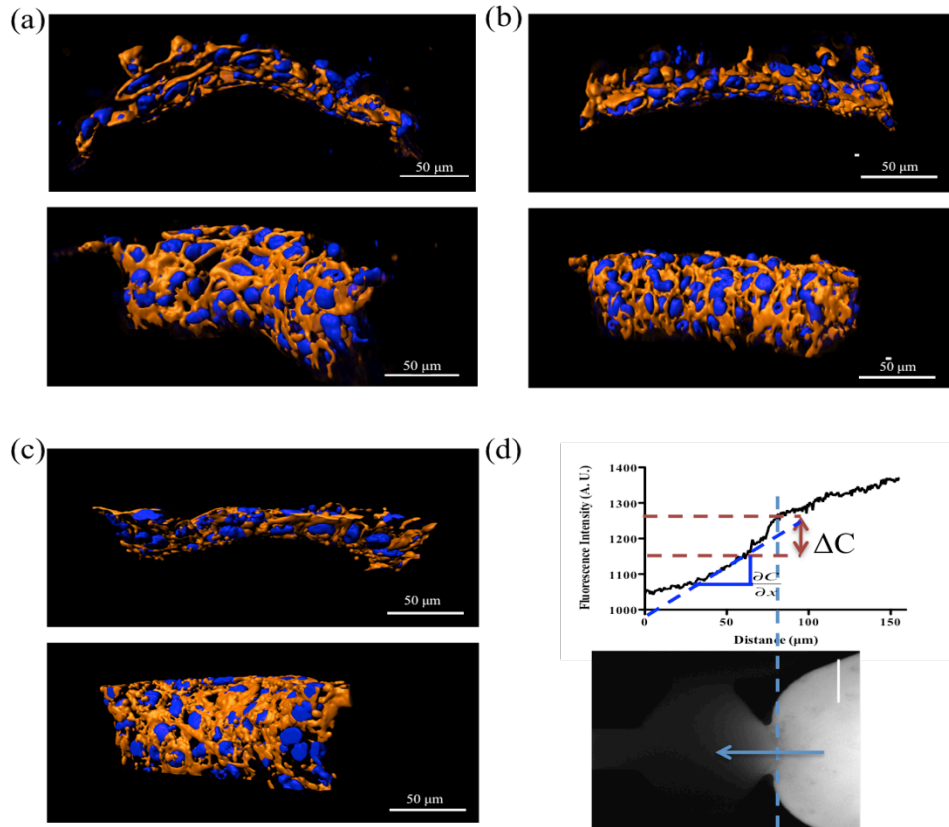


**Figure 3-3. Confocal images of endothelial cell layers in three different microfluidic devices: (a) top view (top) and side view (bottom) of cell layer in device 1; (b) top view (top) and side view (bottom) of cell layer in device 2; (c) top view (top) and side view (bottom) of cell layer in device 3 (blue indicates cell nucleus stained by DAPI and orange represents cytoskeletal F-actin labeled by rhodamine phalloidin). (d) Measurement of endothelial cell layer permeability. The permeability of the endothelial cell layer was measured using the fluorescence intensity profile of FITC-dextran solution after 2 h diffusion from bottom channel to the gel scaffold. The blue arrow indicates the direction of the fluorescence gradient. (scale bar: 200 μm)**

chemoattractants have similar diffusive behaviors.<sup>15</sup> In addition to examining the center line of gel chamber, we found that the fluorescence gradient becomes steady after 2 h at other positions, including the gel-endothelial cell interface and the vertical direction across cell layer that characterizes the gradient from top to bottom (Fig. 3-2(a) and (b)), suggesting that gradients in various parts of the microfluidic devices reach stabilization after the first 2 h and can be maintained for a long time. Furthermore, the results of confocal and dark-field imaging confirm the confluency of the whole endothelial cell layer structure on the side wall of gel scaffold (Fig. 3-1(f)) and the confocal images of three different devices clearly indicate good reproducibility of cell layer configuration from device to device (Fig. 3-3(a) - (c)). The permeability of the endothelial cell layer was measured by analyzing fluorescence images of the device after 2 h diffusion of fluorescein isothiocyanate (FITC)-dextran solution across the endothelial cell layer from the bottom channel to the gel scaffold (Fig. 3-3(d)); the measured permeability was  $5.73 \times 10^{-7}$  m/s, a value similar to those reported in the other *in vitro* systems with a non-permeable endothelial cell layer,<sup>15,29</sup> indicating a good seal between the endothelial cell layer and PDMS substrate. Together, these device characterizations suggest that this microfluidic platform will be a good model for the *in vivo* neutrophil TEM system.

### **3-3-2. Neutrophil TEM under single chemoattractant gradients**

With a well-characterized device, the neutrophil TEM process was first examined under single chemoattractant gradients. For each chemoattractant, three different concentrations (10 ng/mL, 20 ng/mL, and 50 ng/mL) were employed to build up chemical gradients

from the right channel to the left channel; neutrophil migration in the gel chamber was monitored every other hour after neutrophil injection into the device. The images at 5 h (Fig. 3-4(a) - (c)) clearly show that a number of neutrophils migrate into the gel region across the endothelial cell layer in each condition. To quantify the results of neutrophil TEM, we simply counted the number of cells in different regions of the gel chamber (Fig. 3-4(g) and (h)) with linear and continuous gradients so that the effects of localized chemoattractant concentrations on neutrophil polarization could be determined. The largest concentrations (50 ng/mL) for all the chemoattractants (fMLP: 114 nM; LTB<sub>4</sub>: 147 nM; IL-8: 5.95 nM) lead to significant differences between the neutrophils present in the left and right portions of the device; however, there is no significant difference found with lower chemoattractant concentrations (10 ng/mL and 20 ng/mL) except for 20 ng/mL IL-8 (Fig. 3-5(a) - (c)). It is worth mentioning that different gel interface shapes caused by various surface tensions do not lead to the considerable deviation in average values of three replicates since the flat gradient shape in the vertical direction across the cell layer is not sensitive to small changes in the gel interface position (Fig. 3-2(b)). Additionally, the arc-shaped interfaces do not influence the number of neutrophils interacting with the endothelial cell layer due to the significant larger dimension of bottom channel for neutrophil injection. The amount of chemoattractants in each part of the gel chamber is proportional to the total chemoattractant concentration presented in the side channel, so the concentration differences between the left and right gel region become larger as the total chemoattractant concentrations increase. Neutrophils sense a

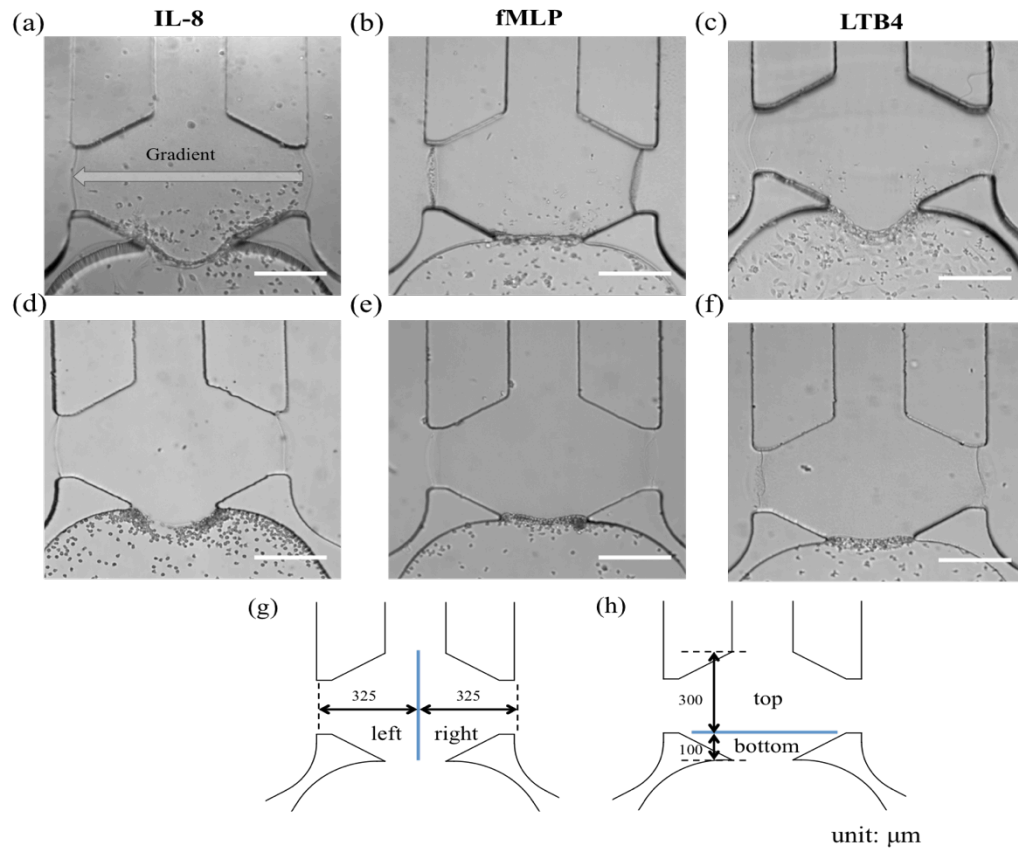


**Figure 3-4. Bright-field images of neutrophil TEM after 5 h neutrophil injection under single chemoattractant gradients (gradient direction is indicated in (a)): (a) 50 ng/mL of IL-8; (b) 50 ng/mL of fMLP; (c) 50 ng/mL of LTB4. Bright-field images of neutrophil migration without an endothelial cell layer after 5 h neutrophil injection under single chemoattractant gradients: (d) 50 ng/mL of IL-8; (e) 50 ng/mL of fMLP; (f) 50 ng/mL of LTB4. Division of collagen gel chamber into two different parts for analysis: (g) left and right parts; (h) top and bottom parts. (scale bar: 200 μm)**

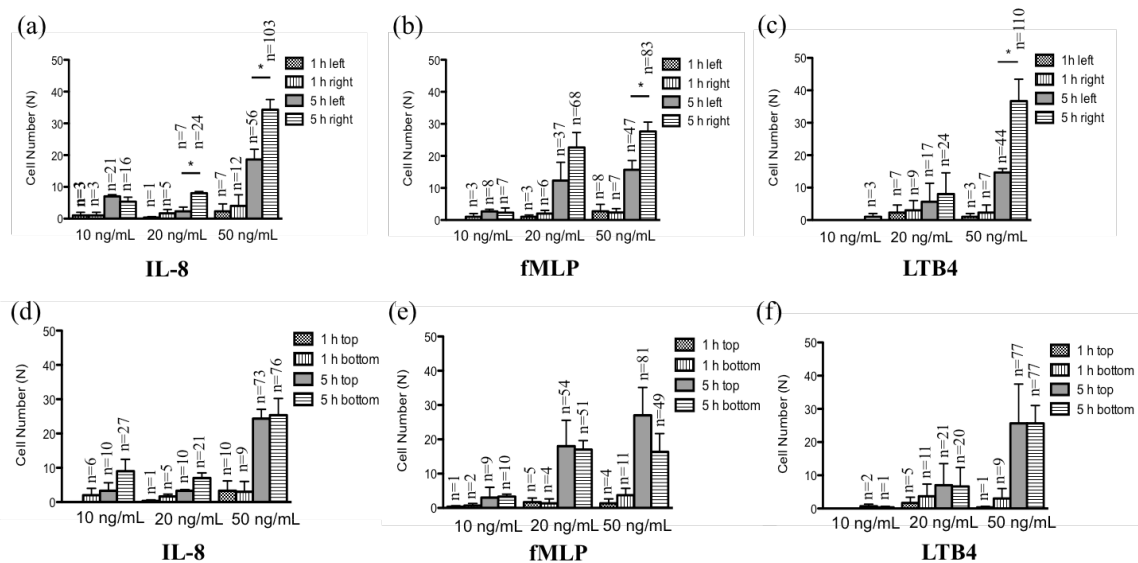


**Figure 3-5. Quantitative analysis of neutrophil TEM after 1 h and 5 h neutrophil injection under various single chemoattractant gradients (\*,  $p < 0.05$ , using a two-tailed unpaired t-test). The number of neutrophils in the left and right parts under (a) 10 ng/mL, 20 ng/mL, and 50 ng/mL of IL-8 gradient; (b) 10 ng/mL, 20 ng/mL, and 50 ng/mL of fMLP gradient; (c) 10 ng/mL, 20 ng/mL, and 50 ng/mL of LTB4 gradient. The number of neutrophils in the top and bottom parts under (d) 10 ng/mL, 20 ng/mL, and 50 ng/mL of IL-8 gradient; (e) 10 ng/mL, 20 ng/mL, and 50 ng/mL of fMLP gradient; and (f) 10 ng/mL, 20 ng/mL, and 50 ng/mL of LTB4 gradient. Error bars represent the standard error of the mean and the total number of cells (including 3 different biological replicates) analyzed in each condition is indicated for the corresponding column.**

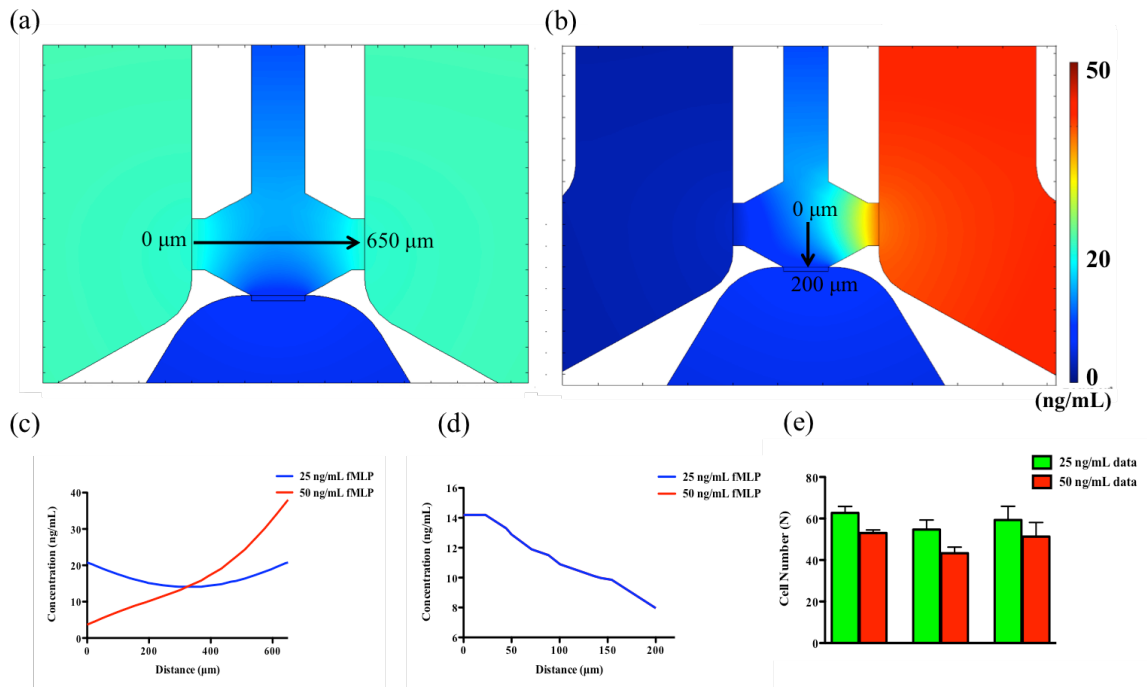


**Figure 3-6. Comparison of gradient profiles in single chemoattractant gradients and no gradient conditions. The COMSOL simulation results of fMLP solution in the microfluidic device after 5 h diffusion: (a) 25 ng/mL of fMLP solution in both side channels; (b) 50 ng/mL of fMLP solution in the right channel. The gradient profiles of two conditions along the (c) center line of gel chamber (indicated in (a)) in the horizontal direction and (d) the center line (indicated in (b)) in the vertical direction. (e) The total numbers of neutrophils located in the gel scaffold after 5 h transmigration for these two conditions. Error bars represent the standard error of the mean.**

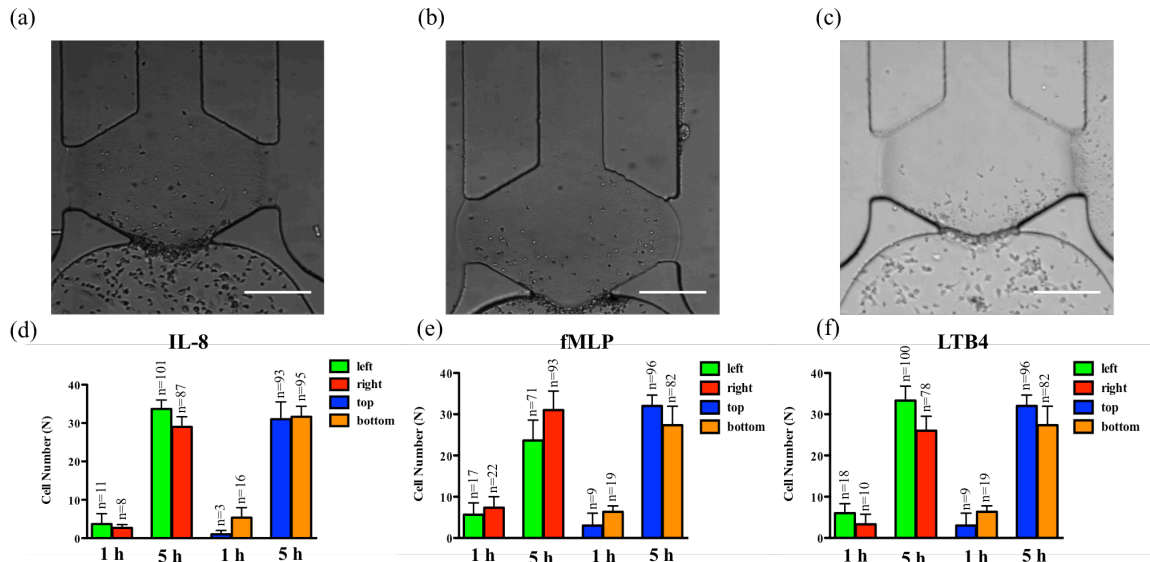


**Figure 3-7. Neutrophil migration results under no gradient conditions. Bright-field images of neutrophil TEM at 5 h after neutrophil injection: (a) 25 ng/mL IL-8 in both side channels; (b) 25 ng/mL fMLP in both side channels; (c) 25 ng/mL LTB4 in both side channels. Quantitative analysis of neutrophil numbers in different parts of the gel chamber at 1 h and 5 h after neutrophil injection: (d) 25 ng/mL IL-8 in both side channels; (e) 25 ng/mL fMLP in both side channels; (f) 25 ng/mL LTB4 in both side channels. Error bars represent the standard error of the mean and the total number of cells (including 3 different biological replicates) analyzed in each condition is indicated for the corresponding column. (scale bar: 200  $\mu$ m)**

steeper gradient in the condition of 50 ng/mL chemoattractant compared to the lower concentrations, and many more neutrophils prefer moving towards the chemoattractant sources (i.e. the steeper portion of the chemoattractant gradient) on the right side. On the contrary, no statistical difference is observed between the cell numbers located in the top and bottom portion of the gel-filled chamber for any of the three chemoattractants, even at the highest concentrations (Fig. 3-5(d) - (f)). The flat slope of the fluorescence gradient in the vertical direction (Fig. 3-2(b)) suggests that chemoattractant molecules distribute evenly between the top and bottom regions, and the small concentration difference is not enough to induce significant neutrophil migration. To examine neutrophil TEM without chemical gradients in the horizontal direction, 25 ng/mL of each chemoattractant was placed in both side channels such that the average concentration is the same as the single chemical gradient condition (50 ng/mL). The simulation results using fMLP as a model chemoattractant indicate that the gradient profile is symmetric along the horizontal direction in the “no gradient” condition while the gradient profiles in the vertical direction are the same for single chemoattractant gradient and “no gradient” conditions, which means these two conditions both have the steepest gradient in the perpendicular direction and the same total amounts of chemoattractant molecules in the gel scaffold because of the identical average concentration (Fig. 3-6). The neutrophil migration results reveal no significant difference in cell numbers between the left and right device regions in the “no gradient” condition, and there are still not statistically more neutrophils moving into the top device region (Fig. 3-7). Thus, we can conclude that the symmetric gradient profile diminishes the polarization of neutrophil TEM in the horizontal direction,

and the migration of cells along the vertical direction is determined by the average concentration of chemoattractants in the side channels. Based on the results above, this work reveals that high chemoattractant concentrations with steep chemical gradients are able to cause distinguishable neutrophil TEM processes, which is consistent with disease models where excessive amounts of neutrophils accumulate around infection sites, likely induced by the high level of chemoattractants in the context of diseases.

### **3-3-3. The role of endothelial cell layer in neutrophil transmigration**

One interesting phenomenon revealed in this study is that neutrophils do not migrate into the gel chamber without an endothelial cell layer in any of the presented conditions; without the endothelial cell layer, neutrophils only gather at the interface between the gel chamber and the bottom channel after 5 h migration (Fig. 3-4(d) - (f)). The collagen gel with a small pore size (Fig. 3-8(a)) functions as a physical barrier to prevent the infiltration of neutrophils and endothelial cells into the gel, and neutrophils must undergo morphological changes before entering the gel due to the comparatively large diameter of a single neutrophil ( $\sim 10 \mu\text{m}$ ). A morphological difference is clear between the spherical neutrophils without an endothelial cell layer and the stretched neutrophils that are moving through the gel chamber in the presence of an endothelial cell layer (Fig. 3-8(b) and (c)). To assess the possibility that biological molecules secreted by the endothelial cells promote the neutrophil morphological changes, all the molecules in the endothelial cell conditioned-medium after overnight ( $\sim 12$  h) chemoattractant-activation were collected and placed in the aforementioned microfluidic devices without adding the actual

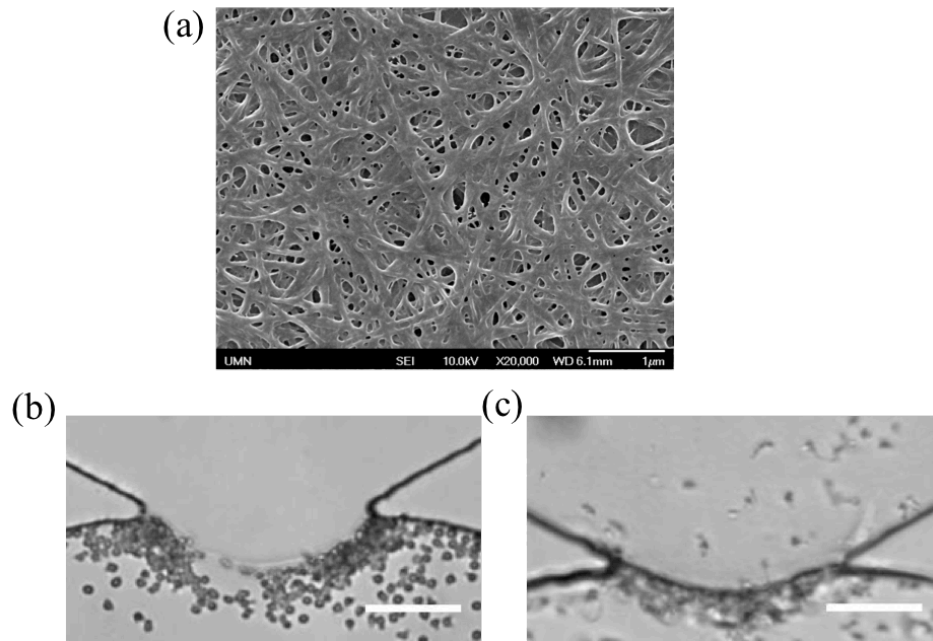


**Figure 3-8. (a) SEM image of collagen gel porous fiber structure. (scale bar: 1 μm). The morphological changes of neutrophils (a) without an endothelial cell layer and (b) with an endothelial cell layer. (scale bar: 100 μm)**

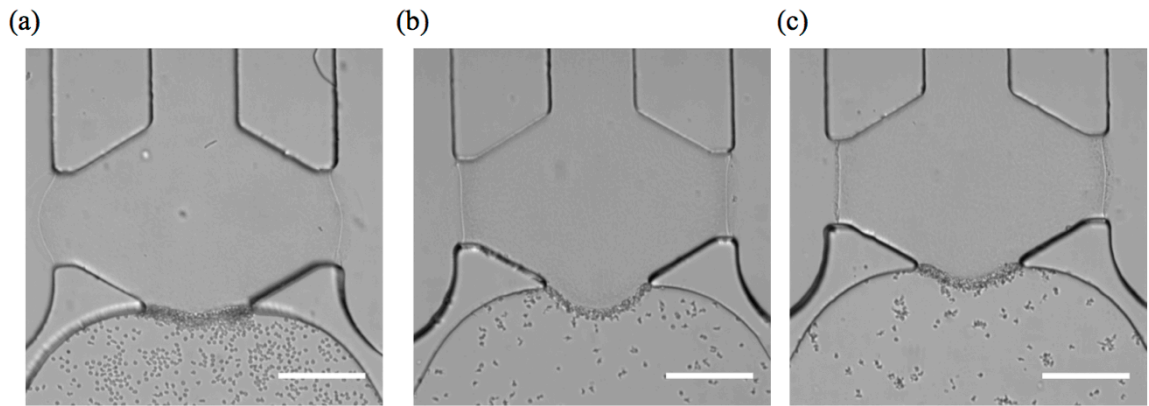


**Figure 3-9. Bright-field images of neutrophil transmigration without endothelial cells at 5 h after neutrophil injection: (a) 50 ng/mL of IL-8 conditioned medium; (b) 50 ng/mL of fMLP conditioned medium; (c) 50 ng/mL of LTB4 conditioned medium. (scale bar: 200  $\mu$ m)**

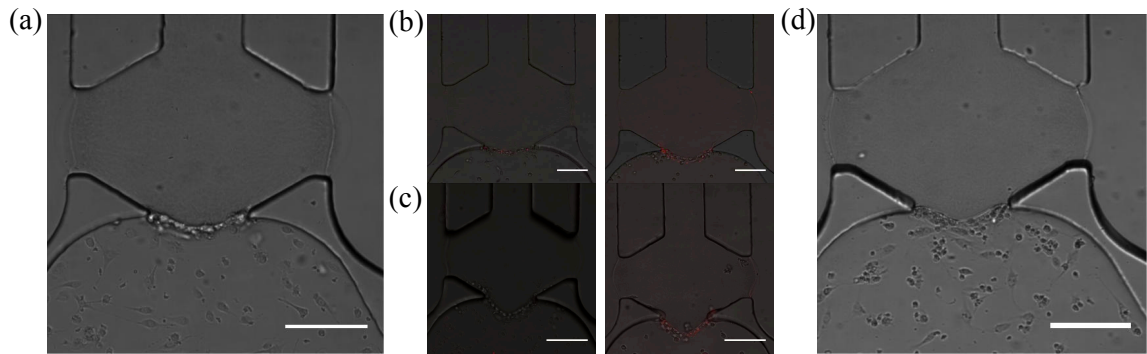


**Figure 3-10. (a) Neutrophil TEM at 5 h in chemoattractant-free condition. (b) P-selectin expression in the absence of IL-8 (left) and in the presence of 50 ng/mL of IL-8 (right) using APC-conjugated antibody fluorescence imaging. (c) ICAM-1 expression in the absence of IL-8 (left) and in the presence of 50 ng/mL of IL-8 (right) using APC-conjugated antibody fluorescence imaging. The overlay of bright-field image and fluorescence image was accomplished using Adobe Photoshop CS software, and the transparency of fluorescence image was set as 70%. (d) Neutrophil TEM at 5 h under 50 ng/mL IL-8 gradient with p-selectin and ICAM-1 antibodies. (scale bar: 200  $\mu$ m)**

endothelial cells. The timescale used herein is suitable to maintain activity of the endothelial cell-secreted species.<sup>30-32</sup> Neutrophils were introduced as previously described, images were captured, and cells were counted. Even in the presence of the endothelial cell-secreted soluble molecules, neutrophils stayed in the bottom channel instead of penetrating into the collagen gel (Fig. 3-9), signifying that the biological secretion alone is not strong enough to induce neutrophil deformation. Some previous work<sup>33-35</sup> indicates that the mechanical interactions between neutrophils and endothelial cells initiate the disruption of cell-cell junctions and enable neutrophils to undergo morphological changes to complete the extravasation step. The biological molecules regulating this process, such as intercellular adhesion molecule-1 (ICAM-1), guanine exchange factor (GEF), and myosin light chain kinase (MLCK),<sup>33</sup> are either intracellular species or molecules expressed on the surfaces of cells, and thus not secreted as soluble factors into the free medium, meaning that secreted molecules cannot promote neutrophil migration in the absence of the actual endothelial cell layer; however, more experiments will be pursued in the future to further explore mechanical effects in a biologically relevant environment. In addition to inducing shape change in neutrophils, another important role of endothelial cells in neutrophil TEM is to express surface receptors for triggering neutrophil attachment. The result of chemoattractant-free control conditions (Fig. 3-10(a)) shows that no neutrophil attachment or migration is detected without chemoattractant signals, even in the presence of an endothelial cell layer. To examine the effects of chemoattractants on endothelial cell activation, the expression of two major adhesion molecules known to regulate neutrophil-endothelial cell interaction, p-selectin

and intercellular adhesion molecule-1 (ICAM-1),<sup>5,36</sup> were visualized using antibody fluorescence imaging (Fig. 3-10(b) and (c)). After activation by 50 ng/mL of IL-8 gradient (fMLP and LTB4 data not shown), endothelial cells display a much higher level of adhesion molecules than the condition in the absence of chemoattractant, suggesting that chemoattractant activation is the main driving force for receptor expression, and non-activated endothelial cells are not able to induce neutrophil TEM process. Further evidence was obtained by examining neutrophil TEM under the same IL-8 gradient but with the antibodies for adhesion molecules, and no neutrophil TEM was detected after 5 h cell addition (Fig. 3-10(d)). Based on the observations above, the role of endothelial cells in neutrophil TEM must: (1) promote the morphological changes of neutrophils to enable cell extravasation into the ECM and (2) present the surface receptor molecules for initiating neutrophil attachment and migration.

#### **3-3-4. Neutrophil TEM under competing chemoattractants gradients**

To examine neutrophil TEM under competing gradients, different types of chemoattractants at 50 ng/mL were placed in two opposing side channels. The results of single chemoattractant gradient conditions reveal that 50 ng/mL of each chemoattractant is capable of inducing similar numbers of neutrophils to transmigrate across the endothelial cell layer, so 50 ng/mL was used as the concentration for developing competing gradients. Of the three chemoattractants pairs, significant differences in cell numbers between the left and right regions of the gel chamber, thus indicating a neutrophil preference for one chemoattractant or the other, are observed in the conditions

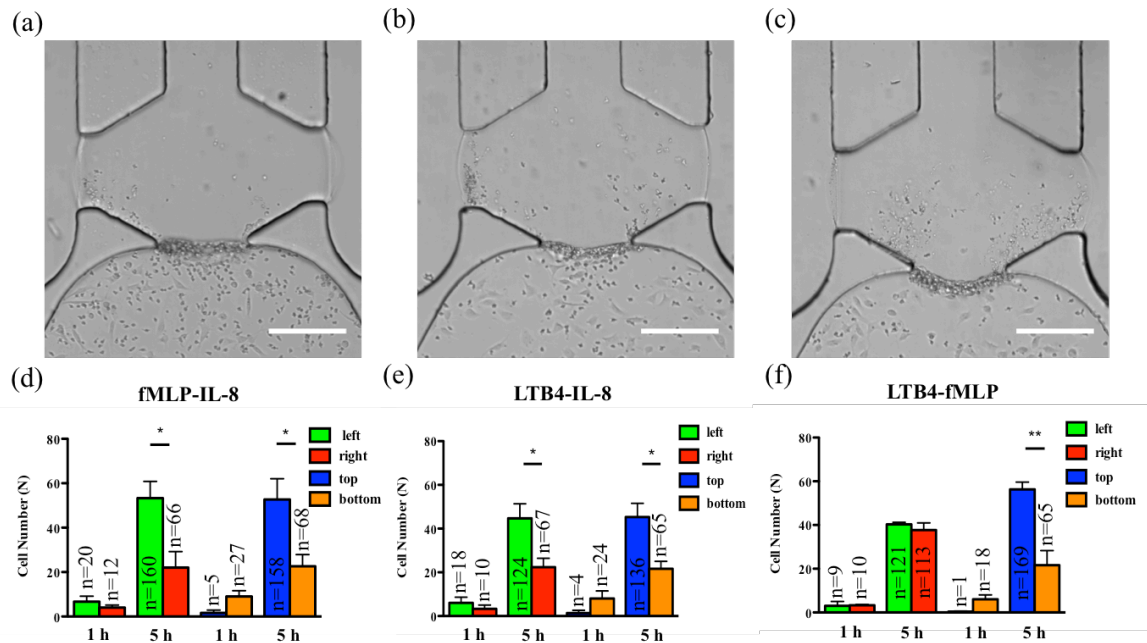


**Figure 3-11. Characterization of neutrophil TEM under competing gradients. Bright-field images of neutrophil TEM 5 h after neutrophil injection (left channel vs. right channel): (a) 50 ng/mL fMLP vs. 50 ng/mL IL-8; (b) 50 ng/mL LTB4 vs. 50 ng/mL IL-8; (c) 50 ng/mL LTB4 vs. 50 ng/mL fMLP. Quantitative analysis of neutrophil numbers in different parts of gel chamber 1 h and 5 h after neutrophil injection: (d) 50 ng/mL fMLP vs. 50 ng/mL IL-8; (e) 50 ng/mL LTB4 vs. 50 ng/mL IL-8; (f) 50 ng/mL LTB4 vs. 50 ng/mL fMLP (\*,  $p < 0.05$ , \*\*,  $p < 0.005$ , using a two-tailed unpaired t-test). Error bars represent the standard error of the mean and the total number of cells (including 3 different biological replicates) analyzed in each condition is indicated for the corresponding column. (scale bar: 200  $\mu$ m)**

of fMLP vs. IL-8 and LTB4 vs. IL-8 (the former chemoattractant is in the left channel) while there is no significant difference found in the condition of LTB4 vs. fMLP (Fig. 3-11). Statistically, more neutrophils migrate towards the other type of chemoattractant in IL-8-containing competing gradients, which means both fMLP and LTB4 are dominant chemoattractants over IL-8 during the neutrophil TEM process. The comparison between LTB4 and fMLP indicates that these two chemoattractants have similar abilities to mediate the polarization of neutrophil TEM. Considering the results above, the hierarchy among these chemoattractants is  $fMLP = LTB4 > IL-8$ . Although neutrophil migration under competing gradients has been studied in previous research using microfluidic platforms,<sup>37-39</sup> these studies did not incorporate the endothelial cell layer into the devices, and the hierarchy among multiple chemoattractants was only obtained in simplified microenvironments. The hierarchy reported herein agrees with the previous conclusion that the p38 mitogen-activated protein (MAP) pathway related to fMLP overwhelms the phosphatidylinositol 3-kinase (PI3K) signaling pathway activated by IL-8.<sup>40,41</sup> As another PI3K pathway-controlled chemoattractant, the competence of LTB4 in attracting neutrophil migration is enhanced in the presence of the endothelial cell layer; better understanding of the molecular mechanisms behind this behavior will be the focus of future work. Unlike the single chemoattractant gradients, all the competing gradients conditions demonstrate significant differences in the number of cells in the top and bottom regions of the gel chamber, confirming the observation that the increase in the total amount of chemoattractants (from 50 ng/mL to 100 ng/mL) enables the production of steeper gradients and thus, statistically distinct neutrophil TEM.

### **3-3-5. Synergistic chemoattractant effects on neutrophil TEM**

In the conditions of single chemoattractant gradients, 50 ng/mL of each chemoattractant was not able to induce significant differences between the number of neutrophils migrating into the top and bottom portions of the gel-filled chamber due to the flat gradient shape in the vertical direction. A previous study suggested cooperative interplay taking place between two different chemoattractants to promote neutrophil migratory responses.<sup>37</sup> With this neutrophil transendothelial migration model, we also hypothesized that various chemoattractants coexisting in the channel, at the same total chemoattractant concentration as the single chemoattractant gradients, would influence neutrophil TEM in the vertical direction. The mixture of any two chemoattractants, with 25 ng/mL concentration for each one, was employed to replace single chemoattractant solution in this experiment. For all three conditions, significant differences are observed between the number of cells in the top and bottom portions of the chamber (Fig. 3-12), which means that these chemoattractants function through synergistic effects to mediate the neutrophil TEM process. This is likely attributable to the fact that multiple chemoattractants trigger downstream signaling pathways using different surface receptors cooperatively, thus speeding up the responses of neutrophil migration. On the other hand, a single chemoattractant only binds to the corresponding receptor in a competitive manner that reduces the efficiency of initiating neutrophil TEM. In addition, the combination of any two chemoattractants does not alter the chemoattractant concentration gradients from right to left, and the significant differences between the number of cells in

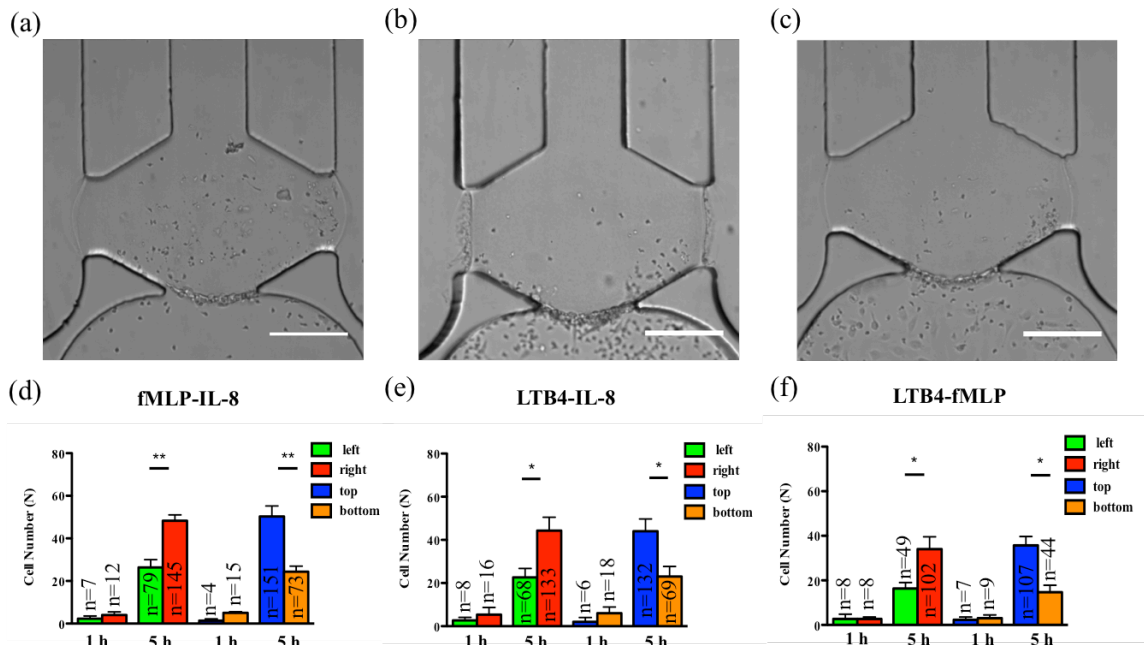


**Figure 3-12. Examination of synergistic effects by mixing two different chemoattractants in the right side channel. Bright-field images of neutrophil TEM 5 h after neutrophil injection: (a) 25 ng/mL fMLP and 25 ng/mL IL-8 in the right channel; (b) 25 ng/mL LTB4 and 25 ng/mL IL-8 in the right channel; (c) 25 ng/mL LTB4 and 25 ng/mL fMLP in the right channel. Quantitative analysis of neutrophil numbers in different parts of the gel chamber 1 h and 5 h after neutrophil injection: (d) 25 ng/mL fMLP and 25 ng/mL IL-8 in the right channel; (e) 25 ng/mL LTB4 and 25 ng/mL IL-8 in the right channel; (f) 25 ng/mL LTB4 and 25 ng/mL fMLP in the right channel (\*,  $p < 0.05$ , \*\*,  $p < 0.005$ , using a two-tailed unpaired t-test). Error bars represent the standard error of the mean and the total number of cells (including 3 different biological replicates) analyzed in each condition is indicated for the corresponding column. (scale bar: 200  $\mu\text{m}$ )**

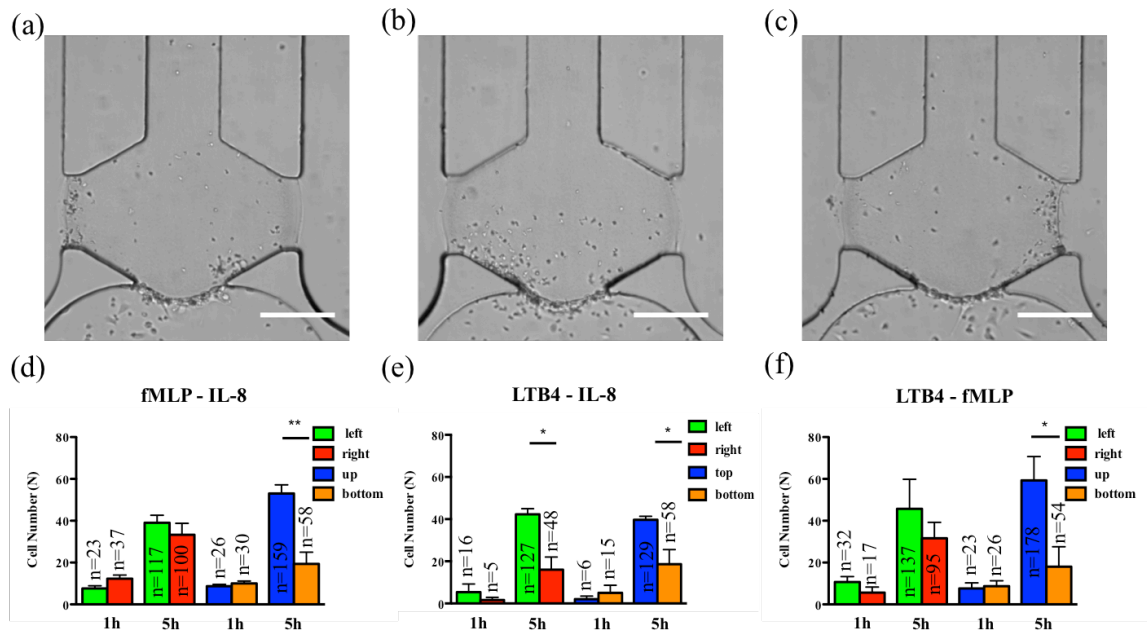


**Figure 3-13. Synergistic effects of any two chemoattractants in separate channels. Bright-field images of neutrophil TEM 5 h after neutrophil injection: (a) 25 ng/mL fMLP vs. 25 ng/mL IL-8; (b) 25 ng/mL LTB4 vs. 25 ng/mL IL-8; (c) 25 ng/mL LTB4 vs. 25 ng/mL fMLP. Quantitative analysis of neutrophil count in different parts of the gel chamber 1 h and 5 h after neutrophil injection: (d) 25 ng/mL fMLP vs. 25 ng/mL IL-8; (e) 25 ng/mL LTB4 vs. 25 ng/mL IL-8; (f) 25 ng/mL LTB4 vs. 25 ng/mL fMLP (\*,  $p < 0.05$ , \*\*,  $p < 0.005$ , using a two-tailed unpaired t-test). Error bars represent the standard error of the mean and the total number of cells (including 3 different biological replicates) analyzed in each condition is indicated for the corresponding column. (scale bar: 200  $\mu\text{m}$ )**

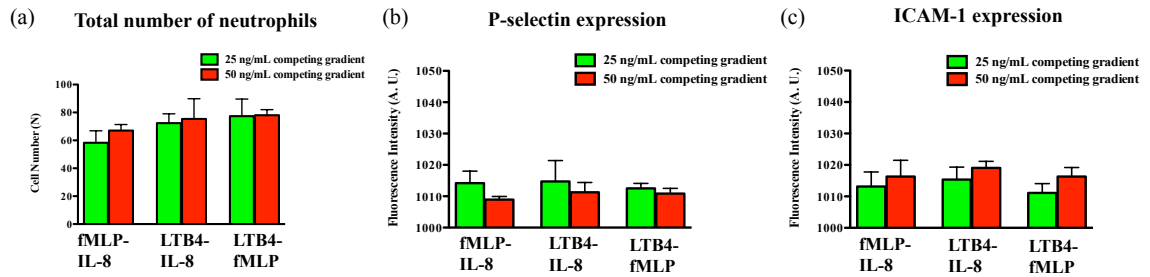


**Figure 3-14. The comparison of 25 ng/mL and 50 ng/mL competing gradient conditions. (a) The total numbers of neutrophils located in the gel chamber after 5 h transmigration for two conditions. (b) The fluorescence intensity of P-selectin expression on the surface of endothelial cells for two competing gradients conditions. (c) The fluorescence intensity of ICAM-1 expression on the surface of endothelial cells for two competing gradients conditions. Error bars represent the standard error of the mean.**

the left and right portions of the chamber remain unchanged compared to the single chemoattractant gradients. We also evaluated the synergistic effects within the competing gradients by introducing 25 ng/mL of two different chemoattractants in the side channels separately. Compared to integrating two chemoattractants in one side channel, competing gradients provide a symmetric distribution of different chemoattractant molecules across the gel chamber but maintain the same total amount of chemoattractants in the top and bottom regions. All three competing gradients still indicate synergistic effects in the vertical direction compared to placing 25 ng/mL of the same chemoattractant in both side channels (Fig. 3-7) while the hierarchy among these three chemoattractants is disrupted, and the significant difference between the cell numbers in the left and right portions of the chamber is only found in the LTB<sub>4</sub>-IL-8 pair (Fig. 3-13). Another interesting discovery is that the total cell numbers completing transmigration across the endothelial cell layer after 5 h observation is not statistically different for 25 ng/mL and 50 ng/mL competing gradient conditions although the total concentration of chemoattractants for 50 ng/mL competing gradients is twice that in 25 ng/mL competing gradient conditions. Further examination of adhesion molecule expression (p-selectin and ICAM-1) reveals that there is no significant difference in the levels of receptor molecule expression for these two conditions (Fig. 3-14), and thus, the activation of endothelial cells by chemoattractants must be saturated with 25 ng/mL competing gradient. Based on the results of competing gradients and consideration of synergistic effects, it is clear that neutrophils prioritize and integrate different chemoattractant signals simultaneously during the neutrophil TEM process.

### 3-4. Conclusions

An *in vivo*-like neutrophil TEM model was fabricated as a microfluidic platform incorporating a biomimetic hydrogel matrix and a vertical endothelial cell layer to examine neutrophil migratory responses in various complex microenvironments. We found that the profiles of single chemical gradients are heavily dependent on the total concentrations of each chemoattractant, and only the largest concentration (50 ng/mL) was able to induce significantly more neutrophils moving towards chemoattractant sources with all considered chemoattractants due to the steepest gradient shapes. In addition, the single chemoattractant gradient experiments without the cultured endothelial cell layer reveal that endothelial cells play a crucial role in promoting neutrophil morphological changes and expression of relevant adhesion molecules. The creation of competing chemoattractant gradients across the hydrogel matrix reveals the hierarchy among three common neutrophil chemoattractants (fMLP = LTB<sub>4</sub> > IL-8), and this order confirms the previous conclusion that the p38 MAP pathway is dominant over the PI3K pathway for neutrophil migration, but the introduction of an endothelial cell layer enhances the ability of LTB<sub>4</sub> to promote neutrophil migration. Compared to the conditions of single chemoattractant gradients, the coexistence of two different chemoattractants in the same total amount indicate a statistically higher number of cells migrating into the collagen gel, implying synergistic effects between any two neutrophil chemoattractants. This is the first report of competing and synergistic effects among various chemoattractants in the neutrophil TEM process. In conclusion, this research describes a promising candidate platform for neutrophil immunology studies and

provides new insights on the mechanisms of cellular interactions that can be used to predict *in vivo* neutrophil behaviors during the migration process.

## Chapter 4

### A Versatile Microfluidic Platform for the Study of Angiogenesis and Inflammation

Adapted from:

Wu, X.; Newbold, M. A.; Gao, Z.; Haynes, C. L., **2016**, *submitted*.

#### **4-1. Introduction**

Angiogenesis, known as the formation of new blood vessels from the pre-existing vascular system, is an essential biological process mediated by a delicate balance between pro- and anti-angiogenic molecules.<sup>1,2</sup> In a variety of physiological conditions, such as wound healing, tissue growth, and reproductive organ development,<sup>3-5</sup> angiogenesis is considered to be an indispensable element; in addition, angiogenesis plays a vital role in numerous diseases characterized by the overproliferation of blood vessels, including cancer, arthritis, atherosclerosis, and cardiovascular diseases.<sup>6-9</sup> In these pathological events, angiogenesis functions to transport oxygen and metabolites from normal blood vessels to diseased locations while waste products or malignant cells can be released through the angiogenesis network. There is an increasing body of evidence that inflammation contributes significantly to the pathogenesis of angiogenic diseases.<sup>10-12</sup> Immune cells are arsenals of pro-angiogenic factors that can be synthesized and secreted to promote neovascularization; angiogenic endothelial cells in the newly formed blood vessels, in turn, may facilitate leukocyte infiltration into the surrounding tissues. Among the various classes of immune cells, neutrophils receive a lot of attention because they are a major type of white blood cell in the human circulatory system, acting as the first line of defense against pathogens or invading microorganisms.<sup>13-15</sup> One of the most important characteristics in neutrophil-associated inflammation is neutrophil migration to infection sites along a chemokine gradient through the endothelial cell wall lining the blood vessel. Neutrophil migratory behaviors have been studied extensively in previous studies;<sup>16-18</sup> however, the mechanistic connection between neutrophil migration

and endothelial angiogenesis is not clear, especially how neutrophil migration responds to angiogenic endothelial growth and the regulatory effects of neutrophil migration on the stability of angiogenic structures. The investigation of this mutually dependent relationship will reveal novel insights about the detailed mechanisms of cellular interactions between neutrophils and angiogenic endothelial cells while also offering guidance for pharmaceutical approaches targeting angiogenesis-associated diseases.

Microfluidic platforms are promising model systems for *in vitro* microvasculature because of the precise control of the cell geometries and molecular diffusion patterns. Traditional *in vivo* models, such as the chick chorioallantoic membrane (CAM) assay and *in vivo* Matrigel plug assay,<sup>19,20</sup> are not good candidates for angiogenesis studies due to the expensive preparation work and high cell variability; furthermore, it's difficult to isolate the direct interplay between neutrophil migration and endothelial angiogenesis in the complex *in vivo* milieu. This complexity also makes quantitative analysis challenging.<sup>21-23</sup> Some conventional *in vitro* approaches, such as chamber-based endothelial cell migration assays and matrix-assisted tubule formation assays,<sup>24-26</sup> fail to create/support stable molecular gradients of pro-angiogenic factors with high spatiotemporal resolution, thus impairing the reproducibility of angiogenesis growth even though these methods are operated in a quick and quantifiable manner. Compared to the traditional assays mentioned above, a microfluidic platform is a powerful candidate for evaluating neutrophil migration and endothelial angiogenesis simultaneously. First, microfluidic devices are capable of establishing stable linear chemical gradients with moderate physiological time frames and well-defined spatial resolution for both

neutrophil migration and endothelial angiogenesis stimuli,<sup>27,28</sup> such that more reliable quantitative results can be obtained with uniform experimental conditions. Second, the introduction of a gel matrix scaffold within the device enables the regeneration of an *in vivo*-like endothelial cell layer structure by culturing cells in the vertical direction, which also facilitates the screening of neutrophil migration and endothelial angiogenesis on the same horizontal two-dimensional (2D) plane using standard bright-field microscopy. This gel scaffold also mimics the extracellular matrix (ECM) where cell migration and angiogenesis occurs. Finally, microfluidic devices made with transparent materials facilitate straightforward optical measurements in a robust and dynamic microenvironment, thereby supporting a full set of functional data output, such as projected cell area calculations, cell number counting, and fluorescence imaging. These parameters advance our understanding of the detailed cellular biology in neutrophil inflammation-associated angiogenesis. The development of microfluidic systems have efficiently filled a gap that separated conventional *in vivo* assays from *in vitro* assays and will yield new insights into angiogenesis research.

In this study, we employed a simple microfluidic device to evaluate neutrophil migratory behaviors under a steady chemical gradient in the presence of endothelial angiogenesis; meanwhile, we also assessed the effects of neutrophil migration on the stability of endothelial angiogenesis structures. A detailed examination of surface molecule expression on endothelial cells under different conditions was conducted to reveal chemical details about the cross-talk between neutrophil migration and endothelial angiogenesis. This microfluidic platform successfully links inflammation with

angiogenesis, demonstrating a significant example that illuminates complicated *in vivo* physiological processes in a versatile *in vitro* platform.

## **4-2. Experimental details**

### **4-2-1. Device fabrication**

As described in the previous chapters, the devices were fabricated using photolithography methods. A film (CAD/Art Service Inc., Bandon, OR) with microfluidic channel patterns was used to transfer the device design onto a chrome photomask plate coated with positive photoresist (Nanoflim, Westlake Village, CA) via UV light exposure. After removing the cross-linked photoresist, the exposed chrome layer in the channel patterns was etched down and the residual photoresist was removed by piranha solution (1:1 volume ratio of 30% hydrogen peroxide and 99.9% sulfuric acid, Avantor Performance Materials, Phillipsburg, NJ). To make the microfluidic device mold, the channel patterns on the photomask were printed on a 4-inch silicon wafer with a 100- $\mu\text{m}$ -thick SU-8 50 photoresist layer (Microchem, Newton, MA) through UV exposure. After that, the silicon wafer was immersed in SU-8 developer (Microchem, Newton, MA) to remove photoresist not in the channel patterns. The SU-8 mold was then covered by a 10:1 mass ratio mixture of Sylgard 184 silicone elastomer base and curing agent (Ellsworth Adhesives, Germantown, WI) and kept at 95 °C overnight on a hotplate. Before permanently attaching the polydimethylsiloxane (PDMS) layer to a glass slide, side channel reservoirs and small gel inlets were punched using 3.5 mm and 1 mm disposable

biopsy punches (Integra Miltex, Plainsboro, NJ), respectively. The permanent attachment was completed under oxygen plasma for 10 seconds at 100 L/h oxygen flow rate and 100 W.

#### **4-2-2. Endothelial cell culture and neutrophil isolation**

The human endothelial cell line hy926 purchased from American Type Culture Collection (ATCC, Manassas, VA) was used in this work as a suitable phenotype for angiogenesis studies.<sup>29-31</sup> Endothelial cells were cultured in a flask containing Dulbecco's Modified Eagle Medium (DMEM, formula: 4mM L-glutamine, 4.5 g/L L-glucose, and 1.5 g/L sodium pyruvate, Gibco, Carlsbad, CA) supplemented with 10% fetal bovine serum and 1% penicillin and streptomycin (Sigma-Aldrich, St. Louis, MO). Medium renewal was conducted every 2 to 3 days and cells were removed using 1× trypsin solution (Sigma-Aldrich, St. Louis, MO) if necessary for device injection. Only the cells between the third and tenth passage were used in these experiments.

Neutrophils were isolated from ethylenediaminetetraacetic acid (EDTA)-anticoagulated freshly drawn human blood samples prepared by Memorial Blood Center (St. Paul, MN). Samples were collected according to IRB protocol E&I ID no. 07809 and used immediately after collection. By layering the blood sample on the same volume of mono-poly resolving medium (Fisher Scientific, Waltham, MA), a distinct neutrophil band was obtained after density gradient centrifugation. Neutrophils were washed using 2.5 mL of red blood cell lysis buffer (Miltenyi Biotec Inc., Auburn, CA) several times until only

white cells were seen at the bottom of centrifuge tube. Finally, neutrophils were re-suspended in HBSS buffer containing 2% HSA at an appropriate cell density.

#### **4-2-3. Device preparation**

Prior to injecting gel, microfluidic devices were incubated with 30  $\mu$ L of 1 mg/mL poly-D-Lysine (PDL) solution (Sigma-Aldrich, St. Louis, MO) for at least 4 h under 5% CO<sub>2</sub> at 37 °C. The treatment with PDL solution can enhance the attachment of endothelial cells to the gel matrix, and sterilized Milli-Q water (Millipore, Billerica, MA) was used to wash devices twice to remove any excess PDL that may cause cell death. Devices were then placed in the oven at 65 °C for 24 to 48 h for hydrophobicity restoration. Cooled devices were injected with 2 mg/mL Collagen type I gel solution (BD Biosciences, San Jose, CA) through both gel inlets and kept in a humid pipette box for 40 minutes under 5% CO<sub>2</sub> at 37 °C. Following the quick polymerization of collagen gel, 20  $\mu$ l of DMEM medium was introduced into each side channel, and the medium in the four reservoirs was aspirated before endothelial cell seeding. Trypsinized endothelial cells were re-suspended at a density between 8 and 10  $\times 10^5$  cells/mL, and then 10  $\mu$ L of cells was added into one side channel for attachment on the gel. The pressure difference between two side channels promoted cell attachment in just 30 min; following this, the excess cells in the reservoirs were removed, and 30  $\mu$ L of fresh medium was added in each reservoir of the two side channels. Further cell growth on the side wall of the gel was achieved by incubating the devices in a 37 °C incubator with 5% CO<sub>2</sub> for overnight. After formation of the endothelial cell layer attached to the gel, the medium in all the reservoirs

was aspirated, and 30  $\mu\text{L}$  of 20 or 50 ng/mL vascular endothelial growth factor (VEGF, Sigma-Aldrich, St. Louis, MO) solution was placed in each reservoir of the side channel without cells while 30  $\mu\text{L}$  of new medium was added into each reservoir of the side channel containing endothelial cells. The same step was repeated after 24 h to further stimulate endothelial angiogenic growth. After 2-day incubation with VEGF solution, appropriate angiogenesis (the collagen gel still fills the gel scaffold without obvious shrinkage and the layered structure of endothelial cells is kept at the gel-channel interface, Fig. 4-5(b) and (c)) was observed in the gel chamber, and the device was ready for the neutrophil injection. The devices without VEGF activation were also prepared as the experimental controls. The structure of the endothelial cell layer and collagen gel were visualized using a confocal microscope and scanning electron microscope (SEM), respectively.

#### **4-2-4. Neutrophil migration experiments**

First, the medium in the reservoirs of one side channel containing endothelial cells was replaced with Hank's buffered salt solution (HBSS, Sigma-Aldrich, St. Louis, MO) containing 2% human serum albumin (HSA, Sigma-Aldrich, St. Louis, MO) in the same volume, and the VEGF solution in the reservoirs of the other side channel was changed to 20 or 50 ng/mL of interleukin-8 (IL-8, Sigma-Aldrich, St. Louis, MO) solution. After 2 h diffusion of chemokine solution, 5  $\mu\text{L}$  of neutrophil resuspension in HBSS buffer at a density of  $4 - 5 \times 10^6$  cells/mL was added into the side channel with the endothelial cells. Neutrophil migration was observed by imaging (Metamorph ver. 7.7.5 imaging software)

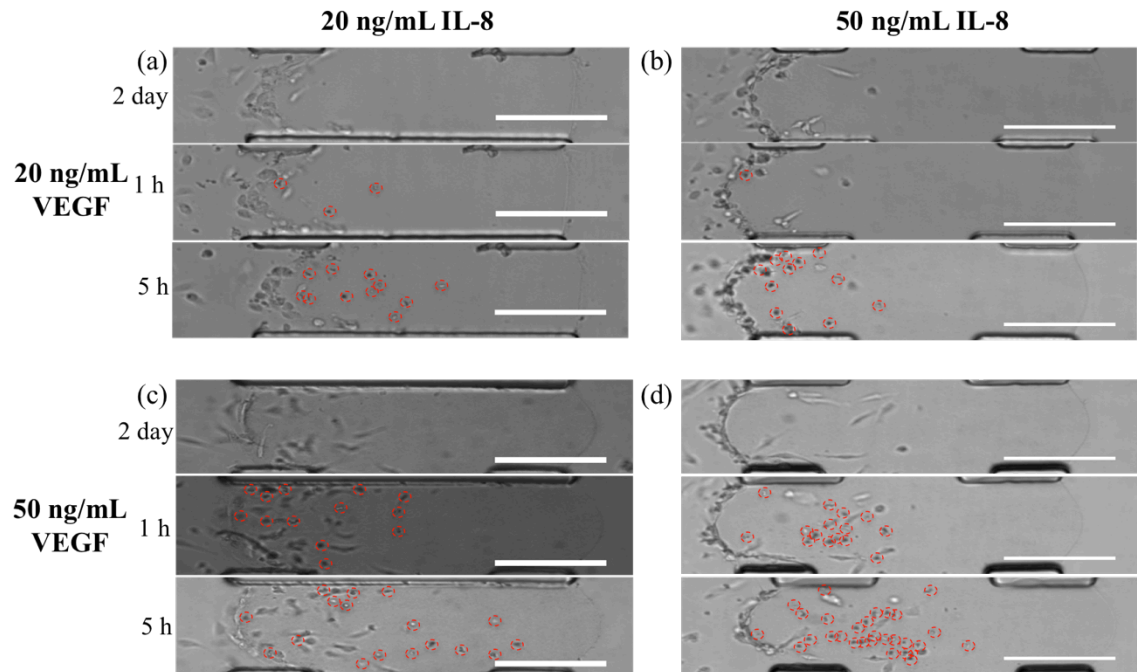


**Figure 4-1. Illustration of determining the locations of neutrophils in the gel scaffold at 1 h and 5 h after neutrophil injection: (a) 2-day 20 ng/mL VEGF treatment and 20 ng/mL IL-8 gradient; (b) 2-day 20 ng/mL VEGF treatment and 50 ng/mL IL-8 gradient; (c) 2-day 50 ng/mL VEGF treatment and 20 ng/mL IL-8 gradient and (d) 2-day 50 ng/mL VEGF treatment and 50 ng/mL IL-8 gradient. New round-shaped cells with around 10- $\mu$ m-diameter appearing from 1h to 5 h are neutrophils. (scale bar: 200  $\mu$ m)**

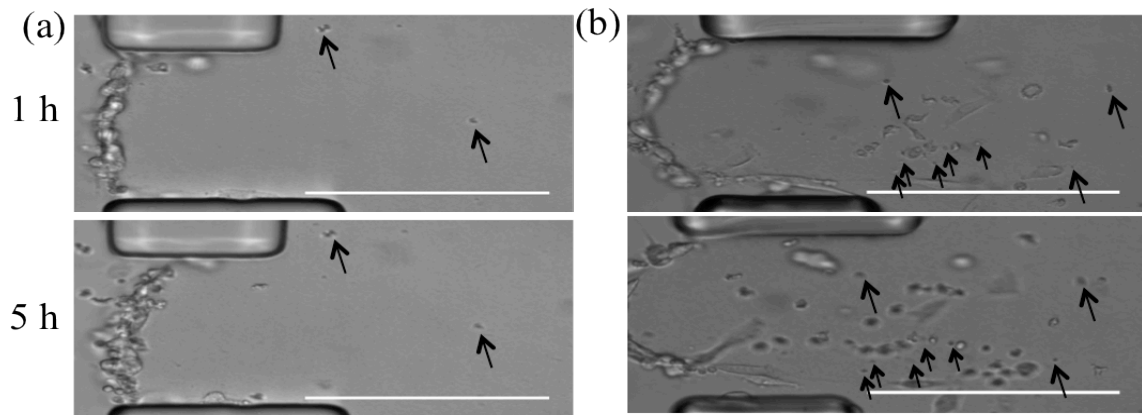


**Figure 4-2. Comparison of 1 h and 5 h images to determine the location of debris or other non-cell objects: (a) no VEGF treatment and 20 ng/mL IL-8 condition and (b) 2-day 50 ng/mL VEGF treatment and 50 ng/mL IL-8 condition. The debris or other objects are indicated by black arrows and do not move during neutrophil migration. (scale bar: 200  $\mu$ m)**

once every other hour for 5 h on an inverted microscope equipped with a 10× objective (Nikon, Melville, NY) and a CCD camera (QuantEM, Photometrics, Tucson, AZ). The images of neutrophil migration at 1 h and 5 h after neutrophil loading were compared with the 2-day angiogenesis image prior to cell injection to locate the neutrophils in the gel scaffold (Fig. 4-1), and the number of neutrophils (new round-shaped cells with around 10- $\mu$ m-diameter appearing after neutrophil loading) were counted for data analysis. If necessary, a 20x objective was employed to further discriminate neutrophils from endothelial cells and identify debris or other objects (Fig. 4-2) based on the size differences and objects movements from 1 h to 5 h. For each condition with neutrophil injection, cells from five different donors were collected for data analysis to reduce sample-to-sample variation; to minimize experiment analysis time, only one randomly chosen angiogenesis channel (angiogenesis channel is illustrated as the rectangle area in the gel chamber and there are two angiogenesis channels inside each gel chamber, Fig. 4-4(a)) from each device is included for cell number counting.

#### **4-2-5. Angiogenesis inhibitor experiments**

To investigate the direct effects of the endothelial angiogenesis inhibitor, endostatin, on angiogenesis structure, 30  $\mu$ L of endostatin solution (5, 10, and 20  $\mu$ g/mL) in HBSS buffer was placed in each reservoir of the endothelial cell channel, and 30  $\mu$ L of HBSS buffer was added in each reservoir of the opposite channel. The change in projected angiogenic endothelial cell area located in the angiogenesis channel with endostatin treatment was monitored every other hour for 5 h, and the projected cell area at different

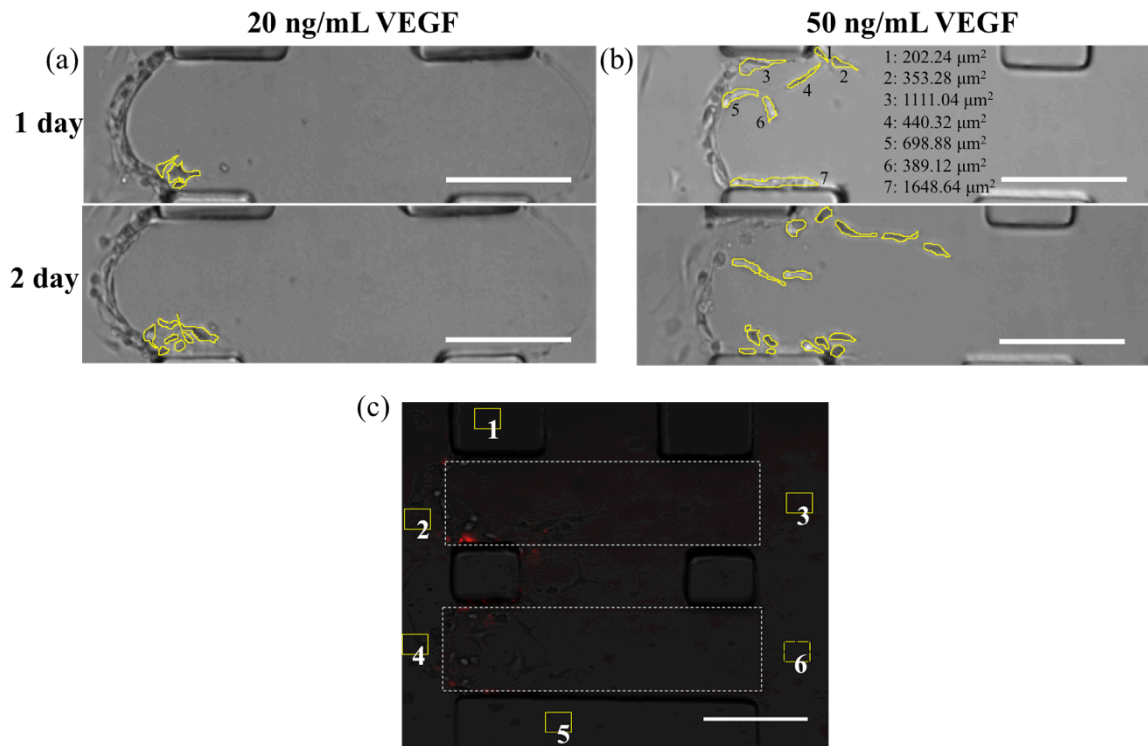


**Figure 4-3. Illustration of selecting angiogenic endothelial cells in the gel scaffold for projected angiogenic cell area calculations: (a) 1-day and 2-day 20 ng/mL VEGF treatment and (b) 1-day and 2-day 50 ng/mL VEGF treatment. As an example, the area of each angiogenic endothelial cell calculated by ImageJ software is shown in the condition of 1-day 50 ng/mL VEGF treatment. Illustration of doing background subtraction for surface molecule expression imaging. Three small squares ( $50 \times 50$  pixels) are chosen for calculating the background signal (1,2, and 3 are selected for background calculation of top angiogenesis channel while 4,5, and 6 are selected for background calculation of bottom angiogenesis channel). (scale bar: 200  $\mu\text{m}$ )**

**Table 4-1. The results of neutrophil numbers and projected angiogenic endothelial cell area of three different conditions analyzed by two researchers.**

	Researcher 1		Researcher 2	
	Neutrophil number	Endothelial cell area ( $\mu\text{m}^2$ )	Neutrophil number	Endothelial cell area ( $\mu\text{m}^2$ )
Sample 1 2 day		8883.2		8302.1
1 h	11	8686.4	10	8033.3
5 h	12	6236.2	14	5926.4
Sample 2 2 day		4441.6		4438.8
1 h	15	3689.0	15	3642.9
5 h	30	3089.3	31	3381.8
Sample 3 2 day		2488.3		2227.2
1 h	1	1674.2	1	1897.0
5 h	7	2273.3	9	1802.2

**Table 4-2. The intraclass correlation coefficient results calculated by SPSS Statistics software.**

Intraclass Correlation Coefficient (Neutrophil number)	Single Measures	0.992
	Average Measures	0.996
Intraclass Correlation Coefficient (Endothelial cell area)	Single Measures	0.992
	Average Measures	0.996

---

time points was measured using ImageJ software (National Institutes of Health, Bethesda, MD). Endothelial cells were selected using the curves drawn around the outline of cells, and the integral pixel areas occupied by the cells were calculated according to the scale relative to the actual length scale in images (Fig. 4-3(a) and (b)). For conditions with neutrophil migration, endostatin solution was introduced into the endothelial cell channel after 2 h chemokine molecule diffusion, and then 5  $\mu$ L of neutrophil suspension at the desired density was added into the same channel immediately with no change in the chemokine channel. To confirm the reliability of our quantitative methods for neutrophil number counting and endothelial cell area calculation, several random images from different conditions were analyzed by another researcher without knowledge of the initial outcome. The results of neutrophil number counting and endothelial cell area measurement obtained by the two researchers were compared using SPSS Statistics software (IBM, Armonk, NY), and the calculated intraclass correlation coefficients (ICC) indicate a perfect match ( $ICC > 0.75$ )<sup>2</sup> between the results from two different researchers (Table 4-1 and 4-2); thus, our quantitative methods are highly reliable.

#### **4-2-6. Receptor expression**

The angiogenic endothelial cells with 2-day VEGF treatment were prepared as described in the previous sections, and 20 or 50 ng/mL of IL-8 solution was placed in the reservoirs of the other side channel for 7 h incubation (the medium in all the reservoirs was HBSS buffer). The initial 2 h is for the chemokine molecule diffusion, and the following 5 h is for the adhesion molecule activation to make sure the length of time is the same as that in

neutrophil migration experiments. After 7 h incubation, the medium in the reservoirs was removed, and side channels were washed twice using 1× phosphate-buffered saline (PBS, Sigma-Aldrich, St. Louis, MO) solution by filling one reservoir with 40  $\mu$ L PBS and letting it flow along the channels to fill the other one. Then, 30  $\mu$ L of antibody solution in PBS was added into each reservoir of the endothelial cell channel while PBS solution was injected into the other channel. Following the 2 h antibody incubation, both of the side channels were rinsed with PBS solution twice, and the mean gray value of each angiogenesis channel selected as a “region of interest” was measured using ImageJ software. To perform the proper fluorescence quantitation, background subtraction was completed by selecting three small dark squares (50  $\times$  50 pixels) around each angiogenesis channel (two squares are located in two side channels while the other one is outside the channels), and the mean gray value of each square was calculated using ImageJ software (Fig. 4-3(c)). The average fluorescence intensity value of these three squares was employed as the background of this angiogenesis channel. The adhesion molecules for neutrophil migration were screened using 5  $\mu$ g/mL of P-selectin antibody conjugated with allophycocyanin (APC) or 2.5  $\mu$ g/mL of intercellular adhesion molecule-1 (ICAM-1) antibody conjugated with APC (eBioscience, San Diego, CA) separately. The receptor molecules for endostatin binding were visualized using a mixture of 5  $\mu$ g/mL integrin  $\alpha$ 5 antibody conjugated with fluorescein isothiocyanate (FITC) (Abcam, Cambridge, MA) and 5  $\mu$ g/mL integrin  $\beta$ 1 antibody conjugated with APC (eBioscience, San Diego, CA). In the endostatin control condition, 20  $\mu$ g/mL of endostatin solution was placed in the endothelial channel after the initial 2 h chemokine diffusion to examine the

influence of the angiogenesis inhibitor on the expression of p-selectin and ICAM-1. The fluorescence intensities of three different angiogenesis channels (not necessarily from different microfluidic devices since a uniform endothelial cell line was used here) are included in each condition.

#### **4-2-7. Numerical simulation and fluorescence gradient imaging**

The diffusion behaviors of 50 ng/mL VEGF solution in the gel chamber from 0 to 24 h were verified using simulation software COMSOL 4.3b. Based on the previous study, diffusion coefficients for VEGF in the collagen gel, free solution, and endothelial cell layer were assumed to be  $6.6 \times 10^{-11} \text{ m}^2/\text{s}$ ,  $2.5 \times 10^{-9} \text{ m}^2/\text{s}$ , and  $1.2 \times 10^{-11} \text{ m}^2/\text{s}$ , respectively.<sup>27</sup> In the fluorescence gradient imaging experiments, 100  $\mu\text{M}$  of Rhodamine 6G in HBSS buffer was placed in the side channel without endothelial cells for the characterization of chemical gradients. Chemical gradients were visualized in the conditions of no VEGF, 2-day 20 ng/mL VEGF treatment, and 2-day 50 ng/mL VEGF treatment. The fluorescence intensities in the gel chamber were monitored using MetaMorph ver. 7.7.5 imaging software at different time points from 5 min to 24 h.

#### **4-2-8. Confocal imaging**

The configuration of the endothelial cell layer after overnight incubation was characterized using Nikon A1R MP confocal microscope (Nikon, Melville, NY) and a standard inverted microscope. Briefly, medium in all the reservoirs was removed and the channels were rinsed with 40  $\mu\text{L}$  of  $1\times$  PBS solution twice. Following the PBS wash, 30

$\mu\text{L}$  of 4% (wt/vol) paraformaldehyde (PFA, Sigma-Aldrich, St. Louis, MO) was added in each reservoir to fix the cells for 15 min. The same volume of 0.1% (vol/vol) Triton X-100 was placed in each reservoir for the permeabilization of endothelial cell membranes after two PBS washes. Then, a mixture of 5  $\mu\text{g}/\text{mL}$  4,6-diamidino-2-phenylindole dilactate (DAPI dilactate) and 6.6  $\mu\text{M}$  rhodamine phalloidin (Life Technologies, Carlsbad, CA) solution in 30  $\mu\text{L}$  was added in each reservoir for staining the cells. The pipette box containing devices was wrapped with aluminum foil and placed in the dark for 1 h incubation. Finally, devices were washed using PBS twice to remove unbound fluorescent agents. All the confocal images were deconvoluted using AutoQuant X 3.0.4 software (Media Cybernetics, Rockville, MD) and processed with Imaris software (Bitplane AG, Zurich, Switzerland).

### **4-3. Results and discussion**

#### **4-3-1. Characterization of the microfluidic device**

The microfluidic device used in this study consists of two symmetrical side channels connected by two gel chambers for gel injection through the small inlet, and there are two angiogenesis channels included in one gel chamber separated by two small non-channel squares (Fig. 4-4(a) and (b)). The gel introduction into the device leads to the separation of two side channels, and endothelial cells are seeded into one channel for angiogenic growth. After overnight incubation, an endothelial cell layer forms on the side wall of the gel, then VEGF is added into the device as a pro-angiogenic signaling factor. The

confocal images (Fig. 4-4(d) and (e)) reveal that the overnight incubation allows the formation of a confluent endothelial cell monolayer in a 3D configuration. The extent of endothelial angiogenic growth is expected to be dependent on the diffusive behaviors of VEGF molecules in the gel chamber, and the simulation result shown in Fig. 4-4(c) clearly indicates that 50 ng/mL VEGF solution presents a linear gradient along the horizontal direction even after 24 h diffusion, but the concentration in the side channel decreases substantially after 24 h diffusion. To maintain a similar level of VEGF stimulation each day, fresh VEGF solution with the same original concentration was added into the channel to replace the old solution after 24 h diffusion. Based on the projected angiogenic cell area results (Fig. 4-5), we found that 50 ng/mL VEGF induces significantly more endothelial cell angiogenic growth into each angiogenesis channel than the 20 ng/mL VEGF on both day 1 and day 2, which suggests a physiological difference between the two concentrations of VEGF. To our surprise, several disconnected endothelial cells migrated into the gel chamber along the VEGF gradient instead of forming a connected tubular structure after 2-day VEGF incubation. Although endothelial angiogenesis is actually a process combining cell proliferation and migration,<sup>32</sup> the results we observed here indicate that migration is the dominant driving force over proliferation in endothelial angiogenesis since a major portion of our angiogenic endothelial cells in the gel scaffold migrated far away from the endothelial cell layer at the gel-channel interface. In a proliferation-participating angiogenesis process, most angiogenic endothelial cells should stay connected with the cell layer to form a tubular structure when growing. One interesting finding we observed in the

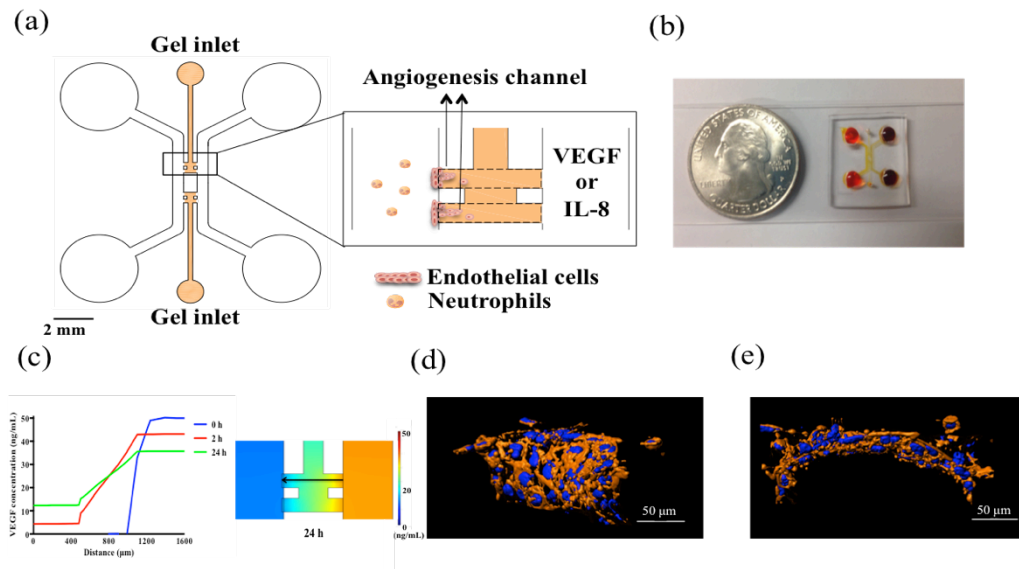


**Figure 4-4. Characterization of the microfluidic device. (a) Schematic of the microfluidic device. Endothelial cells are cultured in a side channel for angiogenesis growth, and neutrophil migration occurs under an IL-8 gradient. The box identifying the location of the schematic inset shows two angiogenesis channels (selected in a dashed box drawn around the outline of angiogenesis channel) in the gel chamber and the position of endothelial cell layer and neutrophils. (b) Top view photograph of a real device compared to the size of a quarter. (c) COMSOL simulation result of 50 ng /mL VEGF diffusion in the gel chamber after 24 h. The line plot (left) indicates the profiles of the gradient across the whole device at different time points. The color graph (right) shows the distribution of molecules in the device after 24 h diffusion. Confocal images of the endothelial cell layer on the side wall of the collagen gel: (d) side view; (e) top view (Blue indicates DAPI-stained nucleus and orange represents rhodamine phalloidin-stained cytoskeletal F-actin).**

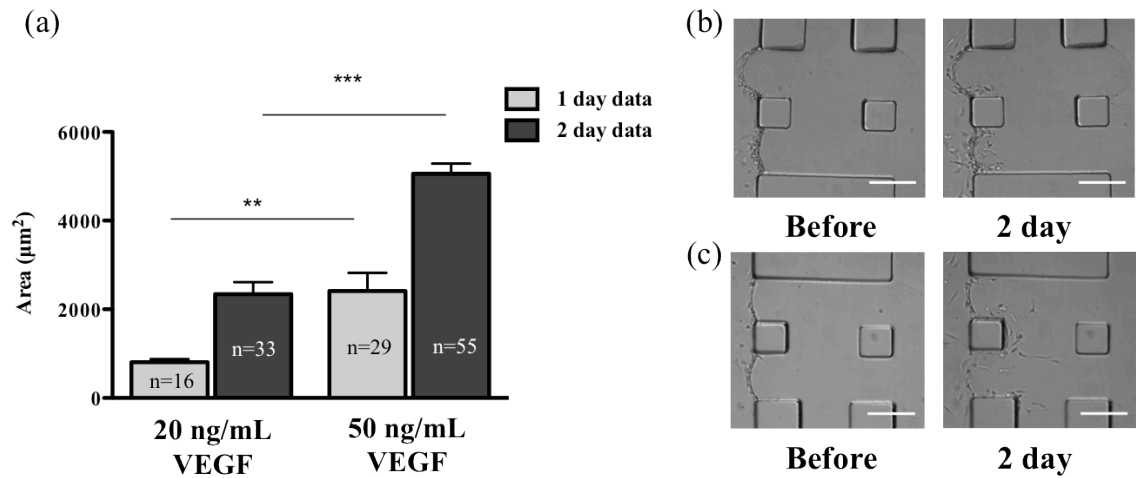


**Figure 4-5. The comparison of endothelial angiogenesis with 20 and 50 ng/mL of VEGF stimulation. (a) Comparison of endothelial cell area in each angiogenesis channel (not necessarily from different devices) with 20 and 50 ng/mL VEGF activation (five different angiogenesis channels, \*\*,  $p < 0.005$ , \*\*\*,  $p < 0.0005$ , using a two-tailed unpaired t-test and the total angiogenic endothelial cell number of five selected channels is indicated for the corresponding column). Error bars represent standard error of the mean. (b) Bright-field images of angiogenesis growth before VEGF addition and after 2-day 20 ng/mL VEGF activation. (c) Bright-field images of angiogenesis growth before VEGF addition and after 2-day 50 ng/mL VEGF activation. (scale bar: 150  $\mu\text{m}$ )**

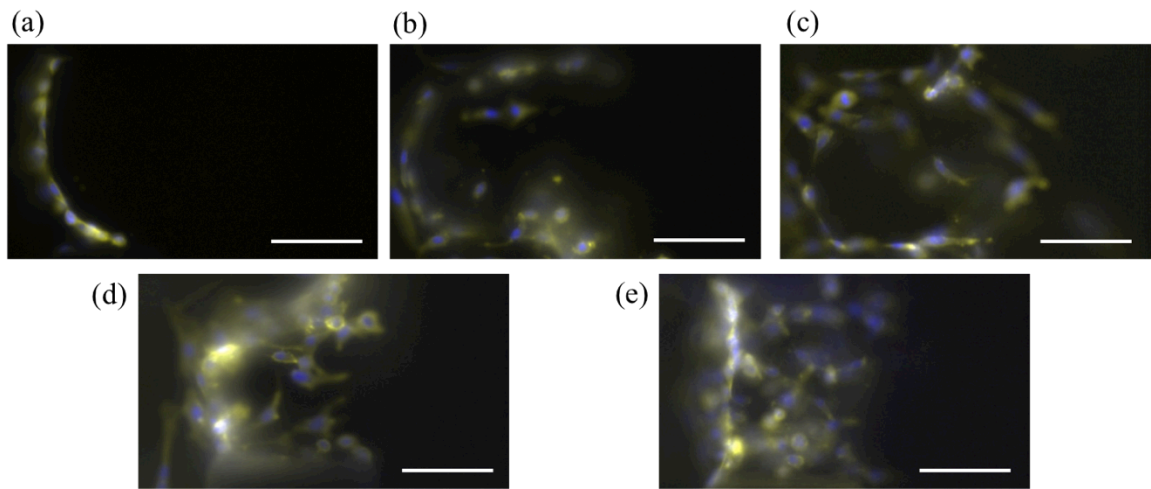


**Figure 4-6. Epifluorescence imaging of endothelial angiogenesis after 2 day incubation: (a) low endothelial cell density without VEGF activation; (b) low endothelial density with 20 ng/mL VEGF activation; (c) low endothelial cell density with 50 ng/mL VEGF activation; (d) high endothelial cell density with 20 ng/mL VEGF activation and (e) high endothelial cell density with 50 ng/mL VEGF activation (Blue indicates DAPI-stained nucleus and yellow represents rhodamine phalloidin-stained cytoskeletal F-actin). (scale bar: 200  $\mu\text{m}$ )**

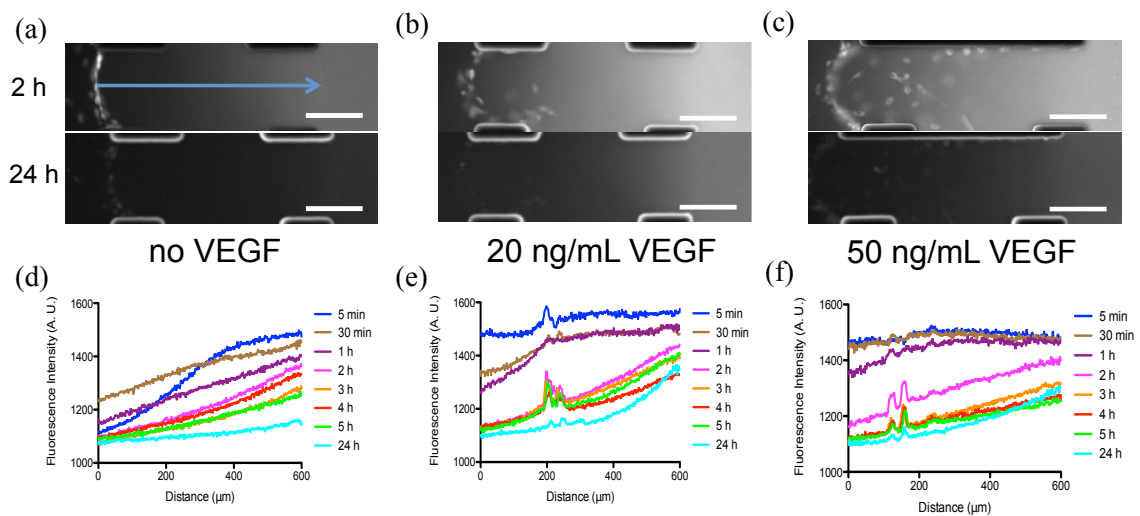


**Figure 4-7. Fluorescence imaging of chemical gradients in the microfluidic device. Real-time tracking of fluorescence gradients in the device after 2 h and 24 h diffusion: (a) no VEGF treatment; (b) 2-day 20 ng/mL VEGF treatment; (c) 2-day 50 ng/mL VEGF treatment. The arrow indicates the fluorescent gradient direction from low intensity to high intensity. The fluorescence intensities of gradients at different time points from 5 min to 24 h with (d) no VEGF treatment, (e) 2-day 20 ng/mL VEGF treatment, or (f) 2-day 50 ng/mL VEGF treatment. (scale bar: 150 μm)**

condition optimization experiments may account for the higher rates of cell migration. Different endothelial cell densities were incubated in the microfluidic channels overnight for the initial cell layer formation to determine the optimal endothelial cell density condition. Endothelial cells at a higher density ( $2.5 - 3 \times 10^6$  cells/mL) were seeded into the device and incubated with VEGF solution for 2 days. The fluorescence imaging results (Fig. 4-6) suggest that the angiogenesis growth is confined to a region close to the gel interface rather than showing the migration of disconnected cells into the gel scaffold far from the cell layer at the gel-channel interface. Although the higher cell density impedes the emergence of migration-biased angiogenesis, the increased cell numbers may result in a multilayer cellular structure on the side wall of the gel scaffold that does not represent a realistic *in vivo* environment; hence, lower cell density was employed here to form the endothelial cell monolayer. Following the development of this microfluidic angiogenesis model, neutrophils were placed in the endothelial cell channel while IL-8 solution, a common chemokine used to attract neutrophil migration,<sup>33,34</sup> was added into the other channel to replace the VEGF solution. In addition to investigating neutrophil migration under biologically distinct angiogenesis conditions, in this system, one must also consider the impacts of endothelial angiogenesis on the IL-8 gradient profile. Rhodamine 6G, a fluorescence reagent with a similar diffusion coefficient to IL-8 in the collagen gel,<sup>35,36</sup> was used in fluorescence imaging experiments for gradient visualization. Comparison of the gradient profiles in three different conditions (no VEGF treatment, 2-day 20 ng/mL VEGF treatment, and 2-day 50 ng/mL VEGF treatment) indicates that the gradients along the center line of the angiogenesis channel are linear and stable after 2 h

diffusion for all conditions considered; furthermore, the real-time fluorescence intensities of gradients after 2 h are quite similar in all three conditions, and the gradients do not decay significantly even after experiencing a 24-h molecular diffusion (Fig. 4-7). This stability is likely due to the compact structure of the gel with small pore sizes limiting the diffusion of fluorescent molecules to a slow rate, and thus, the shape of the gradients can be retained for a long time period. All these results reveal that the growth of endothelial angiogenesis into the gel chamber does not disrupt the profile of chemical gradients, which means that any measured effects on neutrophil migration can be attributed to different VEGF concentrations.

#### **4-3-2. Neutrophil migration with endothelial angiogenesis**

Neutrophil migration under an IL-8 gradient was first studied with this well-characterized angiogenesis model simply by counting the number of neutrophils migrating into the angiogenesis channel across the endothelial cell layer (Fig. 4-8(a) and (b)). To differentiate neutrophils from endothelial cells in the angiogenesis channel, the device image with endothelial angiogenesis before neutrophil injection was applied as the control for identifying the neutrophils. All four angiogenesis channels in each selected device had similar numbers of neutrophils completing migration (data not shown), so only one random angiogenesis channel from each device was chosen for data analysis. As a typical chemokine molecule for neutrophil migration, a high level of IL-8 is found in the context of a number of angiogenesis-related diseases, such as cancer and arthritis,<sup>37,38</sup> a fact that implies the importance of neutrophil migration during angiogenic activity.

Two different concentrations of IL-8, 20 and 50 ng/mL, were applied herein to represent the chemokine concentration in healthy conditions (20 ng/mL) and pathological conditions (50 ng/mL).<sup>39,40</sup> Under 20 ng/mL IL-8 gradient, neutrophil migration results indicate that 50 ng/mL VEGF condition with larger projected angiogenic endothelial cell area induces significantly more neutrophils migrating into the angiogenesis channel after 5 h IL-8 activation compared to the smaller VEGF concentration (20 ng/mL) or no VEGF treatment condition ( $p < 0.05$ , Fig. 4-8(c)). But for the 1 h IL-8-activation condition, there was no statistical difference found in number of migrating neutrophils when comparing the 20 ng/mL and 50 ng/mL VEGF conditions. In the experiments under the 50 ng/mL IL-8 gradient ( $p < 0.05$ , Fig. 4-8(d)), although there is no significant difference observed for no VEGF and 20 ng/mL VEGF conditions, the 50 ng/mL VEGF condition still demonstrates a much higher ability to induce neutrophil migration after 5 h IL-8 activation. On the other hand, at each specific VEGF condition, no significant difference was found when comparing neutrophil migration between two distinct IL-8 gradients; however, 50 ng/mL IL-8 gradient induces much more neutrophil migration statistically than the 20 ng/mL IL-8 gradient without VEGF activation ( $p < 0.05$ , Fig. 4-9). This difference suggests that the amount of neutrophils completing migration is predominantly influenced by the presence or absence of VEGF while chemokine concentration regulates neutrophil migration when endothelial angiogenesis is not involved. To confirm this conclusion, we further evaluated the expression of adhesion molecules that play critical roles in mediating neutrophil migration on the surface of endothelial cells. In the cascade of this complicated cellular interaction, p-selectin expressed by the endothelial cells is

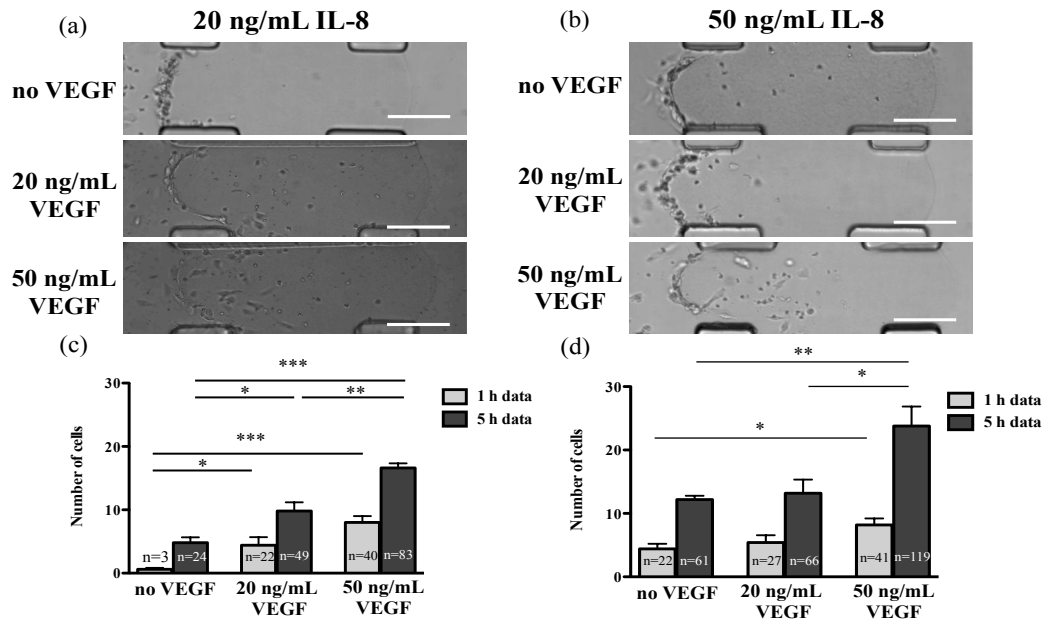


**Figure 4-8.** The results of neutrophil migration in the presence of endothelial angiogenesis. Bright-field images of neutrophil migration at 5 h after injection in the conditions of (a) 20 ng/mL and (b) 50 ng/mL IL-8 gradient. Three different VEGF concentrations, 0, 20, and 50 ng/mL VEGF, were examined in each IL-8 condition. Analysis data of neutrophil numbers migrating into the angiogenesis channel under (c) 20 ng/mL and (d) 50 ng/mL of IL-8 gradient. The neutrophil numbers in the angiogenesis channels at 1 h and 5 h after injection were counted. The data from each condition was collected using five different blood samples in different devices and one random angiogenesis channel from each device was used for data analysis (\*,  $p < 0.05$ , \*\*,  $p < 0.005$ , \*\*\*,  $p < 0.0005$ , using a two-tailed unpaired t-test and the total neutrophil number of five selected channels is listed for the corresponding column). Error bars represent standard error of the mean. (scale bar: 150  $\mu\text{m}$ )

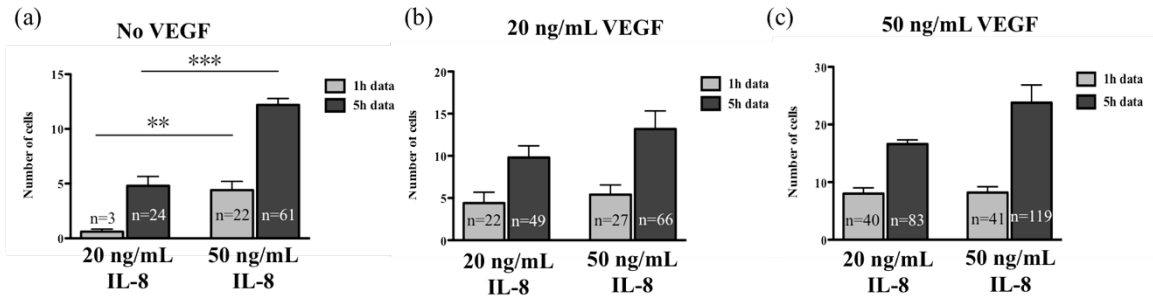


**Figure 4-9. Data analysis of neutrophil migration at different VEGF concentrations: (a) no VEGF; (b) 2-day 20 ng/mL VEGF treatment; (c) 2-day 50 ng/mL VEGF treatment. The neutrophil numbers in the angiogenesis channels at 1 h and 5 h time points were counted. (\*\*,  $p < 0.005$ , \*\*\*,  $p < 0.0005$ , using a two-tailed unpaired t-test, five different neutrophils samples were included in each condition and the total neutrophil number from five selected channels is listed for each corresponding column). Error bars represent standard error of the mean.**

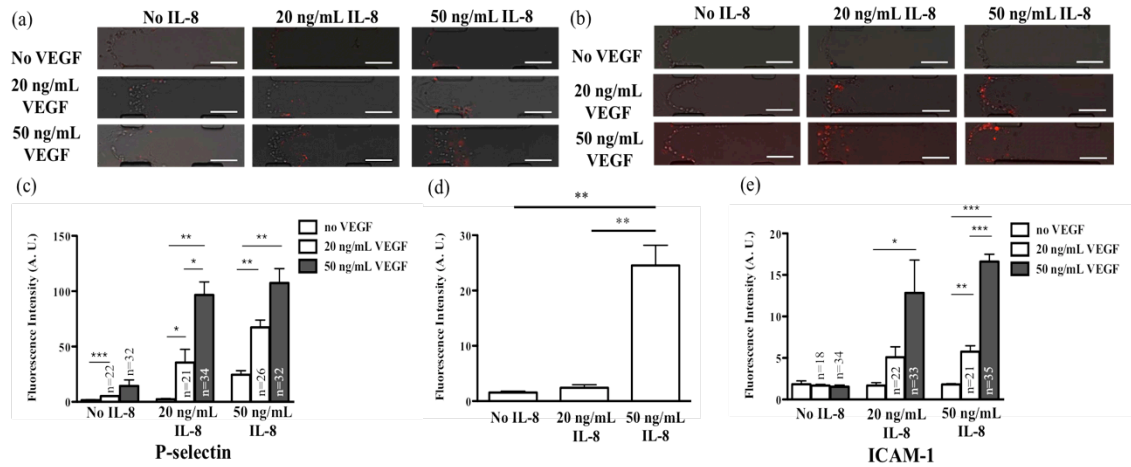


**Figure 4-10. Fluorescence imaging of (a) p-selectin and (b) ICAM-1 molecule expression on endothelial cells under different VEGF treatment conditions. The overlay of a bright-field image and a fluorescence image was achieved using software Adobe Photoshop CS, and the transparency of the fluorescence images was set at 70%. Fluorescence intensities (after background subtraction) indicating adhesion molecule expression on endothelial cells in various conditions: (c) p-selectin expression; (d) comparison of “no VEGF” control condition using different IL-8 concentrations in p-selectin expression (same data as shown in 4-10(c) but including statistical significance); (e) ICAM-1 expression. The fluorescence intensities of three different angiogenesis channels (not necessarily from different devices) are included in each condition (\*,  $p < 0.05$ , \*\*,  $p < 0.005$ , \*\*\*,  $p < 0.0005$ , using a two-tailed unpaired t-test and the total angiogenic endothelial cell number of three selected channels is listed for each condition containing VEGF). Error bars represent standard error of the mean. (scale bar: 150  $\mu\text{m}$ )**

known to capture surrounding neutrophils to establish initial attachment while ICAM-1 is known to be responsible for mediating firm adhesion of neutrophils to endothelial cells.<sup>41-</sup>

<sup>43</sup> The fluorescence intensity data summary of p-selectin expression (Fig. 4-10(a) and (c) where the brightness and contrast for each fluorescence image was adjusted if necessary) indicates a similar pattern as seen in the aforementioned neutrophil migration results; generally, larger VEGF concentration leads to a higher level of p-selectin expression at a given IL-8 concentration while there is no significant difference observed between the two IL-8 concentrations (20 ng/mL and 50 ng/mL) using the same VEGF condition; the comparison of “no VEGF” control condition (Fig. 4-10(d)) still displays an IL-8 concentration-dependent trend for p-selectin expression. Although lower fluorescence intensities were detected in ICAM-1 expression, the data summary (Fig. 4-10(c) and (e)) also shows a proportional relationship between VEGF concentration and adhesion molecule expression without the influence of various IL-8 levels. It is worth mentioning that strong red fluorescence signals were mainly found around the endothelial cell layer at the gel-channel interface while the angiogenic endothelial cells in the gel scaffold did not express receptor molecules at a high level. Since some previous studies<sup>44,42</sup> have suggested a phenotypic change for migrating endothelial cells during the angiogenesis process, it is reasonable to speculate that migrating cells have altered receptor expression patterns compared to other cells that do not migrate deeply into the gel scaffold. It would be interesting to examine the differences between migrating endothelial cells and other endothelial cells in receptor expression; however, this is beyond the scope of the current work. Based on the adhesion molecule expression results above, we can conclude that

VEGF treatment is the key factor to induce differences in endothelial cell adhesion molecule expression while IL-8 concentration only affects the results without VEGF treatment. Also, the promotion in neutrophil migration and adhesion molecule expression with higher VEGF level treatment is likely attributable to the increased endothelial cell surface area contact sites for both IL-8 activation and surface expression of P-selectin and ICAM-1. Another possible explanation for the effects imparted by large VEGF concentrations on neutrophil migration is the degradation of the collagen gel caused by angiogenic endothelial cell growth. Endothelial cells are known to secrete various matrix metalloproteinase molecules (MMP) after VEGF activation to degrade the structure of the surrounding extracellular matrix<sup>45,46</sup> such that angiogenesis can be initiated to promote endothelial cell growth. The micro-scale structure of pure collagen gel without endothelial angiogenesis was characterized using scanning electron microscopy (SEM) at three different time points which correspond to the time for each VEGF injection and neutrophil seeding. Without interference from angiogenic endothelial cell growth, pure collagen gel maintains a nearly stable geometry with a pore size from 1 – 2  $\mu\text{m}$  even after long incubation times (Fig. 4-11); which is too small for endothelial cell expansion (at least 5  $\mu\text{m}$  for elongated endothelial cells), so there must be some destruction that occurs in the gel structure to allow angiogenic endothelial cell growth. This destruction would leave more physical space for neutrophil migration compared to the condition without angiogenesis. However, degradation of the collagen gel does not influence the chemokine gradient profile greatly, which means the pore size after degradation is still not large enough to influence the gradient profile or that angiogenic endothelial cells occupying

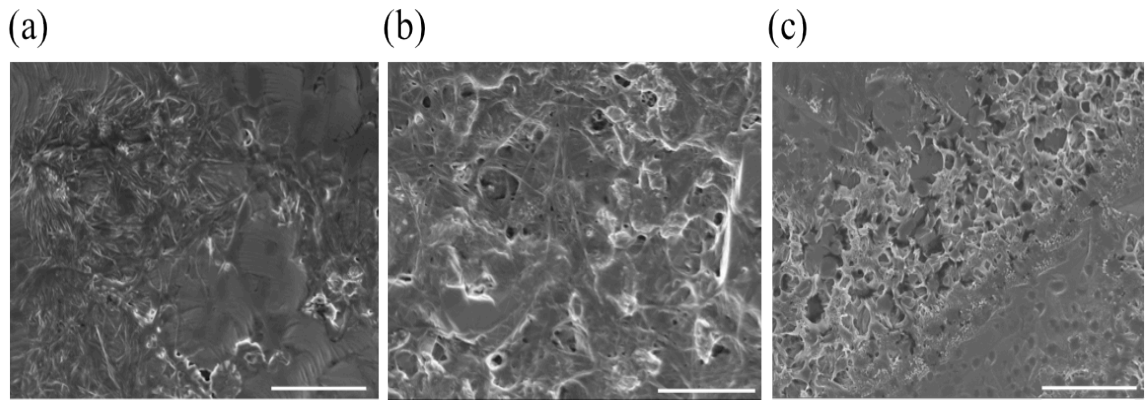


**Figure 4-11. SEM images of micro-scale structure in pure gel solution without cells at different time points. (a) Image was taken after overnight incubation of gel solution in a 37 °C incubator with 5% CO<sub>2</sub>. (b) Image was taken after 24 h incubation from the time point of taking first image. (C) Image was taken after another 24 h incubation from the time point of taking second image. (scale bar: 10 μm)**

these pores stabilize the shape of the chemical gradient since the cell membrane and cytoskeleton structure can block the free diffusion of chemokine molecules and function as the part of gel scaffold. To sum up, neutrophil migration is substantially enhanced in an angiogenesis model mainly due to a high level of adhesion molecule expression on endothelial cells; more importantly, the physiological implications of these results indicate that the inflammatory responses of neutrophils will be promoted in angiogenesis-associated diseases.

#### **4-3-3. The effects of an angiogenesis inhibitor on neutrophil migration**

Endostatin, a C-terminal fragment derived from collagen XVIII, is an endogenous angiogenesis inhibitor that can induce cell apoptosis in addition to blocking the proliferation of endothelial cells.<sup>47-49</sup> Due to the low cytotoxicity and broad-spectrum anti-angiogenic activity, endostatin has potential therapeutic value for various diseases, especially in cancer research.<sup>50</sup> To monitor the inhibitory effects of endostatin on endothelial cells, the optimal experimental concentration was first studied by adding different previously studied concentrations of endostatin<sup>47,51</sup> into the microfluidic side channel containing endothelial cells to trigger a quick decrease in projected angiogenic endothelial cell area. By calculating the projected cell area in the angiogenesis channel, the introduction of endostatin was found to induce a considerable reduction in cell area in the absence of any pro-angiogenic factors (Fig. 4-12). For the 20 ng/mL VEGF condition, the projected cell area before endostatin addition was assumed to be 100%, and all of the three endostatin concentrations caused significant decreases in cell area after 5 h

incubation compared to the no endostatin control ( $p < 0.05$ ). There was no significant difference between 10  $\mu\text{g}/\text{mL}$  and 20  $\mu\text{g}/\text{mL}$  endostatin, though both of them were significantly more effective than the 5  $\mu\text{g}/\text{mL}$  endostatin dose in decreasing projected angiogenic cell area ( $p < 0.05$ ). Even with 2-day 50  $\text{ng}/\text{mL}$  VEGF treatment, endostatin maintains the ability to induce endothelial cell apoptosis by decreasing projected cell area, but the effects from different concentrations of endostatin are statistically indistinguishable. To differentiate 10  $\mu\text{g}/\text{mL}$  and 20  $\mu\text{g}/\text{mL}$  endostatin, the data at 1 h and 5 h for each endostatin concentration were compared; only the 20  $\mu\text{g}/\text{mL}$  dose shows a time-dependent decrease in cell area for both VEGF conditions (Fig. 4-13), revealing that 20  $\mu\text{g}/\text{mL}$  endostatin is the best concentration for the studies that follow since it shows a powerful time-dependent anti-angiogenic effect.

Next, neutrophil migration was examined as described before, but with 20  $\mu\text{g}/\text{mL}$  of endostatin added to the microfluidic device. Compared to the neutrophil migration results without endostatin, the addition of endostatin did not statistically change the number of neutrophils migrating into the angiogenesis channel in any condition (Fig. 4-14). This result may be because of the low toxicity of endostatin to other cell types; a detailed adhesion molecule expression experiment indicates that endostatin has no impact on the expression of p-selectin or ICAM-1 molecules that are known to mediate the neutrophil migration process (Fig. 4-15). At first glance, these results seem to be in conflict with the previous conclusion that adhesion molecule expression is proportional to the projected angiogenic cell area and that a decrease in cell area may downregulate the adhesion molecule expression. However, the absolute value of the change in cell area induced by

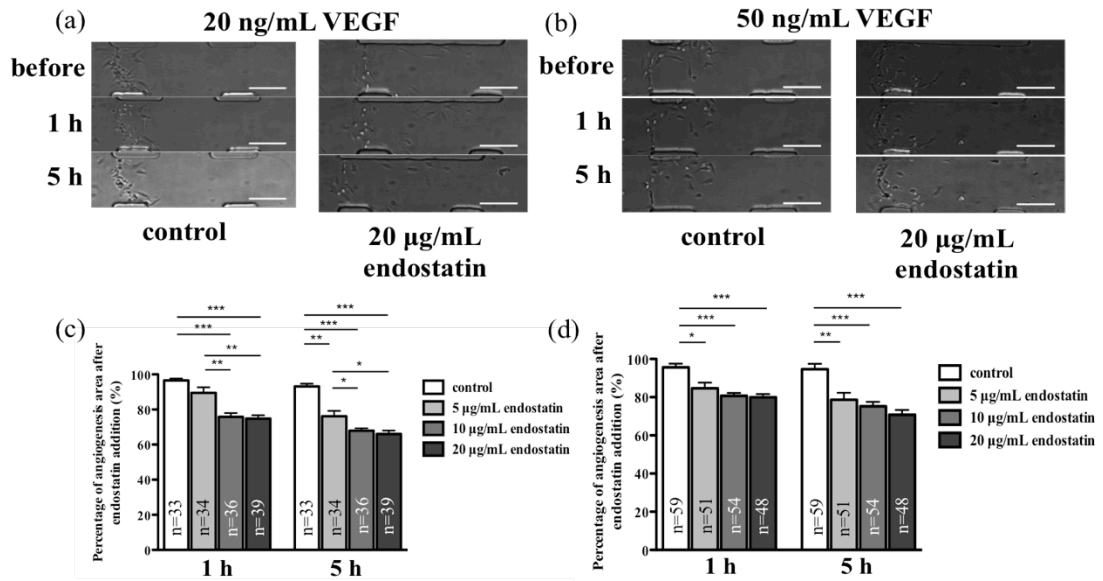


**Figure 4-12.** The inhibitory effects of endostatin on projected angiogenic endothelial cell area in the angiogenesis channel (5 replicates, not necessarily from different devices). Bright-field images of angiogenesis without endostatin treatment and with 20 µg/mL endostatin incubation at different time points (before drug addition, 1 h, and 5 h after drug addition) after (a) 2-day 20 ng/mL VEGF treatment or (b) 2-day 50 ng/mL VEGF treatment. Data analysis of projected angiogenic area change after 1 h and 5 h endostatin addition using 0, 5 µg/mL, 10 µg/mL, or 20 µg/mL of endostatin with (c) 2-day 20 ng/mL VEGF treatment or (d) 2-day 50 ng/mL VEGF treatment. The projected angiogenic area before drug addition is assumed to be 100%. (\*,  $p < 0.05$ , \*\*,  $p < 0.005$ , \*\*\*,  $p < 0.0005$ , using a two-tailed unpaired t-test, five different angiogenesis channels are included in one condition and the total angiogenic endothelial cell number of five selected channels is listed for each column). Error bars represent standard error of the mean. (scale bar: 150 µm)

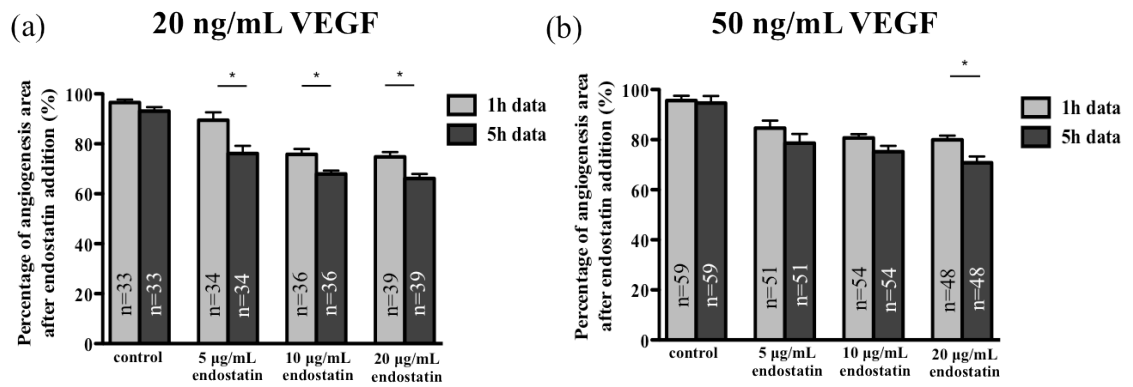


**Figure 4-13. Time-dependent studies of projected angiogenic cell area change in the presence of different concentrations of endostatin (0, 5 µg/mL, 10 µg/mL, and 20 µg/mL of endostatin) with (a) 2-day 20 ng/mL VEGF treatment or (b) 2-day 50 ng/mL VEGF treatment. (\*,  $p < 0.05$ , using a two-tailed unpaired t-test, five different angiogenesis channels not necessarily from different devices are included in one condition and the total number of angiogenic endothelial cell from five selected channels is listed for each column). Error bars represent standard error of the mean.**

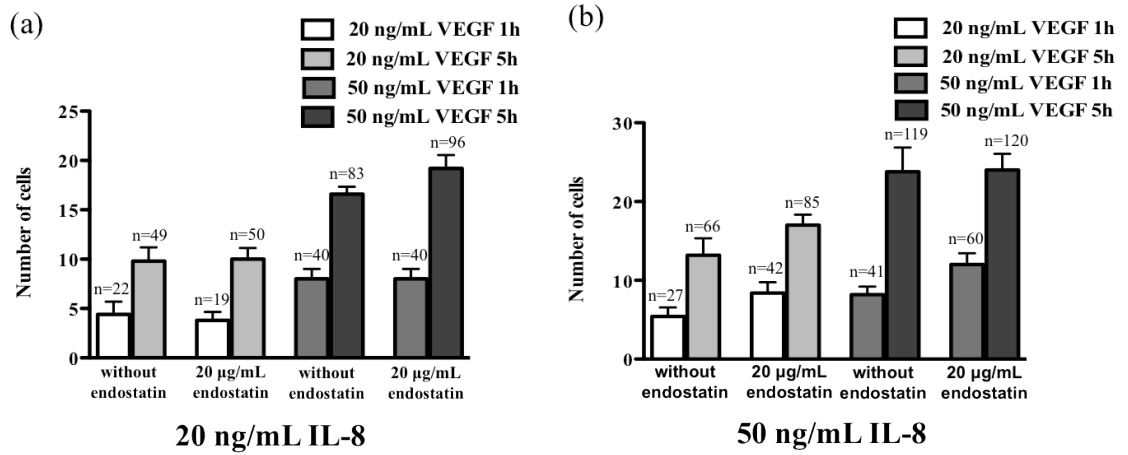


**Figure 4-14.** The comparison of neutrophil numbers migrating into the angiogenesis channel with and without endostatin. (a) Data summary of neutrophil migration with 20 ng/mL and 50 ng/mL VEGF treatment under 20 ng/mL IL-8 gradient. (b) Data summary of neutrophil migration with 20 ng/mL and 50 ng/mL VEGF treatment under 50 ng/mL IL-8 gradient. There are no significant differences using a two-tailed unpaired t-test (five different neutrophil samples are included in one condition and total cell number of five selected channels is listed above each corresponding column). Error bars represent standard error of the mean.

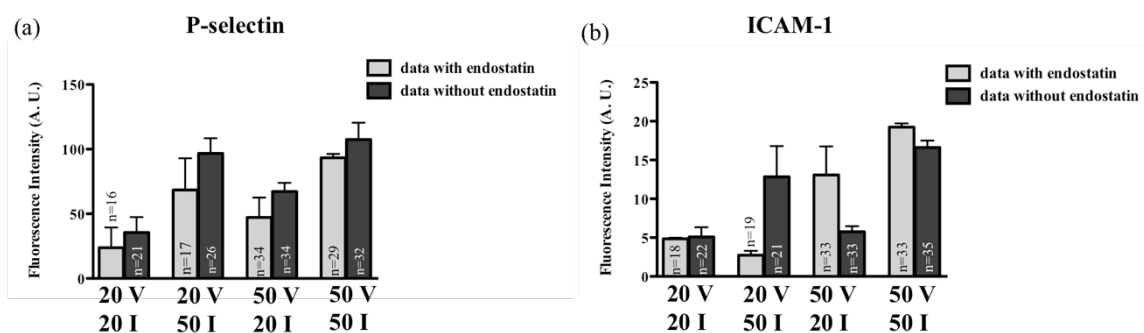


**Figure 4-15. Comparison of adhesion molecule expression with and without 20 µg/mL endostatin for (a) p-selectin expression and (b) ICAM-1 expression. The fluorescence intensities of three different angiogenesis channels (not necessarily from different devices) are included in each condition. “V” represents VEGF and “I” represents IL-8, for example, “20V 20I” stands for the condition with 20 ng/mL VEGF and 20 ng/mL IL-8. There are no significant differences using a two-tailed unpaired t-test (three different angiogenesis channels (not necessarily from different devices) are included in one condition and the total angiogenic endothelial cell number of three selected channels is listed for each corresponding channel). Error bars represent standard error of the mean.**

20  $\mu\text{g/mL}$  endostatin is about 700  $\mu\text{m}^2$  for 20 ng/mL VEGF condition and 1300  $\mu\text{m}^2$  for 50 ng/mL VEGF condition while the area difference between 20 ng/mL and 50 ng/mL VEGF conditions after 2-day treatment is about 2700  $\mu\text{m}^2$  (Fig. 4-5 (a)). The projected cell area decrease in the angiogenesis channel after endostatin addition is not large enough to produce a significant decrease in adhesion molecule expression.

#### **4-3-4. The effects of neutrophils on the stability of the angiogenesis structure**

Beyond the evaluation of neutrophil migration in the presence of an angiogenesis inhibitor, the change in projected angiogenic cell area with the coexistence of endostatin and neutrophil migration was studied extensively to assess the effects of neutrophil migration on the stability of the angiogenesis structure. The projected endothelial cell area change upon incubation with only 20  $\mu\text{g/mL}$  endostatin was used as the negative control condition, and we found that the process of neutrophil migration slows down the rate of decrease in angiogenic cell area. Meanwhile, the stabilizing effects from neutrophil migration was lessened under a 50 ng/mL IL-8 gradient; however, at lower IL-8 concentration (20 ng/mL), stabilization in both 20 ng/mL and 50 ng/mL VEGF conditions was maintained (Fig. 4-16). As the control experiments, the endostatin treated-angiogenesis model was seeded with non-activated neutrophils and an IL-8 gradient separately to determine which factor is most critical in stabilizing the angiogenesis structure against drug inhibition. Separately, non-IL-8 activated neutrophils or an IL-8 gradient without neutrophils was not able to stabilize the angiogenesis structure (Fig. 4-17) although IL-8 was shown as a cytokine to promote angiogenesis,<sup>52</sup> this is probably

attributable to the short time incubation and high concentration of endostatin masking the angiogenic properties of IL-8. These results demonstrate that the combination of neutrophils and chemokine gradients is a key factor that leads to the stabilization of angiogenesis structure, which is in agreement with the previous finding that neutrophils release angiogenic factors after chemokine activation.<sup>53,54</sup> To follow, the relationship between IL-8 concentration and stabilization effects on neutrophil migration was studied using endostatin-related receptor molecule expression experiments. Endostatin serves as an angiogenesis inhibitor through a variety of pathways, such as arresting the cell cycle during G1 phase and inhibiting cell migration through the disruption of cell-matrix adhesion.<sup>55</sup> One of the most important pathways through which endostatin acts is binding to the integrin  $\alpha_5\beta_1$  receptor on the surface of endothelial cells, thus activating the downstream Src family kinases involved in regulating cell proliferation and mobility.<sup>56,57</sup> A mixture of the fluorescent antibodies for integrin  $\alpha_5$  and  $\beta_1$  receptors was incubated with IL-8-activated endothelial cells to visualize the expression of endostatin-related surface receptors. For both of the integrin receptors, the expression indicates an IL-8 concentration-dependent trend, and 50 ng/mL of IL-8 induces significantly more  $\alpha_5$  receptor expression than 20 ng/mL of IL-8 in both VEGF conditions while more  $\beta_1$  receptor expression was observed for 50 ng/mL of IL-8 compared to 20 ng/mL IL-8 in the 20 ng/mL VEGF condition ( $p < 0.5$ , Fig. 4-18). There is another statistical difference for  $\alpha_5$  receptor expression between 20 and 50 ng/mL VEGF conditions after 50 ng/mL IL-8 activation ( $p < 0.5$ ). All of these observations reveal that higher levels of IL-8 activation or larger projected angiogenic cell area can induce more integrin receptor

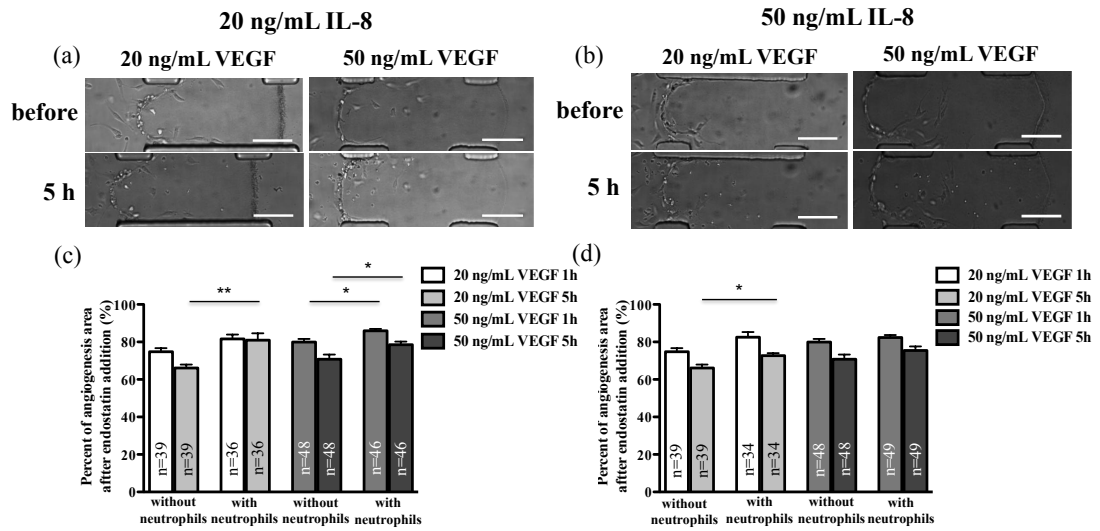


**Figure 4-16. The effects of neutrophil migration on the stability of angiogenesis structures in the presence of endostatin. Bright-field images of neutrophil migration before and after 5 h endostatin addition in various conditions (a) 20 ng/mL IL-8 gradient or (b) 50 ng/mL IL-8 gradient, scale bar: 150  $\mu$ m. Data analysis of projected angiogenic endothelial cell area in the angiogenesis channel after 1 h and 5 h endostatin addition with the coexistence of neutrophil migration for (c) 20 ng/mL IL-8 gradient or (d) 50 ng/mL IL-8 gradient. The projected cell area before endostatin addition was assumed to be 100% (\*,  $p < 0.05$ , \*\*,  $p < 0.005$ , using a two-tailed unpaired t-test, five different neutrophil samples are included in each condition and the total number of angiogenic endothelial cell of five selected channels is indicated for each corresponding column). Error bars represent standard error of the mean. (scale bar: 150  $\mu$ m)**

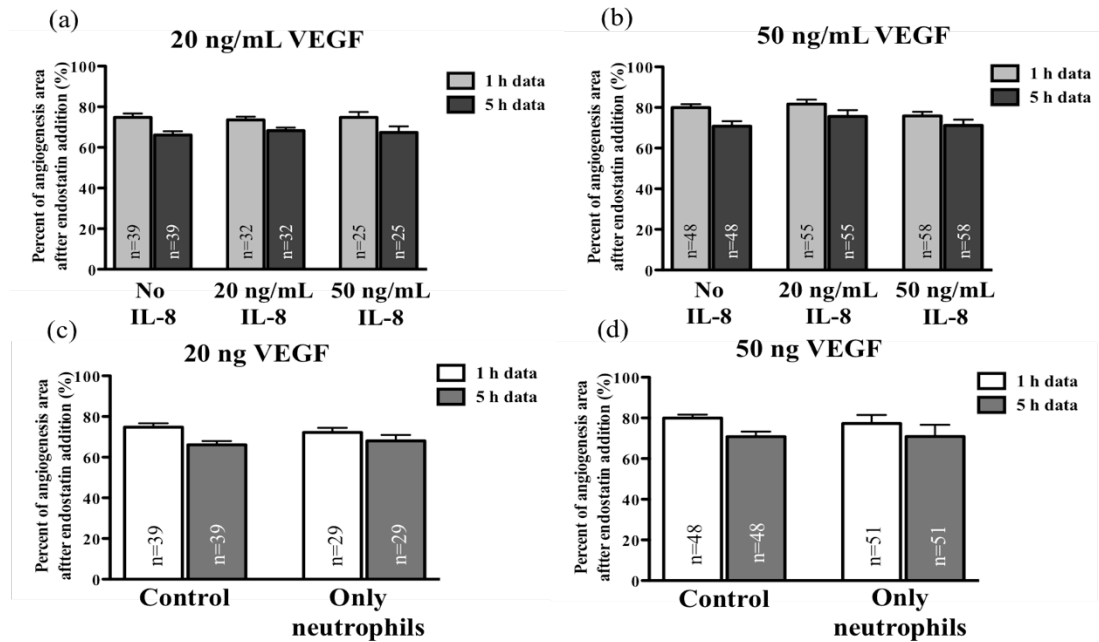


**Figure 4-17.** Analysis of projected angiogenic endothelial cell area in the angiogenesis channel (5 replicates, not necessarily from different devices) after 1 h and 5 h endostatin addition: with only an IL-8 gradient after (a) 2-day 20 ng/mL VEGF treatment or (b) 2-day 50 ng/mL VEGF treatment and with only non-activated neutrophils after (c) 2-day 20 ng/mL VEGF treatment or (d) 2-day 50 ng/mL VEGF treatment. There are no significant differences using a two-tailed unpaired t-test and the total angiogenic endothelial cell number of five selected channels is listed for each corresponding column. Error bars represent standard error of the mean.

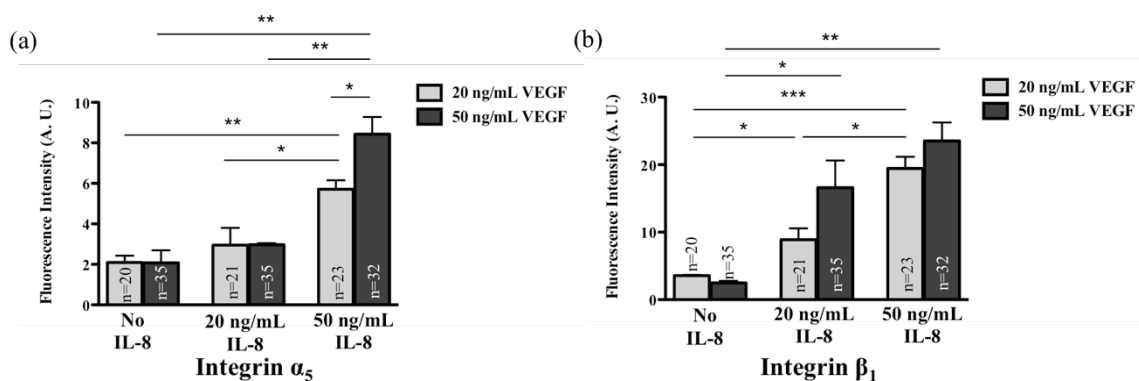


**Figure 4-18. Fluorescence intensities (after background subtraction) indicating integrin receptor expression on VEGF treated-endothelial cells under various IL-8 concentrations: (a) integrin  $\alpha_5$  expression; (b) integrin  $\beta_1$  expression. The fluorescence intensities of three different angiogenesis channels (not necessarily from different microfluidic devices) are included in each condition (\*,  $p < 0.05$ , \*\*,  $p < 0.005$ , \*\*\*,  $p < 0.0005$ , using a two-tailed unpaired t-test and the total angiogenic endothelial cell number of three selected channels is listed for each corresponding channel). Error bars represent standard error of the mean.**

expression for endostatin binding: this interplay supports the result that a 50 ng/mL of IL-8 gradient diminishes the stabilizing effects of neutrophil migration on angiogenesis structure. Considering the endostatin-treated angiogenesis model, endostatin does not influence the number of migrating neutrophils while activated neutrophils compete with endostatin to stabilize the angiogenesis structure in an IL-8 concentration-dependent fashion. Together, these observations demonstrate that the participation of neutrophil inflammation should be considered when designing therapies for angiogenesis-relevant diseases.

#### **4-4. Conclusion**

A microfluidic model was developed in this work to study the connection between two important physiological processes, neutrophil migration and endothelial angiogenesis. Under the stimulation of a pro-angiogenic factor, endothelial angiogenesis occurs in the extracellular matrix, which allows significantly more neutrophils to complete migration along the chemokine gradient. More importantly, increasing projected angiogenic endothelial cell area suggests a positive effect on neutrophil migration since endothelial cells with angiogenic treatment provide more surface contact sites for chemokine activation and, therefore, adhesion molecule expression. This endothelial angiogenesis may degrade the extracellular matrix to create more space for neutrophil recruitment. Furthermore, neutrophil migration stabilizes the endothelial angiogenesis structure in the presence of an angiogenesis inhibitor, and this effect is found to be controlled by the chemokine concentration; high levels of chemokine induce higher receptor expression for

angiogenesis inhibitor binding. This investigation of the interdependent relationships between neutrophil migration and endothelial angiogenesis is helpful for understanding the detailed mechanisms of these two complicated physiological processes. These studies also have implications for pharmaceutical application in angiogenesis-associated diseases and suggest a need to prevent or minimize neutrophil migration and secretion during treatment.

## **Chapter 5**

### **Microfluidic Study of Endothelial Cell-HeLa Cell Interactions under Biomimetic Conditions**

**Adapted from:**

**Wu, X.; Cliff, E. R.; Newbold, M. A.; Haynes. C. L., 2016, *in preparation*.**

## 5-1. Introduction

Examination of cellular interactions occurring through direct mechanical contact or paracrine effects is necessary to characterize the function of various cell and tissue types in complex biological systems. One representative example of these critical cell-cell interactions is cancer metastasis, the spread of cancer from primary sites to distant organs in the human body, coordinated by heterotypic cell interactions between endothelial cells and cancer cells.<sup>1-4</sup> During the process of cancer metastasis, these interactions contribute to several linked critical steps, playing an essential role in early stages of cancer metastasis.<sup>5-7</sup> Specifically, cancer cells proliferate at the primary site and drive angiogenesis or endothelial cell migration by secreting soluble factors for the transport of nutrients and oxygen; meanwhile, activated endothelial cells initiate degradation of the extracellular matrix and enable cancer coalescence into the vascular systems. Disrupted blood vessel structures leave space for cancer cell intravasation where detached malignant cells invade the circulatory system to colonize new sites. Since this close intercellular communication has been identified as one major target for cancer metastasis treatment,<sup>8-10</sup> investigation of the detailed mechanisms of endothelial-cancer cell interactions is of pivotal importance to understand and potentially overcome the pathogenesis of cancer.

To date, a great many efforts have been made to characterize the interplay between endothelial cells and cancer cells. Traditional *in vivo* assays are heavily based on transplant methods that require the injection of cancer cells into animal models;<sup>11-14</sup> however, these approaches suffer by making use of animals and having poor precision

based on biological discrepancies. Also, it is hard to glean quantitative information about specific cellular interactions in the dynamic and complex milieu that includes multiple cell types. Several *in vitro* approaches have been employed to study cellular interaction by co-culturing different cell types onto biocompatible substrates, such as physically separating cells with a porous filter membrane,<sup>15,16</sup> growing confluent cell layers over two complementary detachable substrates,<sup>17,18</sup> and patterning various cell populations through the use of highly controllable surface chemistry.<sup>19,20</sup> Although these *in vitro* approaches achieve cell co-culture in a precise and dynamic fashion that improves performance for quantification, the main drawback is the lack of physiological relevance, since these configurations are not biomimetic. Recent advances in microfluidic technologies have indicated great potential to overcome these limitations, allowing precise control over the spatial orientation of cells as well as the inclusion of physiological cues.<sup>21-23</sup> One critical advance in microfluidic platform development, compared to other *in vitro* approaches, is the introduction of a hydrogel scaffold into the microchannels to simulate the function of the extracellular matrix that separates endothelial cells from cancer cells *in vivo* and supports the formation of an endothelial cell layer that mimics the lining of the inner walls of blood vessels. Another important feature of the hydrogel scaffold is that it supports stable chemical gradients with high spatiotemporal resolution by confining molecular diffusion within the porous structure, facilitating quantitative analysis of cell migration inside the hydrogel scaffold. To date, microfluidic platforms exploiting this feature have focused only on the transendothelial migration of cancer cells and have not provided cell co-culture models for long-term

cellular interaction studies; furthermore, these studies did not introduce multiple biomimetic factors into a single microfluidic device to investigate endothelial cell-cancer cell interactions<sup>21-23</sup> – that is the aim of this work.

Herein, we developed a versatile microfluidic cell co-culture platform incorporating a gel scaffold to explore the interactions between endothelial cells and HeLa cancer cells at the extracellular matrix interface. Several key physiological factors in the context of cancer metastasis, including chemical gradients, flow rate, and tissue hypoxia, were successively introduced into the designed cell co-culture system, and the migratory behaviors of each cell type under various conditions were studied. To establish chemical gradients across the cell co-culture model, two different types of tumor cytokine molecules with the abilities to regulate cell migration, interleukin-8 (IL-8)<sup>24,25</sup> and tumor necrosis factor-alpha (TNF- $\alpha$ ),<sup>26,27</sup> were presented within the device in a gradient format. Next, the flow rate producing a similar shear rate as that found in human blood vessels was applied to examine cellular interactions in dynamic conditions. Finally, a mixture of oxygen-scavenging reagents was introduced into an extra chemical reaction channel to decrease the oxygen level across the entire device to simulate hypoxia. Although the effects of hypoxic conditions on cancer cell migration and cell co-culture models have been previously measured using microfluidic devices,<sup>28-30</sup> there are two major areas for improvement: (1) those methods require large gas tanks and precise flow control systems, and (2) they fail to recapitulate the three-dimensional (3D) configuration of the endothelial cell layer and incorporate other physiological factors. In our work, all three factors are eventually combined in a single device to create a more realistic biomimetic

microenvironment for cellular interaction studies, including chemical gradients across the hydrogel scaffold, shear rate over the cell layer, and hypoxic conditions within the cell co-culture model. Overall, the goal of this work is to fundamentally deepen the mechanistic insights about cellular interactions in a biomimetic environment and offer a promising microfluidic platform to study heterotypic cellular interactions at large.

## **5-2. Experimental details**

### **5-2-1. Device fabrication**

Microfluidic devices were fabricated using standard photolithography methods. Briefly, the channel design was transferred onto a chrome photomask plate coated with a positive photoresist layer (Nanofilm, Westlake Village, CA) through UV exposure. The transparent channel patterns were left on the photomask plate after a series of cleaning and etching steps. To prepare the microfluidic device mold, a 4-inch silicon wafer was spin-coated with 120- $\mu\text{m}$ -thick negative SU-8 50 photoresist (MicroChem, Newton, MA) and the channel patterns were imprinted on the SU-8 mold through the previously made photomask plate *via* UV light exposure. Following the baking step, the silicon wafer was placed in SU-8 developer (MicroChem, Newton, MA) to remove the photoresist without exposure. Then, a 10:1 mass ratio mixture of polydimethylsiloxane (PDMS) prepolymer (Ellsworth Adhesives, Germantown, WI) was poured on the prepared SU-8 mold and cured on a hot plate at 95 °C overnight. For the devices used in hypoxia experiments, half of the total required PDMS was cured on the SU-8 mold first and then polycarbonate

sheets (McMaster-Carr, Elmhurst, IL) were placed on the first PDMS layer and sandwiched with the second PDMS layer. In this step, a small amount of PDMS prepolymer was added on both sides of polycarbonate sheets to prevent bubble production when pouring the second layer of PDMS. The reservoirs of the three main channels were punched at appropriate locations using 3.5 mm or 1 mm disposable biopsy punches (Integra Miltex, Plainsboro, NJ) while gel chamber inlets were punched using 1 mm biopsy punches. Finally, the PDMS layer was cut and then bonded to a glass slide in an oxygen plasma chamber for 10 seconds at 100 L/h oxygen flow rate and 100 W.

### **5-2-2. Cell culture**

Human endothelial cells (hy926) and HeLa cells<sup>31-3331-33</sup> were purchased from American Type Culture Collection (ATCC, Manassas, VA) and stored in a liquid nitrogen storage container (MVE XC33/22, Select Genetics, Washington, PA). Upon thawing, both endothelial cells and HeLa cells were dispensed into 25 cm<sup>2</sup> flasks containing 6 mL of Dulbecco's Modified Eagle Medium (DMEM, formula: 4mM L-glutamine, 4.5 g/L L-glucose, and 1.5 g/L sodium pyruvate, Gibco, Carlsbad, CA) supplemented with 10% fetal bovine serum and 1% penicillin and streptomycin (Sigma-Aldrich, St. Louis, MO). Cells were fed every two or three days; when necessary, cells were detached using 1× trypsin solution (Sigma-Aldrich, St. Louis, MO) for device injection. Cells were only used between the third and tenth passages.

### **5-2-3. Device preparation**

First, 30  $\mu\text{L}$  of 1 mg/mL poly-D-lysine (PDL) solution (Sigma-Aldrich, St. Louis, MO) was injected into the device through the gel chamber inlet for 4 h incubation under 5%  $\text{CO}_2$  at 37  $^\circ\text{C}$ . After washing with 30  $\mu\text{L}$  of sterilized Milli-Q water (Millipore, Billerica, MA) twice, devices were placed in the oven at 65  $^\circ\text{C}$  for 24 to 48 h. Then, 2 mg/mL collagen type I gel solution (BD Biosciences, San Jose, CA) was carefully injected into the gel chamber through the gel inlet. Devices were then kept in humid pipette boxes to avoid evaporation, and a quick gel polymerization was carried out under 5%  $\text{CO}_2$  at 37  $^\circ\text{C}$  for 40 min. For the devices with large medium reservoirs (3.5-mm-diameter) used in the chemical gradient and hypoxia experiments, 20  $\mu\text{L}$  of cell culture medium was forcibly injected into each channel of the microfluidic device, and the medium in all six reservoirs was removed before loading cells. For smaller medium reservoir devices used in the flow rate experiments, Finntip pipette tips (Thermo Fisher Scientific, Waltham, MA) were inserted into all six small medium inlets (1-mm-diameter) for cell loading. A small amount of cell culture medium (about 30  $\mu\text{L}$ ) was manually injected into each channel through pipette tips using 1 mL syringes (Covidien, Dublin, Ireland), and the medium in each tip was aspirated to make the liquid level as low as possible. Endothelial cells were re-suspended in the cell culture medium at a density of  $1.5 - 2 \times 10^6$  cells/mL, and then 20  $\mu\text{L}$  of endothelial cells were seeded into an open reservoir or a pipette tip of the left channel to allow the cells to attach on the side wall of the gel scaffold due to the pressure difference between the left channel and other channels. Following the initial endothelial cell incubation for 30 min, the medium was removed from the left reservoirs or pipette tips, and 20  $\mu\text{L}$  of HeLa cell suspension ( $2.5 - 3 \times 10^6$  cells/mL) was added in an open

reservoir or a pipette tip of the right channel to allow HeLa cell layer attachment to the gel scaffold. After another 30 min incubation, the medium in the right reservoirs or pipette tips was aspirated again, and 30  $\mu$ L of fresh medium was added in each reservoir or pipette tip. Finally, all the devices were placed in the CO<sub>2</sub> incubator (New Brunswick Scientific, Edison, NJ) overnight to achieve confluent growth of the cell layers.

#### **5-2-4. Cell co-culture experiments**

##### *Chemical gradients*

Following the formation of cell layers in the devices after overnight incubation, the medium in the desired reservoirs was replaced with the same volume of cytokine molecule solution to develop various chemical gradient conditions. To be specific, the medium was removed from all the reservoirs, and 30  $\mu$ L of cytokine solution (IL-8 or TNF- $\alpha$ , Sigma-Aldrich, St. Louis, MO) at 20 or 50 ng/mL was placed in each reservoir of one side channel while 30  $\mu$ L of fresh cell culture medium was placed in each reservoir of other channels to create chemical gradients. For “no gradient” conditions, the 20 ng/mL IL-8 condition was established by placing 20 ng/mL IL-8 solution in the reservoirs of the two side channels and 25 ng/mL IL-8 solution in the reservoirs of the bottom channel. In contrast, to achieve the “no gradient” 50 ng/mL IL-8 condition, 50 ng/mL IL-8 solution was added into both side channels and 63 ng/mL IL-8 solution was added into the bottom channel. All the concentrations used in TNF- $\alpha$  “no gradient” conditions were the same as those in IL-8 experiments except that the concentration in the bottom channel was changed to 62 ng/mL for the 50 ng/mL TNF- $\alpha$  condition. The

determination of cytokine solution concentration for all “no gradient” conditions is described below. All the devices were incubated under 5% CO<sub>2</sub> at 37 °C for 24 h and imaged using MetaMorph ver. 7.7.5 imaging software on an inverted microscope equipped with a 10x objective and a CCD camera (QuantEM Photometrics, Tucson, AZ). Then, the liquid in all the reservoirs was replaced with a fresh aliquot of the same solution, and the devices were incubated for another 24 h before imaging a second time. Cells may migrate into the gel scaffold in the cell co-culture model instead of maintaining a layered structure, and the area of new migrating cells in the gel scaffold is calculated to indicate the effects of cellular interactions on each cell type. In detail, the cell migration area in the gel scaffold was selected by tracing the outline of cells manually and measured using ImageJ software (National Institutes of Health, Bethesda, MD). Three different devices are included in each condition for data analysis.

#### *Flow rate*

To introduce the desired flow rate into the side channels, a syringe containing fresh cell culture medium or 200 µM L-N<sup>G</sup>-monomethyl arginine citrate (L-NMMA, Cayman Chemical, Ann Arbor, MI) solution was connected with the devices by inserting tubing into one Finntip pipette tip of the desired side channel after the first overnight cell co-culture. The syringe pump (Harvard Apparatus, Holliston, MA) was operated at the flow rate of 5 or 15 µL/min for delivering solution, and the devices were imaged twice, after 24 and 48 h fluid flowing. The images were analyzed using the same methods mentioned

above. During experiments, all devices, including the syringe pump set-up, were placed in the incubator under 5% CO<sub>2</sub> at 37 °C.

### *Hypoxic environment*

To create a hypoxic environment across the cell co-culture system, a pair of oxygen scavenging solutions was injected into the extra chemical reaction channel (Fig. 5-1(b)) of the microfluidic device. Prior to injecting chemical solution, all six open reservoirs of each device were covered with duct tape (3M, St. Paul, MN) to further decrease the permeability of oxygen from atmosphere into the device as well as prevent the evaporation of medium from the reservoirs. For oxygen scavenging, 100 mg/mL pyrogallol (benzene-1,2,3-triol, Sigma-Aldrich, St. Louis, MO) and 1 M NaOH (Avantor, Center Valley, PA) solution were introduced through two separate inlets of the chemical reaction channel, and the mixing process occurred in the channel (verified by flowing water and 10 μM fluorescein isothiocyanate (FITC)-dextran (Sigma-Aldrich, St. Louis, MO) solution into the channel with fluorescence intensity monitored at different positions). To achieve oxygen concentration calibration, the oxygen concentration profile across the device was calibrated by placing 5 mg/mL of the oxygen-sensitive dye solution (tris(2,2'-bipyridyl) dichlororuthenium (II) hexahydrate, Sigma-Aldrich, St. Louis, MO) in all three main channels.<sup>34</sup> The diffusion of the dye molecules across the gel scaffold inside the device should reach equilibrium quickly due to the large diffusion coefficient of small molecules so that the change in fluorescence emission intensity can be monitored. First, the fluorescence emission intensity from the dye across the overall

device was recorded in air. Then, pure nitrogen gas and the oxygen scavenging reaction were flowed into the chemical reaction channel for 1 h successively to adjust the oxygen level in the device. The flow rate of pure nitrogen gas was set at 4 L/min, and the oxygen scavenging reaction was injected at 10  $\mu$ L/min. Since the dye is quenched by the presence of oxygen, the fluorescence intensities in various conditions were monitored and used to calculate oxygen concentration across the device according to the Stern-Volmer equation below:<sup>34,35</sup>

$$\begin{aligned} \frac{I_0}{I_{air}} = 1 + K_q [O_2]_{air} \\ \frac{I_0}{I} = 1 + K_q [O_2] \end{aligned} \quad \Rightarrow \quad [O_2] = \frac{1}{K_q} \times \left\{ \frac{I_{air}}{I} [1 + K_q [O_2]_{air}] - 1 \right\} \quad (1)$$

where  $I_0$  and  $I$  represent the fluorescence intensity with pure nitrogen gas and chemical reaction flowing, respectively, and  $K_q$  is the quenching constant. Following the calibration, the oxygen scavenging reaction was injected into the chemical reaction channel for 48 h, and the effects of hypoxia on the cell co-culture model were determined by analyzing the cell images at 24 and 48 h time points. The devices with liquid leaking or cell contamination during 48 h chemical solution injection were eliminated from final data analysis.

#### *Combined effects of chemical gradients, flow, and hypoxic conditions*

Finally, to analyze the combined effects of chemical gradients, flow rate, and hypoxia, devices similar to those used for hypoxia experiments were used with two important modifications: (1) small inlets were punched at the ends of the left side channel to allow

flow and (2) large reservoirs were still punched for the other channels to allow chemical gradient formation. Cell culture medium was flowed into the left side channel at 5  $\mu\text{L}/\text{min}$ , and 50 ng/mL IL-8 solution was placed in the reservoirs of the right side channel to develop chemical gradients. Oxygen scavenging chemical solution was injected through the right chemical reaction channel at 10  $\mu\text{L}/\text{min}$  to decrease the oxygen level in the device. Again, the cell population in all devices were imaged on an inverted microscope every 24 h and analyzed using ImageJ software.

#### **5-2-5. Numerical simulation**

The static diffusion behavior of 50 ng/mL IL-8 solution across the microfluidic device from 0 to 24 h was verified using the simulation software COMSOL 4.3b (COMSOL, Inc., Burlington, MA). The diffusion coefficients of IL-8 in the collagen gel, free solution, and cell layer were assumed to be  $6.75 \times 10^{-11} \text{ m}^2/\text{s}$ ,  $8.4 \times 10^{-11} \text{ m}^2/\text{s}$ , and  $6.32 \times 10^{-12} \text{ m}^2/\text{s}$ , respectively.<sup>36</sup> In the “no gradient” condition, the concentrations of IL-8 in both side channels were set at 50 ng/mL, while the concentration in the bottom channel was predicted by keeping the constant concentration profile along the center line of the gel scaffold - according to the COMSOL model, 63 ng/mL was the appropriate IL-8 concentration for the bottom channel. The simulation of 20 ng/mL IL-8 and all TNF- $\alpha$  gradients conditions were conducted using the same method. Since there is no value reported for the diffusion coefficients of TNF- $\alpha$ , we calculated the diffusion coefficients for TNF- $\alpha$  according to a published paper,<sup>37</sup> and the diffusion coefficients of TNF- $\alpha$  in the collagen gel, free solution, and cell layer were assumed to be  $5.38 \times 10^{-11} \text{ m}^2/\text{s}$ ,  $6.7 \times$

$10^{-11}$  m<sup>2</sup>/s, and  $5.04 \times 10^{-12}$  m<sup>2</sup>/s, respectively. In addition to the chemical gradient conditions, the shear rate level in the side channel was also studied using COMSOL software in the presence of 5 or 15  $\mu$ L/min flow rate.

#### **5-2-6. Fluorescence imaging and permeability measurement**

Fluorescence imaging was applied to characterize the profiles of chemical gradients in the complex dynamic conditions. To examine the impacts of flow rate on secretion by HeLa cells, 10  $\mu$ M FITC-dextran (10 kDa) solution was flowed into the right side channel at 5  $\mu$ L/min, and the fluorescence gradient across the gel scaffold was observed at 24 and 48 h time points. In the combined effects experiments, the same fluorescent dye, 10  $\mu$ M FITC-dextran solution was placed in the right side channel to study the gradient profile in the gel scaffold at various time points while the 5  $\mu$ L/min flow rate was maintained in the left side channel.

For the cell layer permeability measurement, 10  $\mu$ M FITC-dextran solution was placed in one side channel to test the permeability of endothelial or HeLa cell layer. After 5 h diffusion of fluorescent molecules, the flux balance at the interface of cell layer and gel scaffold was established to calculate the permeability:

$$J = -D \frac{\partial C}{\partial x} \quad (2)$$

where  $J$  is flux,  $D$  is diffusion coefficient of FITC-dextran ( $6.75 \times 10^{-11}$  m<sup>2</sup>/s) in the collagen gel and  $x$  is the position.

$$Flux = -P\Delta C \quad (3)$$

where  $P$  is permeability and  $C$  is concentration.

### **5-2-7. Confocal imaging**

The configurations of the endothelial cell or HeLa cell layers in different conditions were characterized using Nikon A1R MP confocal microscope (Nikon, Melville, NY). Briefly, medium in all the reservoirs or pipette tips was removed, and the channels were rinsed twice with 40  $\mu$ L of 1 $\times$  PBS solution. Following the PBS wash, 30  $\mu$ L of 4% (wt/vol) paraformaldehyde (PFA, Sigma-Aldrich, St. Louis, MO) was added in each reservoir or tip for 15 minutes to fix the cells. The same volume of 0.1% (vol/vol) Triton X-100 was placed in each reservoir or tip for the permeabilization of cell membranes after two PBS washes. Then, a mixture of 5  $\mu$ g/mL 4,6-diamidino-2-phenylindole dilactate (DAPI dilactate) and 6.6  $\mu$ M Alexa 488 phalloidin (Life Technologies, Carlsbad, CA) solution in 30  $\mu$ L was added in each reservoir or tip for staining the cells. The pipette box containing the devices was wrapped with aluminum foil and placed in the dark for 1 h incubation. Finally, devices were washed using PBS twice to remove unbound fluorescent agents. All the confocal images were deconvoluted using AutoQuant X 3.0.4 software (Media Cybernetics, Rockville, MD) and processed with Imaris software (Bitplane AG, Zurich, Switzerland).

## **5-3. Results and discussion**

### **5-3-1. Characterization of the cell co-culture model**

The microfluidic device used for developing a cell co-culture model is composed of three main channels and a central chamber for gel loading, while an extra pair of chemical

reaction channels is added in the hypoxia device on either side of the central chamber (Fig. 5-1(a) and (b)). In the experimental design, collagen gel is introduced into the central chamber to simulate the extracellular matrix and then, endothelial cells are cultured on the side wall of the gel scaffold in the left side channel while HeLa cells are employed as the cancer cell model cultured on the opposite side wall in the right side channel. First, the permeability of each cell layer was measured by visualizing the diffusion of fluorescent probe molecules across the cell layer from the corresponding side channel into the gel scaffold (Fig. 5-2). By establishing the flux balance at the interface of the cell layer and the gel scaffold, the calculated permeability of the cultured endothelial and HeLa cell layer are  $8.8 \times 10^{-7}$  and  $5.8 \times 10^{-7}$  m/s, respectively; these values are close to the results reported in previous studies with intact cell layer configurations,<sup>38,39</sup> which indicates good integrity of the cell layer structures achieved in this system. The confocal imaging results further demonstrate the confluent 3D configuration of the endothelial cell and HeLa cell layers on the side walls of the gel scaffold after overnight incubation (Fig. 5-3). To evaluate the response of individual cell types to the cell co-culture microenvironments, only the cell migration caused by the paracrine effects can be taken into account, and control experiments with single cell type culture were performed to account for the contribution of spontaneous cell migration without cell-cell communication. In single cell type culture conditions (Fig. 5-4), endothelial cells were found to protrude into the gel scaffold after 72 h incubation, but HeLa cells remained attached to the side wall after long-term culture. Hence, the cell-cell interactions are studied within 48 h so that the self-migration of endothelial cells at 72 h

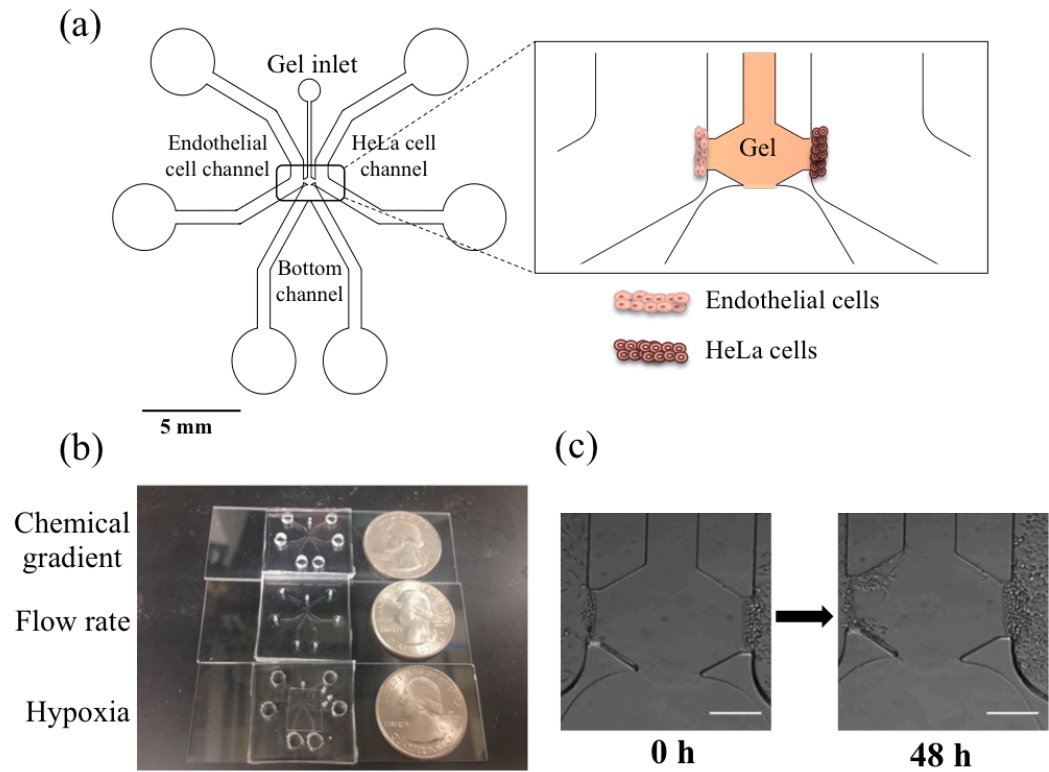


**Figure 5-1. (a) Schematic of microfluidic device used in chemical gradient experiments. The collagen gel is injected into the central chamber for co-culturing different cell types on the opposite side walls. (b) Photograph of the microfluidic devices with the size comparison to quarter coins (top: chemical gradient device; middle: flow rate device; bottom: hypoxia device with the extra chemical reaction channels on both sides). (c) Bright-field images of the central chamber within the device showing changes in the cell co-culture model from 0 h to 48 h incubation. (scale bar: 200 μm)**

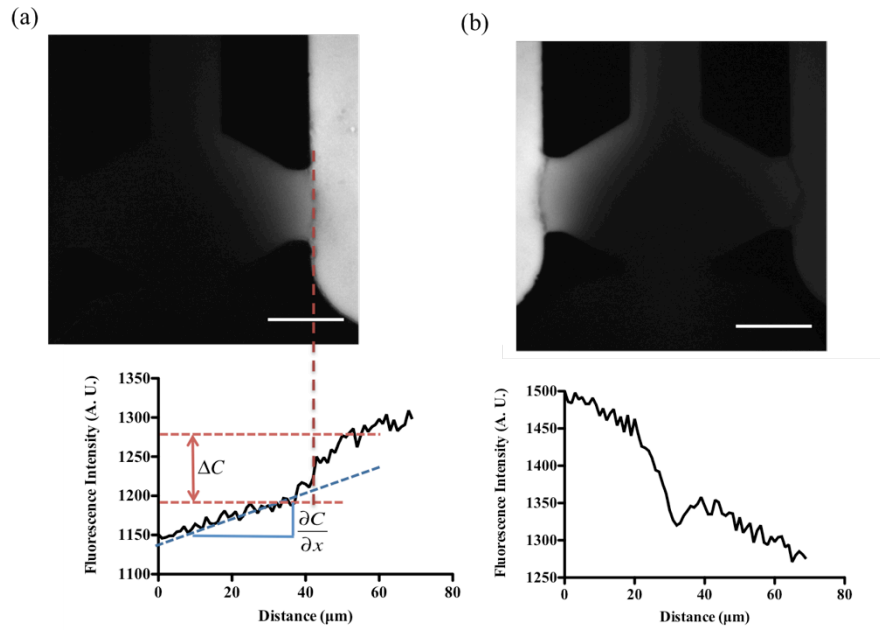


**Figure 5-2. The permeability measurements of (a) HeLa cell layer and (b) endothelial cell layer using the fluorescence intensity profiles of FITC-dextran solution across the cell-gel interface after 5 h diffusion. (scale bar: 200  $\mu\text{m}$ )**

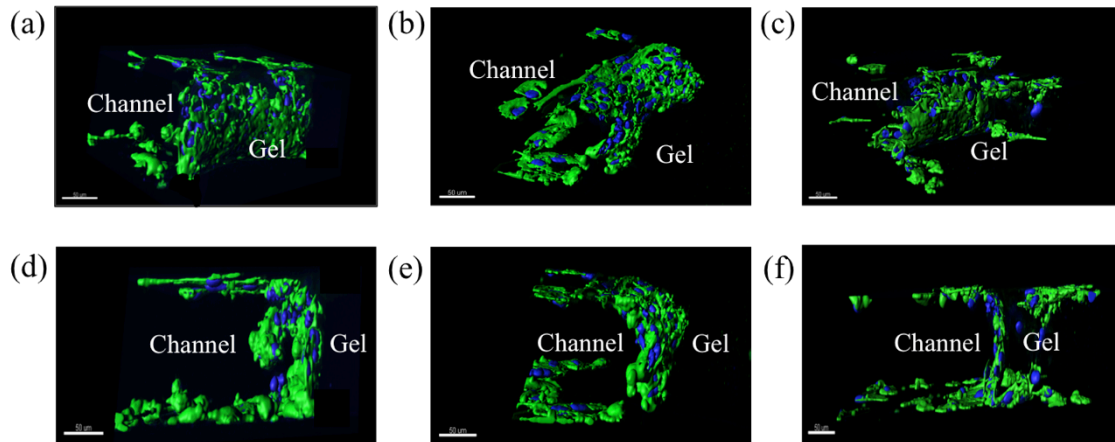


**Figure 5-3. 3D confocal imaging of cell layers on the side wall of the gel scaffold within the microfluidic device depicted in Figure 1. The 45° angle view of (a) an overnight-cultured endothelial cell layer; (b) an overnight-cultured HeLa cell layer and (c) an endothelial cell layer after 2-day cell co-culture. The side view of (d) overnight-cultured endothelial cell layer; (e) an overnight-cultured HeLa cell layer and (f) an endothelial cell layer after 2-day cell co-culture (scale bar: 50  $\mu\text{m}$ ). (Blue indicates DAPI-stained nucleus and green represents Alexa 488 phalloidin-stained cytoskeletal F-actin. The positions of the gel scaffold and side channel are indicated in the figures.) (scale bar: 50  $\mu\text{m}$ )**

is not included in the data analysis. Initial study of the characterized cell co-culture model showed that endothelial cells migrate obviously into the gel scaffold toward the HeLa cells after 48 h of co-culture while HeLa cells barely enter the gel region (Fig. 5-1(c) and 5-3). This observation implies that HeLa cells may function as an attractive source stimulating endothelial cell migration by secreting soluble factors in this cell co-culture model. Among various molecules known to be secreted by cancer cells, vascular endothelial growth factor (VEGF) is considered to be largely responsible for triggering endothelial cell migration, thus we hypothesized that soluble VEGF was one important actor in this interaction.<sup>40,41</sup> Measurement of the effect of presenting the VEGF antibody in our cell co-culture model reveals that a high concentration (10  $\mu\text{g}/\text{mL}$ ) of VEGF antibody in the left side channel effectively decreases the invasion of endothelial cells into the gel scaffold compared to a low concentration (1  $\mu\text{g}/\text{mL}$ ) and no antibody conditions after 48 h incubation ( $p < 0.05$ , Fig. 5-5). These observations support the hypothesis that VEGF participates in the endothelial cell-HeLa cell interaction as a secreted soluble factor. With preliminary characterization of the cell co-culture model, several essential physiological factors could be introduced into this model to probe the cellular interactions under biomimetic conditions.

### **5-3-2. The effects of chemical gradients**

Two different types of cytokine molecules, IL-8 and TNF- $\alpha$ , were employed herein to study the effects of chemical gradients on cellular interactions at the concentrations of either 20 or 50 ng/mL. The chemical gradients were developed by placing cytokine

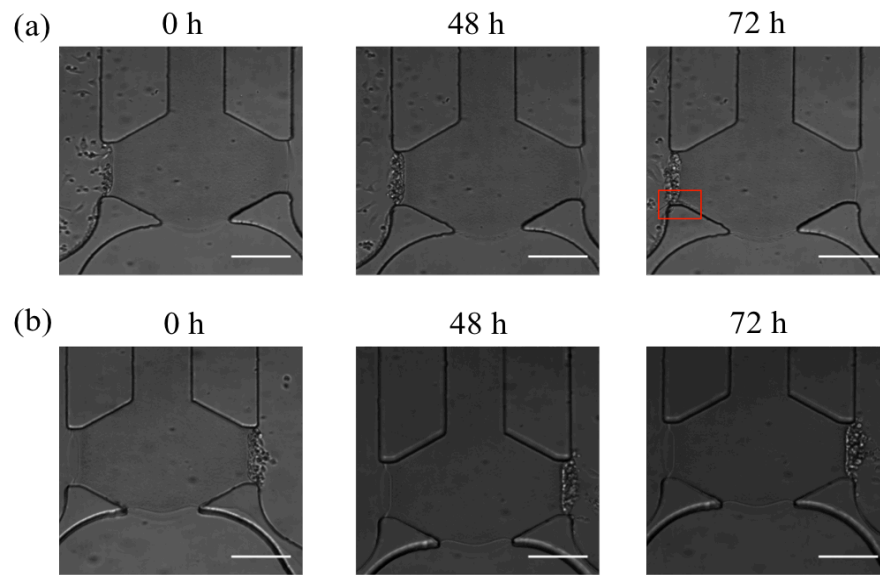


**Figure 5-4. Single cell type culture in the device for incubation time optimization: (a) an endothelial cell layer culture at 0, 48, and 72 h; (b) a HeLa cell layer culture at 0, 48, and 72 h. The images at 0 h represent the formation of cell layers after initial overnight incubation, and the red square indicates the protrusion of endothelial cells into the gel scaffold after 72 h. (scale bar: 200  $\mu\text{m}$ )**

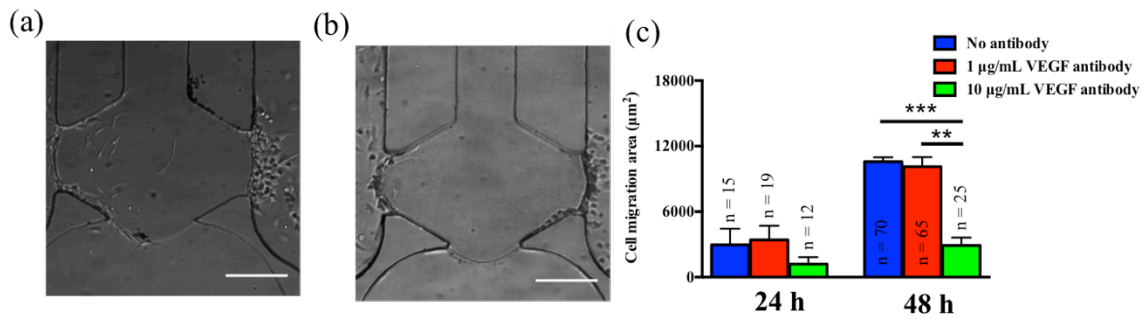


**Figure 5-5. The results of VEGF antibody studies: (a) a bright-field image of cell migration with 1 µg/mL VEGF antibody in the left side channel after 48 h incubation (scale bar: 200 µm); (b) a bright-field image of cell migration with 10 µg/mL VEGF antibody in the left side channel after 48 h incubation (scale bar: 200 µm); (c) data analysis of VEGF antibody incubation at 24 and 48 h time points. Three replicates are included in each condition, and the total cell number (n) of three replicates analyzed in each condition is indicated for the corresponding bar, \*\*,  $p < 0.005$ , \*\*\*,  $p < 0.0005$ , using a two-tailed unpaired t-test. Error bars represent standard error of the mean.**

solution in either side channel to enable stable linear diffusion of cytokine molecules from the side channel into the gel scaffold. Regarding the directions of chemical gradients, the gradient from the right to left channel is defined as a positive gradient for endothelial cells and a negative gradient for HeLa cells since cytokine molecules move towards endothelial cells and away from HeLa cells in this condition; similarly, the gradient from the left to right channel is defined as a positive gradient for HeLa cells and a negative gradient for endothelial cells. In addition to the chemical gradient conditions, flat concentration profiles of cytokine molecules at 20 or 50 ng/mL were created to examine cellular interactions in a microenvironment with the cytokines but without gradients by introducing cytokine solution in all three main channels. The concentration distribution of cytokine molecules in the microfluidic device can be simulated and visualized using COMSOL numerical simulation software. The simulation results for the 50 ng/mL IL-8 positive gradient for endothelial cells (Fig. 5-6(a) and (b)) confirms the formation of a gradient along the middle line of the gel scaffold, but the steepness of the gradient decreases gradually from 2 h to 24 h due to diffusion; based on this information, fresh solution was added into all reservoirs after 24 h to promote stability of the gradient shape. For the conditions without a gradient, 50 ng/mL IL-8 solution was placed in both side channels, and the necessary concentration of IL-8 in the bottom channel was predicted using the simulation software. When 63 ng/mL IL-8 solution was placed in the bottom channel, the cytokine concentration along the middle line of the gel scaffold remains constant at 50 ng/mL from 2 h to 24 h (Fig. 5-6(c) and (d)), which is suitable for producing the desired “no gradient” condition. With the same approach, gradient profiles

can be generated for 20 ng/mL IL-8 gradients conditions and all the TNF- $\alpha$  gradients conditions (data not shown). Then, the effects of chemical gradients on cellular interactions between endothelial cells and HeLa cells were studied under 50 ng/mL chemical gradient of each cytokine. After 48 h incubation, the cell migration area results reveal that 50 ng/mL negative gradients for endothelial cells significantly inhibit the endothelial cell migration into the gel scaffold for both cytokines ( $p < 0.05$ , Fig. 5-7). This inhibition indicates that negative cytokine gradients guide the migration of endothelial cells competitively with the soluble factors secreted by HeLa cells from the opposite direction; however, positive gradients and “no gradient” conditions do not induce additive effects in regulating endothelial cell migration compared to the control condition without any cytokine solution. On the other hand, HeLa cells are not shown to sense the gradients actively as only a small amount of HeLa cells invade the gel region in each condition. For 24 h incubation, a 50 ng/mL IL-8 positive gradient induces significantly more endothelial cell migration towards HeLa cells ( $p < 0.05$ ), but there is no significant difference found among various conditions of TNF- $\alpha$ , and HeLa cell migration is not sensitive to any gradient condition (Fig. 5-8). The results of smaller concentration gradients (20 ng/mL) follow similar trends at 48 h incubation where negative gradients were able to decrease endothelial cell migration into the gel region although the only statistically significant difference was between the control and the negative gradient condition for IL-8 ( $p < 0.05$ , Fig. 5-9). Unlike the larger concentration, 20 ng/mL positive gradients of neither cytokine promoted penetration of endothelial cells into the gel scaffold significantly at the 24 h time point (Fig. 5-10). Again, HeLa cells

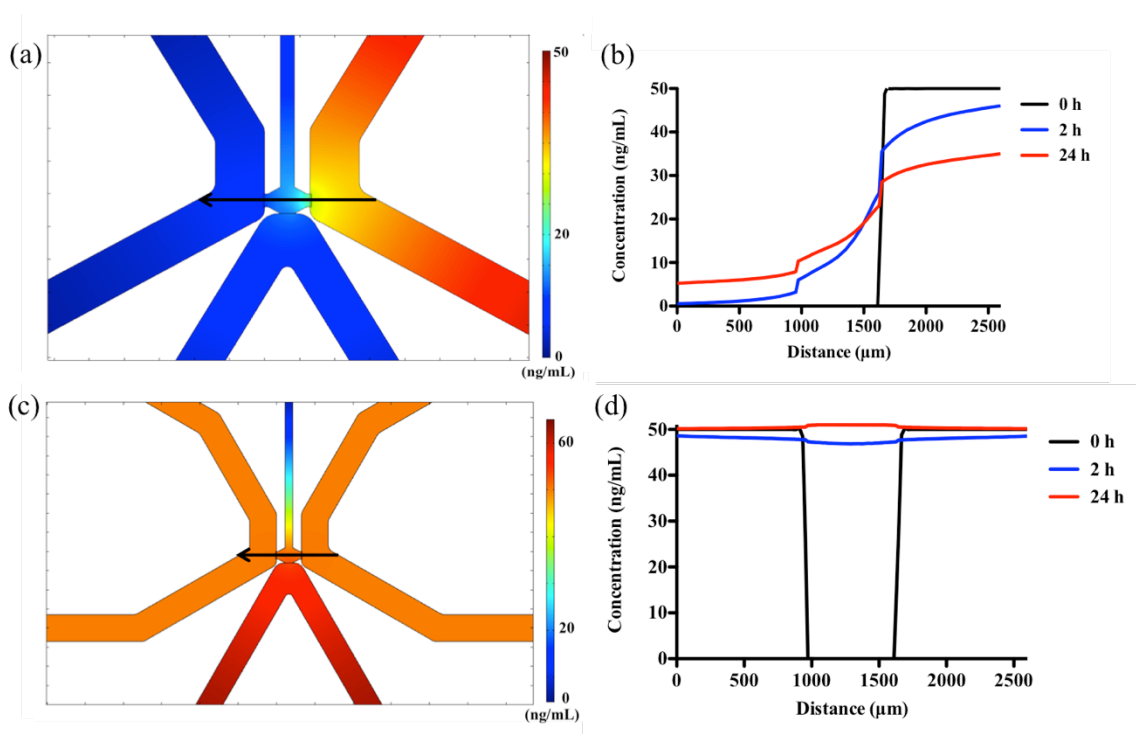


**Figure 5-6. COMSOL simulation results of 50 ng/mL IL-8 gradient in the right channel: (a) the concentration distribution of IL-8 molecules in the overall device and (b) the gradient profiles across the center line of gel scaffold at different time points. COMSOL simulation results for the 50 ng/mL IL-8 no gradient condition: (c) the concentration distribution of IL-8 molecules in the overall device and (d) the gradient profiles across the center line of gel scaffold at different time points. The black arrows indicate the direction of the chemical gradient.**

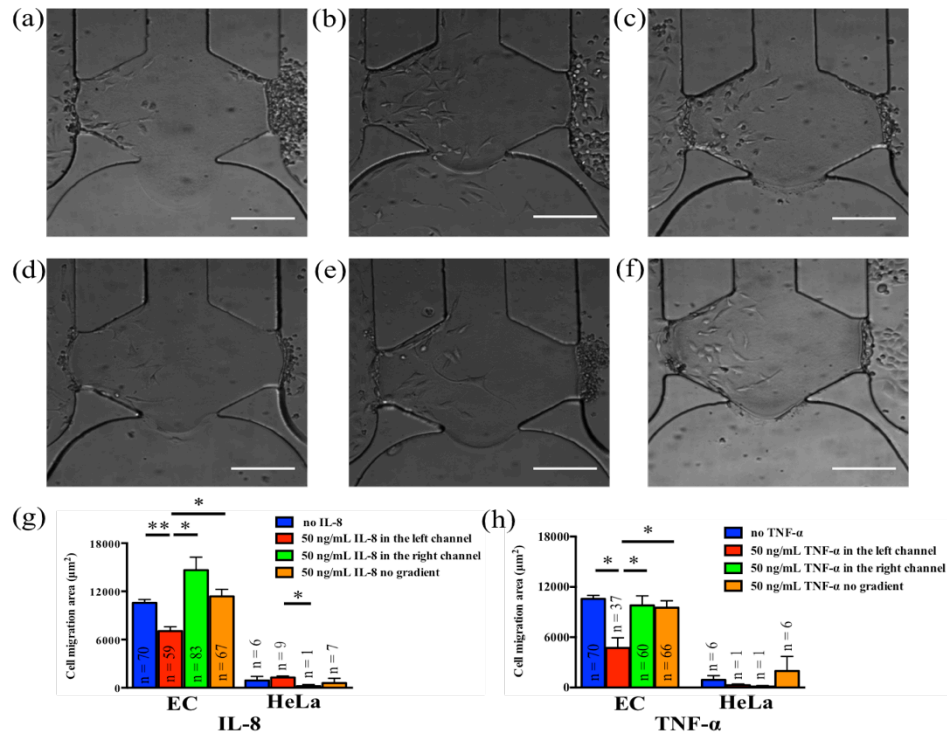


**Figure 5-7. The effects of chemical gradients on cell migration after 48 h incubation. The bright-field images (scale bar: 200  $\mu\text{m}$ ) of cell migration into the center microfluidic chamber under various gradient profiles at the 48 h time point: (a) 50 ng/mL IL-8 in the left channel; (b) 50 ng/mL IL-8 in the right channel; (c) 50 ng/mL IL-8 no gradient condition; (d) 50 ng/mL TNF- $\alpha$  in the left channel; (e) 50 ng/mL TNF- $\alpha$  in the right channel and (f) 50 ng/mL TNF- $\alpha$  no gradient condition. Data analysis of cell migration area under (g) 50 ng/mL IL-8 gradients and (h) 50 ng/mL TNF- $\alpha$  gradients conditions after 48 h incubation. Three device replicates are included in each condition, and the total cell number (n) of three replicates analyzed in each condition is indicated in or above the corresponding bar, \*,  $p < 0.05$ , \*\*,  $p < 0.005$ , using a two-tailed unpaired t-test. Error bars represent standard error of the mean.**

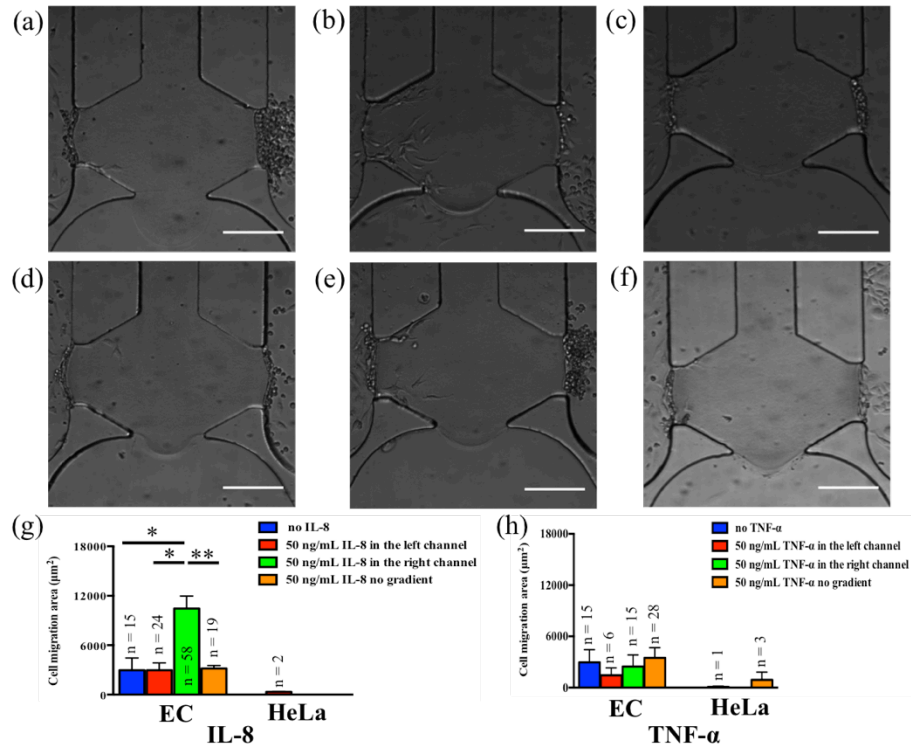


**Figure 5-8.** The effects of different chemical gradients on cell migration after 24 h incubation. The bright-field images (scale bar: 200  $\mu\text{m}$ ) of cell migration under various gradient profiles at 24 h time point: (a) 50 ng/mL IL-8 in the left channel; (b) 50 ng/mL IL-8 in the right channel; (c) 50 ng/mL IL-8 no gradient condition; (d) 50 ng/mL TNF- $\alpha$  in the left channel; (e) 50 ng/mL TNF- $\alpha$  in the right channel and (f) 50 ng/mL TNF- $\alpha$  no gradient condition. Data analysis of cell migration area under (g) 50 ng/mL IL-8 gradients, and (h) 50 ng/mL TNF- $\alpha$  gradients conditions after 24 h incubation. Three replicates are included in each condition, and the total cell number (n) of three replicates analyzed in each condition is indicated for the corresponding bar, \*,  $p < 0.05$ , \*\*,  $p < 0.005$ , using a two-tailed unpaired t-test. Error bars represent standard error of the mean.

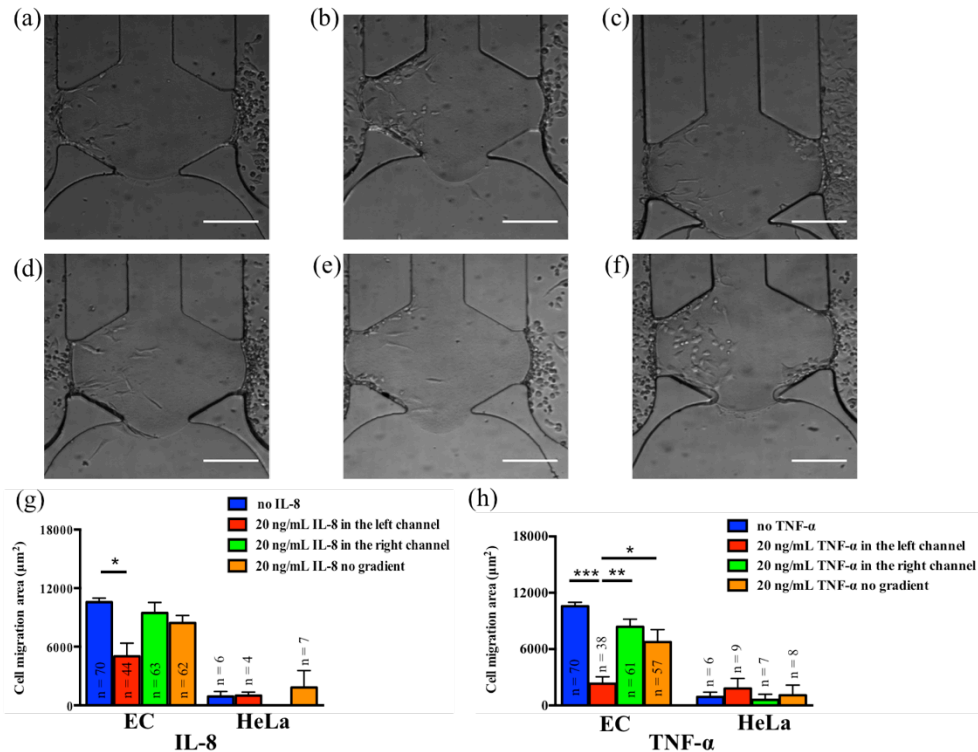


**Figure 5-9.** The effects of different chemical gradients on cell migration after 48 h incubation. The bright-field images (scale bar: 200 µm) of cell migration under various gradient profiles at 48 h time point: (a) 20 ng/mL IL-8 in the left channel; (b) 20 ng/mL IL-8 in the right channel; (c) 20 ng/mL IL-8 no gradient condition; (d) 20 ng/mL TNF- $\alpha$  in the left channel; (e) 20 ng/mL TNF- $\alpha$  in the right channel, and (f) 20 ng/mL TNF- $\alpha$  no gradient condition. Data analysis of cell migration area under (g) 20 ng/mL IL-8 gradients and (h) 20 ng/mL TNF- $\alpha$  gradients conditions after 48 h incubation. Three replicates are included in each condition, and the total cell number (n) of three replicates analyzed in each condition is indicated for the corresponding bar, \*,  $p < 0.05$ , \*\*,  $p < 0.005$ , \*\*\*,  $p < 0.0005$ , using a two-tailed unpaired t-test. Error bars represent standard error of the mean.

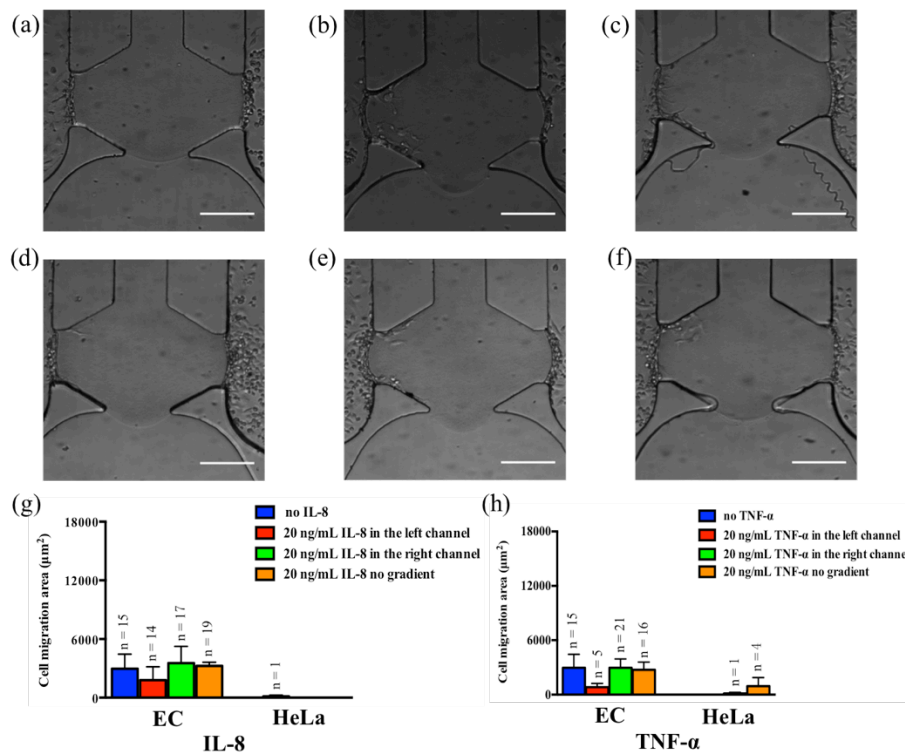


**Figure 5-10.** The effects of different chemical gradients on cell migration after 24 h incubation. The bright-field images (scale bar: 200 µm) of cell migration under various gradient profiles at 24 h time point: (a) 20 ng/mL IL-8 in the left channel; (b) 20 ng/mL IL-8 in the right channel; (c) 20 ng/mL IL-8 no gradient condition; (d) 20 ng/mL TNF- $\alpha$  in the left channel; (e) 20 ng/mL TNF- $\alpha$  in the right channel, and (f) 20 ng/mL TNF- $\alpha$  no gradient condition. Data analysis of cell migration area under (g) 20 ng/mL IL-8 gradients and (h) 20 ng/mL TNF- $\alpha$  gradients conditions after 24 h incubation. Three replicates are included in each condition, and the total cell number (n) of three replicates analyzed in each condition is indicated for the corresponding bar, \*,  $p < 0.05$ , \*\*,  $p < 0.005$ , \*\*\*,  $p < 0.0005$ , using a two-tailed unpaired t-test. Error bars represent standard error of the mean.

barely moved into the gel scaffold in any of the 20 ng/mL gradient conditions. Based on the results above, we can conclude that (1) the polarization of the chemical gradients reveals a time- and concentration-dependent effect on cellular interactions where negative gradients dominantly control the endothelial cell migration after long-term co-culture and positive gradients only show additive impacts on endothelial cell migration towards HeLa cells for the 50 ng/mL IL-8 condition with short time co-culture; (2) the endothelial cell migration is not sensitive to the total amount of cytokine molecules in the cell co-culture system since all “no gradient” conditions, containing more total cytokine molecules than the gradient conditions, led to results that were indistinguishable from control conditions; and (3) HeLa cells appear to grow in a much smaller area of the gel scaffold than endothelial cells in all conditions. Finally, monitoring HeLa cell migration under various cytokine gradients without endothelial cell co-culturing indicates weak responses by HeLa cells to cytokine gradients (data not shown here) so that the introduction of endothelial cells is not the reason for compromised HeLa cell migration.

### **5-3-3. The effects of flow rate**

Because the small inlets are punched at the ends of each channel to replace the large medium reservoirs used in the chemical gradient devices (Fig. 5-11(a) and 5-1(b)), the cell co-culture model was studied first with the static medium-filled pipette tips inserted into the small inlets to determine any effects of the device configuration change on cellular interactions. Compared to the control condition from the chemical gradient experiments, there was no statistical difference found for total cell migration area due to

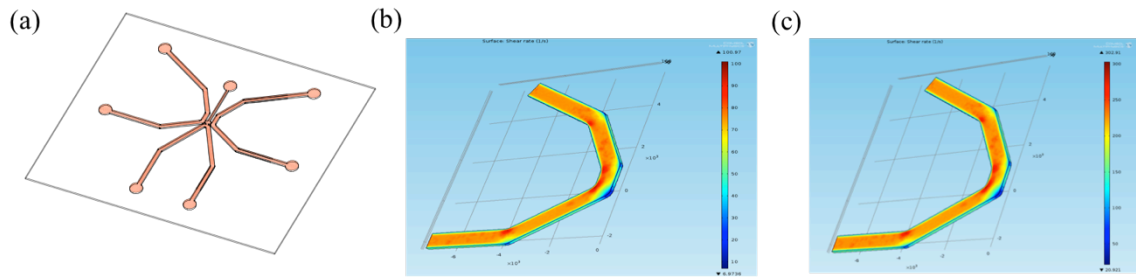


**Figure 5-11. (a) Schematic of microfluidic device used for flow rate study. (b) COMSOL simulation result of shear rate produced by 5  $\mu\text{L}/\text{min}$  flow rate in the side channel. (c) COMSOL simulation result of shear rate produced by 15  $\mu\text{L}/\text{min}$  flow rate in the side channel. The channel width is 700  $\mu\text{m}$  (the shear rate scale bar in (b) goes from 10 (blue) to 100  $\text{s}^{-1}$  (red) and the scale bar in (c) goes from 20 (blue) to 300  $\text{s}^{-1}$  (red)).**

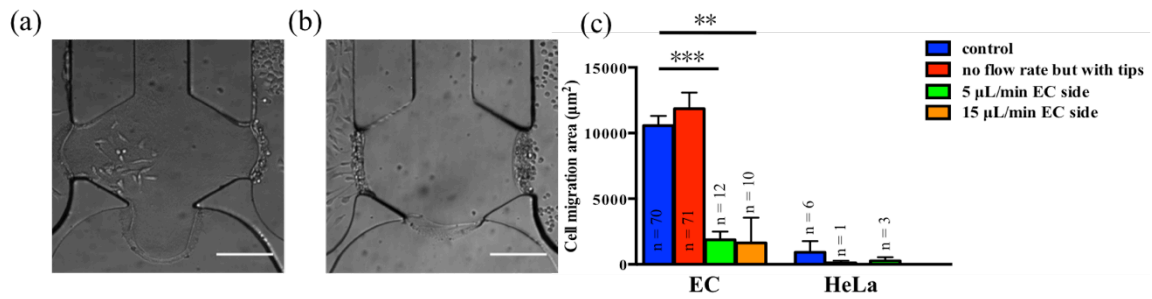


**Figure 5-12. Bright-field images (scale bar: 200  $\mu\text{m}$ ) of (a) cell migration with a pipette tip inserted into the inlets but no flow rate introduced at 48 h. (b) cell migration with 15  $\mu\text{L}/\text{min}$  flow rate in the left side channel at 48 h. (c) Data analysis of cell migration area under various flow rate conditions. Three replicates are included in each condition and the total cell number (n) of three replicates analyzed in each condition is indicated for the corresponding bar, \*\*,  $p < 0.005$ , \*\*\*,  $p < 0.0005$ , using a two-tailed unpaired t-test. Error bars represent standard error of the mean.**

the configuration change in the device to achieve flow (Fig. 5-12(a) and (c)). To make all the conditions consistent, the control data in the chemical gradient experiments was also applied for the data analysis of flow rate and hypoxic conditions below. A flow rate of 5  $\mu\text{L}/\text{min}$  was introduced into different side channels to simulate physiological shear rates (from 50 to 100  $\text{s}^{-1}$ ) in large veins and descending aorta (Fig. 5-11(b)).<sup>42</sup> With the flow rate in either side channel or both side channels, endothelial cell migration towards HeLa cells was significantly decreased after 48 h under flow conditions ( $p < 0.05$ ), while no difference was measured for HeLa cell migration between control and flow conditions (Fig. 5-13). The intracellular signaling pathway of endothelial nitric oxide synthase (eNOS) activated by shear rate is implicated in regulating endothelial cell migration due to the release of bioactive nitric oxide (NO), which may attenuate the sprouting growth of endothelial cells in the presence of flow.<sup>43,44</sup> An inhibitor of the eNOS pathway, L-NMMA,<sup>45</sup> was introduced into the left side channel at 200  $\mu\text{M}$  to block the production of NO. As expected, endothelial cell migration was recovered to a significantly higher level than flowing pure medium through the channel ( $p < 0.05$ , Fig. 5-13), but there was still a statistically significant difference between the control and L-NMMA conditions; further study will be required to determine other contributing factors to the decrease in endothelial cell migration. In parallel, confocal imaging studies of the endothelial cell layer after 48 h flow (Fig. 5-14) show that the cell layer is not confluent and some cells are lost. This damage in the 3D configuration of the endothelial cell layer may also contribute to the weak cell migration response after 48 h cell co-culture. We also found that the shear rate is able to remove the attached cells in the channels while the HeLa cell

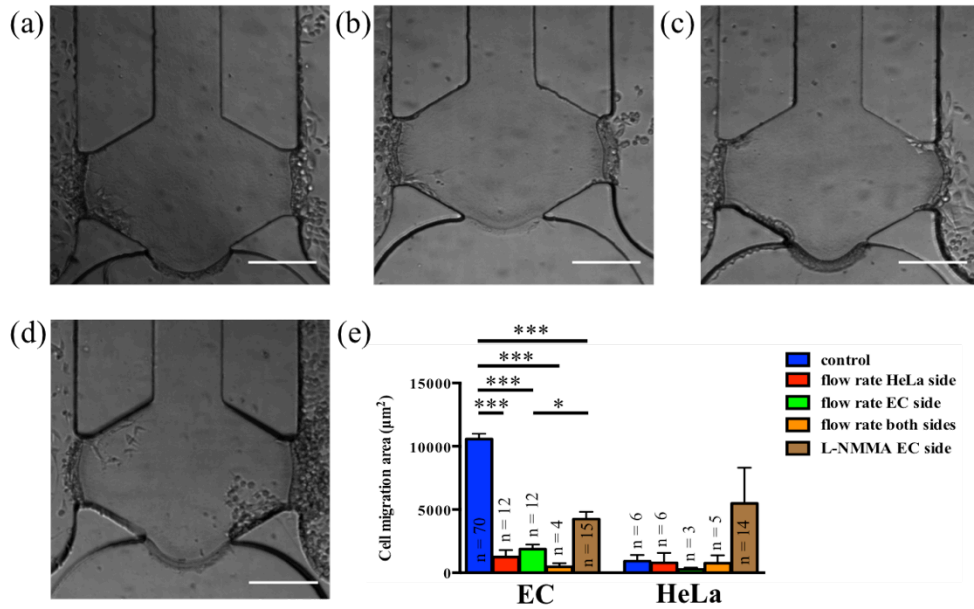


**Figure 5-13. The effects of flow rate on cell migration after 48 h medium flowing. The bright-field images (scale bar: 200 µm) of cell migration into the center microfluidic chamber in different flow rate conditions at the 48 h time point: (a) 5 µL/min cell culture medium flowing in the left channel; (b) 5 µL/min cell culture medium flowing in the right channel; (c) 5 µL/min cell culture medium flowing in both side channels; and (d) 5 µL/min cell culture medium containing 200 µM L-NMMA flowing in the left channel. (e) Data analysis of cell migration area under various flow rate conditions after 48 h medium flowing. Three device replicates are included in each condition, and the total cell number (n) of these replicates analyzed in each condition is indicated in or above the corresponding bar, \*,  $p < 0.05$ , \*\*\*,  $p < 0.0005$ , using a two-tailed unpaired t-test. Error bars represent standard error of the mean.**

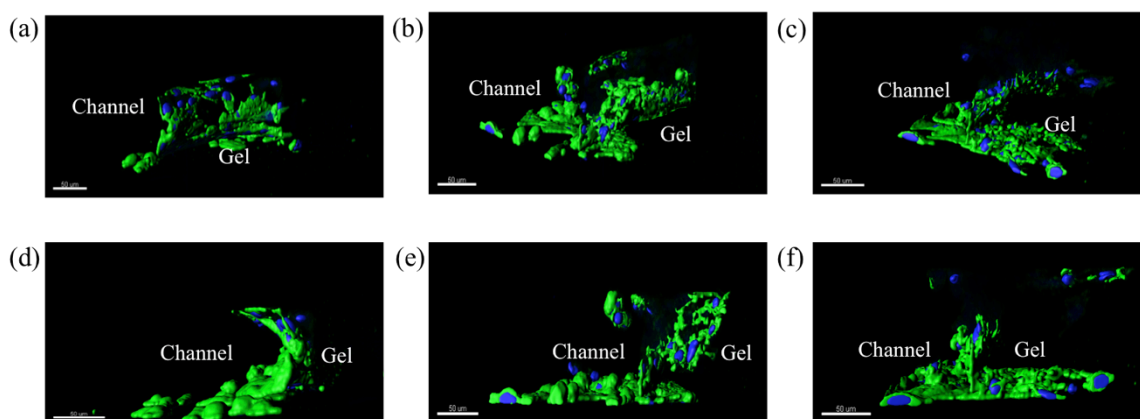


**Figure 5-14. Confocal imaging of the endothelial cell layer after 48 h cell co-culture in different conditions. Images depict a 45° angle view of the endothelial cell layer under the conditions of (a) 5  $\mu\text{L}/\text{min}$  flow rate; (b) oxygen scavenging reaction on the left side and (c) oxygen scavenging reaction on the right side. The side view of endothelial cell layer under the conditions of (a) 5  $\mu\text{L}/\text{min}$  flow rate; (b) oxygen scavenging reaction on the left side and (c) oxygen scavenging reaction on the right side (scale bar: 50  $\mu\text{m}$ ). In all images, blue indicates DAPI-stained nucleus and green represents Alexa 488 phalloidin-stained cytoskeletal F-actin. The positions of the gel scaffold and side channel are indicated in the images.**

population with the flow rate in the right side channel (Fig. 5-14(b) and (c)) is visually smaller than those without flow rate (Fig. 5-14(a) and (d)), which may indicate the detrimental effects of shear rate on cell adhesion, especially for HeLa cells. The higher flow rate (15  $\mu\text{L}/\text{min}$ ) recapitulates the shear rate in the ascending aorta and venules (Fig. 5-11(c))<sup>35</sup> and demonstrates a comparable endothelial cell migration to that in the 5  $\mu\text{L}/\text{min}$  condition (Fig. 5-12(b) and (c)). This similarity suggests that 5  $\mu\text{L}/\text{min}$  (or less) is a saturating flow rate to inhibit endothelial cell migration in this cell co-culture model. Since there is no previous evidence showing detrimental effects of shear rate on soluble factor production from cancer cells, one possible cause of this endothelial cell migration inhibition when medium is flowing in the right side channel is that soluble factors secreted by the HeLa cells may be washed away. In this circumstance, endothelial cells would receive inadequate activation signals to initiate migration. To investigate this hypothesis, we introduced medium containing 10  $\mu\text{M}$  FITC-dextran into the right side channel to simulate the soluble factors secreted by HeLa cells and observed the distance that the fluorescent molecules traveled across the gel scaffold. The images demonstrate that fluorescent molecules do not easily reach the endothelial cells in the presence of flow; the negative control fluorescence experiment (without any fluorescent molecules) demonstrates that the fluorescence intensity near the endothelial cells remains unchanged from the control condition to 24 or 48 h FITC-dextran flow (Fig. 5-15). This result implies that the soluble factors released by HeLa cells in the right side channel fail to arrive at the left side channel to initiate endothelial cell migration. In short, the application of flow in the side channels greatly decreases endothelial cell migration into

the gel scaffold even at the low shear rate level by triggering the NO signaling pathway,

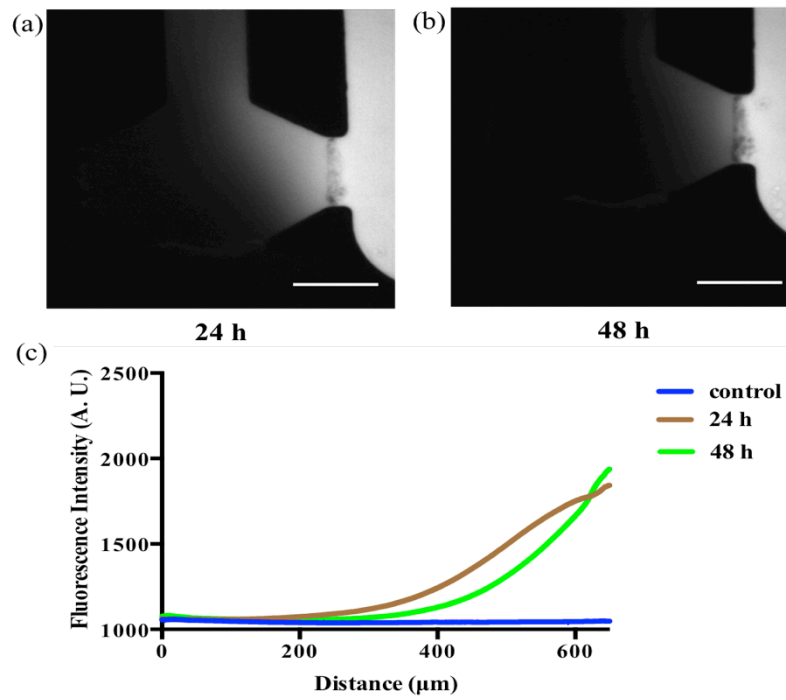


**Figure 5-15.** The cell culture medium containing 10  $\mu\text{M}$  FITC-dextran is flowed into the right side channel: (a) fluorescence image taken at 24 h (scale bar: 200  $\mu\text{m}$ ); (b) fluorescence image taken at 48 h (scale bar: 200  $\mu\text{m}$ ); and (c) the fluorescence intensity profiles across the gel scaffold for 24 h, 48 h, and the control condition without any fluorescent molecule.

the gel scaffold even at the low shear rate level by triggering the NO signaling pathway, damaging the endothelial cell layer structure, and removing soluble factors.

#### **5-3-4. The hypoxic and the combined effects**

Hypoxia is one of the major features of cancer pathogenesis that increases patient treatment resistance,<sup>46,47</sup> thus, understanding the effects of an hypoxic environment on cellular interactions between endothelial cells and HeLa cells may help to characterize mechanisms of cancer pathogenesis. To explore hypoxia effects, a pair of new chemical reaction channels was added on both sides of the previously described device to import an oxygen scavenging solution (Fig. 5-16(a) and 5-1(b)). This oxygen scavenging solution is a mixture of 1 M NaOH and 100 mg/mL pyrogallol solution where pyrogallol is known to convert into the ionic form, sensitive to oxygen, in basic conditions.<sup>35</sup> The PDMS-embedded polycarbonate sheet in this device stabilizes the low oxygen concentration across the cell co-culture chamber due to the low diffusion coefficient of oxygen in polycarbonate sheets (Fig. 5-16(b)).<sup>34</sup> This oxygen scavenging chemical reaction is known to exhibit good incubator compatibility,<sup>35</sup> allowing the oxygen calibration results obtained in ambient conditions to be applicable to the cell co-culture platform. Prior to performing oxygen calibration, it was necessary to determine the appropriate time periods for nitrogen gas and chemical reaction introduction. Preliminary results demonstrated that the fluorescence signals from the oxygen-sensitive dye across the overall device remained stable from 30 min to 24 h; the 1 h time point was chosen for further analysis to maintain high cell viability in addition to good fluorescence signal

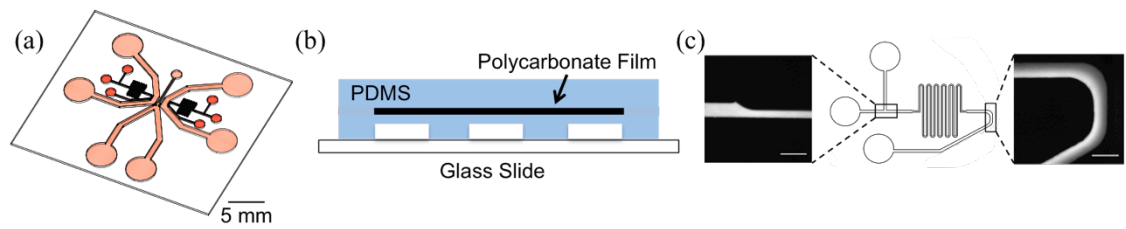


**Figure 5-16. (a) Schematic of microfluidic device used for hypoxia effects study. (b) A polycarbonate film is embedded into the PDMS layer of the hypoxia microfluidic device to decrease the oxygen permeability. (c) The fluorescence imaging shows the mixing of solution from two different inlets occurring in the chemical reaction channel. (scale bar: 200  $\mu\text{m}$ )**

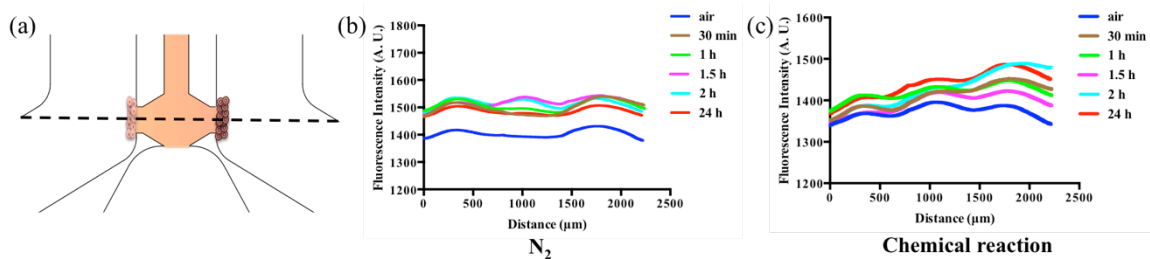


**Figure 5-17. Condition optimization for nitrogen gas and chemical reaction flowing in oxygen concentration calibration. (a) The fluorescence intensity profiles along the center line of gel scaffold across the overall device are recorded. (b) The time dependence of nitrogen gas flowing. (c) The time dependence of oxygen scavenging chemical reaction flowing.**

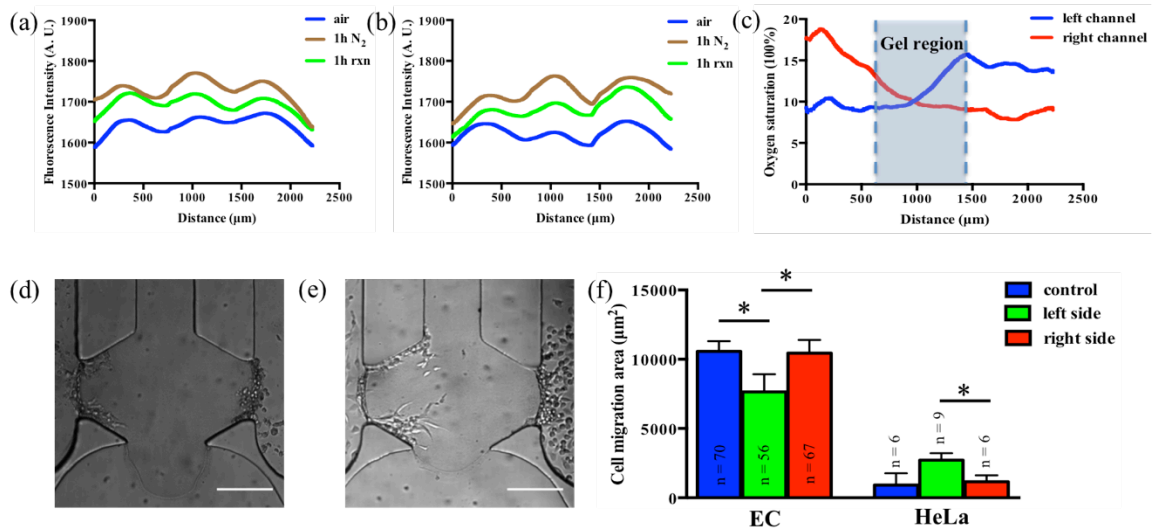


**Figure 5-18.** The effects of hypoxia on cell migration during microfluidic cell co-culture. Fluorescence intensity profiles of an oxygen-sensitive dye across the device by flowing nitrogen gas and oxygen scavenging solution into (a) the left chemical reaction channel and (b) the right chemical reaction channel (the concave parts of the fluorescence intensity profiles are due to the gel-solution interfaces). (c) Oxygen concentration profiles in the presence of the oxygen scavenging reaction; the gel region is labeled in a block. Bright-field images (scale bar: 200 μm) of cell migration after 48 h flowing with oxygen scavenging reaction in (d) the left chemical reaction channel and (e) the right chemical reaction channel. (f) Data analysis of cell migration area at 48 h time point. Three device replicates are included in each condition, and the total cell number (n) of three replicates analyzed in each condition is indicated in or above the corresponding bar, \*,  $p < 0.05$ , using a two-tailed unpaired t-test. Error bars represent standard error of the mean.

stability (Fig. 5-17). There were some fluctuations found for each fluorescence intensity line scan due to the presence of the gel scaffold, and the fluorescence intensity does not change linearly at the interface between the gel chamber and solution channel. The calculated oxygen concentration profiles reveal that an oxygen concentration gradient develops across the cell co-culture system when oxygen scavenging solution is injected, and the gradient direction is determined by the location of the chemical reaction side channel that contains the oxygen scavenging reaction (Fig. 5-18(a)-(c)). The steeper oxygen gradient can be easily found inside the gel region between two different cell types (Fig. 5-18(c)) such that each cell type experiences a distinct oxygen concentration. With this approach, the lowest oxygen saturation level achieved within this device was around 8%; although this value is still higher than the oxygen level inside solid tumors, the oxygen concentration obtained in this device is very close to the venous oxygen level reported near tumor sites<sup>48</sup> and lower than that of normal cell culture conditions, which is sufficient for creating biomimetic environments for cellular interaction studies. Cell migration studies under hypoxic conditions suggest that lower oxygen concentration on the left side of the device induces a significant reduction in endothelial cell migration compared to other conditions after 48 h incubation ( $p < 0.05$ ) while the oxygen scavenging reaction flowing on the right side does not induce any statistical difference compared to the control (Fig. 5-18(d)-(f)). The lower oxygen level on the left side appears to inhibit endothelial cell migration significantly; however, hypoxia is known to upregulate the expression of VEGF in HeLa cells that may potentially promote the migration of endothelial cells into the gel scaffold,<sup>49,50</sup> so the adverse effects of hypoxia

on endothelial cell migration is counteracted when the lower oxygen level is on the right side. Similar to the flow rate experiments, low oxygen levels on both sides of the device induce damage in the 3D endothelial cell layer structure based on confocal imaging results (Fig. 5-14); this suggests that both shear rate and hypoxic conditions may have cytotoxic effects on endothelial cell layers. Further examination of cytotoxicity in this 3D configuration will be a focus of future work.

Finally, all three physiological factors investigated separately, including chemical gradients, flow rate, and hypoxia, were combined together into a single device to investigate cell-cell communication in a complex biomimetic environment. In the physiological microenvironment, cancer cells act as the primary source of cytokine molecules (so, in this case, they are delivered from the right to the left channel)<sup>51,52</sup> while flow is introduced into the endothelial cell channel to mimic blood vessel effects; finally, lower oxygen concentration is localized around the HeLa cancer cells. To be specific, 50 ng/mL IL-8 solution was placed in the large reservoirs of right side channel, and the oxygen scavenging solution was continuously injected through the right chemical reaction channel while cell culture medium was flowed through the left side channel. As shown in Fig. 5-19(a), the flow rate in the left side channel did not disrupt the fluorescence gradient profile across the gel scaffold originating from the right side channel after 48 h diffusion, which means that the IL-8 gradient is also available in the combined effects condition. With 48 h cell co-culture, a significant difference in endothelial cell migration area was discovered between the control and the combined effects condition ( $p < 0.05$ , Fig. 5-19(b) and (c)). This migration area decrease is

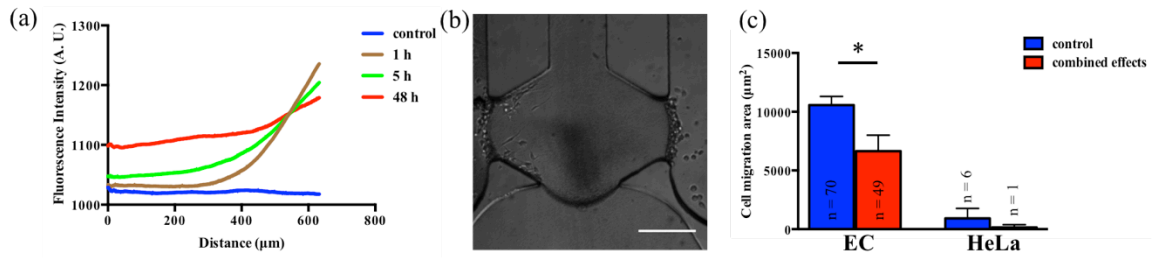


**Figure 5-19.** The combined effects of three different physiological factors on cell migration. (a) Fluorescence gradient profiles across the gel scaffold with the flow rate in left channel. (b) Bright-field image (scale bar: 200 μm) of cell migration after 48 h co-culturing with combined effects: 50 ng/mL IL-8 in right channel, 5 μL/min cell culture medium flowing in the left channel, and oxygen scavenging reaction injected continuously on the right side. (c) Data analysis of cell migration area at the 48 h time point. Three device replicates are included in each condition, and the total cell number (n) of three replicates analyzed in each condition is indicated in or above the corresponding bar, \*,  $p < 0.05$ , using a two-tailed unpaired t-test. Error bars represent standard error of the mean.

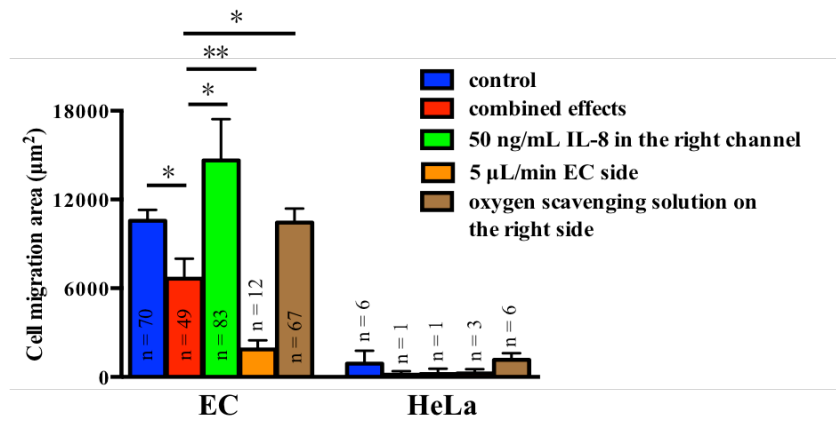


**Figure 5-20. Comparison of cell migration data in various conditions at the 48 h time point. Three replicates are included in each condition, and the total cell number (n) of three replicates analyzed in each condition is indicated for the corresponding bar, \*,  $p < 0.05$ , \*\*,  $p < 0.005$ , using a two-tailed unpaired t-test. Error bars represent standard error of the mean.**

attributable to the collective impact of three different factors since the flow rate tends to suppress endothelial cell migration significantly but a positive chemical gradient for endothelial cells and hypoxia around the cancer cells are able to maintain an endothelial cell migration area similar to that of the control condition. Finally, this combined experiment results in significant promotion of endothelial cell migration compared to the simple flow condition, while the cell migration data in the positive gradient and hypoxia conditions are still statistically higher than that of the combined effects ( $p < 0.05$ , Fig. 5-20).

#### **5-4. Conclusion**

A microfluidic cell co-culture system containing biomimetic microenvironments was established to explore cellular interactions between endothelial cells and HeLa cells. To create a biomimetic cell co-culture model, different types of cells were patterned on opposite side walls of a gel scaffold with high spatiotemporal resolution, and following that, multiple essential physiological factors were introduced into the developed cell co-culture model for further mechanistic study. HeLa cells, used as the cancer cell model in this work, release VEGF molecules that can induce endothelial cell migration into the gel scaffold, but HeLa cells themselves are not induced to detach from their original position. The application of cytokine chemical gradients suggests a polarization-influenced regulation of endothelial cell migration where negative gradients draw endothelial cells away from the HeLa cells and positive gradients had additive effects to promote endothelial cell migration. Flow with a shear rate similar to that found in blood vessels

significantly inhibited endothelial cell migration towards the cancer cells. When the oxygen scavenging reaction was integrated into the cell co-culture system to decrease the oxygen levels across the overall device, endothelial cell migration was dependent on the delicate balance between the adverse effects caused by low oxygen concentration and the enhancing function of high VEGF secretion. Finally, all three physiological factors were introduced into the same device to examine the combined effects among the various factors. In summary, this work presents a versatile microfluidic platform to investigate cell-cell communication important in cancer metastasis, aiming to provide deeper mechanistic perspective about this physiological process and also promote extension of this microfluidic model for other heterotypic cellular interaction studies.

## **Chapter 6**

### **Platelet and Neutrophil Adhesion Study Using Microfluidic System**

**Adapted from:**

**Wu, X.; Haynes, C. L., 2016, *in preparation*.**

## 6-1. Introduction

Neutrophils and platelets, known as the predominant cell types in the human circulatory system, interact with each other during critical physiological events.<sup>1,2</sup> As the major type of white blood cells, neutrophils play an important role in host defense and have critical functions in the pathogenesis of various diseases. Following the specific profiles of chemical gradients, neutrophils transmigrate through the endothelial cell layer lining blood vessel walls to arrive at inflammatory sites and then secrete biological molecules that can mediate immune response.<sup>3-5</sup> Interactions with endothelial cells and other surrounding blood cells may have profound impacts on neutrophil migration by influencing the kinetics or affinity of neutrophil adhesion on the endothelial cell layer, one of the key steps involved in the whole migration process. Platelets are bloodborne anuclear fragments of bone marrow megakaryocytes containing multiple chemical messenger-containing granules. Secretion from these granules releases adhesion molecules, plasma proteins, and small non-protein molecules (ADP, ATP, serotonin, etc.). Through these secretion events, platelets play important physiological roles in modulating inflammation and hemostasis both directly and through interactions with other blood cells.<sup>6-8</sup> Adhesion of platelets to endothelial cells is clearly important;<sup>9-14</sup> however, the molecular details of this interaction are not well characterized. More importantly, these two cell types, as well as others in the blood stream, are constantly exposed to dynamic shear rates induced by blood flow, ranging from  $<1000 \text{ s}^{-1}$  -  $10000 \text{ s}^{-1}$  in normal to disease conditions.<sup>15-17</sup> This work aims to characterize the effects of various

shear rates on neutrophil and platelet adhesion to provide mechanistic insight into the pathogenesis of disease conditions such as thrombosis.

To create physiologically relevant shear rates for cell adhesion studies in this work, microfluidic channels with different dimensions were fabricated. Microfluidics fabrication techniques make it straightforward to adjust the channel dimensions to mimic blood vessels such that higher shear rate level in disease conditions can be produced within narrower channels. Microfluidics also offers the ability to control flow spatially and temporally by using external perfusion pumps, which also allows for high measurement replicate numbers and the use of small volumes of blood. The combination of polydimethylsiloxane (PDMS) and glass slides as the device fabrication materials provides a defined and biocompatible surface for the endothelial cell layer to explore platelet and neutrophil adhesion.<sup>18</sup> In addition, the optically transparent surface of the PDMS facilitates in situ multicolor imaging of different cell types in microfluidic channels, which is helpful for quantification of cell adhesion behaviors.

Herein, endothelial cells were cultured on the bottom glass surface of a microfluidic channel to mimic the human blood vessel. Microchannel regions with different widths were designed to develop a wide range of shear rates (from  $1000 \text{ s}^{-1}$  to  $10000 \text{ s}^{-1}$ ). First, platelets with or without pre-activation are injected through the channels to achieve platelet adhesion on the cultured endothelial cell layer, and then neutrophils are introduced into the system to examine the effects of platelet-neutrophil interactions on neutrophil adhesion. A series of antibody studies aiming to reveal molecular-level details

about platelet-neutrophil interactions were conducted, offering novel insight on the relationship between shear rate levels and cell adhesion behaviors.

## **6-2. Experimental details**

### **6-2-1. Device fabrication**

Straight microfluidic channels with different narrow regions were fabricated using standard photolithography methods. First, the channel design was transferred onto a chrome photomask plate coated with positive photoresist layer (Nanofilm, Westlake Village, CA) through UV exposure. This photomask plate was then utilized for making a microfluidic device mold on a 4-inch silicon wafer with 120- $\mu\text{m}$ -thick negative SU-8 50 photoresist (MicroChem, Newton, MA) coating. Following the UV exposure and baking steps, the channel patterns were imprinted on the silicon wafer and the excessive photoresist was removed using SU-8 developer solution (MicroChem, Newton, MA). A 10:1 mass ratio mixture of polydimethylsiloxane (PDMS) prepolymer (Ellsworth Adhesives, Germantown, WI) was poured onto the prepared SU-8 mold and cured on a hot plate at 95 °C overnight. The inlets and outlets were punched at appropriate locations using 1 mm disposable biopsy punches (Integra Miltex, Plainsboro, NJ). Finally, the PDMS layer was cut and then bonded to a glass slide in an oxygen plasma chamber for 10 seconds at 100 L/h oxygen flow rate and 100 W.

### **6-2-2. Cell culture and isolation**

Human endothelial cells (hy926) were purchased from American Type Culture Collection (ATCC, Manassas, VA) and stored in a liquid nitrogen storage container (MVE XC33/22, Select Genetics, Washington, PA). Upon thawing, endothelial cells were added into 75 cm<sup>2</sup> flasks containing 20 mL of Dulbecco's Modified Eagle Medium (DMEM, formula: 4mM L-glutamine, 4.5 g/L L-glucose, and 1.5 g/L sodium pyruvate, Gibco, Carlsbad, CA) supplemented with 10% fetal bovine serum and 1% penicillin and streptomycin (Sigma-Aldrich, St. Louis, MO). Cells were fed every two or three days; when necessary, cells were detached using 1× trypsin solution (Sigma-Aldrich, St. Louis, MO) for device injection. Cells were only used between the third and tenth passages.

For each microfluidic channel, platelets and neutrophils were isolated from the blood sample of the same donor. Neutrophils were isolated from freshly drawn human blood samples prepared by Memorial Blood Center (St. Paul, MN). Briefly, through layering the blood sample on the same volume of mono-poly resolving medium (Fisher Scientific, Waltham, MA), a distinct neutrophil band was obtained after density gradient centrifugation. Neutrophils were washed using 2.5 mL of red blood cell lysis buffer (Miltenyi Biotec Inc., Auburn, CA) several times until only white cells were seen at the bottom of centrifuge tube. Finally, neutrophils were re-suspended in HBSS buffer containing 2% HSA at an appropriate cell density. To easily visualize neutrophils in the microfluidic channel, isolation neutrophils were labeled with 5 µg/mL 4', 6-diamidino-2-phenylindole (DAPI, Invitrogen, Carlsbad, CA) in the dark for 30 min.

For the platelet isolation, about 5 mL of blood sample was transferred into a 15 mL centrifuge tube, and centrifuged at 270xg for 20 min without brake. Then, the top two-

thirds of the platelet rich plasma (PRP) layer were transferred into a new centrifuge tube. Hirudin (Sigma-Aldrich, St. Louis, MO) was added at a concentration of 10 U/mL, and then the PRP was again centrifuged at 800xg for 10 min with low brake. The platelet poor plasma (PPP) was removed and the pellet was re-suspended into Tyrode's buffer. The PRP was placed in the incubator for 30 min, and then centrifuged again at 800 xg for 10 min with low brake after adding ACD buffer. The formed pellet was again re-suspended in Tyrode's buffer and the platelets were kept in the incubator again for 30 min for rest prior to being incubated with 2  $\mu$ M 5-chloromethylfluorescein (CMFDA, Invitrogen, Carlsbad, CA) dye for 30 min so that platelets adhered onto endothelial cells could be fluorescently monitored. CMFDA is the dye designed to freely pass through cell membranes; however, once inside the cell are transformed into cell-impermeant products.

### **6-2-3. Endothelial cell coating of a microfluidic channel**

First, 250  $\mu$ g/mL of human fibronectin (Sigma-Aldrich, St. Louis, MO) in sterilized Milli-Q water was injected through the channel, and the device was incubated under 5% CO<sub>2</sub> at 37°C for an hour. Meanwhile, endothelial cells were treated with trypsin and detached from the T-flask. After centrifugation, fibronectin solution was removed from each channel and the obtained cell pellet was re-suspended into cell culture medium with the desired cell density ( $5-8 \times 10^6$  cells/mL). The cell suspension was injected through the channel, and the device was kept in the incubator. After an initial 2 h incubation, the medium was exchanged to remove non-adherent cells, and the endothelial cells in the channel were fed once every day. Cells were cultured in the device for a minimum of 4

days and maximum of 6 days to ensure that endothelial cells covered the entire channel surface.

#### **6-2-4. Cell injection experiments**

First, platelets with CMFDA labeling (around  $1 \times 10^7$  cells/mL) were injected into the endothelial cell-coated channels at 5  $\mu$ L/min for 30 min. In the conditions of platelet activation, platelets were activated by 5  $\mu$ M adenosine diphosphate (ADP, Sigma-Aldrich, St. Louis, MO), and the cells were injected into the channel immediately after ADP addition. Tyrode's buffer was introduced into the channel at the same flow rate for 15 min to remove non-adherent platelets. Following this, neutrophils without pre-activation ( $3-4 \times 10^6$  cells/mL) were injected at 5  $\mu$ L/min for 30 min to achieve neutrophil adhesion in the presence of platelets on the endothelial cell layer, and HBSS buffer was then flowed for 15 min to wash non-adherent cells. Finally, different regions of each channel (called as up normal, inlet, narrow, outlet, and down normal) were imaged using MetaMorph ver. 7.7.5 imaging software on an inverted microscope equipped with a 40x objective and a CCD camera (QuantEM Photometrics, Tucson, AZ). The platelet number per 10 endothelial cells was used for statistical analysis. To examine the functions of surface receptor molecules in cell adhesion behaviors, the corresponding antibody molecules were incubated with platelets or neutrophils prior to the cell injection. ADP-activated platelets were mixed with anti-human p-selectin (eBioscience, San Diego, CA) and anti-human CD41/61 (BioLegend, San Diego, CA) for 5 min before injection. Neutrophils were activated by 50 ng/mL interleukin-8 (IL-8) first and then mixed with

anti-human CD11b APC (eBioscience, San Diego, CA) for 5 min before injection. Each cell injection condition was done in 5 biological replicates (from 5 different donors) unless otherwise specified.

#### **6-2-5. Surface adhesion molecule expression of endothelial cells**

The expression of adhesion molecules on the surface of endothelial cells under the influence of various shear rate levels was detected using fluorescence imaging. Endothelial cells were pre-activated by the flow rate (5  $\mu\text{L}/\text{min}$ ) for 30 min, and a mixture of allophycocyanin (APC)-labeled anti-human ICAM-1 (eBioscience) and fluorescein isothiocyanate (FITC)-labeled anti-human von-Willebrand factor (Abcam) was injected through the channel for 15 min to incubate with endothelial cells. After another 30 min incubation with endothelial cells in the static condition, excess fluorescent labeling reagents were removed by flow. The control condition was conducted without endothelial cell pre-activation by the flow rate. Again, different regions of each channel were imaged using MetaMorph ver. 7.7.5 imaging software on an inverted microscope equipped with a 40x objective and a CCD camera. The average gray value of each region before shear activation was recorded as the background signal. Five different microfluidic channels were measured in each condition.

#### **6-2-6. The effects of flow rate on platelet and neutrophil aggregation**

Platelets with or without ADP pre-activation were injected through different microfluidic channels without an endothelial cell layer cultured on the bottom. Platelet suspension

coming out from the outlet was collected using a pipette. For each microfluidic channel, 20  $\mu\text{L}$  of collected platelet suspension was added on the coverslip for fluorescence imaging to count the number of platelet aggregates, and this step was replicated three times (60  $\mu\text{L}$  in all for each channel). The same protocol was used for neutrophil aggregate counting.

### **6-3. Results and discussion**

#### **6-3-1. Characterization of the microfluidic system**

As shown in Fig. 6-1(a), there are three different narrow dimensions created in the microfluidic channels: 20%, 50%, and 80% narrow channels. Since the width of normal part of each channel is 400  $\mu\text{m}$ , 20%, 50%, and 80% narrow channels have the widths of 320  $\mu\text{m}$ , 200  $\mu\text{m}$ , and 80  $\mu\text{m}$ , respectively. To make the shear rate level change gradually in the microfluidic channels, the inlet and outlet regions were designed to connect the narrow region and normal channel part (Fig. 6-1(a)). In our experiments, we focus on studying cell adhesion in the regions with shear rate change, so the normal channel part connecting to the inlet region is defined as “up normal” while the inlet part connecting to the narrow region is defined as “inlet”. The “down normal” and “outlet” parts are defined as the same way. The central part of the narrow region is selected for cell adhesion study. Cell adhesion in five different parts (up normal, inlet, narrow part, outlet, and down normal) was examined by randomly imaging a small part (204.8  $\mu\text{m} \times 204.8 \mu\text{m}$ ) in each region. The COMSOL simulation results (Fig. 6-1(b)) clearly indicated that the shear rate

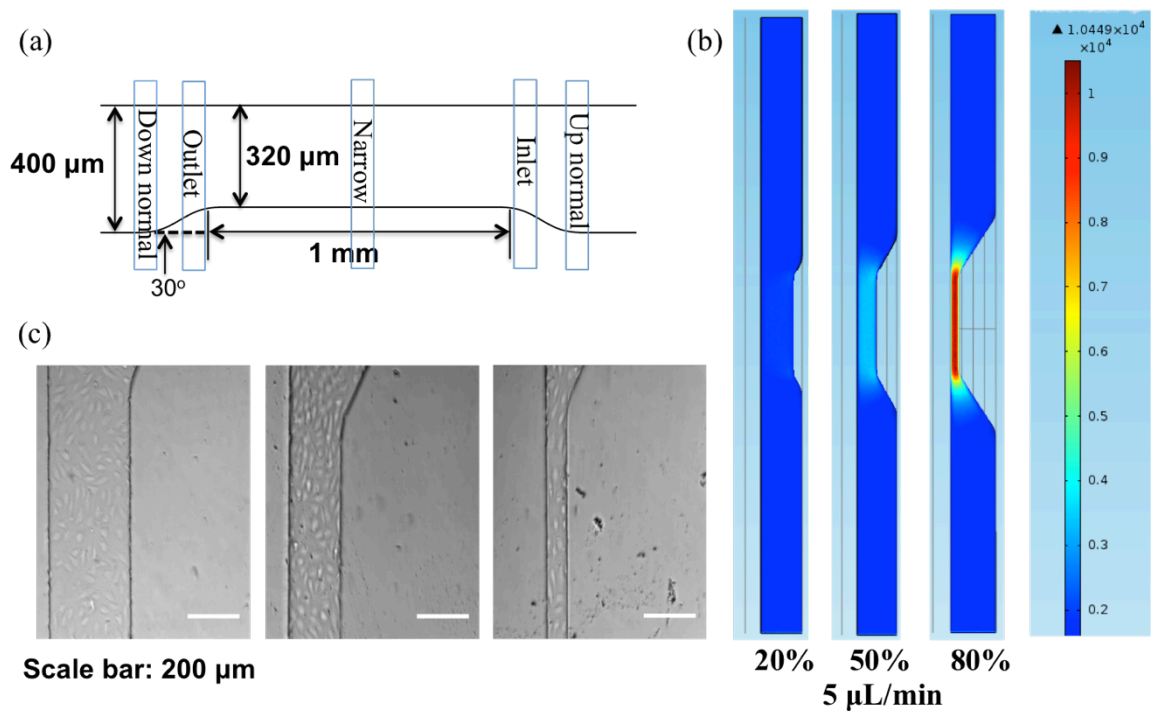


**Figure 6-1. (a) The schematic of 20% narrow channel (The width of microfluidic channel is 400 μm and the narrow region is 320 μm wide, 1 mm long.). Five different parts (up normal, inlet, narrow, outlet, and down normal) for cell adhesion study are indicated in the blue boxes. (b) COMSOL simulation results of microfluidic channels with different dimensions. (c) Bright-field images of endothelial cell layer formation on the bottom of different microfluidic channels after 5-day culture.**

inside different microfluidic channels induced by 5  $\mu\text{L}/\text{min}$  flow rate is correlated to the width of the channel, which suggests that the smaller dimension results in the higher shear rate. The shear rates created in different microfluidic channels range from those relevant in normal physiological conditions to those in a thrombotic disease microenvironment (from  $<1000 \text{ s}^{-1}$  to  $>10000 \text{ s}^{-1}$ ). After 5-day cell culturing on the bottom of the device, endothelial cells formed a layered structure in different microfluidic channels (Fig. 6-1(c)), and the layered structure was visually intact and confluent. With this microfluidic system, platelet and neutrophil adhesion behaviors were studied separately.

### **6-3-2. Platelet adhesion**

There are three factors impacting platelet adhesion in our system: endothelial cell surface molecule expression, ADP pre-activation of platelets, and the effects of shear rate on platelet activation. The receptor for von-Willebrand factor (vWF) on the surface of endothelial cells is responsible for initiating platelet adhesion.<sup>9,19,20</sup> A detailed examination of the relationship between shear rate and vWF expression was conducted to determine the effects of surface adhesion molecule expression on platelet adhesion. The antibody imaging results (Fig. 6-2) showed that although different shear rate levels (20%, 50%, and 80% narrow channel condition) increase the average fluorescence intensity in each condition compared to the control condition without shear rate activation, there was no significant difference found among various shear rate levels and channel regions. These results suggest that the expression of vWF on endothelial cells was not dependent

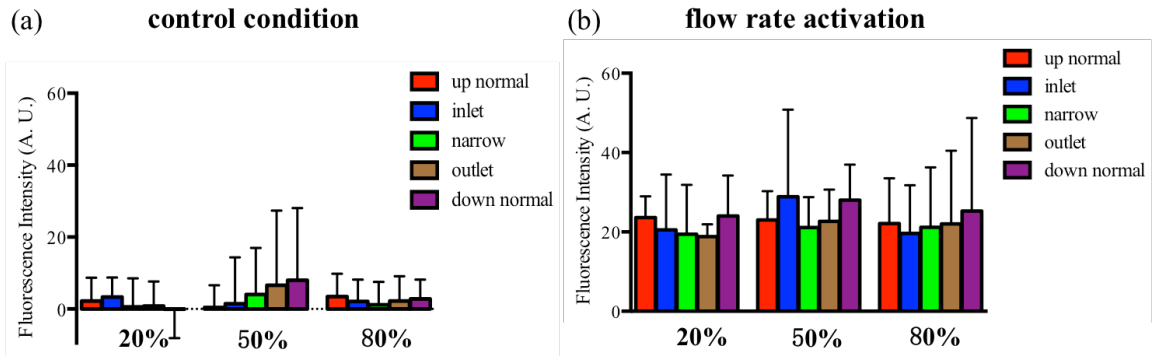
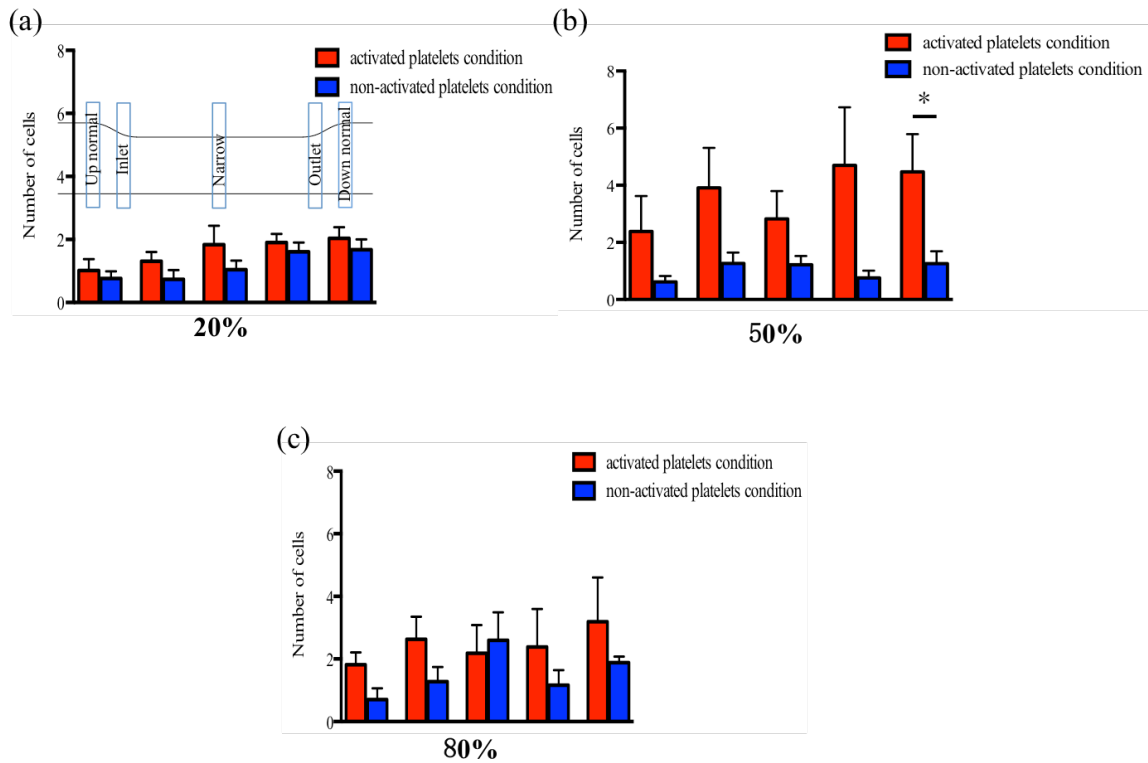


**Figure 6-2. The fluorescence intensities of vWF antibody binding on endothelial cell surfaces under control and flow rate activation conditions. (a) The expression of vWF in different microfluidic channels under control condition without shear rate activation. (b) The expression of vWF in different microfluidic channels under flow rate activation condition. Five different replicates (channels) are included in each condition. Error bars represent standard error of the mean.**

on the changes in shear rate levels; even the lower shear rate level existing in the widest channel (20% narrow channel) was able to enhance the expression of the vWF receptor on endothelial cells. Considering the effects of ADP pre-activation on platelet adhesion, the platelet numbers in different regions of microfluidic channels were counted, and the platelet number per 10 endothelial cells was used for statistical analysis. In almost all the conditions (Fig. 6-3), ADP pre-activation did not induce significantly more platelets adhering to the endothelial cell layer compared to the non-activated condition; this may be attributable to the fact that the introduction of shear rate promoted the expression of vWF to a similar level for all the dimensions and ADP pre-activation is not important in further helping platelet adhesion. Another critical factor examined here is the effects of shear rate on platelet activation. Aggregation of platelets is one important signal indicating activation of platelets.<sup>21-23</sup> By counting the number of platelet aggregates after flowing cells through different microfluidic channels (Fig. 6-5 and 6-6), we found that 20% and 50% narrow channels up-regulated the activation of platelets without ADP pre-activation (Fig. 6-4) and the numbers of platelet aggregates in these two conditions are much higher than those of control condition (no shear rate activation). However, for the condition with ADP pre-activation, shear rate was not capable of inducing significantly higher activation of platelets, which implies that shear rate activation does not contribute to promoting platelet adhesion in the presence of ADP pre-activation. There was no significant enhancement found in the number of platelet aggregates for the 80% narrow channel without ADP pre-activation, likely because the high flow speed of platelets and short dwell time in the microfluidic channel did not induce platelet activation to a **Figure**



**6-3. The effects of ADP pre-activation on platelet adhesion on an endothelial cell layer. (a) The results of platelet adhesion in different regions of 20% narrow channel. (b) The results of platelet adhesion in different regions of 50% narrow channel. (c) The results of platelet adhesion in different regions of 80% narrow channel. For all graphs, the columns from left to right represent up normal, inlet, narrow, outlet, and down normal, respectively (indicated in (a)). Platelets from five different donors were used in each condition for data analysis, \*,  $p < 0.05$ , using a two-tailed unpaired t-test. Error bars represent standard error of the mean.**

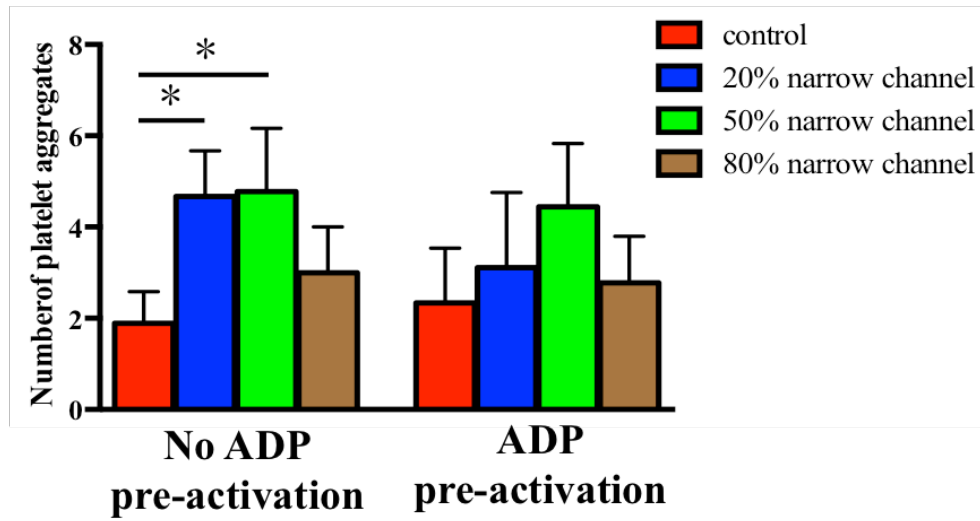


**Figure 6-4. The effects of shear rate levels on platelet aggregation. Platelets with or without ADP pre-activation were injected through 20%, 50%, and 80% channels, respectively. The control condition represents the platelets without channel injection and five different channels were included in each condition. \*,  $p < 0.05$ , using a two-tailed unpaired t-test. Error bars represent standard error of the mean.**

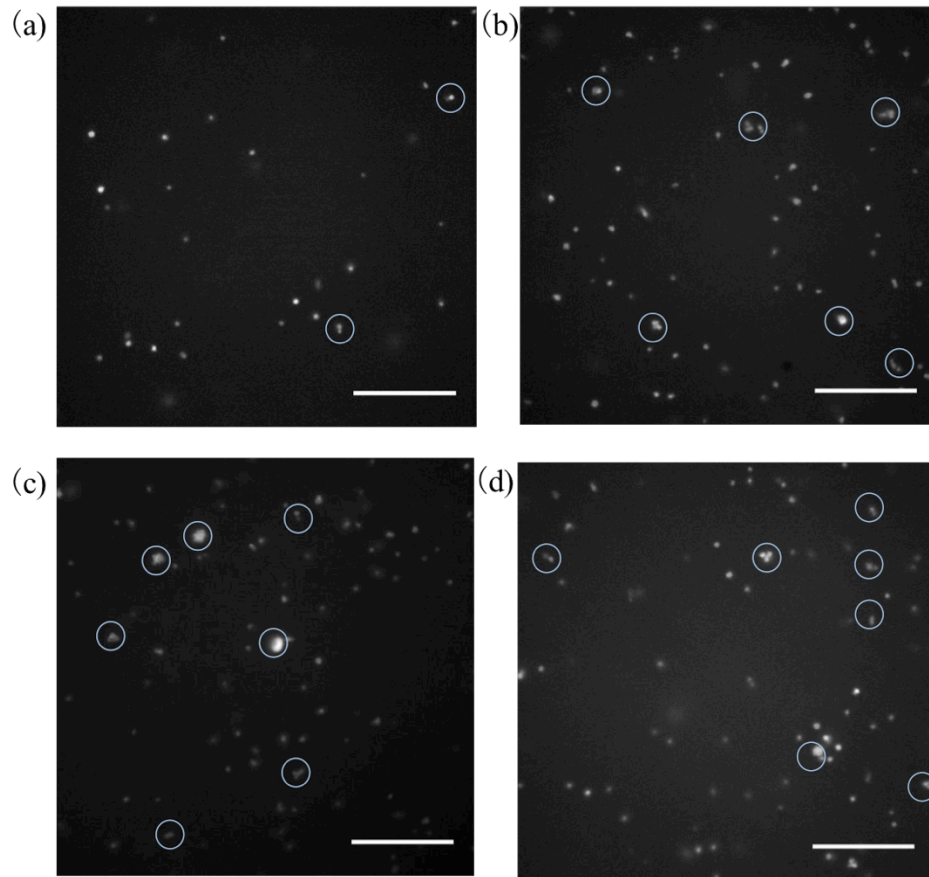


**Figure 6-5. The aggregation of platelets without ADP pre-activation after flowing through different microfluidic channels: (a) control condition without flowing through the channel; (b) flowing through 20% narrow channel; (c) flowing through 50% narrow channel and (d) flowing through 80% narrow channel. Platelets are labeled with CMFDA, and the aggregates are indicated in the blue circles. (scale bar: 50  $\mu\text{m}$ )**

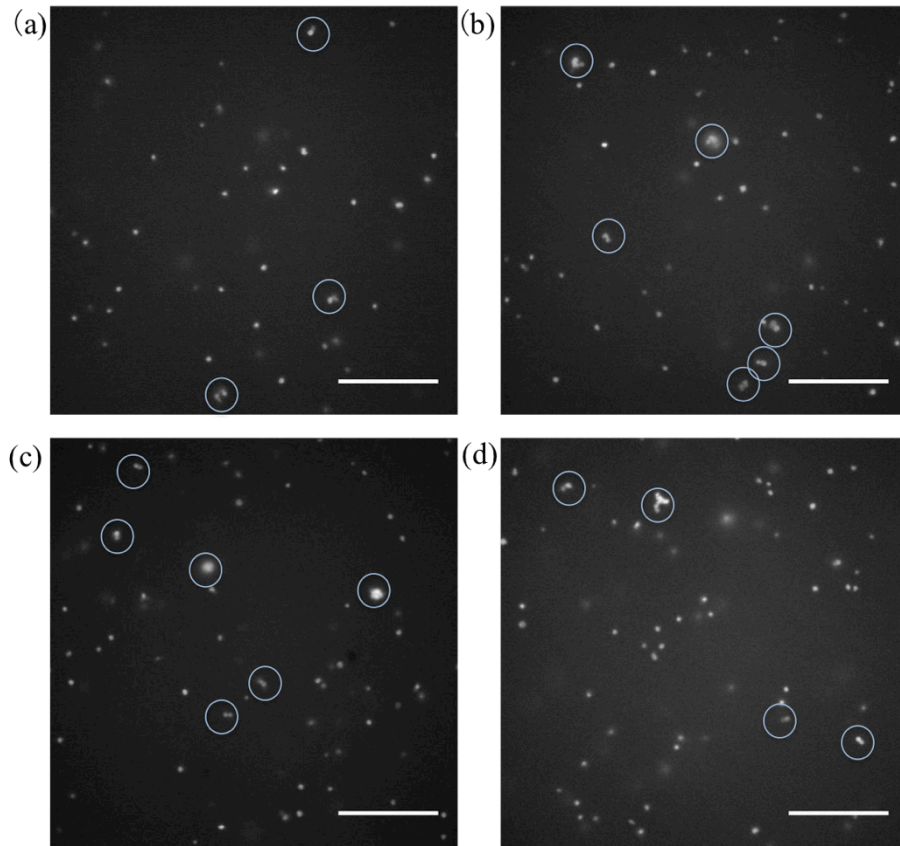


**Figure 6-6. The aggregation of platelets with ADP pre-activation after flowing through different microfluidic channels: (a) control condition without flowing through the channel; (b) flowing through 20% narrow channel; (c) flowing through 50% narrow channel and (d) flowing through 80% narrow channel. Platelets are labeled with CMFDA, and the aggregates are indicated in the blue circles. (scale bar: 50  $\mu\text{m}$ )**

significantly higher level. Based on the results above, we can conclude that ADP pre-activation is not important in enhancing platelet adhesion since both vWF receptor expression on the endothelial cell surface and shear rate level in the microfluidic channel are able to initiate adhesion of platelets on the endothelial cell layer.

### **6-3-3. Neutrophil adhesion**

Similar to platelet adhesion, there are several factors impacting neutrophil adhesion in our system. Since neutrophils were injected after the platelet adhesion and the neutrophils did not have any pre-activation, the factors impacting neutrophil adhesion include surface adhesion molecule expression of endothelial cells, shear rate activation, and the interactions between platelets and neutrophils. In this section, we will focus on the surface molecule expression and shear rate activation while the cellular interactions will be discussed in the next section. ICAM-1 plays the important role in initiating neutrophil adhesion on an endothelial cell surface,<sup>24-26</sup> and the expression of ICAM-1 molecules on the surface of endothelial cells was monitored using an antibody-facilitated imaging method (Fig. 6-7). Similar to the results of vWF expression, in the presence shear rate, the average fluorescence intensity of ICAM-1 antibody for each condition is higher than that of the control condition without shear rate; however, the introduction of shear rate gave comparable results of ICAM-1 expression for three different microfluidic channels, and different regions in each channel cannot be discriminated. The effects of shear rate on neutrophil aggregation were also determined using the same method used for the platelet aggregation study. Compared to the control condition without shear rate

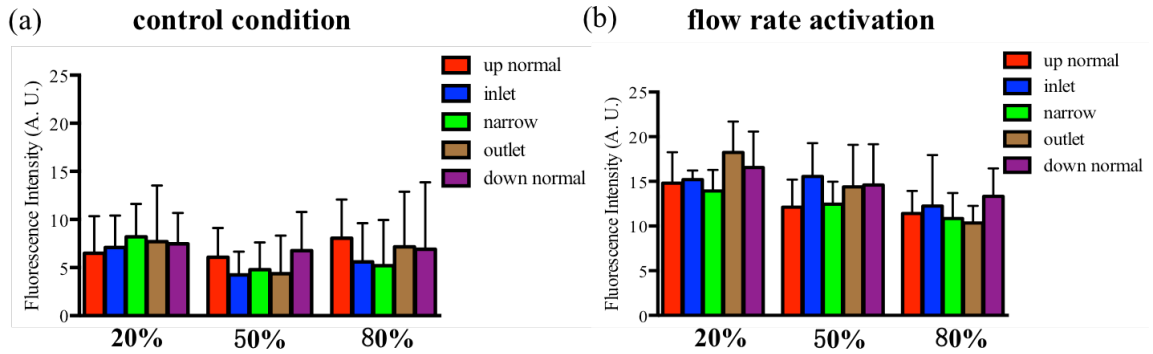


**Figure 6-7. The fluorescence intensities resulting from ICAM-1 antibody binding on endothelial cell surface under control and flow rate activation conditions. (a) The expression of ICAM-1 in different microfluidic channels under control condition without shear rate activation. (b) The expression of ICAM-1 in different microfluidic channels under flow rate activation condition. Five different replicates (channels) are included in each condition. Error bars represent standard error of the mean.**

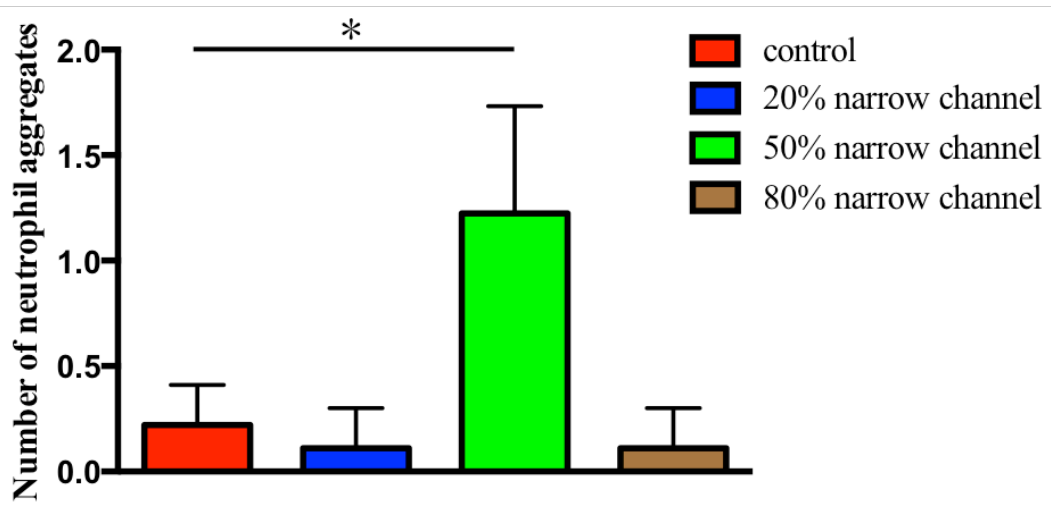


**Figure 6-8. The effects of shear rate levels on neutrophil aggregation. Neutrophils were injected through 20%, 50%, and 80% channels. Control condition represents the neutrophils without channel injection, and five different channels were included in each condition. \*,  $p < 0.05$ , using a two-tailed unpaired t-test. Error bars represent standard error of the mean.**

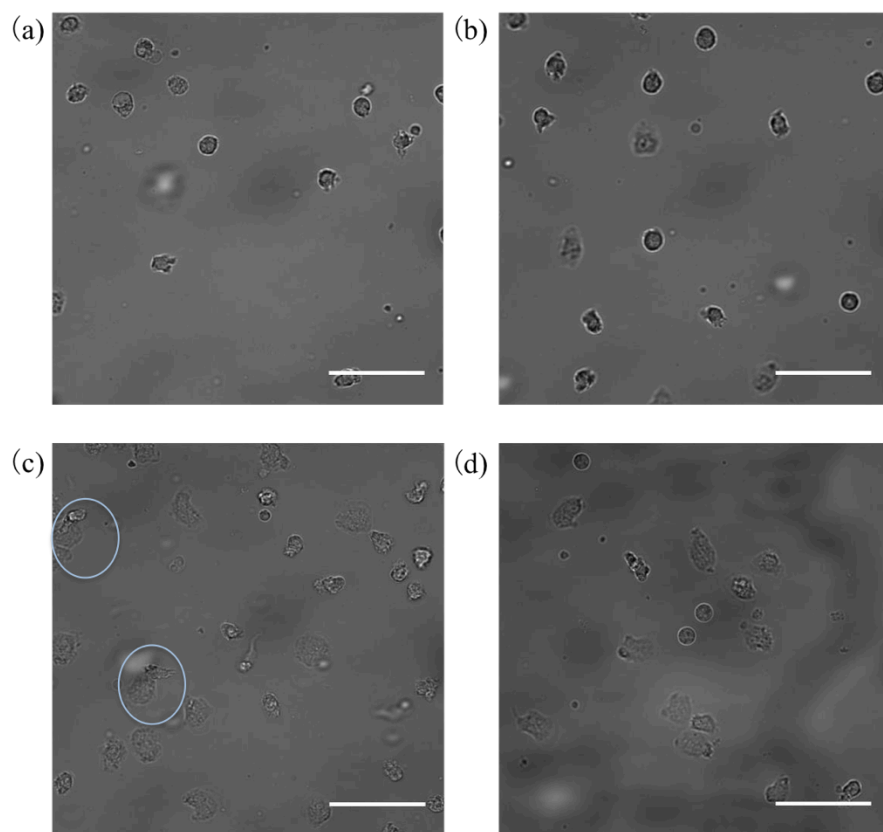


**Figure 6-9. The aggregation of neutrophils after flowing through different microfluidic channels: (a) control condition without flowing through the channel; (b) flowing through 20% narrow channel; (c) flowing through 50% narrow channel and (d) flowing through 80% narrow channel. The aggregates are indicated in the blue circles. (scale bar: 50  $\mu\text{m}$ )**

activation (Fig. 6-8 and 6-9), a significant difference was only found for 50% narrow channel, which suggests the possibility that the aggregation of neutrophils was selective for the dimensions of that microfluidic channel. Lower shear rate in the wider channel (20% narrow channel) was not large enough to induce the neutrophil aggregation while the dwell time of neutrophils in the microfluidic channel with a larger shear rate (80% narrow channel) was too short for activation.

#### **6-3-4. The interactions between neutrophils and platelets**

To investigate the effects of platelet-neutrophil interactions on neutrophil adhesion, neutrophils were injected into the microfluidic channels following the platelet adhesion. The initial results (Fig. 6-10) showed that the ADP pre-activation of platelets significantly enhanced the numbers of neutrophils adhering to the endothelial cell layer in 50% narrow channel, mainly in the narrow, outlet, and down normal regions. This is probably because that neutrophil adhesion requires significant dwell time in the microfluidic channel, so there was no statistical difference found in up normal and inlet regions. Interestingly, less significant promotion of neutrophil adhesion was obtained in the 20% and 80% narrow channels, which may be due to the fact that only the shear rate produced in the 50% microfluidic channel greatly improved the activation level of neutrophils, and thus, activated neutrophils have more opportunities to interact with the platelets or endothelial cells. Also, platelet activation plays an important role in the process of neutrophil adhesion, and activation of only neutrophils is not sufficient to significantly improve neutrophil adhesion. To clarify the role of platelet activation in

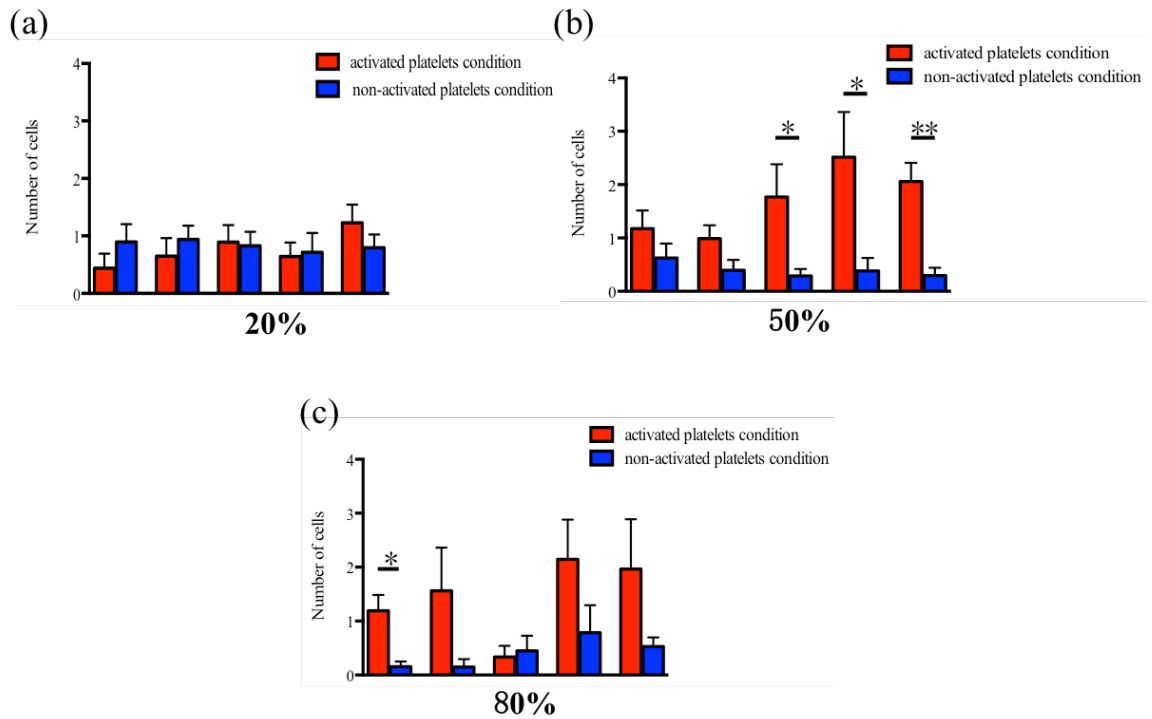


**Figure 6-10. The results of neutrophil adhesion on the endothelial cell layer. (a) The results of neutrophil adhesion in different regions of 20% narrow channel. (b) The results of neutrophil adhesion in different regions of 50% narrow channel. (c) The results of neutrophil adhesion in different regions of 80% narrow channel. For all graphs, the columns from left to right represent up normal, inlet, narrow, outlet, and down normal part, respectively (indicated in Fig. 6-3(a)). Neutrophils from five different donors were used in each condition for data analysis, \*,  $p < 0.05$ , using a two-tailed unpaired t-test. Error bars represent standard error of the mean.**

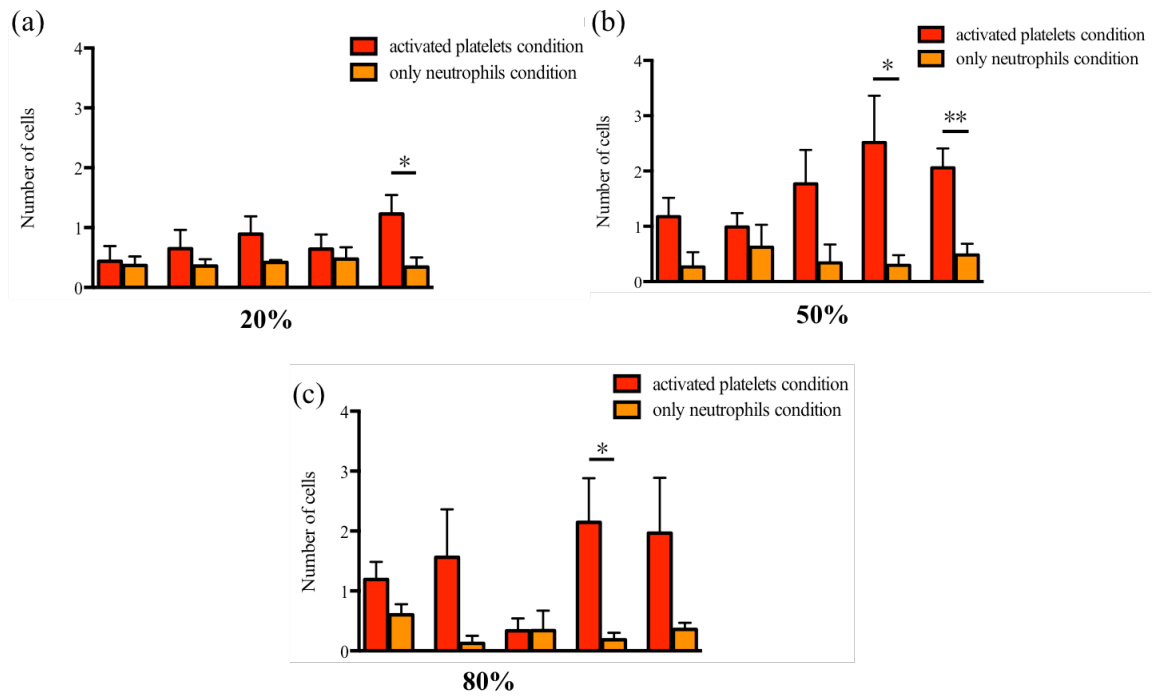


**Figure 6-11. The results of neutrophil adhesion on the endothelial cell layer with or without activated platelets. (a) The results of neutrophil adhesion in different regions of 20% narrow channel. (b) The results of neutrophil adhesion in different regions of 50% narrow channel. (c) The results of neutrophil adhesion in different regions of 80% narrow channel. For all the graphs, the columns from left to right represent up normal, inlet, narrow, outlet, and down normal part, respectively (indicated in Fig. 6-3(a)). Neutrophils from five different donors were used in each condition for data analysis, \*,  $p < 0.05$ , \*\*,  $p < 0.005$ , using a two-tailed unpaired t-test. Error bars represent standard error of the mean.**

the neutrophil adhesion process, neutrophil adhesion on the endothelial cell layer without platelet injection was studied. The results (Fig. 6-11) clearly showed that the absence of activated platelets down-regulated the neutrophil adhesion, especially in the 50% narrow channel, which suggests that both platelet and neutrophil activation are important in triggering neutrophil adhesion. Although previous results indicate that there was no apparent difference between platelets with or without ADP pre-activation for platelet adhesion, ADP activation should have positive effects in regulating neutrophil adhesion, which need to be further investigated in the future.

The next question to be explored is what types of surface receptor molecules are involved in platelet-neutrophil interactions in our microfluidic system. First, two types of receptor molecules on the surface of platelets, p-selectin and CD41/CD61 were chosen as the target molecules for mechanistic studies.<sup>27-30</sup> By incubating platelets with the corresponding antibody molecules prior to the injection, we found that p-selectin may participate in the process of platelet adhesion (Fig. 6-12 (a)-(c)) since there are significant differences found in 50% and 80% narrow channels by comparing the APD pre-activated conditions and p-selectin antibody conditions. For neutrophil adhesion, statistical differences were gleaned mainly in the 50% narrow channel (Fig. 6-12 (d)-(f)), which suggests that p-selectin is involved in the interactions between platelets and neutrophils. The blocking of p-selectin on the surface of platelets significantly decreased the number of neutrophils adhering to the endothelial cell layer, and p-selectin likely functions as the receptor molecule initiating neutrophil adhesion. On the other hand, CD41/CD61 is not as deeply involved in the platelet-neutrophil interactions as p-selectin since the only

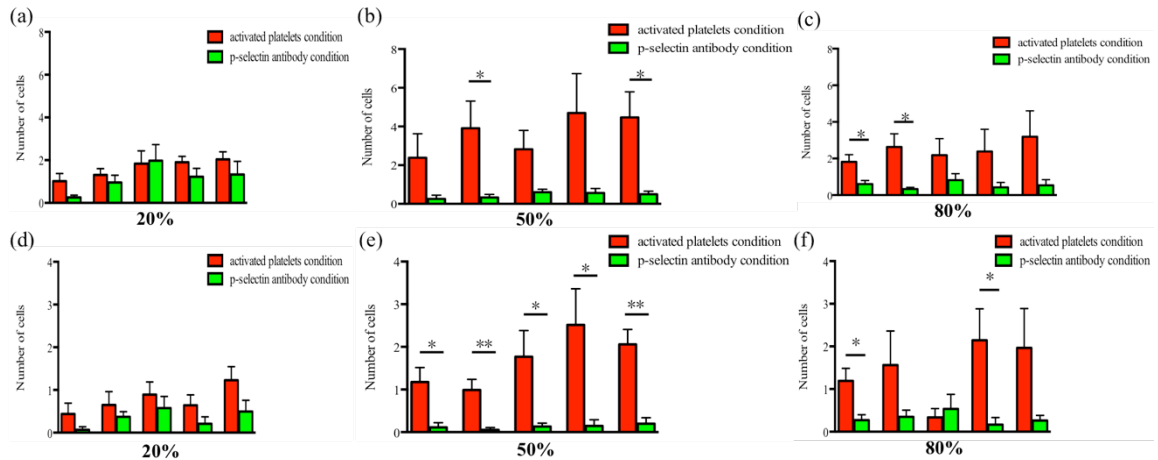


**Figure 6-12. The effects of p-selectin antibody incubation on cell adhesion. The results of platelet adhesion in different regions of (a) 20% narrow channel; (b) 50% narrow channel and (c) 80% narrow channel with (green) or without (red) p-selectin antibody incubation. The results of neutrophil adhesion in different regions of (d) 20% narrow channel; (e) 50% narrow channel and (f) 80% narrow channel with (green) or without (red) p-selectin antibody incubation. For all graphs, the columns from left to right represent up normal, inlet, narrow, outlet, and down normal part, respectively (indicated in Fig. 6-3(a)). Platelets and neutrophils from five different donors were used in each condition for data analysis, \*,  $p < 0.05$ , \*\*,  $p < 0.005$ , using a two-tailed unpaired t-test. Error bars represent standard error of the mean.**

significant differences were found in the inlet and down normal regions of the 50% narrow channels (Fig. 6-13 (d)-(f)). Similarly, CD41/CD61 also contributes to platelet adhesion while the introduction of antibody molecules decreased the platelet adhesion in microfluidic channels (Fig. 6-13 (a)-(c)). In addition to the examination of platelet surface receptor molecules, an important type of receptor molecule on the neutrophil surface, CD11b,<sup>31,32</sup> was considered in the antibody study. The results (Fig. 6-14) revealed that neutrophil adhesion with antibody incubation was also most sensitive to the dimension of the 50% narrow channel, and incubation with the antibody significantly decreased the number of neutrophils attaching to the endothelial cell layer in almost all regions of the 50% narrow channel, but the impacts of antibody incubation on neutrophil adhesion in the 20% and 80% narrow channels is limited due to less significant differences found for these two microfluidic channels. In conclusion, both platelet and neutrophil activation play the important role in promoting neutrophil adhesion in our microfluidic model; more importantly, neutrophil adhesion is highly regulated by the shear rate level produced in the microfluidic channel while the blocking effects of antibody addition is most prominent in the 50% narrow channel.

#### **6-4. Conclusion**

A simple microfluidic channel system was developed in this study to investigate the adhesion behaviors of platelets and neutrophils on the endothelial cell layer. These studies revealed that the expression of adhesion molecules on endothelial cell surfaces was enhanced by the shear rates produced in various microfluidic channels, but there is

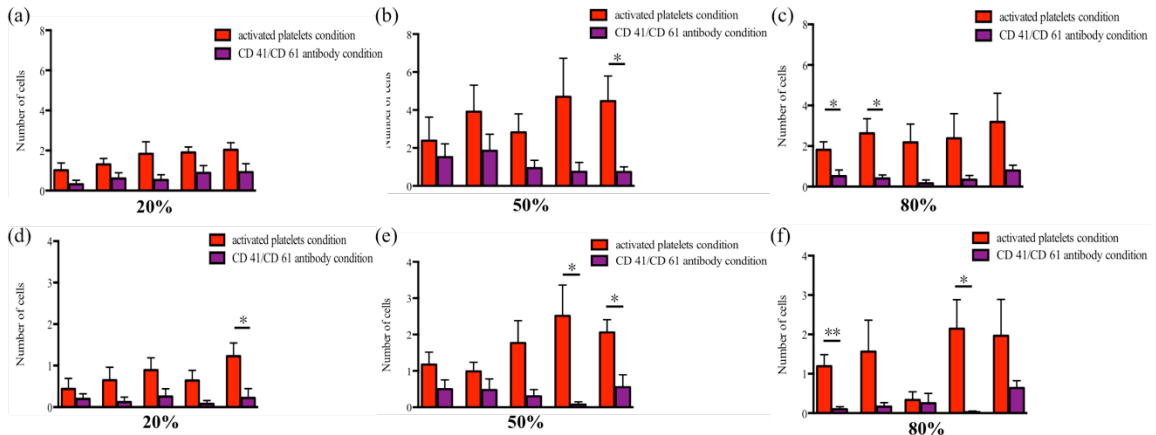


**Figure 6-13. The effects of CD41/CD61 antibody incubation on cell adhesion. The results of platelet adhesion in different regions of (a) 20% narrow channel; (b) 50% narrow channel and (c) 80% narrow channel with (purple) or without (red) CD41/CD61 antibody incubation. The results of neutrophil adhesion in different regions of (d) 20% narrow channel; (e) 50% narrow channel and (f) 80% narrow channel with (purple) or without (red) p-selectin antibody incubation. For all the graphs, the columns from left to right represent up normal, inlet, narrow, outlet, and down normal part, respectively (indicated in Fig. 6-3(a)). Platelets and neutrophils from five different donors were used in each condition for data analysis, \*,  $p < 0.05$ , \*\*,  $p < 0.005$ , using a two-tailed unpaired t-test. Error bars represent standard error of the mean.**

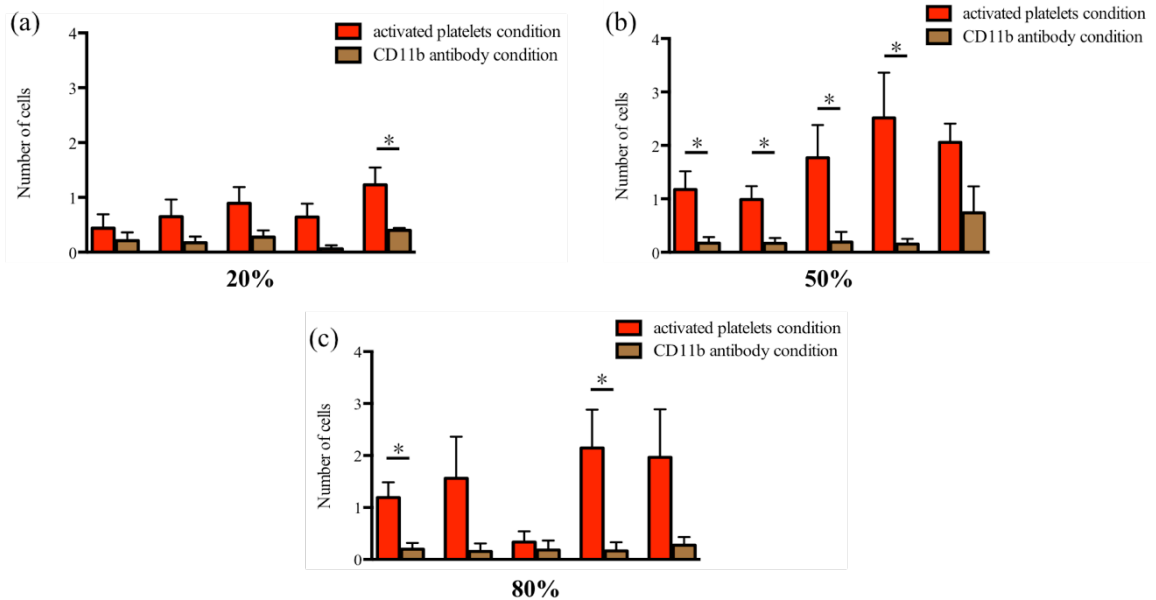


**Figure 6-14. The effects of CD11b antibody incubation on neutrophil adhesion. (a) The results of neutrophil adhesion in different regions of 20% narrow channel. (b) The results of neutrophil adhesion in different regions of 50% narrow channel. (c) The results of neutrophil adhesion in different regions of 80% narrow channel. For all the graphs, the columns from left to right represent up normal, inlet, narrow, outlet, and down normal part, respectively (indicated in Fig. 6-3(a)). Neutrophils from five different donors were used in each condition for data analysis, \*,  $p < 0.05$ , using a two-tailed unpaired t-test. Error bars represent standard error of the mean.**

no statistical difference among the channel dimensions considered herein. Shear rate is able to promote the aggregation of platelets and neutrophils in 20% or 50% narrow channels, and a delicate balance exists between the shear rate level and the dwell time of cells in the microfluidic channel. Larger shear rate produced by narrower channels may induce higher cell activation levels, but the dwell time of cells in these channels are too short for activation. Finally, the mechanisms of the platelet-neutrophil interactions in the microfluidic system were examined in detail. Through blocking the surface receptor molecules using the corresponding antibody molecules, we can conclude that several important surface receptor molecules (p-selectin, CD41/CD61, and CD11b) are involved in the platelet-neutrophil interactions, and the effects of activated platelets on neutrophil adhesion are regulated by the dimension of microfluidic channel – neutrophil adhesion was influenced most strongly in the 50% narrow channel. This study presents a simple model to study platelet and neutrophil adhesion on endothelial cell layers and systematically reveals the effects of different factors on cell adhesion behaviors, providing mechanistic insights on the process of platelet-neutrophil interactions.

## Perspective

As described in the chapters above, microfluidics has been successfully utilized as a powerful tool for cell biology studies. The stable chemical gradients created in the microfluidic channels allow study of the interactions of neutrophils with various physiologically relevant factors in the migratory process, such as drug stimulation, complicated chemoattractant gradient patterns, and endothelial cell angiogenesis. Also, we demonstrated the use of microfluidics to recapitulate heterotypic cellular interactions in an integrated biomimetic environment. Lastly, the relationship between cell adhesion and shear rate levels was extensively probed in a simple microfluidic system. All these efforts offer a novel research platform with the ability to simulate physiological microenvironments and characterize cellular behaviors with a high spatiotemporal resolution; more importantly, the obtained results are able to reveal the mechanistic insights on the pathogenesis of relevant diseases. Based on the current achievements, future work should focus on developing more complicated *in vivo*-like milieu inside microfluidic devices to explore cellular response in the context of diseases. For instance, the hypoxia condition can be combined with the endothelial angiogenesis to study the mechanisms of tumor growth and migration since both hypoxia and angiogenesis are important characteristics of cancer. A highly integrated biomimetic environment based on microfluidic platform can even effectively simulate the functions of human organs much like “organ-on-a-chip” mentioned in the Chapter 1. In this thesis, we have partially presented a microfluidic vascular model to examine the behaviors of different types of blood cells by creating a three-dimensional endothelial cell wall. The long-term goal of

this field will be the generation of vascular network within microfluidic devices such that the functions and migration of relevant cell types are monitored in a more realistic environment.

Although great advances in understanding *in vivo* cellular behaviors have been achieved by using microfluidics technique, there are several limitations existing to impede the widespread adoption of microfluidics in biology research community. Some limitations have been mentioned in the conclusion part of Chapter 1, such as the connection with detection methods, human cell use, and intricate device fabrication work. In addition to these drawbacks, the lack of standard microfluidic materials for cell culture has made cellular behaviors variable in different devices. As a result, the mass production methods for commercial microfluidic devices are quite different from the devices used in the lab due to different materials for the fabrication. Microscopic cell culture within the microfluidic device may also lead to the different results of cellular behaviors. Small volume use, large surface area to volume, and gas/nutrient exchange rates, should all be taken into account when performing microfluidic cell culture. Considering all these difficulties in the field of microfluidic cell research, it is a necessity to encourage collaboration between physical scientists and engineers, and molecular and cell biologists to remove the incompatibilities between the standards of engineers and biologists.

## References

### Chapter 1

- (1) Liu, Y.; Zeng, G. *J. Immunother.* **2012**, *35*, 299-308.
- (2) Asthagiri, A. R.; Lauffenburger, D. A. *Annu. Rev. Biomed. Eng.* **2000**, *2*, 31-53.
- (3) Tchao, J.; Han, L.; Lin, B.; Yang, L.; Tobita, K. *Sci. Rep.* **2014**, *4*, 6614-6624.
- (4) Jackson, S. P.; Nesbitt, W. S.; Westein, E. *J. Thromb. Haemost.* **2009**, *7*, 17-20.
- (5) Whitesides, G. M. *Nature* **2006**, *442*, 368-373.
- (6) Yin, H.; Marshall, D. *Curr. Opin. Biotechnol.* **2012**, *23*, 110-119.
- (7) Spurgeon, S. L.; Jones, R. C.; Ramakrishnan, R. *PLoS ONE* **2008**, *3*, e1662.
- (8) Wang, L.; Li, P. C. H. *Anal. Chim. Acta* **2011**, *687*, 12-27.
- (9) Zheng, B.; Roach, L. S.; Ismagilov, R. F. *J. Am. Chem. Soc.* **2003**, *125*, 11170-11171.
- (10) Roper, M. G.; Shackman, J. G.; Dahlgren, G. M.; Kennedy, R. T. *Anal. Chem.* **2003**, *75*, 4711-4717.
- (11) Ziaie, B.; Baldi, A.; Lei, M.; Gu, Y.; Siegel, R. A. *Adv. Drug Deliv. Rev.* **2004**, *56*, 145-172.
- (12) Yager, P.; Edwards, T.; Fu, E.; Helton, K.; Nelson, K.; Tam, M. R.; Weigl, B. H. *Nature* **2006**, *442*, 412-418.
- (13) Whitesides, G. M.; Ostuni, E.; Takayama, S.; Jiang, X.; Ingber, D. E. *Annu. Rev. Biomed. Eng.* **2001**, *3*, 335-373.
- (14) Zhang, X.; Li, L.; Luo, C. *Lab Chip* **2016**, *16*, 1757-1776.
- (15) Li, D.; Shao, L.; Chen, B.-C.; Zhang, X.; Zhang, M.; Moses, B.; Milkie, D. E.; Beach, J. R.; Hammer, J. A.; Pasham, M.; Kirchhausen, T.; Baird, M. A.; Davidson, M. W.; Xu, P.; Betzig, E. *Science* **2015**, *349*.
- (16) Puchner, E. M.; Walter, J. M.; Kasper, R.; Huang, B.; Lim, W. A. *Proc. Natl. Acad. Sci. U.S.A.* **2013**, *110*, 16015-16020.
- (17) Sigal, Yaron M.; Speer, Colenso M.; Babcock, Hazen P.; Zhuang, X. *Cell*, *163*, 493-505.
- (18) Jans, D. C.; Wurm, C. A.; Riedel, D.; Wenzel, D.; Stagge, F.; Deckers, M.; Rehling, P.; Jakobs, S. *Proc. Natl. Acad. Sci. U.S.A.* **2013**, *110*, 8936-8941.
- (19) Shim, S.-H.; Xia, C.; Zhong, G.; Babcock, H. P.; Vaughan, J. C.; Huang, B.; Wang, X.; Xu, C.; Bi, G.-Q.; Zhuang, X. *Proc. Natl. Acad. Sci. U.S.A.* **2012**, *109*, 13978-13983.
- (20) Honigsmann, A.; Mueller, V.; Ta, H.; Schoenle, A.; Sezgin, E.; Hell, S. W.; Eggeling, C. *Nat Commun.* **2014**, *5*, 5412.
- (21) Olshausen, Philipp v.; Defeu Soufo, Hervé J.; Wicker, K.; Heintzmann, R.; Graumann, Peter L.; Rohrbach, A. *Biophys. J.* *105*, 1171-1181.
- (22) Potcoava, M. C.; Futia, G. L.; Aughenbaugh, J.; Schlaepfer, I. R.; Gibson, E. A. *BIOMEDO* **2014**, *19*, 111605-111605.
- (23) Li, J.; Cheng, J.-X. *Sci. Rep.* **2014**, *4*, 6807.
- (24) Shen, Y.; Xu, F.; Wei, L.; Hu, F.; Min, W. *Angew. Chem. Int. Ed.* **2014**, *53*, 5596-5599.
- (25) Lu, F.-K.; Basu, S.; Igras, V.; Hoang, M. P.; Ji, M.; Fu, D.; Holtom, G. R.; Neel, V.

- A.; Freudiger, C. W.; Fisher, D. E.; Xie, X. S. *Proc. Natl. Acad. Sci. U.S.A.* **2015**, *112*, 11624-11629.
- (26) Fu, D.; Zhou, J.; Zhu, W. S.; Manley, P. W.; Wang, Y. K.; Hood, T.; Wylie, A.; Xie, X. S. *Nat. Chem.* **2014**, *6*, 614-622.
- (27) Amatore, C.; Arbault, S.; Guille, M.; Lemaître, F. *Chem. Rev.* **2008**, *108*, 2585-2621.
- (28) Bhargava, A.; Lin, X.; Novak, P.; Mehta, K.; Korchev, Y.; Delmar, M.; Gorelik, J. *Circ. Res.* **2013**, *112*, 1112-1120.
- (29) Liu, X.; Li, W.; Hou, T.; Dong, S.; Yu, G.; Li, F. *Anal. Chem.* **2015**, *87*, 4030-4036.
- (30) Norris, J. L.; Caprioli, R. M. *Chem. Rev.* **2013**, *113*, 2309-2342.
- (31) Prideaux, B.; Stoeckli, M. *J. Proteomics* **2012**, *75*, 4999-5013.
- (32) Hoshino, K.; Huang, Y.-Y.; Lane, N.; Huebschman, M.; Uhr, J. W.; Frenkel, E. P.; Zhang, X. *Lab Chip* **2011**, *11*, 3449-3457.
- (33) Kang, J. H.; Krause, S.; Tobin, H.; Mammoto, A.; Kanapathipillai, M.; Ingber, D. E. *Lab Chip* **2012**, *12*, 2175-2181.
- (34) Wang, C.; Ye, M.; Cheng, L.; Li, R.; Zhu, W.; Shi, Z.; Fan, C.; He, J.; Liu, J.; Liu, Z. *Biomaterials* **2015**, *54*, 55-62.
- (35) Wu, W.-T.; Martin, A. B.; Gandini, A.; Aubry, N.; Massoudi, M.; Antaki, J. F. *Microfluid. Nanofluid.* **2016**, *20*, 1-11.
- (36) Sofla, A.; Cirkovic, B.; Hsieh, A.; Miklas, J. W.; Filipovic, N.; Radisic, M. *Biomicrofluidics* **2013**, *7*, 014110.
- (37) Wang, X.; Chen, S.; Kong, M.; Wang, Z.; Costa, K. D.; Li, R. A.; Sun, D. *Lab Chip* **2011**, *11*, 3656-3662.
- (38) Liberale, C.; Cojoc, G.; Bragheri, F.; Minzioni, P.; Perozziello, G.; La Rocca, R.; Ferrara, L.; Rajamanickam, V.; Di Fabrizio, E.; Cristiani, I. *Sci. Rep.* **2013**, *3*, 1258.
- (39) Chen, Y.; Wu, T.-H.; Kung, Y.-C.; Teitell, M. A.; Chiou, P.-Y. *Analyst* **2013**, *138*, 7308-7315.
- (40) Carlo, D. D.; Wu, L. Y.; Lee, L. P. *Lab Chip* **2006**, *6*, 1445-1449.
- (41) Lin, L.; Chu, Y.-S.; Thiery, J. P.; Lim, C. T.; Rodriguez, I. *Lab Chip* **2013**, *13*, 714-721.
- (42) Wang, Y.; Tang, X.; Feng, X.; Liu, C.; Chen, P.; Chen, D.; Liu, B.-F. *Anal. Bioanal. Chem.* **2014**, *407*, 1139-1148.
- (43) Wang, L.; Flanagan, L. A.; Jeon, N. L.; Monuki, E.; Lee, A. P. *Lab Chip* **2007**, *7*, 1114-1120.
- (44) Moon, H.-S.; Kwon, K.; Kim, S.-I.; Han, H.; Sohn, J.; Lee, S.; Jung, H.-I. *Lab Chip* **2011**, *11*, 1118-1125.
- (45) Agresti, J. J.; Antipov, E.; Abate, A. R.; Ahn, K.; Rowat, A. C.; Baret, J.-C.; Marquez, M.; Klibanov, A. M.; Griffiths, A. D.; Weitz, D. A. *Proc. Natl. Acad. Sci. U.S.A.* **2010**, *107*, 4004-4009.
- (46) Ding, X.; Lin, S.-C. S.; Lapsley, M. I.; Li, S.; Guo, X.; Chan, C. Y.; Chiang, I. K.; Wang, L.; McCoy, J. P.; Huang, T. J. *Lab Chip* **2012**, *12*, 4228-4231.
- (47) Zinchenko, A.; Devenish, S. R. A.; Kintses, B.; Colin, P.-Y.; Fischlechner, M.; Hollfelder, F. *Anal. Chem.* **2014**, *86*, 2526-2533.

- (48) Warkiani, M. E.; Guan, G.; Luan, K. B.; Lee, W. C.; Bhagat, A. A. S.; Kant Chaudhuri, P.; Tan, D. S.-W.; Lim, W. T.; Lee, S. C.; Chen, P. C. Y.; Lim, C. T.; Han, J. *Lab Chip* **2014**, *14*, 128-137.
- (49) Wyatt Shields Iv, C.; Reyes, C. D.; Lopez, G. P. *Lab Chip* **2015**, *15*, 1230-1249.
- (50) Husic, S.; Murthy, S. K.; Koppes, A. N. *Anal. Chem.* **2016**, *88*, 354-380.
- (51) Zaretsky, I.; Polonsky, M.; Shifrut, E.; Reich-Zeliger, S.; Antebi, Y.; Aidelberg, G.; Waysbort, N.; Friedman, N. *Lab Chip* **2012**, *12*, 5007-5015.
- (52) Deng, Y.; Zhang, Y.; Sun, S.; Wang, Z.; Wang, M.; Yu, B.; Czajkowsky, D. M.; Liu, B.; Li, Y.; Wei, W.; Shi, Q. *Sci. Rep.* **2014**, *4*, 7499.
- (53) Ridley, A. J.; Schwartz, M. A.; BurrIDGE, K.; Firtel, R. A.; Ginsberg, M. H.; Borisy, G.; Parsons, J. T.; Horwitz, A. R. *Science* **2003**, *302*, 1704-1709.
- (54) Kim, D.; Haynes, C. L. *Anal. Chem.* **2012**, *84*, 6070-6078.
- (55) Kim, D.; Haynes, C. L. *Anal. Chem.* **2013**, *85*, 10787-10796.
- (56) Wu, X.; Kim, D.; Young, A. T.; Haynes, C. L. *Analyst* **2014**, *139*, 4056-4063.
- (57) Nguyen, T. A.; Yin, T.-I.; Reyes, D.; Urban, G. A. *Anal. Chem.* **2013**, *85*, 11068-11076.
- (58) Sarkar, S.; Cohen, N.; Sabhachandani, P.; Konry, T. *Lab Chip* **2015**, *15*, 4441-4450.
- (59) Chen, Q.; Wu, J.; Zhang, Y.; Lin, J.-M. *Anal. Chem.* **2012**, *84*, 1695-1701.
- (60) Li, Y.-S. J.; Haga, J. H.; Chien, S. *J. Biomech.* **38**, 1949-1971.
- (61) Jang, K.-J.; Cho, H. S.; Kang, D. H.; Bae, W. G.; Kwon, T.-H.; Suh, K.-Y. *Integr. Biol.* **2011**, *3*, 134-141.
- (62) Muthard, R. W.; Diamond, S. L. *Lab Chip* **2013**, *13*, 1883-1891.
- (63) Varma, S.; Voldman, J. *Lab Chip* **2015**, *15*, 1563-1573.
- (64) Tang, Z.; Akiyama, Y.; Itoga, K.; Kobayashi, J.; Yamato, M.; Okano, T. *Biomaterials* **2012**, *33*, 7405-7411.
- (65) Vaupel, P.; Mayer, A. *Cancer Metastasis Rev.* **2007**, *26*, 225-239.
- (66) Funamoto, K.; Zervantonakis, I. K.; Liu, Y.; Ochs, C. J.; Kim, C.; Kamm, R. D. *Lab Chip* **2012**, *12*, 4855-4863.
- (67) Nourmohammadzadeh, M.; Lo, J. F.; Bochenek, M.; Mendoza-Elias, J. E.; Wang, Q.; Li, Z.; Zeng, L.; Qi, M.; Eddington, D. T.; Oberholzer, J.; Wang, Y. *Anal. Chem.* **2013**, *85*, 11240-11249.
- (68) Chang, C.-W.; Cheng, Y.-J.; Tu, M.; Chen, Y.-H.; Peng, C.-C.; Liao, W.-H.; Tung, Y.-C. *Lab Chip* **2014**, *14*, 3762-3772.
- (69) Kim, J.; Hegde, M.; Jayaraman, A. *Lab Chip* **2010**, *10*, 43-50.
- (70) Zervantonakis, I. K.; Hughes-Alford, S. K.; Charest, J. L.; Condeelis, J. S.; Gertler, F. B.; Kamm, R. D. *Proc. Natl. Acad. Sci. U.S.A.* **2012**, *109*, 13515-13520.
- (71) Chen, M. B.; Srigunapalan, S.; Wheeler, A. R.; Simmons, C. A. *Lab Chip* **2013**, *13*, 2591-2598.
- (72) Huh, D.; Torisawa, Y.-s.; Hamilton, G. A.; Kim, H. J.; Ingber, D. E. *Lab Chip* **2012**, *12*, 2156-2164.
- (73) van de Stolpe, A.; den Toonder, J. *Lab Chip* **2013**.
- (74) Ghaemmaghani, A. M.; Hancock, M. J.; Harrington, H.; Kaji, H.; Khademhosseini, A. *Drug Discov. Today* **2012**, *17*, 173-181.

- (75) Huh, D.; Matthews, B. D.; Mammoto, A.; Montoya-Zavala, M.; Hsin, H. Y.; Ingber, D. E. *Science* **2010**, *328*, 1662-1668.
- (76) Domansky, K.; Inman, W.; Serdy, J.; Dash, A.; Lim, M. H. M.; Griffith, L. G. *Lab Chip* **2010**, *10*, 51-58.
- (77) Agarwal, A.; Goss, J. A.; Cho, A.; McCain, M. L.; Parker, K. K. *Lab Chip* **2013**, *13*, 3599-3608.
- (78) Sung, J. H.; Kam, C.; Shuler, M. L. *Lab Chip* **2010**, *10*, 446-455.

## **Chapter 2**

- (1) Mantovani, A.; Cassatella, M. A.; Costantini, C.; Jaillon, S. *Nat. Rev. Immunol.* **2011**, *11*, 519-531.
- (2) Douwes, J.; Gibson, P.; Pekkanen, J.; Pearce, N. *Thorax* **2002**, *57*, 643-648.
- (3) Monteseirin, J. *J. Invest. Allergol. Clin. Immunol.* **2009**, *19*, 340-354.
- (4) Quint, J. K.; Wedzicha, J. A. *J. Allergy and Clin. Immunol.* **2007**, *119*, 1065-1071.
- (5) Hoenderdos, K.; Condliffe, A. *Am. J. Respir. Cell Mol. Biol.* **2013**, *48*, 531-539.
- (6) Hurd, S. *Chest* **2000**, *117*, 1-4.
- (7) Fahy, J. V. *Proc. Am. Thorac. Soc.* **2009**, *6*, 256-259.
- (8) Barnes, P. J. *J. Allergy and Clin. Immunol.* **2007**, *119*, 1055-1062.
- (9) Simpson, J. L.; Phipps, S.; Gibson, P. G. *Pharmacol. Ther.* **2009**, *124*, 86-95.
- (10) Qazi, B. S.; Tang, K.; Qazi, A. *Int. J. Inflamm.* **2011**, *2011*:908468.
- (11) Richardson, R. M.; Pridgen, B. C.; Haribabu, B.; Ali, H.; Snyderman, R. *J. Biol. Chem.* **1998**, *273*, 23830-23836.
- (12) Zeilhofer, H. U.; Schorr, W. *Curr. Opin. Hematol.* **2000**, *7*, 178-182.
- (13) Cicchetti, G.; Allen, P. G.; Glogauer, M. *Crit. Rev. Oral Biol. Med.* **2002**, *13*, 220-228.
- (14) Rhee, S. G.; Bae, Y. S. *J. Biol. Chem.* **1997**, *272*, 15045-15048.
- (15) Wu, D.; Huang, C. K.; Jiang, H. *J. Cell Sci.* **2000**, *113*, 2935-2940.
- (16) Chapman, R. W.; Phillips, J. E.; Hipkin, R. W.; Curran, A. K.; Lundell, D.; Fine, J. S. *Pharmacol. Ther.* **2009**, *121*, 55-68.
- (17) Vlahos, C. J.; Matter, W. F.; Brown, R. F.; Traynorkaplan, A. E.; Heyworth, P. G.; Prossnitz, E. R.; Ye, R. D.; Marder, P.; Schelm, J. A.; Rothfuss, K. J.; Serlin, B. S.; Simpson, P. J. *J. Immunol.* **1995**, *154*, 2413-2422.
- (18) Sapey, E.; Stockley, J. A.; Greenwood, H.; Ahmad, A.; Bayley, D.; Lord, J. M.; Insall, R. H.; Stockley, R. A. *Am. J. Respir. Crit. Care Med.* **2011**, *183*, 1176-1186.
- (19) Akgul, C.; Moulding, D. A.; Edwards, S. W. *FEBS Letters* **2001**, *487*, 318-322.
- (20) Yasui, K.; Agematsu, K.; Shinozaki, K.; Hokibara, S.; Nagumo, H.; Yamada, S.; Kobayashi, N.; Komiyama, A. *J. Leukocyte Biol.* **2000**, *68*, 194-200.
- (21) Culpitt, S. V.; de Matos, C.; Russell, R. E.; Donnelly, L. E.; Rogers, D. F.; Barnes, P. J. *Am. J. Respir. Crit. Care Med.* **2002**, *165*, 1371-1376.
- (22) Condoneto, A.; Vilela, M. M. S.; Cambiucci, E. C.; Ribeiro, J. D.; Guglielmi, A. A. G.; Magna, L. A.; Denucci, G. *Br. J. Clin. Pharmacol.* **1991**, *32*, 557-561.
- (23) Li, Y.-H.; Zhu, C. *Clin. Exp. Metastasis* **1999**, *17*, 423-429.
- (24) Zicha, D.; Dunn, G. A.; Brown, A. F. *J. Cell Sci.* **1991**, *99*, 769-775.

- (25) Toetsch, S.; Olwell, P.; Prina-Mello, A.; Volkov, Y. *Integr. Biol.* **2009**, *1*, 170-181.
- (26) Whitesides, G. M. *Nature* **2006**, *442*, 368-373.
- (27) Oh, H.; Siano, B.; Diamond, S. Neutrophil Isolation Protocol. **2008**, e745.
- (28) Lin, F.; Nguyen, C.-C.; Wang, S.-J.; Saadi, W.; Gross, S.; Jeon, N. *Ann. Biomed. Eng.* **2005**, *33*, 475-482.
- (29) Gryniewicz, G.; Poenie, M.; Tsien, R. Y. *J. Biol. Chem.* **1985**, *260*, 3440-3450.
- (30) Xu, Y.; Loison, F.; Luo, H. R. *Proc. Natl. Acad. Sci. U.S.A.* **2010**, *107*, 2950-2955.
- (31) Simon, H.-U. *Immunol. Rev.* **2003**, *193*, 101-110.
- (32) Fox, S.; Leitch, A. E.; Duffin, R.; Haslett, C.; Rossi, A. G. *J. Innate Immun.* **2010**, *2*, 216-227.
- (33) Yasui, K.; Hu, B.; Nakazawa, T.; Agematsu, K.; Komiyama, A. *J. Clin. Invest.* **1997**, *100*, 1677-1684.
- (34) Mentz, F.; Mossalayi, M.; Ouaz, F.; Baudet, S.; Issaly, F.; Ktorza, S.; Semichon, M.; Binet, J.; Merle-Beral, H. *Blood* **1996**, *88*, 2172-2182.
- (35) Yasui, K.; Agematsu, K.; Shinozaki, K.; Hokibara, S.; Nagumo, H.; Nakazawa, T.; Komiyama, A. *J. Leukocyte Biol.* **2000**, *67*, 529-535.
- (36) White, J. R.; Lee, J. M.; Young, P. R.; Hertzberg, R. P.; Jurewicz, A. J.; Chaikin, M. A.; Widdowson, K.; Foley, J. J.; Martin, L. D.; Griswold, D. E.; Sarau, H. M. *J. Biol. Chem.* **1998**, *273*, 10095-10098.
- (37) Weiner, O. D.; Neilsen, P. O.; Prestwich, G. D.; Kirschner, M. W.; Cantley, L. C.; Bourne, H. R. *Nat. Cell Biol.* **2002**, *4*, 509-513.
- (38) Vlahos, C. J.; Matter, W. F.; Hui, K. Y.; Brown, R. F. *J. Biol. Chem.* **1994**, *269*, 5241-5248.

### **Chapter 3**

- (1) Amulic, B.; Cazalet, C.; Hayes, G. L.; Metzler, K. D.; Zychlinsky, A. *Ann. Rev. Immunol.* **2012**, *30*, 459-489.
- (2) Kolaczowska, E.; Kubes, P. *Nat Rev Immunol.* **2013**, *13*, 159-175.
- (3) Burg, N. D.; Pillinger, M. H. *Clin. Immunol.* **2001**, *99*, 7-17.
- (4) Wright, H. L.; Moots, R. J.; Bucknall, R. C.; Edwards, S. W. *Rheumatology* **2010**, *49*, 1618-1631.
- (5) Borregaard, N. *Immunity* **2010**, *33*, 657-670.
- (6) van Buul, J. D.; Hordijk, P. L. *Arterioscler. Thromb. Vasc. Biol.* **2004**, *24*, 824-833.
- (7) Roth, S. J.; Carr, M. W.; Rose, S. S.; Springer, T. A. *J. Immunol. Methods* **1995**, *188*, 97-116.
- (8) Ding, Z.; Xiong, K.; Issekutz, T. B. *J. Leukocyte Biol.* **2001**, *69*, 458-466.
- (9) Xu, J.; Gao, X.-P.; Ramchandran, R.; Zhao, Y.-Y.; Vogel, S. M.; Malik, A. B. *Nat. Immunol.* **2008**, *9*, 880-886.
- (10) Whitesides, G. M. *Nature* **2006**, *442*, 368-373.
- (11) Chung, S.; Sudo, R.; Mack, P. J.; Wan, C.-R.; Vickerman, V.; Kamm, R. D. *Lab Chip* **2009**, *9*, 269-275.
- (12) Jeong, G. S.; Han, S.; Shin, Y.; Kwon, G. H.; Kamm, R. D.; Lee, S.-H.; Chung, S. *Anal. Chem.* **2011**, *83*, 8454-8459.
- (13) Polacheck, W. J.; Charest, J. L.; Kamm, R. D. *Proc. Natl. Acad. Sci. U.S.A.* **2011**,

108, 11115-11120.

- (14) Chen, M. B.; Srigunapalan, S.; Wheeler, A. R.; Simmons, C. A. *Lab Chip* **2013**, *13*, 2591-2598.
- (15) Han, S.; Yan, J.-J.; Shin, Y.; Jeon, J. J.; Won, J.; Eun Jeong, H.; Kamm, R. D.; Kim, Y.-J.; Chung, S. *Lab Chip* **2012**, *12*, 3861-3865.
- (16) Kim, D.; Haynes, C. L. *Anal. Chem.* **2013**, *85*, 10787-10796.
- (17) Sackmann, E. K.; Berthier, E.; Young, E. W. K.; Shelef, M. A.; Wernimont, S. A.; Huttenlocher, A.; Beebe, D. J. *Blood*, **2012**, *120*, e45-e53.
- (18) Schaff, U. Y.; Xing, M. M. Q.; Lin, K. K.; Pan, N.; Jeon, N. L.; Simon, S. I. *Lab Chip* **2007**, *7*, 448-456.
- (19) Snyderman, R.; Pike, M. C. *Ann. Rev. Immunol.* **1984**, *2*, 257-281.
- (20) Sadik, C. D.; Kim, N. D.; Luster, A. D. *Trends Immunol.* *32*, 452-460.
- (21) Van Eeden, S. E.; Terashima, T. *Leuk. Lymphoma* **2000**, *37*, 259-271.
- (22) Reilly, I. A.; Knapp, H. R.; Fitzgerald, G. A. *J. Clin. Pathol.* **1988**, *41*, 1163-1167.
- (23) Mathis, S. P.; Jala, V. R.; Lee, D. M.; Haribabu, B. *J. Immunol.* **2010**, *185*, 3049-3056.
- (24) Cavicchioni, G.; Fraulini, A.; Falzarano, S.; Spisani, S. *Eur. J. Med. Chem.* **2009**, *44*, 4926-4930.
- (25) Pellegatta, F.; Lu, Y.; Radaelli, A.; Zocchi, M. R.; Ferrero, E.; Chierchia, S.; Gaja, G.; Ferrero, M. E. *Br. J. Pharmacol.* **1996**, *118*, 471-476.
- (26) Pellegatta, F.; Chierchia, S. L.; Zocchi, M. R. *J. Biol. Chem.* **1998**, *273*, 27768-27771.
- (27) Zheng, Y.; Chen, J.; Craven, M.; Choi, N. W.; Totorica, S.; Diaz-Santana, A.; Kermani, P.; Hempstead, B.; Fischbach-Teschl, C.; López, J. A.; Stroock, A. D. *Proc. Natl. Acad. Sci. U.S.A.* **2012**, *109*, 9342-9347.
- (28) Oh, H.; Siano, B.; Diamond, S. *Visualized Exp.*, **2008**, *17*, e745. DOI: 10.3791/745.
- (29) Eaton, B. M.; Toothill, V. J.; Davies, H. A.; Pearson, J. D.; Mann, G. E. *J. Cell. Physiol.* **1991**, *149*, 88-99.
- (30) Dhanabal, M.; Ramchandran, R.; Waterman, M. J. F.; Lu, H.; Knebelmann, B.; Segal, M.; Sukhatme, V. P. *J. Biol. Chem.* **1999**, *274*, 11721-11726.
- (31) Heidemann, J.; Ogawa, H.; Dwinell, M. B.; Rafiee, P.; Maaser, C.; Gockel, H. R.; Otterson, M. F.; Ota, D. M.; Lügering, N.; Domschke, W.; Binion, D. G. *J. Biol. Chem.* **2003**, *278*, 8508-8515.
- (32) Li, A.; Dubey, S.; Varney, M. L.; Dave, B. J.; Singh, R. K. *J. Immunol.* **2003**, *170*, 3369-3376.
- (33) Stroka, K. M.; Hayenga, H. N.; Aranda-Espinoza, H. *PLoS ONE* **2013**, *8*, e61377.
- (34) Burns, A. R.; Bowden, R. A.; MacDonell, S. D.; Walker, D. C.; Odeunmi, T. O.; Donnachie, E. M.; Simon, S. I.; Entman, M. L.; Smith, C. W. *J. Cell Sci.* **2000**, *113*, 45-57.
- (35) Shaw, S. K.; Bamba, P. S.; Perkins, B. N.; Luscinskas, F. W. *J. Immunol.* **2001**, *167*, 2323-2330.
- (36) Boehme, M. W. J.; Raeth, U.; Scherbaum, W. A.; Galle, P. R.; Stremmel, W. *Clin & Exp. Immunol.* **2000**, *119*, 250-254.

- (37) Cho, H.; Hamza, B.; Wong, E. A.; Irimia, D. *Lab Chip* **2014**, *14*, 972-978.
- (38) Kim, D.; Haynes, C. L. *Anal. Chem.* **2012**, *84*, 6070-6078.
- (39) Lin, F.; Nguyen, C.-C.; Wang, S.-J.; Saadi, W.; Gross, S.; Jeon, N. *Ann. Biomed. Eng.* **2005**, *33*, 475-482.
- (40) Heit, B.; Liu, L.; Colarusso, P.; Puri, K. D.; Kubes, P. *J. Cell Sci.* **2008**, *121*, 205-214.
- (41) Heit, B.; Robbins, S. M.; Downey, C. M.; Guan, Z.; Colarusso, P.; Miller, B. J.; Jirik, F. R.; Kubes, P. *Nat. Immunol.* **2008**, *9*, 743-752.

#### **Chapter 4**

- (1) Otrrock, Z. K.; Mahfouz, R. A. R.; Makarem, J. A.; Shamseddine, A. I. *Blood Cells Mol. Dis.* **2007**, *39*, 212-220.
- (2) Battagay, E. J. *J. Mol. Med.* **1995**, *73*, 333-346.
- (3) Tonnesen, M. G.; Feng, X.; Clark, R. A. F. *J. Investig. Dermatol. Symp. Proc.* **2000**, *5*, 40-46.
- (4) Shimo, T.; Nakanishi, T.; Nishida, T.; Asano, M.; Kanyama, M.; Kuboki, T.; Tamatani, T.; Tezuka, K.; Takemura, M.; Matsumura, T.; Takigawa, M. *J. Biochem.* **1999**, *126*, 137-145.
- (5) Reynolds, L. P.; Killilea, S. D.; Redmer, D. A. *FASEB J.* **1992**, *6*, 886-892.
- (6) Nishida, N.; Yano, H.; Nishida, T.; Kamura, T.; Kojiro, M. *Vasc. Health Risk Manag.* **2006**, *2*, 213-219.
- (7) Walsh, D. A. *Rheumatology* **1999**, *38*, 103-112.
- (8) Khurana, R.; Simons, M.; Martin, J. F.; Zachary, I. C. *Circulation* **2005**, *112*, 1813-1824.
- (9) Carmeliet, P.; Jain, R. K. Angiogenesis in cancer and other diseases. *Nature* **2000**, *407*, 249-257.
- (10) Jackson, J. R.; Seed, M. P.; Kircher, C. H.; Willoughby, D. A.; Winkler, J. D.: *FASEB J.* **1997**, *11*, 457-65.
- (11) Ribatti, D.; Crivellato, E.: Immune cells and angiogenesis. *J. Cell. Mol. Med.* **2009**, *13*, 2822-2833.
- (12) Noonan, D.; De Lerma Barbaro, A.; Vannini, N.; Mortara, L.; Albin, A. *Cancer Metast. Rev.* **2008**, *27*, 31-40.
- (13) Kolaczowska, E.; Kubes, P. *Nat. Rev. Immunol.* **2013**, *13*, 159-175.
- (14) Amulic, B.; Cazalet, C.; Hayes, G. L.; Metzler, K. D.; Zychlinsky, A. *Annu. Rev. Immunol.* **2012**, *30*, 459-489.
- (15) Kobayashi, S. D.; Voyich, J. M.; Burlak, C.; DeLeo, F. R. *Arch. Immunol. Ther. Exp.* **2005**, *53*, 505-517.
- (16) Kim, D.; Haynes, C. L. *Anal. Chem.* **2012**, *84*, 6070-6078.
- (17) Wu, X.; Kim, D.; Young, A. T.; Haynes, C. L. *Analyst* **2014**, *139*, 4056-4063.
- (18) Parkos, C. A.; Delp, C.; Arnaout, M. A.; Madara, J. L. *J. Clin. Invest.* **1991**, *88*, 1605-1612.
- (19) Kusaka, M.; Sudo, K.; Fujita, T.; Marui, S.; Itoh, F.; Ingber, D.; Folkman, J. *Biochem. Biophys. Res. Commun.* **1991**, *174*, 1070-1076.
- (20) Passaniti, A.; Taylor, R. M.; Pili, R.; Guo, Y.; Long, P. V.; Haney, J. A.; Pauly, R.

- R.; Grant, D. S.; Martin, G. R. *Lab. Invest.* **1992**, *67*, 519-528.
- (21) Ribatti, D.; Nico, B.; Vacca, A.; Roncali, L.; Burri, P. H.; Djonov, V. *Anat. Rec.* **2001**, *264*, 317-324.
- (22) Couffinhal, T.; Dufourcq, P.; Barandon, L.; Leroux, L.; Duplaa, C. *Front. Biosci.* **2009**, *14*, 3310-3325.
- (23) Auerbach, R.; Lewis, R.; Shinnars, B.; Kubai, L.; Akhtar, N. *Clin. Chem.* **2003**, *49*, 32-40.
- (24) Albini, A.; Benelli, R.; Noonan, D. M.; Brigati, C. *Int. J. Dev. Biol.* **2004**, *48*, 563-571.
- (25) Segura, I.; Serrano, A.; De Buitrago, G. G.; Gonzalez, M. A.; Abad, J. L.; Claveria, C.; Gomez, L.; Bernad, A.; Martinez-A, C.; Riese, H. H. *FASEB J.* **2002**, *16*, 833-841.
- (26) Staton, C. A.; Reed, M. W. R.; Brown, N. J. *Int. J. Exp. Pathol.* **2009**, *90*, 195-221.
- (27) Jeong, G. S.; Han, S.; Shin, Y.; Kwon, G. H.; Kamm, R. D.; Lee, S.-H.; Chung, S. *Anal. Chem.* **2011**, *83*, 8454-8459.
- (28) Li Jeon, N.; Baskaran, H.; Dertinger, S. K. W.; Whitesides, G. M.; Van De Water, L.; Toner, M. *Nat. Biotech.* **2002**, *20*, 826-830.
- (29) D'Haene, N.; Sauvage, S.; Maris, C.; Adanja, I.; Le Mercier, M.; Decaestecker, C.; Baum, L.; Salmon, I. *PLoS ONE* **2013**, *8*, e67029.
- (30) Vacca, A.; Bruno, M.; Boccarelli, A.; Coluccia, M.; Ribatti, D.; Bergamo, A.; Garbisa, S.; Sartor, L.; Sava, G. *Br. J. Cancer* **2002**, *86*, 993-998.
- (31) Dredge, K.; Marriott, J. B.; Macdonald, C. D.; Man, H. W.; Chen, R.; Muller, G. W.; Stirling, D.; Dalgleish, A. G. *Br. J. Cancer* **2002**, *87*, 1166-1172.
- (32) Gerhardt, H. *Organogenesis* **2008**, *4*, 241-246.
- (33) Hammond, M. E.; Lapointe, G. R.; Feucht, P. H.; Hilt, S.; Gallegos, C. A.; Gordon, C. A.; Giedlin, M. A.; Mullenbach, G.; Tekamp-Olson, P. *J. Immunol.* **1995**, *155*, 1428-1433.
- (34) Lin, F.; Nguyen, C. M.-C.; Wang, S.-J.; Saadi, W.; Gross, S. P.; Jeon, N. L. *Biochem. Biophys. Res. Comm.* **2004**, *319*, 576-581.
- (35) Han, S.; Yan, J.-J.; Shin, Y.; Jeon, J. J.; Won, J.; Eun Jeong, H.; Kamm, R. D.; Kim, Y.-J.; Chung, S. *Lab Chip* **2012**, *12*, 3861-3865.
- (36) Gendron, P. O.; Avaltroni, F.; Wilkinson, K. J. *J. Fluoresc.* **2008**, *18*, 1093-1101.
- (37) Waugh, D. J. J.; Wilson, C. *Clin. Cancer Res.* **2008**, *14*, 6735-6741.
- (38) Georganas, C.; Liu, H.; Perlman, H.; Hoffmann, A.; Thimmapaya, B.; Pope, R. M. *J. Immunol.* **2000**, *165*, 7199-7206.
- (39) Chen, Y.; Shi, M.; Yu, G.-Z.; Qin, X.-R.; Jin, G.; Chen, P.; Zhu, M.-H. *World J. Gastroentero.* **2012**, *18*, 1123-1129.
- (40) Lin, Y.; Huang, R.; Chen, L.; Li, S.; Shi, Q.; Jordan, C.; Huang, R.-P. *Int. J. Cancer* **2004**, *109*, 507-515.
- (41) Moore, K. L.; Patel, K. D.; Bruehl, R. E.; Li, F.; Johnson, D. A.; Lichenstein, H. S.; Cummings, R. D.; Bainton, D. F.; McEver, R. P. *J. Cell Biol.* **1995**, *128*, 661-671.
- (42) Yang, L.; Froio, R. M.; Sciuto, T. E.; Dvorak, A. M.; Alon, R.; Luscinskas, F. W. *Blood* **2005**, *106*, 584-592.
- (43) Borregaard, N. *Immunity* **2010**, *33*, 657-670.

- (44) Gerhardt, H.; Golding, M.; Fruttiger, M.; Ruhrberg, C.; Lundkvist, A.; Abramsson, A.; Jeltsch, M.; Mitchell, C.; Alitalo, K.; Shima, D.; Betsholtz, C. *J. Cell Biol.* **2003**, *161*, 1163-1177.
- (45) Rundhaug, J. E. *Clin. Cancer Res.* **2003**, *9*, 551-554.
- (46) Taraboletti, G.; D'Ascenzo, S.; Borsotti, P.; Giavazzi, R.; Pavan, A.; Dolo, V. *Am. J. Pathol.* **2002**, *160*, 673-680.
- (47) Dhanabal, M.; Ramchandran, R.; Waterman, M. J. F.; Lu, H.; Knebelmann, B.; Segal, M.; Sukhatme, V. P. *J. Biol. Chem.* **1999**, *274*, 11721-11726.
- (48) Taddei, L.; Chiarugi, P.; Brogelli, L.; Cirri, P.; Magnelli, L.; Raugei, G.; Ziche, M.; Granger, H. J.; Chiarugi, V.; Ramponi, G. *Biochem. Biophys. Res. Comm.* **1999**, *263*, 340-345.
- (49) Jin, X. M.; Bookstein, R.; Wills, K.; Avanzini, J.; Tsai, V.; LaFace, D.; Terracina, G.; Shi, B.; Nielsen, L. L. *Cancer Gene Ther.* **2001**, *8*, 982-989.
- (50) Kulke, M. H.; Bergsland, E. K.; Ryan, D. P.; Enzinger, P. C.; Lynch, T. J.; Zhu, A. X.; Meyerhardt, J. A.; Heymach, J. V.; Fogler, W. E.; Sidor, C.; Michelini, A.; Kinsella, K.; Venook, A. P.; Fuchs, C. S. *J. Clin. Oncol.* **2006**, *24*, 3555-3561.
- (51) Nyberg, P.; Heikkilä, P.; Sorsa, T.; Luostarinen, J.; Heljasvaara, R.; Stenman, U.-H.; Pihlajaniemi, T.; Salo, T. *J. Biol. Chem.* **2003**, *278*, 22404-22411.
- (52) Li, A.; Dubey, S.; Varney, M. L.; Dave, B. J.; Singh, R. K. *J. Immunol.* **2003**, *170*, 3369-3376.
- (53) Gaudry, M.; Brégerie, O.; Andrieu, V.; El Benna, J.; Pocard, M.-A.; Hakim, J. *Blood* **1997**, *90*, 4153-4161.
- (54) Webb, N. J. A.; Myers, C. R.; Watson, C. J.; Bottomley, M. J.; Brenchley, P. E. *Cytokine* **1998**, *10*, 254-257.
- (55) Hanai, J.-i.; Dhanabal, M.; Karumanchi, S. A.; Albanese, C.; Waterman, M.; Chan, B.; Ramchandran, R.; Pestell, R.; Sukhatme, V. P. *J. Biol. Chem.* **2002**, *277*, 16464-16469.
- (56) Wickström, S. A.; Alitalo, K.; Keski-Oja, J. *Cancer Res.* **2002**, *62*, 5580-5589.
- (57) Sudhakar, A.; Sugimoto, H.; Yang, C.; Lively, J.; Zeisberg, M.; Kalluri, R. *Proc. Natl. Acad. Sci. U. S. A.* **2003**, *100*, 4766-4771.

## **Chapter 5**

- (1) Fidler, I. J. *Nat. Rev. Cancer* **2003**, *3*, 453-458.
- (2) Gupta, G. P.; Massagué, J. *Cell* **2006**, *127*, 679-695.
- (3) Chambers, A. F.; Groom, A. C.; MacDonald, I. C. *Nat. Rev. Cancer* **2002**, *2*, 563-572.
- (4) Poste, G.; Fidler, I. J. The pathogenesis of cancer metastasis. *Nature* **1980**, *283*, 139-146.
- (5) Dudley, A. C. *Cold Spring Harb. Perspect. Med.* **2012**, *2*, a006536.
- (6) Nicolson, G. L. *Curr. Opin. Cell Biol.* **1989**, *1*, 1009-1019.
- (7) Yamaguchi, H.; Wyckoff, J.; Condeelis, J. *Curr. Opin. Cell Biol.* **2005**, *17*, 559-564.
- (8) Ebos, J. M. L.; Lee, C. R.; Cruz-Munoz, W.; Bjarnason, G. A.; Christensen, J. G.; Kerbel, R. S. *Cancer Cell* **2009**, *15*, 232-239.

- (9) Ferrara, N.; Hillan, K. J.; Gerber, H.-P.; Novotny, W. *Nat. Rev. Drug Discov.* **2004**, *3*, 391-400.
- (10) Yoneda, T.; Sasaki, A.; Dunstan, C.; Williams, P. J.; Bauss, F.; De Clerck, Y. A.; Mundy, G. R. *J. Clin. Invest.* **1997**, *99*, 2509-2517.
- (11) Welch, D. *Clin. Exp. Metastasis* **1997**, *15*, 272-306.
- (12) Ausprunk, D. H.; Folkman, J. *Microvasc. Res.* **1977**, *14*, 53-65.
- (13) Gassmann, P.; Kang, M.-L.; Mees, S.; Haier, J. *BMC Cancer* **2010**, *10*, 1-11.
- (14) Wyckoff, J. B.; Wang, Y.; Lin, E. Y.; Li, J.-f.; Goswami, S.; Stanley, E. R.; Segall, J. E.; Pollard, J. W.; Condeelis, J. *Cancer Res.* **2007**, *67*, 2649-2656.
- (15) Peyri, N.; Berard, M.; Fauvel-Lafeve, F.; Trochon, V.; Arbeille, B.; Lu, H.; Legrand, C.; Crepin, M. *Anticancer Res.* **2009**, *29*, 2347-2355.
- (16) Ingthorsson, S.; Sigurdsson, V.; Fridriksdottir, A., Jr.; Jonasson, J. G.; Kjartansson, J.; Magnusson, M. K.; Gudjonsson, T. *BMC Res. notes* **2010**, *3*, 184.
- (17) Kaji, H.; Yokoi, T.; Kawashima, T.; Nishizawa, M. *Lab Chip* **2009**, *9*, 427-432.
- (18) Hui, E. E.; Bhatia, S. N. *Proc. Natl. Acad. Sci. U.S.A.* **2007**, *104*, 5722-5726.
- (19) Dickinson, L. E.; Lutgebaucks, C.; Lewis, D. M.; Gerecht, S. *Lab Chip* **2012**, *12*, 4244-4248.
- (20) Smulovitz, C.; Dickinson, L. E.; Gerecht, S. *Israel J. Chem.* **2013**, *53*, 710-718.
- (21) Zervantonakis, I. K.; Hughes-Alford, S. K.; Charest, J. L.; Condeelis, J. S.; Gertler, F. B.; Kamm, R. D. *Proc. Natl. Acad. Sci. U.S.A.* **2012**, *109*, 13515-13520.
- (22) Chung, S.; Sudo, R.; Mack, P. J.; Wan, C.-R.; Vickerman, V.; Kamm, R. D. *Lab Chip* **2009**, *9*, 269-275.
- (23) Shin, M. K.; Kim, S. K.; Jung, H. *Lab Chip* **2011**, *11*, 3880-3887.
- (24) Waugh, D. J. J.; Wilson, C. *Clin. Cancer Res.* **2008**, *14*, 6735-6741.
- (25) Li, A.; Dubey, S.; Varney, M. L.; Dave, B. J.; Singh, R. K. *J. Immunol.* **2003**, *170*, 3369-3376.
- (26) Wu, Y.; Zhou, B. P. *Br. J. Cancer* **2010**, *102*, 639-644.
- (27) Balkwill, F. *Cancer Metastasis Rev.* **2006**, *25*, 409-416.
- (28) Lin, X.; Chen, Q.; Liu, W.; Zhang, J.; Wang, S.; Lin, Z.; Lin, J.-M. *Sci. Rep.* **2015**, *5*, 9643.
- (29) Acosta, M. A.; Jiang, X.; Huang, P.-K.; Cutler, K. B.; Grant, C. S.; Walker, G. M.; Gamsik, M. P. *Biomicrofluidics* **2014**, *8*, 054117.
- (30) Funamoto, K.; Zervantonakis, I. K.; Liu, Y.; Ochs, C. J.; Kim, C.; Kamm, R. D. *Lab Chip* **2012**, *12*, 4855-4863.
- (31) Pellegatta, F.; Lu, Y.; Radaelli, A.; Zocchi, M. R.; Ferrero, E.; Chierchia, S.; Gaja, G.; Ferrero, M. E. *Br. J. Pharmacol.* **1996**, *118*, 471-476.
- (32) Pellegatta, F.; Chierchia, S. L.; Zocchi, M. R. *J. Biol. Chem.* **1998**, *273*, 27768-27771.
- (33) Kim, D.; Haynes, C. L. *Anal. Chem.* **2013**, *85*, 10787-10796.
- (34) Chang, C.-W.; Cheng, Y.-J.; Tu, M.; Chen, Y.-H.; Peng, C.-C.; Liao, W.-H.; Tung, Y.-C. *Lab Chip* **2014**, *14*, 3762-3772.
- (35) Chen, Y.-A.; King, A. D.; Shih, H.-C.; Peng, C.-C.; Wu, C.-Y.; Liao, W.-H.; Tung, Y.-C. *Lab Chip* **2011**, *11*, 3626-3633.
- (36) Han, S.; Yan, J.-J.; Shin, Y.; Jeon, J. J.; Won, J.; Eun Jeong, H.; Kamm, R. D.;

- Kim, Y.-J.; Chung, S. *Lab Chip* **2012**, *12*, 3861-3865.
- (37) Tyn, M. T.; Gusek, T. W. *Biotechnol. Bioeng.* **1990**, *35*, 327-338.
- (38) Wu, X.; Newbold, M. A.; Haynes, C. L. *Analyst* **2015**, *140*, 5055-5064.
- (39) Eaton, B. M.; Toothill, V. J.; Davies, H. A.; Pearson, J. D.; Mann, G. E. *J. Cell. Physiol.* **1991**, *149*, 88-99.
- (40) Ferrara, N.; Gerber, H.-P.; LeCouter, J. The biology of VEGF and its receptors. *Nat. Med.* **2003**, *9*, 669-676.
- (41) Neufeld, G.; Cohen, T.; Gengrinovitch, S.; Poltorak, Z. *FASEB J.* **1999**, *13*, 9-22.
- (42) Papaioannou, T. G.; Stefanadis, C. *Hellenic J. Cardiol.* **2005**, *46*, 9-15.
- (43) Adamo, L.; Naveiras, O.; Wenzel, P. L.; McKinney-Freeman, S.; Mack, P. J.; Gracia-Sancho, J.; Suchy-Dicey, A.; Yoshimoto, M.; Lensch, M. W.; Yoder, M. C.; Garcia-Cardena, G.; Daley, G. Q. *Nature* **2009**, *459*, 1131-1135.
- (44) Song, J. W.; Munn, L. L. *Proc. Natl. Acad. Sci. U.S.A.* **2011**, *108*, 15342-15347.
- (45) Kashiwagi, S.; Tsukada, K.; Xu, L.; Miyazaki, J.; Kozin, S. V.; Tyrrell, J. A.; Sessa, W. C.; Gerweck, L. E.; Jain, R. K.; Fukumura, D. Perivascular nitric oxide gradients normalize tumor vasculature. *Nat Med* **2008**, *14*, 255-257.
- (46) Vaupel, P.; Mayer, A. *Cancer Metastasis Rev.* **2007**, *26*, 225-239.
- (47) Höckel, M.; Vaupel, P. *J. Natl. Cancer Inst.* **2001**, *93*, 266-276.
- (48) Vaupel, P.; Fortmeyer, H. P.; Runkel, S.; Kallinowski, F. *Cancer Res.* **1987**, *47*, 3496-3503.
- (49) Liu, Y.; Cox, S. R.; Morita, T.; Kourembanas, S. *Circ. Res.* **1995**, *77*, 638-643.
- (50) Enomoto, N.; Koshikawa, N.; Gassmann, M.; Hayashi, J.-I.; Takenaga, K. *Biochem. Biophys. Res. Commun.* **2002**, *297*, 346-352.
- (51) Freund, A.; Chauveau, C.; Brouillet, J.-P.; Lucas, A.; Lacroix, M.; Licznar, A.; Vignon, F.; Lazennec, G. *Oncogene* **2003**, *22*, 256-265.
- (52) Schwartz, B. M.; Hong, G.; Morrison, B. H.; Wu, W.; Baudhuin, L. M.; Xiao, Y.-J.; Mok, S. C.; Xu, Y. *Gynecol. Oncol.* **2001**, *81*, 291-300.

## **Chapter 6**

- (1) Maugeri, N.; Rovere-Querini, P.; Evangelista, V.; Covino, C.; Capobianco, A.; Bertilaccio, M. T. S.; Piccoli, A.; Totani, L.; Cianflone, D.; Maseri, A.; Manfredi, A. A. *Blood* **2009**, *113*, 5254-5265.
- (2) Lam, F. W.; Vijayan, K. V.; Rumbaut, R. E. *Compr. Physiol.* **2015**, *5*, 1265-1280.
- (3) Kolaczowska, E.; Kubes, P. *Nat. Rev. Immunol.* **2013**, *13*, 159-175.
- (4) Nathan, C. *Nat. Rev. Immunol.* **2006**, *6*, 173-182.
- (5) Amulic, B.; Cazalet, C.; Hayes, G. L.; Metzler, K. D.; Zychlinsky, A. Neutrophil Function: From Mechanisms to Disease. *Annu. Rev. Immunol.* **2012**, *30*, 459-489.
- (6) Davi, G.; Patrono, C. *N. Engl. J. Med.* **2007**, *357*, 2482-2494.
- (7) Semple, J. W.; Italiano, J. E.; Freedman, J. *Nat. Rev. Immunol.* **2011**, *11*, 264-274.
- (8) Wagner, D. D.; Burger, P. C. *Arterioscler. Thromb. Vasc. Biol.* **2003**, *23*, 2131-2137.
- (9) Savage, B.; Saldívar, E.; Ruggeri, Z. M. *Cell* **1996**, *84*, 289-297.
- (10) Ruggeri, Z. M.; Orje, J. N.; Habermann, R.; Federici, A. B.; Reininger, A. J. *Blood* **2006**, *108*, 1903-1910.

- (11) Ruggeri, Z. M.; Mendolicchio, G. L. *Circ. Res.* **2007**, *100*, 1673-1685.
- (12) Westein, E.; van der Meer, A. D.; Kuijpers, M. J. E.; Frimat, J.-P.; van den Berg, A.; Heemskerk, J. W. M. *Proc. Natl. Acad. Sci. U.S.A.* **2013**, *110*, 1357-1362.
- (13) Zwaginga, J. J.; Torres, H. I. G.; Lammers, J.-W. J.; Sixma, J. J.; Koenderman, L.; Kuijper, P. H. M. *Arterioscler. Thromb. Vasc. Biol.* **1999**, *19*, 1549-1554.
- (14) Koseoglu, S.; Meyer, A. F.; Kim, D.; Meyer, B. M.; Wang, Y.; Dalluge, J. J.; Haynes, C. L. *Anal. Chem.* **2015**, *87*, 413-421.
- (15) Jeong, S.-K.; Rosenson, R. S. *BMC Neurol.* **2013**, *13*, 36-36.
- (16) Hathcock, J. J. *Arterioscler. Thromb. Vasc. Biol.* **2006**, *26*, 1729-1737.
- (17) Li, M.; Hotaling, N. A.; Ku, D. N.; Forest, C. R. *PLoS ONE* **2014**, *9*, e82493.
- (18) Colace, T. V.; Tormoen, G. W.; McCarty, O. J. T.; Diamond, S. L. *Annu. Rev. Biomed. Eng.* **2013**, *15*, 283-303.
- (19) Sakariassen, K. S.; Bolhuis, P. A.; Sixma, J. J. *Nature* **1979**, *279*, 636-638.
- (20) Ruggeri, Z. M. *Best Pract. Res. Clin. Haematol.* **2001**, *14*, 257-279.
- (21) Jy, W.; Horstman, L. L.; Park, H.; Mao, W.-W.; Valant, P.; Ahn, Y. S. *Am. J. Hematol.* **1998**, *57*, 33-42.
- (22) Rinder, C. S.; Bohnert, J.; Rinder, H. M.; Mitchell, J.; Ault, K.; Hillman, R. *Anesthesiology* **1991**, *75*, 388-393.
- (23) Zhang, J.-n.; Bergeron, A. L.; Yu, Q.; Sun, C.; McIntire, L. V.; López, J. A.; *Thromb. Haemost.* **2002**, *88*, 817-821.
- (24) Bochner, B. S.; Lusinskas, F. W.; Gimbrone, M. A.; Newman, W.; Sterbinsky, S. A.; Derse-Anthony, C. P.; Klunk, D.; Schleimer, R. P. *J. Exp. Med.* **1991**, *173*, 1553-1557.
- (25) Yang, L.; Froio, R. M.; Sciuto, T. E.; Dvorak, A. M.; Alon, R.; Lusinskas, F. W. *Blood* **2005**, *106*, 584-592.
- (26) Lawrence, M. B.; Springer, T. A. *Cell* **1991**, *65*, 859-873.
- (27) Brown, K. K.; Henson, P. M.; Maclouf, J.; Moyle, M.; Ely, J. A.; Scott Worthen, G. *Am. J. Respir. Cell Mol. Biol.* **1998**, *18*, 100-110.
- (28) Konstantopoulos, K.; Neelamegham, S.; Burns, A. R.; Hentzen, E.; Kansas, G. S.; Snapp, K. R.; Berg, E. L.; Hellums, J. D.; Smith, C. W.; McIntire, L. V.; Simon, S. I. *Circulation* **1998**, *98*, 873-882.
- (29) Zarbock, A.; Singbartl, K.; Ley, K. *J. Clin. Invest.* **2006**, *116*, 3211-3219.
- (30) Zarbock, A.; Polanowska-Grabowska, R. K.; Ley, K. *Blood Rev.* **2007**, *21*, 99-111.
- (31) Parkos, C. A.; Delp, C.; Arnaout, M. A.; Madara, J. L. *J. Clin. Invest.* **1991**, *88*, 1605-1612.
- (32) Hu, H.; Varon, D.; Hjemdahl, P.; Savion, N.; Schulman, S.; Li, N. *Thromb. Haemost.* **2003**, *90*, 679-687.

# XIAOJIE WU

425 13th Ave SE, Apt 1103, Minneapolis, MN, 55414  
612-670-1740      wuxx0406@umn.edu

## EDUCATION

**Ph. D. Candidate, Chemistry** August 2016  
**Development of Biomimetic Microfluidic Platforms for Cellular Interaction Study**  
Department of Chemistry, University of Minnesota, Twin Cities      Minneapolis, MN

**Master of Science in Chemistry** March 2013  
Department of Chemistry, University of Minnesota, Twin Cities      Minneapolis, MN

**Bachelor of Science in Chemistry** June 2011  
**Highly Selective Detection of Single-Nucleotide Polymorphisms using Toehold-Mediated Strand Displacement Reaction**  
College of Chemistry and Molecular Engineering, Peking University      Beijing, China

## RESEARCH EXPERIENCE

### **Graduate Research Assistant, Haynes Lab**

Department of Chemistry, University of Minnesota, Twin Cities

- Initiate research creating *in vivo*-like microenvironments using microfluidic devices for cellular biology and pharmaceutical studies
- Explore the effects of asthma-related drugs on white blood cell migratory and apoptosis behaviors using a gradient microfluidic device
- Perform microfluidic studies of white blood cell transendothelial migration under physiologically relevant condition
- Investigate the mutually dependent relationship between white blood cell migration and endothelial angiogenesis in a biomimetic microfluidic microenvironment
- Develop a microfluidic cell-cell co-culture model for endothelial cell-tumor cell interactions studies in a biomimetic tumor-associated hypoxic environment
- Conduct platelet biology research using a microfluidic platform to examine the role of platelet-neutrophil aggregates in thrombosis disease model

### **Undergraduate Research, Liu Lab**

College of Chemistry and Molecular Engineering, Peking University

- Participated in detecting small protein with aptamer-functionalized gold nanoparticles based on quartz crystal microbalance (QCM) biosensor
- Established QCM platform for highly sensitive determination of mercury(II) ion using oligonucleotide-modified nanoparticles
- Designed and optimized fluorescent system to characterize single-nucleotide polymorphisms (SNP) using toehold-mediated strand displacement reaction

- Translated the toehold-mediated strand displacement reaction from fluorescent system to QCM platform for SNP detection with nanoparticle-aided signal enhancement

### **TEACHING EXPERIENCE**

**Teaching Assistant, General Chemistry Lab** September 2011-January 2012  
Department of Chemistry, University of Minnesota, Twin Cities

**Teaching Assistant, Analytical Chemistry Lab** January 2012-May 2013  
Department of Chemistry, University of Minnesota, Twin Cities

**Graduate Mentor of NNIN Research Experience for Undergraduates (REU)**  
Department of Chemistry, University of Minnesota, Twin Cities  
June 2013-August 2013

**Graduate Mentor of Lando REU program**  
Department of Chemistry, University of Minnesota, Twin Cities  
June 2015-August 2015

### **HONORS AND AWARDS**

**University of Minnesota**  
Beaker and Bunsen award for Graduate Student Research Symposium June 2014

**Peking University (Undergraduate)**  
National Undergraduate Student Innovative Training Program Funding  
September 2009-June 2010

Freshman Fellowship of Peking University September 2007

Silver prize in National Chemistry Olympiad Contest February 2007

### **PUBLICATIONS**

1. **Wu, X.**; Gruba, S.; Haynes, C. L. Perspective: The Power of Single Cell Analysis, *J. Am. Chem. Soc. in preparation.*
2. **Wu, X.**; Haynes, C. L. Investigating the Role of Platelet-Neutrophil Aggregates in Microfluidic Thrombosis Model, *in preparation.*
3. **Wu, X.**; Cliff, E.; Newbold, M. A.; Haynes, C. L. Using Microfluidic Platforms to Develop a Model of Cell-Cell Communication in Cancer, *in preparation.*
4. **Wu, X.**; Newbold, M. A.; Gao, Z.; Haynes, C. L. A Versatile Microfluidic Platform for the Study of Angiogenesis and Inflammation, *submitted to BMB: general subjects.*

5. **Wu, X.**; Newbold, M. A.; Haynes, C. L. Recapitulation of in vivo-like Neutrophil Transendothelial Migration Using a Microfluidic Platform, *Analyst*, 2015, **140**, 5055-5064.
6. **Wu, X.**; Kim, D.; Young, A. T.; Haynes, C. L. Exploring Inflammatory Disease Drug Effects on Neutrophil Function, *Analyst*, 2014, **139**, 4056-4063.
7. Kim, D.; **Wu, X.**; Young, A. T.; Haynes, C. L. Microfluidic-Based in vivo Mimetic Systems for the Study of Cellular Biology, *Acc. Chem. Res.*, 2014, **47**, 1165-1173.
8. Wang, D.; Tang, W.; **Wu, X.**; Wang, X.; Chen, G.; Chen, Q.; Li, N.; Liu, F. Highly Selective Detection of Single-Nucleotide Polymorphisms Using a Quartz Crystal Microbalance Biosensor Based on the Toehold-Mediated Strand Displacement Reaction, *Anal. Chem.*, 2012, **84**, 7008-7014.
9. Chen, Q.; **Wu, X.**; Wang, D.; Tang, W.; Li, N.; Liu, F. Oligonucleotide-Functionalized Gold Nanoparticle-Enhanced QCM-D Sensor for Mercury (II) Ions with High Sensitivity and Tunable Dynamic Range, *Analyst*, 2011, **136**, 2572-2577
10. Chen, Q.; Tang, W.; Wang, D.; **Wu, X.**; Li, N.; Liu, F. Amplified QCM-D Biosensor for Protein Based on Aptamer-Functionalized Gold Nanoparticles, *Biosens. Bioelectron.*, 2010, **26**, 575-579.

#### **PRESENTATIONS, POSTERS AND EXHIBITS**

1. **Wu, X.**; Cliff, E.; Newbold, M. A.; Haynes, C. L. Using Microfluidic Platforms to Develop a Model of Cell-Cell Communication in Cancer, Institute for Engineering in Medicine Annual Conference, Sep. 2015, Minneapolis.
2. **Wu, X.**; Cliff, E.; Newbold, M. A.; Haynes, C. L. Using Microfluidic Platforms to Develop a Model of Cell-Cell Communication in Cancer, Lab-On-a-Chip, Microfluidics & Microarrays World Congress, Sep. 2015, San Diego.
3. **Wu, X.**; Kim, D.; Haynes, C. L. Exploration of Drug Effects on Neutrophil Chemotaxis Based on Microfluidic Platform, 64<sup>th</sup> Pittcon Conference & Expo, Mar. 2013, Philadelphia.
4. Chen, Q.; **Wu, X.**; Wang, D.; Tang, W.; Li, N.; Liu, F. A Highly Sensitive QCM Sensor for Mercury(II) Based on Target Inhibition and Gold Nanoparticle Amplification, 3rd National Conference of Life Analytical Chemistry, Aug. 2010, Beijing.
5. Presented "Microfluidic Models of Vascular Functions: Recapitulation of in vivo-like Neutrophil Transendothelial Migration Using a Microfluidic Platform" at Graduate Student Research Symposium, Minneapolis, MN, June 10, 2014.
6. Presented "Microfluidic Models of Vascular Functions: Recapitulation of in vivo-like Neutrophil Transendothelial Migration Using a Microfluidic Platform" at Graduate Student Research Symposium, Minneapolis, MN, June 10, 2014.
7. Cliff, E.; **Wu, X.**; Haynes, C. L. Using Microfluidic Platforms to Develop a Model of Cell-Cell Communication in Cancer, 2015 Summer Undergraduate Research Symposium, Aug. 2015, Minneapolis.
8. Newbold, M. A.; **Wu, X.**; Haynes, C. L. Investigation of *in vivo*-like Neutrophil Transendothelial Migration Using a Microfluidic Platform, 2014 Summer

Undergraduate Research Symposium, Aug. 2014, Minneapolis.

9. Young, A. T.; **Wu, X.**; Haynes, C. L. Exploring the Effects of Theophylline on Neutrophil Function in Inflammatory Diseases, 2013 Summer Undergraduate Research Symposium, Aug. 2013, Minneapolis.

### **SKILLS**

**Microfluidic Device Fabrication:** Photolithography, Soft lithography, Oxygen Plasma System, Ion Etching System, Wafer Cutting, Surface Profiler, UV-Ozone Cleaner

**Laboratory Instruments:** Cell Culture Skills, Optical Microscopy (Epifluorescence, Confocal, Hyperspectral, Dark-field), Plate Reader, Cyclic Voltammetry, UV-Vis Spectroscopy, Fluorescence Spectroscopy, QCM Biosensor, SPR Biosensor

**Computer Software:** AutoCAD, COMSOL, Mathematics, ImageJ, Graphpad, Microsoft Office

### **PUBLIC AND OTHER SERVICE**

West 7<sup>th</sup> Community Center Outreach, St. Paul (educational chemistry experiments for kids) July 2012, 2013, 2014, 2015

Moderator of 2015 Chemistry Department Graduate Research Symposium June 2015